Thermal-stability Studies of Electrode Materials for Lithium-ion Batteries

by

Junwei Jiang

Submitted in partial fulfillment of the requirements
for the degree of Doctor of Philosophy

Dalhousie University
Halifax, Nova Scotia

April 2005

© Copyright by Junwei Jiang, 2005.

Library and Archives Canada

Published Heritage Branch

395 Wellington Street
Ottawa ON K1A 0N4
Canada

Bibliothèque et Archives Canada

Direction du Patrimoine de l'édition

395, rue Wellington
Ottawa ON K1A 0N4
Canada

Your file Votre référence
ISBN: 0-494-00963-2
Our file Notre référence
ISBN: 0-494-00963-2

NOTICE:
The author has granted a non-exclusive license allowing Library and Archives Canada to reproduce, publish, archive, preserve, conserve, communicate to the public by telecommunication or on the Internet, loan, distribute and sell theses worldwide, for commercial or non-commercial purposes, in microform, paper, electronic and/or any other formats.

The author retains copyright ownership and moral rights in this thesis. Neither the thesis nor substantial extracts from it may be printed or otherwise reproduced without the author's permission.

AVIS:
L'auteur a accordé une licence non exclusive permettant à la Bibliothèque et Archives Canada de reproduire, publier, archiver, sauvegarder, conserver, transmettre au public par télécommunication ou par l'Internet, prêter, distribuer et vendre des thèses partout dans le monde, à des fins commerciales ou autres, sur support microforme, papier, électronique et/ou autres formats.

L'auteur conserve la propriété du droit d'auteur et des droits moraux qui protège cette thèse. Ni la thèse ni des extraits substantiels de celle-ci ne doivent être imprimés ou autrement reproduits sans son autorisation.

In compliance with the Canadian Privacy Act some supporting forms may have been removed from this thesis.

While these forms may be included in the document page count, their removal does not represent any loss of content from the thesis.

Conformément à la loi canadienne sur la protection de la vie privée, quelques formulaires secondaires ont été enlevés de cette thèse.

Bien que ces formulaires aient inclus dans la pagination, il n'y aura aucun contenu manquant.

Canada

DALHOUSIE UNIVERSITY

To comply with the Canadian Privacy Act the National Library of Canada has requested that the following pages be removed from this copy of the thesis:

Preliminary Pages
- Examiners Signature Page (pii)
- Dalhousie Library Copyright Agreement (piii)

Appendices
- Copyright Releases (if applicable)

Table of Contents

List of Figures viii

List of Tables xxiii

Abstract xxv

List of Abbreviations and Symbols used xxvi

Acknowledgements xxx

1. Introduction

1.1 Battery development 1

1.2 Electrochemistry of lithium-ion batteries 1

1.3 State of the art lithium-ion battery technology today 4

1.3.1 Negative electrode material development 4

1.3.2 Trend for positive electrode material development 6

1.3.3 Salt 10

1.3.4 Solvent 12

1.3.5 Binder 13

1.3.6 Separator 14

1.4 Introduction to the thermal stability of lithium-ion batteries 14

1.4.1 Oven test 16

1.4.2 Thermal tests for lithium-ion battery electrode materials in the laboratory 18

1.4.2.1 Thermal Gravimetric Analysis (TGA) 19

1.4.2.2 Accelerating Rate Calorimetry (ARC) 19

1.4.3 Prediction of oven test behavior of full lithium-ion cells from ARC results 27

1.5 Scope of this thesis 27

2. Experimental section 29

2.1 Synthesis of electrode materials 29

2.1.1 $Li_4Ti_5O_{12}$ 29

2.1.2 VO_2 (B) 29

2.1.3 New positive electrode materials in the x $Li[Ni_{1/2}Mn_{1/2}]O_2$ • y $LiCoO_2$ • z $Li[Li_{1/3}Mn_{2/3}]O_2$ pseudoternary system 30
2.2 Electrode preparation for ARC or electrochemical tests 31
2.2.1 Electrodes with PVDF binder 31
2.2.1.1 Thin film electrodes for electrochemical tests 31
2.2.1.2 Pellet electrodes for ARC 31
2.2.2 Pellet electrodes with EPDM binder 32
2.2.3 Powder electrodes without binder 33
2.3 Cell construction for different electrodes 34
2.3.1 Cell construction for thin-film electrode 34
2.3.2 Cell construction for pellet electrodes 35
2.3.3 Cell construction for powder electrode without binder 36
2.4 Rinsing procedure for electrodes to be studied by ARC 37
2.5 Other techniques 39
2.5.1 Electrochemical Test System 39
2.5.2 Scanning Electron Microscopy (SEM) 39
2.5.3 Powder X-ray Diffraction 39
2.5.3.1 Rietveld refinement 40
2.5.4 Surface Area Measurement 41

3. Baseline studies of the thermal stability of $LiCoO_2$/MCMB cells 44
3.1 ARC studies 44
3.1.1 MCMB 44
3.1.1.1 Lithium intercalated graphite 45
3.1.1.2 Reactivity of $Li_{0.81}C_6$ with EPDM and PVDF binder 47
3.1.1.3 Reaction between $Li_{0.81}C_6$ and solvents or electrolytes .. 50
3.1.1.4 Effects of binder on the thermal stability of $Li_{0.81}C_6$ in $LiPF_6$ EC/DEC electrolyte 61
3.1.2 $LiCoO_2$ 64
3.1.2.1 SEM images of $LiCoO_2$ with different particle size 65
3.1.2.2 Binder 65
3.1.2.3 Effects of particle size of $LiCoO_2$ on its thermal stability 65

3.1.2.4 Changes to the mass ratio of $Li_{0.5}CoO_2$ and EC/DEC solvent 67
3.1.2.5 Effects of salts on the thermal stability of $Li_{0.5}CoO_2$ 72
3.1.3 Prediction of oven test behavior of full cells (graphite/$LiCoO_2$) based on ARC results on $Li_{0.81}C_6$ and $Li_{0.5}CoO_2$ 74
3.2 Oven tests of Lithium-ion cells (graphite/$LiCoO_2$) 75
3.2.1 140°C oven test 76
3.2.2 130°C oven test 80

4. Thermal stability studies on negative electrode materials with different lithium binding energies 83
4.1 $Li_4Ti_5O_{12}$ 84
4.2 VO_2 (B) 93
4.3 Thermal-stability comparison of $Li_{0.81}C_6$, $Li_7Ti_5O_{12}$, and $Li_{0.5}VO_2$ (B) ... 100
4.3.1 EC/DEC solvent 100
4.3.2 $LiPF_6$ and LiBOB based electrolytes 103

5. Existing alternate positive electrode materials ($LiMn_2O_4$ and $LiFePO_4$) 106
5.1 $LiMn_2O_4$ with the spinel structure 108
5.1.1 Reaction sequence in EC/DEC 110
5.1.2 Reaction kinetics 114
5.1.2.1 Activation energy (E_a) 114
5.1.2.2 Fitting ARC curves using E_a 116
5.1.3 Thermal stability in $LiPF_6$ or LiBOB based electrolyte 120
5.2 Olivine $LiFePO_4$ 123
5.2.1 Charged $LiFePO_4$ ($FePO_4$) 124
5.2.2 Thermal stability 126
5.3 Thermal-stability comparisons of $LiMn_2O_4$ and $LiFePO_4$ with $LiCoO_2$. 131

6. Layered positive electrode materials in the pseudoternary system, x $Li[Mn_{1/2}Ni_{1/2}]O_2$ • y $LiCoO_2$ • z $Li[Li_{1/3}Mn_{2/3}]O_2$ (x + y + z = 1) 132
6.1 $Li[(Ni_{0.5}Mn_{0.5})_xCo_{1-x}]O_2$ (binary system between $Li[Ni_{0.5}Mn_{0.5}]O_2$ and $LiCoO_2$) 132
6.1.1 $Li[(Ni_{0.5}Mn_{0.5})_xCo_{1-x}]O_2$ (x = 0.2, 0.4, 0.7, 0.9, and 1) samples 133

6.1.1.1 Sample characterization by SEM, XRD, and BET 133
6.1.1.2 Electrochemical properties 137
6.1.1.3 Thermal stability 141
6.1.2 $Li[(Ni_{0.5}Mn_{0.5})_{0.2}Co_{0.8}]O_2$ samples at 900°C, 1000°C, and 1100°C 144
6.1.2.1 Sample characterization by SEM, BET, and XRD 144
6.1.2.2 Electrochemical properties 146
6.1.2.3 Thermal stability 150
6.1.3 $Li[(Ni_{0.5}Mn_{0.5})_{0.4}Co_{0.6}]O_2$ (x = 0.4) by four different synthesis routes 152
6.1.3.1 Four different synthesis methods 153
6.1.3.2 Sample characterization by SEM, BET, and XRD 153
6.1.3.3 Electrochemical properties 156
6.1.3.4 Thermal stability 158
6.1.4 Thermal reaction sequence of charged $Li[(Ni_{0.5}Mn_{0.5})_xCo_{1-x}]O_2$ samples (4.2 V) 162
6.2 $Li[(Ni_{1/2}Mn_{1/2})_x(Li_{1/3}Mn_{2/3})_{1-x}]O_2$ samples, the $Li[Ni_{1/2}Mn_{1/2}]O_2$ • $Li[Li_{1/3}Mn_{2/3}]O_2$ binary system 178
6.2.1 Sample characterization by SEM, BET, and XRD 180
6.2.2 Electrochemical properties 182
6.2.3 Thermal stability 184
6.3 x $Li[Ni_{1/2}Mn_{1/2}]O_2$ • y $LiCoO_2$ • z $Li[Li_{1/3}Mn_{2/3}]O_2$ pseudoternary system (x + y + z = 1) 187
6.3.1 Introduction 187
6.3.2 $Li[(Ni_{1/2}Mn_{1/2})_xCo_y(Li_{1/3}Mn_{2/3})_z]O_2$ samples (z = 1/6 and 1/3) ... 193
6.3.2.1 Sample characterization by SEM and XRD 193
6.3.2.2 Electrochemical properties and thermal stability 199

7. Conclusions and future work 214
7.1 Conclusions 214
7.2 Future work 217

References 221

List of Figures

Figure 1.1 Schematic diagram of a commercialized lithium-ion cell during discharge. Reprinted with permission from the authors..... 2

Figure 1.2 Binding energies of lithium in various lithium compounds versus lithium metal 3

Figure 1.3 Layered structure of $LiCoO_2$ 6

Figure 1.4 A thermocouple was attached to surface of an 18650-size cell charged to 4.2 V in (a). The cell then was put into a constant temperature oven 16

Figure 1.5 Measured oven exposure data for a commercial 18650 cell. Reprinted with permission from the author..... 17

Figure 1.6 Oven exposure data for a MCMB/$LiMn_2O_4$ cell with 1.0 M $LiPF_6$ EC/DEC (1:2 by volume) electrolyte. Reprinted with permission from the author 18

Figure 1.7 Schematic of an Accelerating Rate Calorimeter (ARC)..... 19

Figure 1.8 A picture of the ARC when the blast shell is open..... 20

Figure 1.9 An ARC sample tube hooked on the tip of the sample thermocouple in the center cavity of the jacket..... 21

Figure 1.10 ARC tubes for ARC experiments..... 22

Figure 1.11 ARC curves of 50 mg DTBP started at 90°C. Temperature vs. time in panel (a) and self-heating rate (SHR) vs. temperature in panel (b)..... 23

Figure 1.12 ARC tube (a) before ARC, (b) in the middle of the ARC experiment around 130°C (between the two spikes in Figure 1.11b), and (c) after ARC..... 24

Figure 1.13 Self-heating rate versus temperature for 50 mg of DTBP (solid line) and the fitted result (dashed line) where $\alpha_0 = 0.001$, $\gamma = 4.9\times10^{14}$ min^{-1}, $E_a = 132$ kJ mol^{-1}, $\Delta T =$ 87 K..... 26

Figure 2.1 Pictures of a positive electrode pellet (a), 2325-size coin cell (b), and an ARC tube (c) 32

Figure 2.2 Construction of 2325 lithium coin cell used for electrochemical testing 34

Figure 2.3 Construction of 2325 lithium coin cell with MCMB pellet electrode. Reprinted with permission from the authors..... 35

Figure 2.4 Construction of 2325 lithium coin cell with a positive electrode material 36

Figure 2.5 Construction of lithium cell with MCMB powder electrode without binder 37

Figure 2.6 XRD patterns of lithiated MCMB ($Li_{0.81}C_6$) with 7% PVDF binder before (a) and after the rinsing procedure (b) 38

Figure 2.7 XRD sample holder for air and moisture sensitive samples 40

Figure 2.8 XRD pattern and the corresponding two-phase Rietveld refinement of the $LiCoO_2$ (phase I) and Si (phase II) sample 42

Figure 3.1 A SEM image of the MCMB sample used (average particle size of about 20 μm) 44

Figure 3.2 A schematic diagram of the staged phases of Li intercalated graphite. "A" and "B" represent graphite sheets. Sheet "B" shifts relative to the adjacent sheet, "A", by a distance of $(3)^{-1/2}a$ in the [010] reciprocal lattice direction. a is the in-plane graphite lattice constant..... 45

Figure 3.3 XRD patterns of (a) MCMB and (b) $Li_{0.81}C_6$ with 2% EPDM before or (c) after the DMC rinse..... 46

Figure 3.4 Fitting the Bragg peaks from the LiC_6 and LiC_{12} phases in the XRD pattern of rinsed $Li_{0.81}C_6$ 47

Figure 3.5 Self-heating rate versus temperature for 200 mg $Li_{0.81}C_6$ with 2% EPDM binder (a), 50 mg $Li_{0.81}C_6$ (2% EPDM) with 35 mg PVDF (b), 3 mg lithium metal with 30 mg PVDF (c), and 6 mg lithium metal with 60 mg PVDF (d). All the experiments were started at 90°C 49

Figure 3.6 Self-heating rate versus temperature for $Li_{0.81}C_6$ reacting with different solvents, DMC (a), DEC (b), EC (c), or EC/DEC (d) indicated with dashed lines or 1.0 M $LiPF_6$ in these solvents indicated with solid lines 50

Figure 3.7 XRD patterns of $Li_{0.81}C_6$ ARC samples after reacting with EC/DEC solvent stopped at 243°C (a) or 253°C after the thermal runaway (b) and with 1.0 M $LiPF_6$ EC/DEC electrolyte stopped at 243°C (c) 52

Figure 3.8 Proposed reaction sequence between $Li_{0.81}C_6$ and EC/DEC solvent during the temperature range between 90 and 260°C correlated to ARC results 53

Figure 3.9 SHR vs. T of 50 mg of $Li_{0.81}C_6$ reacting with 50 mg of EC/DEC in panel (a) and 35 mg of $Li_{0.81}C_6$ reacting with 35 mg of EC/DEC (b). The ARC sample was initially heated to 90°C 54

Figure 3.10 Self-heating rate versus temperature for 100 mg of $Li_{0.81}C_6$ with the same amount of EC/DEC (a) or 0.25 M (b), 0.5 M (c), or 1.0 M $LiPF_6$ EC/DEC electrolyte (d), heated initially to 90°C 55

Figure 3.11 Self-heating rate versus temperature for 100 mg of $Li_{0.81}C_6$ with 25 (panel a) or 50 mg (panel b) of 1.0 M $LiPF_6$ EC/DEC in solid line. Self-heating rate versus temperature for 100 mg of $Li_{0.81}C_6$ with 100 mg of 0.25 M and 0.5 M $LiPF_6$ EC/DEC shown in (a) and (b), respectively, in the dashed line for comparison 56

Figure 3.12 XRD patterns of $Li_{0.81}C_6$ ARC samples after reacting with EC/DEC solvent and different concentrations of $LiPF_6$ in EC/DEC shown in Figure 3.10. Figure 3.12a is the same as Figure 3.7b 57

Figure 3.13 Self-heating rate versus temperature for 100 mg of $Li_{0.81}C_6$ with the same amount of EC/DEC (a) or 0.2 M (b), 0.4 M (c), or 0.8 M LiBOB EC/DEC electrolyte (d), heated initially to 90°C 59

Figure 3.14 Comparison of the self-heating rate versus temperature of approximately 100 mg lithiated MCMB in two different electrolytes. In this case the samples were forced to 120°C at 10°C/min before the exotherms were monitored: (a) 100 mg $LiPF_6$ EC/DEC, and (b) 100 mg LiBOB EC/DEC 60

Figure 3.15 Self-heating rate versus temperature for 100 mg $Li_{0.81}C_6$ (7% PVDF) with 100 mg $LiPF_6$/LiBOB EC/DEC mixed electrolytes heated to 90°C 61

Figure 3.16 Self-heating rate versus temperature for 100 mg $Li_{0.81}C_6$ with 2% PVDF (a) or 2% EPDM (b) heated in 100 mg 1.0 M $LiPF_6$ EC/DEC electrolyte 62

Figure 3.17 XRD patterns of ARC samples stopped at 247°C (a) or 350°C (b) for 100 mg $Li_{0.81}C_6$ reacted with 100 mg 1.0 M $LiPF_6$ EC/DEC electrolyte heated initially to 90°C 63

Figure 3.18 Self-heating rate versus temperature for 100 mg of $Li_{0.81}C_6$ containing 1% (a), 2% (b), 3.5% (c), 7% (d), and 14% PVDF (e) heated with 100 mg 1.0 M $LiPF_6$ EC/DEC electrolyte 64

Figure 3.19 SEM pictures of three $LiCoO_2$ materials with different particle sizes (diameters of approximately 0.8 μm, 2 μm, and 5 μm, respectively) 65

Figure 3.20 Self-heating rate versus temperature of 200 mg rinsed $Li_{0.5}CoO_2$ heated initially to 90°C 66

Figure 3.21 Self-heating rate versus temperature for the three $Li_{0.5}CoO_2$ samples reacting with EC/DEC solvent heated initially to 110°C 66

Figure 3.22 Self-heating rate versus temperature for the three $Li_{0.5}CoO_2$ samples with 1.0 M $LiPF_6$ EC/DEC heated initially to 110°C 67

Figure 3.23 Self-heating rate versus temperature for 100 mg of $Li_{0.5}CoO_2$ (1) in 100 mg (a), 150 mg (b), or 200 mg EC/DEC solvent (c) heated initially to 110°C 69

Figure 3.24 Self-heating rate versus temperature for 100 mg $Li_{0.5}CoO_2$ (3) in 100 mg (a), 150 mg (b), or 200 mg EC/DEC solvent (c) heated initially to 110°C 70

Figure 3.25 XRDs of ARC samples stopped at 253°C or 350°C for 100 mg $Li_{0.5}CoO_2$ (3) reacted with 100 mg EC/DEC solvent heated initially to 110°C 71

Figure 3.26 Self-heating rate versus temperature for 100 mg of $Li_{0.5}CoO_2$ (1) reacting with the same amount of EC/DEC, 1.0 M $LiPF_6$ EC/DEC or 0.8 M LiBOB EC/DEC heated initially to 110°C 73

Figure 3.27 Self-heating rate versus temperature for 100 mg of $Li_{0.5}CoO_2$ (3) in 100 mg of EC/DEC or EC/DEC containing the salts, $LiPF_6$ and LiBOB, heated initially to 110°C 73

Figure 3.28 Self-heating rate versus temperature for 100 mg of $LiCoO_2$ (3) in the same amount of EC/DEC or EC/DEC containing the salts, $LiPF_6$ and LiBOB, heated initially to 150°C 74

Figure 3.29 Temperature vs. time for 18650 Li-ion cells (4.2 V) in the 140°C oven test. Data for four cells are shown, two with 1.0 M $LiPF_6$ EC/DEC electrolyte and two with 0.6 M LiBOB EC/DEC electrolyte 76

Figure 3.30 Heating rate, dT/dt vs. temperature, T, for a stainless steel cylinder placed in a 140°C oven to demonstrate the validity of Newton's law 77

Figure 3.31 The data of Figure 3.29 replotted as dT/dt vs. T. The dashed line indicates a cell with no internally generated heat 78

Figure 3.32 Temperature vs. time for 18650 Li-ion cells (4.2 V) in the 140°C oven test. Data for six cells are shown, with the electrolytes indicated in the legend 79

Figure 3.33 Temperature vs. time for 18650 cells (4.2 V) in the 130°C oven test 81

Figure 3.34 The data of Figure 3.33 replotted as dT/dt vs. T. The dashed line indicates a cell with no internally generated heat 81

Figure 4.1 Binding energies of lithium atoms in various lithium compounds versus lithium metal 83

Figure 4.2 The potential (V) versus specific capacity (mA h g^{-1}) for Li/VO_2 (B), Li/$Li_4Ti_5O_{12}$, and Li/MCMB coin cells during the first cycle 84

Figure 4.3 SEM micrograph of synthesized $Li_4Ti_5O_{12}$ having a particle size of approximately 0.3 μm 85

Figure 4.4 The self-heating rate versus temperature of 150 mg of $Li_7Ti_5O_{12}$ reacting with 100 mg of EC/DEC in panel (a), 100 mg 0.8 M LiBOB EC/DEC (b), and 100 mg of 1.0 M $LiPF_6$ EC/DEC (c). The samples for the ARC experiments were initially heated to 90°C (solid lines) or forced to a higher temperature of 160°C (dashed lines) 86

Figure 4.5 XRD patterns of the products of $Li_7Ti_5O_{12}$ after reacting with EC/DEC in panel (a), LiBOB EC/DEC (b), and $LiPF_6$ EC/DEC (c) at 350°C in ARC measurements as shown in Figure 4.4 88

Figure 4.6 Self-heating rate versus temperature for 150 mg of $Li_7Ti_5O_{12}$ reacting with 100 mg 0.5 M $LiPF_6$ EC/DEC in panel (a) or 100 mg 1.0 M $LiPF_6$ EC/DEC in panel (b) both forced to 160°C 90

Figure 4.7 XRD patterns of the products of the reaction of 150 mg of $Li_7Ti_5O_{12}$ with 100 mg of 0.5 M $LiPF_6$ EC/DEC electrolyte 91

Figure 4.8 Self-heating rate versus temperature of 150 mg of uncharged $Li_4Ti_5O_{12}$ with 100 mg EC/DEC in panel (a), or 100 mg of 1.0 M $LiPF_6$ EC/DEC (b). Figure 4.8c shows the SHR vs. T for 150 mg of $Li_7Ti_5O_{12}$ reacting with 100 mg of 1.0 M $LiPF_6$ EC/DEC. The ARC samples were initially heated to 90°C 92

Figure 4.9 XRD patterns of the products of $Li_4Ti_5O_{12}$ after reacting with EC/DEC in panel (a) or $LiPF_6$ EC/DEC (b) at 350°C. Figure 4.9c shows the XRD patterns of the products from the reaction between $Li_7Ti_5O_{12}$ and $LiPF_6$ EC/DEC at 350°C. The ARC data are shown in Figure 4.8 93

Figure 4.10 The $Li_{0.5}VO_2$ (B) structure (Space group C2/m, #12). It is based on a three-dimensional array of corner-shared VO_6 octahedra. ("•" represents lithium atoms) 94

Figure 4.11 SEM micrograph of VO_2 (B) having an average particle size about 5 μm.. 94

Figure 4.12 X-ray diffraction (XRD) pattern of the synthesized VO_2 (B) sample and the fit using Rietveld refinement 95

Figure 4.13 The XRD pattern of $Li_{0.5}VO_2$ (B) in panel (b). The XRD pattern of VO_2 (B) is shown in Figure 4.13a for comparison 96

Figure 4.14 The self-heating rate versus temperature of 150 mg of $Li_{0.5}VO_2$ (B) reacting with 100 mg of EC/DEC panel (a), 100 mg of 0.8 M LiBOB EC/DEC (b), and 100 mg of

1.0 M $LiPF_6$ EC/DEC (c). The ARC experiments were initially heated to 90°C (solid lines) or forced to a higher temperature of 160°C (dashed lines) 97

Figure 4.15 XRD patterns of the products of $Li_{0.5}VO_2$ (B) after reacting with EC/DEC in panel (a), LiBOB EC/DEC (b), and $LiPF_6$ EC/DEC (c) at 350°C in ARC measurements as shown in Figure 4.14 98

Figure 4.16 The XRD patterns of the products from the reactions between $Li_{0.5}VO_2$ (B) and LiBOB EC/DEC electrolyte in ARC measurements stopped at 280°C in panel (b) or 340°C in panel (c). The ARC results are shown in Figure 4.14c. The XRD pattern of VO_2 (B) is added into Figure 4.16a for comparison 99

Figure 4.17 The two processes involved in the reaction between VO_2 (B) and LiBOB EC/DEC electrolytes in the ARC measurements (Figure 4.14c) 99

Figure 4.18 The self-heating rate vs. temperature for 100 mg of EC/DEC reacting with 100 mg of $Li_{0.81}C_6$ in panel (a), 150 mg of $Li_7Ti_5O_{12}$ (b), or $Li_{0.5}VO_2$ (B) in panel (c) shown in solid lines. The dashed line in Figure 4.18a shows the SHR vs. T of 100 mg of $Li_{0.81}C_6$ reacting with 100 mg of 1.0 M $LiPF_6$ EC/DEC 100

Figure 4.19 The potential (vs. Li) of charged negative electrode materials versus the heat released, ΔH (per mole of Li), for $Li_{0.81}C_6$, $Li_7Ti_5O_{12}$, and $Li_{0.5}VO_2$ materials reacting with EC/DEC in the ARC measurements (Figure 4.18) 102

Figure 4.20 The SHR vs. T for 100 mg of 1.0 M $LiPF_6$ EC/DEC reacting with 100 mg of $Li_{0.81}C_6$, 150 mg of $Li_7Ti_5O_{12}$, and $Li_{0.5}VO_2$ (B) shown in panels a, b, and c, respectively. The ARC samples were initially heated to 90°C (solid lines) or forced to a higher temperature of 120°C (dashed line in panel a) or 160°C (dashed lines in panels b and c) 103

Figure 4.21 The SHR vs. T of 100 mg of 0.8 M LiBOB EC/DEC reacting with 100 mg of $Li_{0.81}C_6$, 150 mg of $Li_7Ti_5O_{12}$, and $Li_{0.5}VO_2$ (B) shown in panels a, b, and c, respectively. The ARC samples were initially heated to 90°C (solid lines) or forced to a higher temperature of 120°C (dashed line in panel a) or 160°C (dashed lines in panels b and c) 104

Figure 5.1 The $LiMn_2O_4$ spinel structure (Space group Fd3m, #227). It is based on a cubic close-packed oxygen array with edge-shared MnO_6 octahedra ("•" represents lithium atoms) 106

Figure 5.2 The $LiFePO_4$ olivine structure (Space group Pnma, #62) It is based on a hexagonal-close packed oxygen array with corner-shared FeO_6 octahedra and PO_4 tetrahedra ("•" represents lithium atoms) 107

Figure 5.3 The potential (V) versus specific capacity (mA h g^{-1}) for Li/$LiMn_2O_4$ and Li/$LiFePO_4$ coin cells during the first cycle 107

Figure 5.4 SEM micrograph of $LiMn_2O_4$ having a particle size of approximately 10 μm 109

Figure 5.5 X-ray diffraction (XRD) pattern and the corresponding Rietveld refinement of the $LiMn_2O_4$ sample 109

Figure 5.6 Self-heating rate versus temperature for 100 mg of λ-MnO_2 initially heated to 110°C 110

Figure 5.7 X-ray diffraction (XRD) pattern of λ-MnO_2 in panel (a) for comparison. Panel (b) shows the XRD pattern of λ-MnO_2 after the ARC measurement up to 260°C 111

Figure 5.8 ARC curves (solid line) and fits (dashed line) for 100 mg of λ-MnO_2 reacting with 100 mg EC/DEC in panel (a), 20 mg of λ-MnO_2 with 20 mg EC/DEC (b), and 15 mg of λ-MnO_2 with 20 mg EC/DEC (c) 112

Figure 5.9 X-ray diffraction (XRD) patterns of ARC samples of 15 mg of λ-MnO_2 with 20 mg EC/DEC stopped at 220°C in panel (a) and 20 mg of λ-MnO_2 with 20 mg EC/DEC stopped at 350°C in panel (b) 113

Figure 5.10 Self-heating rate vs. 1000/T (in K^{-1}) of 20 mg of λ-MnO_2 reacting with 20 mg EC/DEC initially forced to different temperature, 180°C, 200°C, 210°C, and 220°C, respectively. The initial points of the experiments ($\alpha_0 \approx 0$) are indicated with black circles..... 115

Figure 5.11a The self-heating rate versus temperature for 20 mg λ-MnO_2 reacting with 20 mg of EC/DEC. Figures 5.11b, c, d, e, and f show the best fit SHR vs. T curves calculated using the reaction models 2, 3, 4, 5, and 6 in Table 5.4, respectively..... 119

Figure 5.12 Self-heating rate versus temperature for 100 mg of λ-MnO_2 reacting with the same amount of 1.0 M $LiPF_6$ EC/DEC (solid line) or 0.8 M LiBOB EC/DEC electrolyte (dashed line) initially heated to 110°C 121

Figure 5.13 Heat-wait-search results [temperature (°C) versus time (minutes)] for 100 mg of 0.8 M LiBOB EC/DEC initially heated to 90°C. A dashed circle indicates an endothermic region..... 122

Figure 5.14 SEM micrographs of three carbon-coated $LiFePO_4$ samples having different particle sizes. From the images it can be observed that the diameters of the primary particles are approximately 3, 7, and 15 μm, respectively 123

Figure 5.15a The SEM image of a particle having many small particles around 0.1 μm dotted on its surface. The EDS dot maps for C, Fe, O, and P are shown in Figures 5.15b, c, d, and e, respectively. The SEM image and the dot maps each of C, Fe, O, and P are similar 124

Figure 5.16 XRD pattern of $LiFePO_4$ (15 μm) charged in the special cell (Figure 2.5) without binder to 3.8 V vs. Li metal and its single-phase Rietveld refinement using the $FePO_4$ structure given in Table 5.6..... 125

Figure 5.17 Self-heating rate versus temperature for 100 mg of delithiated $LiFePO_4$ (7% PVDF binder) having a primary particle size of 3 μm in panel (a), 7 μm (b) and 15 μm (c), respectively, heated with 100 mg of EC/DEC solvent. Panel (d) shows the self-heating rate versus temperature for 100 mg of delithiated $LiFePO_4$ (15 μm) without binder heated with EC/DEC solvent 127

Figure 5.18 Self-heating rate versus temperature of 100 mg of charged $LiFePO_4$ (3 μm, 7 μm, and 15 μm) containing 7% PVDF binder, respectively, heated with 100 mg of 1.0 M $LiPF_6$ EC/DEC (solid line) or 100 mg of 0.8 M LiBOB EC/DEC electrolyte (dashed line) 129

Figure 6.1 The compositions of studied $Li[(Ni_{0.5}Mn_{0.5})_xCo_{1-x}]O_2$ samples (x = 0.2, 0.4, 0.7, 0.9, and 1) indicated with "diamonds" 132

Figure 6.2 SEM micrographs of synthesized $Li[(Ni_{0.5}Mn_{0.5})_xCo_{1-x}]O_2$ samples (x = 0.2, 0.4, 0.7, 0.9, and 1). From the images the average particle size of the $LiCoO_2$ (sample 3 in Section 3.1.2) is approximately 5 μm in panel (a) and the primary particle size of $Li[(Ni_{0.5}Mn_{0.5})_xCo_{1-x}]O_2$ samples is about 0.3 μm..... 134

Figure 6.3 X-ray diffraction (XRD) patterns of $Li[(Ni_{0.5}Mn_{0.5})_xCo_{1-x}]O_2$ samples (x = 0.2, 0.4, 0.7, 0.9, and 1) 135

Figure 6.4 The lattice constants, *a* (Å), *c* (Å), and the *c/a* ratio, in $Li[(Ni_{0.5}Mn_{0.5})_xCo_{1-x}]O_2$ samples as the Co content, 1-x, increases 136

Figure 6.5 Fraction of lithium sites in the lithium layer of $Li[(Ni_{0.5}Mn_{0.5})_xCo_{1-x}]O_2$ occupied by transition metal atoms as a function of Co content, 1-x..... 136

Figure 6.6 Capacity retained (%) as a function of Co content, 1-x, of $Li[(Ni_{0.5}Mn_{0.5})_xCo_{1-x}]O_2$ samples at different rates (4C, 3C, 2C, or C) [79]. Reprinted with permission from the authors..... 137

Figure 6.7 The differential capacity (dQ/dV) vs. potential (V) of $Li/Li[(Ni_{0.5}Mn_{0.5})_xCo_{1-x}]O_2$ cells cycling between 2.5 and 4.4 V at a rate of C/20..... 138

Figure 6.8 Potential (V) versus capacity (mA h g^{-1}) curves for the 1st cycle of the cells with $Li[(Ni_{0.5}Mn_{0.5})_xCo_{1-x}]O_2$ (x = 0.2, 0.4, 0.7, 0.9, and 1) samples synthesized at 900°C..... 139

Figure 6.9 Discharge capacity (m Ah g^{-1}) versus cycle number (2.5 V – 4.4 V, C/4) for the $Li[(Ni_{0.5}Mn_{0.5})_xCo_{1-x}]O_2$ (x = 0.2, 0.4, 0.7, 0.9, and 1) samples..... 140

Figure 6.10 Self-heating rate versus temperature for 100 mg of $Li[(Ni_{0.5}Mn_{0.5})_xCo_{1-x}]O_2$ (x = 0.2, 0.4, 0.7, 0.9, and 1) charged to 4.2 V (solid lines) or 4.4 V vs. Li (dashed lines) heated with 100 mg of EC/DEC solvent. Samples were initially heated to 110°C before exotherm searching began..... 141

Figure 6.11 Self-heating rate versus temperature for 100 mg of $Li[(Ni_{0.5}Mn_{0.5})_xCo_{1-x}]O_2$ (x = 0.2, 0.4, 0.7, 0.9, and 1) charged to 4.2 V vs. Li heated with 30 mg of 1.0 M $LiPF_6$ EC/DEC electrolyte. Samples were initially heated to 110°C before exotherm searching began..... 143

Figure 6.12 SEM micrographs of $Li[(Ni_{0.5}Mn_{0.5})_{0.2}Co_{0.8}]O_2$ samples synthesized at 900°C (a), 1000°C (b), and 1100°C (c). The primary particle sizes are approximately 0.2 μm, 0.8 μm, and 8 μm, respectively..... 144

Figure 6.13 X-ray diffraction (XRD) patterns of $Li[(Ni_{0.5}Mn_{0.5})_{0.2}Co_{0.8}]O_2$ synthesized at 900°C (a), 1000°C (b), and 1100°C (c)..... 145

Figure 6.14 XRD patterns of $Li[(Ni_{0.5}Mn_{0.5})_{0.2}Co_{0.8}]O_2$ synthesized at 900°C and fitted pattern using Rietveld refinement..... 145

Figure 6.15 Differential capacity (dQ/dV) vs. potential (V) for Li/ $Li[(Ni_{0.5}Mn_{0.5})_{0.2}Co_{0.8}]O_2$ synthesized at 900°C, 1000°C, and 1100°C..... 147

Figure 6.16 Differential capacity (dQ/dV) vs. potential (V) for $Li/Li[(Ni_{0.5}Mn_{0.5})_xCo_{1-x}]O_2$ cells with x = 0.025, 0.05, and 0.1 (dashed line) and $Li/LiCoO_2$ cell (solid line). The shaded region is the capacity due to the addition of Ni atoms [23]. Reprinted with permission from the authors 148

Figure 6.17 Capacity (mA h g^{-1}) vs. cycle number for $Li/Li[(Ni_{0.5}Mn_{0.5})_{0.2}Co_{0.8}]O_2$ cells (electrode material synthesized at 900°C, 1000°C, and 1100°C). Data for two cells are shown in each panel..... 149

Figure 6.18 Voltage (V) vs. capacity (mA h g^{-1}) for $Li[(Ni_{0.5}Mn_{0.5})_{0.2}Co_{0.8}]O_2$ (900°C, 1000°C, and 1100°C) charged to 4.4 V for the 1st (solid) and 175th cycles (dashed line). The cells were charged and discharged using a nominal C/4 rate..... 150

Figure 6.19 Self-heating rate versus temperature of 100 mg of $Li[(Ni_{0.5}Mn_{0.5})_{0.2}Co_{0.8}]O_2$ (900°C, 1000°C, and 1100°C) charged to 4.2 V (solid line) or 4.4 V (dashed line) heated with 100 mg of 1.0 M $LiPF_6$ EC/DEC electrolyte initially to 110°C..... 151

Figure 6.20 SEM micrographs of $Li[(Ni_{0.5}Mn_{0.5})_{0.4}Co_{0.6}]O_2$ samples (I), (II), (III), and (IV). From the images the average particle size is approximately 0.2-0.3 μm for samples (I) and (II) and around 0.4-0.5 μm for samples (III) and (IV)..... 154

Figure 6.21 X-ray diffraction (XRD) patterns of $Li[(Ni_{0.5}Mn_{0.5})_{0.4}Co_{0.6}]O_2$ samples in the low scattering angle region from 15° to 50° to show the absence of impurities..... 155

Figure 6.22 X-ray diffraction (XRD) patterns of $Li[(Ni_{0.5}Mn_{0.5})_{0.4}Co_{0.6}]O_2$ samples in the high scattering angle region from 75° to 90° to compare the widths of the Bragg peaks..... 155

Figure 6.23 The differential capacity (dQ/dV) vs. potential (V) of Li/ $Li[(Ni_{0.5}Mn_{0.5})_{0.4}Co_{0.6}]O_2$ cells cycled between 2.5 V and 4.4 V at a rate of C/20..... 156

Figure 6.24 The potential (V) vs. capacity (mA h g^{-1}) of Li/$Li[(Ni_{0.5}Mn_{0.5})_{0.4}Co_{0.6}]O_2$ cells cycled between 2.5 V and 4.4 V at a rate of C/20..... 157

Figure 6.25 Capacity (mA h g^{-1}) vs. cycle number for the Li/$Li[(Ni_{0.5}Mn_{0.5})_{0.4}Co_{0.6}]O_2$ cells made from the four samples..... 158

Figure 6.26 Self-heating rate (SHR) versus temperature (T) for 100 mg $Li[(Ni_{0.5}Mn_{0.5})_{0.4}Co_{0.6}]O_2$ samples charged to 4.2 V heated with 100 mg of EC/DEC solvent. The SHR vs. T of $LiCoO_2$ charged to 4.2 V reacting with EC/DEC has been added in panel (a) for comparison. Samples were initially heated to 110°C before exotherm searching began..... 159

Figure 6.27 Self-heating rate (SHR) versus temperature for 100 mg of $LiCoO_2$ and $Li[(Ni_{0.5}Mn_{0.5})_{0.4}Co_{0.6}]O_2$ samples charged to 4.2 V vs. Li heated with 30 mg of 1.0 M $LiPF_6$ EC/DEC electrolyte. Samples were initially heated to 110°C before exotherm searching began..... 160

Figure 6.28 SHR vs. T for 50 mg of $Li[(Ni_{0.5}Mn_{0.5})_xCo_{1-x}]O_2$ (x = 0.4, 0.7, 0.9, and 1) charged to 4.2 V heated with 50 mg of EC/DEC solvent. There are two ARC measurements for each sample, one stopped at 290°C (solid line) and the other one at 350°C (dashed line)..... 162

Figure 6.29 XRD patterns of $Li[(Ni_{0.5}Mn_{0.5})_xCo_{1-x}]O_2$ (x = 0.4, 0.7, 0.9, and 1) charged to 4.2 V after reacting with EC/DEC to 290°C in the ARC as shown by solid line in Figure 6.28 163

Figure 6.30 Expanded view of the XRD patterns in Figure 6.29..... 164

Figure 6.31 Rietveld profile fitting to the XRD pattern (Figure 6.29a) of the products from the reaction between $Li[(Ni_{0.5}Mn_{0.5})_{0.4}Co_{0.6}]O_2$ and EC/DEC at 290°C. Five phases are needed to describe this pattern. They are M metal (I), $[Li_qM_{1-q}]O$ (II), LiF (III), $MnCO_3$ (IV), and M^*CO_3 (V)..... 165

Figure 6.32 Rietveld profile fitting to the XRD pattern (Figure 6.29d) of the products from the reaction between $Li[Ni_{0.5}Mn_{0.5}]O_2$ and EC/DEC at 290°C. Four phases are needed to describe this pattern. They are M metal (I), $[Li_qM_{1-q}]O$ (II), LiF (III), and $MnCO_3$ (IV)..... 166

Figure 6.33 XRD patterns of $Li[(Ni_{0.5}Mn_{0.5})_xCo_{1-x}]O_2$ (x = 0.4, 0.7, 0.9, and 1) charged to 4.2 V after reacting with EC/DEC to 350°C as shown by dashed line in Figure 6.28..... 168

Figure 6.34 Rietveld profile fitting to the XRD pattern (Figure 6.33a) of the products from the reaction between $Li[(Ni_{0.5}Mn_{0.5})_{0.4}Co_{0.6}]O_2$ and EC/DEC at 350°C. Five phases are needed to describe this pattern. They are M metal (I), $[Li_qM_{1-q}]O$ (II), LiF (III), $MnCO_3$ (IV), and M^*CO_3 (V)..... 169

Figure 6.35 Rietveld profile fitting to the XRD pattern (Figure 6.33d) of the products from the reaction between $Li[Ni_{0.5}Mn_{0.5}]O_2$ and EC/DEC at 350°C. Four phases are needed to describe this pattern. They are M metal (I), $[Li_qM_{1-q}]O$ (II), LiF (III), and $MnCO_3$ (IV)..... 170

Figure 6.36 SHR vs. T for 50 mg of $Li[(Ni_{0.5}Mn_{0.5})_{0.4}Co_{0.6}]O_2$ (x = 0.4) charged to 4.2 V heated with 50 mg of EC/DEC solvent..... 172

Figure 6.37 XRD patterns of $Li[(Ni_{0.5}Mn_{0.5})_{0.4}Co_{0.6}]O_2$ charged to 4.2 V after reacting with EC/DEC. ARC measurements are shown in Figure 6.36..... 172

Figure 6.38 Rietveld profile fitting to the XRD pattern (Figure 6.37a) of the products from the reaction between $Li[(Ni_{0.5}Mn_{0.5})_{0.4}Co_{0.6}]O_2$ and EC/DEC at 242°C. Three phases are needed to describe this pattern. They are $[Li_pM_{1-p}]_3O_4$ (I), LiF (II), and Li_xMO_2 (III)..... 173

Figure 6.39 The compositions of $Li[(Ni_{1/2}Mn_{1/2})_x(Li_{1/3}Mn_{2/3})_{1-x}]O_2$ (x = 1/6, 1/2, and 5/6) studied compounds indicated with "diamonds" 179

Figure 6.40 SEM micrographs of $Li[(Ni_{1/2}Mn_{1/2})_x(Li_{1/3}Mn_{2/3})_{1-x}]O_2$ (x = 1/6, 1/2, 5/6 and 1) samples. From the images the average primary particle size of these four samples is approximately 0.2 μm..... 180

Figure 6.41 The X-ray diffraction (XRD) patterns of the $Li[(Ni_{1/2}Mn_{1/2})_x(Li_{1/3}Mn_{2/3})_{1-x}]O_2$ (x = 1/6, 1/2, and 5/6) samples shown in panels (a), (b), and (c), respectively..... 181

Figure 6.42 The differential capacity [dQ/dV (mA h g^{-1} V^{-1})] versus potential (V) of $Li[(Ni_{1/2}Mn_{1/2})_x(Li_{1/3}Mn_{2/3})_{1-x}]O_2$ with x = 1/6 in panel (a), 1/2 in (b), and 5/6 in (c) from 2.5 V ~ 4.8 V measured at a rate of C/30 (about 10 mA g^{-1})..... 182

Figure 6.43 Potential (V) versus capacity (mA h g^{-1}) for the 1st cycle of the cells with $Li[(Ni_{1/2}Mn_{1/2})_x(Li_{1/3}Mn_{2/3})_{1-x}]O_2$ samples (x = 1/6, 1/2, and 5/6)..... 183

Figure 6.44 The discharge capacity (mA h g^{-1}) versus cycle number of $Li[(Ni_{1/2}Mn_{1/2})_x(Li_{1/3}Mn_{2/3})_{1-x}]O_2$ with x = 1/6 in panel (a), 1/2 in (b), and 5/6 in (c). Cells were charged and discharged between 2.5 V and 4.6 V at a rate of C/6..... 184

Figure 6.45 Self-heating rate (SHR) versus temperature (T) for 100 mg of $Li[(Ni_{1/2}Mn_{1/2})_x(Li_{1/3}Mn_{2/3})_{1-x}]O_2$ samples charged to 4.5 V (x = 1/6), 4.45 V (x = 1/2), and 4.4 V (x = 5/6) reacting with 100 mg of EC/DEC solvent. Figure 6.45d shows the SHR vs. T of $Li[Ni_{1/2}Mn_{1/2}]O_2$ charged to 4.4 V vs. Li reacting with EC/DEC for comparison. All samples were initially heated to 110°C..... 185

Figure 6.46 Self-heating rate (SHR) versus temperature (T) of 100 mg of $Li[(Ni_{1/2}Mn_{1/2})_x(Li_{1/3}Mn_{2/3})_{1-x}]O_2$ charged to 4.8 V vs. Li reacting with 100 mg of EC/DEC solvent (solid line) or 30 mg of 1.0 M $LiPF_6$ EC/DEC electrolyte (dashed line) shown in panels (b), (c), (d), and (e). Figure 6.46a shows the SHR vs. T of $LiCoO_2$ (sample 1 in Section 3.1.2 with a particle size of about 0.8 μm) charged to 4.2 V vs. Li reacting with EC/DEC (solid line) or 1.0 M $LiPF_6$ EC/DEC (dashed line) for comparison. The ARC samples were all initially heated to 110°C..... 186

Figure 6.47 Solid solution samples with compositions in the $LiCoO_2 \bullet Li[Mn_{1/2}Ni_{1/2}]O_2 \bullet Li[Li_{1/3}Mn_{2/3}]O_2$ ternary system described in references [70, 77, 154-161]. Lines a, b, and c represent the binary system between $Li[Mn_{1/2}Ni_{1/2}]O_2$ and $Li[Li_{1/3}Mn_{2/3}]O_2$ phases. This axis has been included three times to help distinguish the large number of data. The compositions indicated with a "◆" are from reference [154] by Zhang *et al.* Compositions indicated by a "□" are from reference [160] by Kim *et al.* Compositions indicated by a "◇" are from reference [161] by Kim *et al.* "○" from reference [71] by Kang *et al.* "▲" from [158] by Sun *et al.* "★" from [156] by Park *et al.* "▼" from [159] by Shin *et al.* "✚" from Yu *et al.* [157], "✕" from Johnson *et al.* [155], "●" from Park *et al.* [73]. The compositions indicated by "☼" and "△" are from previous work of Jeff Dahn's lab [70 and 77]..... 189

Figure 6.48 Discharge capacity (mA h g^{-1}, first discharge cycle) of layered compounds with different compositions described in references [70, 77, 154-161]. Different potential limits for cycling were used by the various authors as indicated below. "◆" 2.5 - 4.6 V from [154] by Zhang *et al.* "□" 2.5 - 4.6 V from [160] by Kim *et al.* "◇" 2.5 - 4.6 V from [161] by Kim *et al.* "○"2.0 – 4.6 V from [71] by Kang *et al.* "▲" 2.5 - 4.6 V from [158] by Sun *et al.* "★" 2.0 - 4.8 V from [156] by Park *et al.* "▼" 2.0 - 4.6 V from [169] by Shin *et al.*, "✚"2.5 – 4.8 V from Yu *et al.* [157], "✕" 2.0 - 5.0 V from Johnson *et al.* [155], "●"2.0 – 4.8 V from Park *et al.* [73]. The compositions indicated by "☼" and "△" 2.5 - 4.8 V are from previous work of Jeff Dahn's lab [70 and 77]..... 190

Figure 6.49 Percent capacity retention over a specified number of cycles of solid solution electrode materials with the compositions indicated. "◆" 2.5 - 4.6 V, 70 cycles from [154] by Zhang *et al.* "□" 2.5 - 4.6 V, 15 cycles from [160] by Kim *et al.* "◇" 2.5 - 4.6 V, 35 cycles from [161] by Kim *et al.* "○" 2.0 – 4.6 V, 65 cycles from [71] by Kang *et al.* "▲" 2.5 - 4.6 V, 10 cycles from [158] by Sun *et al.* "★" 2.0 - 4.8 V, 50 cycles from [156] by Park *et al.* "▼" 2.0 - 4.6 V, 50 cycles from [159] by Shin *et al.* "✚" 2.5 – 4.8 V, 10 cycles from Yu *et al.* [157], "✕" 2.0 - 5.0 V, 10 cycles from Johnson *et al.* [155], "●" 2.0 – 4.8 V, 20 cycles from Park *et al.* [73]. The compositions indicated by "☼" and "△" (2.5 - 4.8 V) are from previous work [70, 77] of Jeff Dahn's lab..... 191

Figure 6.50 The composition of the x $Li[Mn_{1/2}Ni_{1/2}]O_2$ • y $LiCoO_2$ • z $Li[Li_{1/3}Mn_{2/3}]O_2$ (x + y + z = 1) samples studied in this section of the thesis are indicated by triangles. Two rows of samples, one with z = 1/6 and one with z = 1/3 were evaluated. The circles on the left and bottom edges of this ternary system show the composition of samples described in references [75-77] for comparison..... 192

Figure 6.51 SEM micrographs of x $Li[Mn_{1/2}Ni_{1/2}]O_2$ • y $LiCoO_2$ • 1/3 $Li[Li_{1/3}Mn_{2/3}]O_2$ (x + y = 2/3) solid solution samples synthesized at 900°C with Co content, y, increasing from 1/12 in panel (a), 1/6 (c), ¼ (e), 5/12 (g), to 2/3 (i). SEM micrographs of the samples with the same composition fired at 1000°C are shown in the right hand column for comparison..... 193

Figure 6.52 X-ray diffraction (XRD) patterns of x $Li[Mn_{1/2}Ni_{1/2}]O_2$ • y $LiCoO_2$ • 1/3 $Li[Li_{1/3}Mn_{2/3}]O_2$ (x + y = 2/3) samples (1000°C) with different Co content, y = 1/12, 1/6, ¼, 5/12, and 2/3 in the low scattering angle region from 15° to 50° show the absence of any impurities..... 194

Figure 6.53 X-ray diffraction (XRD) patterns of x $Li[Mn_{1/2}Ni_{1/2}]O_2$ • y $LiCoO_2$ • 1/3 $Li[Li_{1/3}Mn_{2/3}]O_2$ (x + y = 2/3) samples (1000°C) with different Co content, y = 1/12, 1/6, ¼, 5/12, and 2/3 in the high scattering angle region from 75° to 90° show the increase in crystallinity with Co content, y..... 195

Figure 6.54 The lattice constants, *a* (Å), *c* (Å), and the *c/a* ratio in x $Li[Mn_{1/2}Ni_{1/2}]O_2$ • y $LiCoO_2$ • 1/3 $Li[Li_{1/3}Mn_{2/3}]O_2$ (x + y = 2/3) solid solution samples (900°C or 1000°C) as the Co content, y, increases..... 197

Figure 6.55 Fraction of lithium sites in the lithium layer of x $Li[Mn_{1/2}Ni_{1/2}]O_2$ • y $LiCoO_2$ • 1/3 $Li[Li_{1/3}Mn_{2/3}]O_2$ (x + y = 2/3) samples (900°C or 1000°C) occupied by transition metal atoms as a function of Co content, y..... 197

Figure 6.56 Signature discharge method to test the rate capability of positive electrode materials. After charging to the high cut-off voltage, the electrode was discharged at a high rate of 2C (solid line) followed by a half an hour open circuit (dashed line). The electrode was then discharged at one half of the original current, C rate. This discharge sequence was repeated a total of 5 times until the discharge rate decreased to C/16... 198

Figure 6.57 Capacity (mA h g^{-1}) vs. cycle number for the x $Li[Mn_{1/2}Ni_{1/2}]O_2$ • y $LiCoO_2$ • 1/3 $Li[Li_{1/3}Mn_{2/3}]O_2$ (x + y = 2/3) samples (1000°C) with y = 1/12, 1/6, ¼, 5/12, and 2/3. The cells were cycled between 2.5 V and 4.3 V at C/4. Every 20 cycles, the cell was programmed to proceed to the signature discharge test to measure the rate capability..... 199

Figure 6.58 Capacity (%) retained as a function of discharge rate for x $Li[Mn_{1/2}Ni_{1/2}]O_2$ • y $LiCoO_2$ • 1/3 $Li[Li_{1/3}Mn_{2/3}]O_2$ (x + y = 2/3) samples (1000°C) from the first signature discharge test in Figure 6.57. These samples have not been charged through the oxygen release plateau..... 200

Figure 6.59 The potential (V) vs. specific capacity (mA h g^{-1}) of Li/{x $Li[Mn_{1/2}Ni_{1/2}]O_2$ • y $LiCoO_2$ • 1/3 $Li[Li_{1/3}Mn_{2/3}]O_2$ (x + y = 2/3) (900°C)} cells charged and discharged between 2.5 and 4.8 V at a rate of C/30..... 201

Figure 6.60 The differential capacity (dQ/dV) vs. potential (V) of Li/{x $Li[Mn_{1/2}Ni_{1/2}]O_2$ • y $LiCoO_2$ • 1/3 $Li[Li_{1/3}Mn_{2/3}]O_2$ (x + y = 2/3) (900°C)} cells charged and discharged between 2.5 and 4.8 V at a rate of C/30..... 202

Figure 6.61 Capacity (mA h g^{-1}) vs. cycle number for the Li/{ $Li[(Ni_{1/2}Mn_{1/2})_xCo_y(Li_{1/3}Mn_{2/3})_{1/3}]O_2$ (x + y = 2/3) (900°C)} cells cycled between 2.5 V and 4.6 V at C/6 after traversal of the O_2-loss plateau. The cells used to produce this data are the same as the cells described in Figures 6.59 and 6.60..... 203

Figure 6.62 Capacity (%) retained as a function of discharge rate for $Li[(Ni_{1/2}Mn_{1/2})_xCo_y(Li_{1/3}Mn_{2/3})_{1/3}]O_2$ (x + y = 2/3) samples (900°C) from the first signature discharge test in Figure 6.61. These samples have been charged through the oxygen release plateau..... 204

Figure 6.63 Self-heating rate (SHR) versus temperature (T) for 100 mg of $Li[(Ni_{1/2}Mn_{1/2})_xCo_y(Li_{1/3}Mn_{2/3})_{1/3}]O_2$ (x + y = 2/3) samples (900°C) charged to 4.8 V vs. Li heated with 100 mg of EC/DEC solvent (solid line) or 30 mg of 1.0 M $LiPF_6$ EC/DEC (dashed line). Samples were initially heated to 110°C before exotherm searching began..... 206

Figure 6.64 Self-heating rate (SHR) versus temperature (T) for 100 mg of $Li[(Ni_{1/2}Mn_{1/2})_xCo_y(Li_{1/3}Mn_{2/3})_{1/3}]O_2$ (x + y = 2/3) samples charged to 4.8 V heated with 30 mg of 1.0 M $LiPF_6$ EC/DEC (solid line - 900°C and dashed line - 1000°C). The SHR vs. T of $LiCoO_2$ charged to 4.2 V reacting with 1.0 M $LiPF_6$ EC/DEC has been added to panel a for comparison (bold line)..... 207

Figure 6.65 The area under the self-heating rate versus temperature curve between 110°C and 180°C is indicated by the shaded region. Panel a is plotted on a logarithmic vertical scale, like Figure 6.64. Panel b is plotted on a linear vertical scale. The parameter, "S", is the area of the shaded region in panel b..... 208

Figure 6.66 Specific discharge capacity (mA h g^{-1}) of $Li[(Ni_{1/2}Mn_{1/2})_xCo_y(Li_{1/3}Mn_{2/3})_z]O_2$ (x + y + z = 1) samples (z = 1/6 or 1/3) synthesized at 900°C or 1000°C cycled from 2.5 to 4.6 V vs. Li at C/30..... 209

Figure 6.67 Specific discharge capacity (mA h g^{-1}) of $Li[(Ni_{1/2}Mn_{1/2})_xCo_y(Li_{1/3}Mn_{2/3})_z]O_2$ (x + y + z = 1) samples (z = 1/6 or 1/3) synthesized at 900°C or 1000°C cycled from 2.5 to 4.6 V vs. Li at C/6..... 210

Figure 6.68 The percent capacity retention (%) of the $Li[(Ni_{1/2}Mn_{1/2})_xCo_y(Li_{1/3}Mn_{2/3})_z]O_2$ (x + y + z = 1) solid solution samples cycled between 2.5 and 4.6 V at C/6 for 70 cycles..... 211

Figure 6.69 Thermal reactivity, S, (described in Figure 6.65) of $Li[(Ni_{1/2}Mn_{1/2})_xCo_y(Li_{1/3}Mn_{2/3})_z]O_2$ (x + y + z = 1) samples made at 900°C or 1000°C charged to 4.8 V reacting with 1.0 M $LiPF_6$ EC/DEC. The values of S obtained in earlier ARC studies of $Li[(Ni_{1/2}Mn_{1/2})_x(Li_{1/3}Mn_{2/3})_{1-x}]O_2$ (x = 1/6, 1/2, and 5/6) charged to 4.8 V [77] and $Li[(Ni_{0.5}Mn_{0.5})_xCo_{1-x}]O_2$ (x = 0.2, 0.4, 0.7, 0.9, and 1) and $LiCoO_2$ charged 4.2 V [76] reacting with 1.0 M $LiPF_6$ EC/DEC were added for comparison..... 212

Figure 6.70 The percentage of C/4 discharge capacity obtained at a 2C discharge for Li/{ $Li[(Ni_{1/2}Mn_{1/2})_xCo_y(Li_{1/3}Mn_{2/3})_z]O_2$ (x + y + z = 1)} cells cycled between 2.5 and 4.6 V after O_2 loss 213

List of Tables

Table 2.1 Comparison of lattice constants of $LiCoO_2$ and Si phases from two-phase Rietveld refinements and from the literature..... 42

Table 4.1 Number of moles of reactants in the ARC samples used..... 89

Table 4.2 Temperature rises in the reaction between 150 mg $Li_7Ti_5O_{12}$ and 100 mg 1.0 M $LiPF_6$ EC/DEC or 100 mg 0.5 M $LiPF_5$ EC/DEC..... 90

Table 4.3 Lattice constants and atom positions for the synthesized VO_2 (B) sample from the XRD refinement. The space group used for the refinement was C2/m ($^{\#}12$). The Bragg R-factor is listed..... 95

Table 4.4 Comparison of three different negative electrode materials, MCMB, $Li_4Ti_5O_{12}$, and VO_2 (B) with different lithium binding energies..... 105

Table 5.1 Lattice constants of $LiMn_2O_4$ before and after charging to 4.4 V vs. Li. The space group used for this refinement was Fd3m ($^{\#}227$). The Bragg R-factors are listed..... 110

Table 5.2 Several typical reaction models for thermal decomposition of solids 116

Table 5.3 The energies ($D°_{298}$, kJ mol^{-1}) of the chemical bonds in diatomic molecules of transition metal oxides (MO) at 298 K [114]..... 117

Table 5.4 Fitting the ARC results for 20 mg of λ-MnO_2 reacting with 20 mg of EC/DEC solvent using the models described in Table 5.2..... 119

Table 5.5 Fitting the ARC results for different amounts of λ-MnO_2 reacting with EC/DEC (shown in Figure 5.8) using model 6 described in Table 5.2..... 120

Table 5.6 Lattice constants and atom positions for 15 μm particle size $LiFePO_4$ and the same material charged to 3.8 V ($FePO_4$) vs. Li/Li^+. The electrochemical cell used to charge the $LiFePO_4$ is shown in Figure 2.5 and there was no binder used in the $LiFePO_4$ electrode (see text). The space group used for the refinement was Pnma ($^{\#}62$). The Bragg R-factor is listed..... 126

Table 5.7 Comparison of three positive electrode materials, $LiCoO_2$, $LiMn_2O_4$, and $LiFePO_4$..... 130

Table 6.1 Lattice constants of $Li[(Ni_{0.5}Mn_{0.5})_{0.2}Co_{0.8}]O_2$ synthesized at different temperatures (900°C, 1000°C, or 1100°C). The space group used for this refinement was R–3m ($^{\#}166$). "u" represents the atomic percentage of transition metal atoms in the Li atom layers. The Bragg R-factors are listed..... 146

Table 6.2 Lattice constants and atom positions for the four $Li[(Ni_{0.5}Mn_{0.5})_{0.4}Co_{0.6}]O_2$ samples from the single-phase Rietveld refinement of the XRD patterns. The space group used for the refinement was R-3m (#166). "u" represents the percentage of the Li sites occupied by transition metal atoms. The Bragg R-factors are listed..... 156

Table 6.3 Lattice constant (*a* and *c*, Å) for $MnCO_3$, $CoCO_3$, and $NiCO_3$. The space group is R-3c (#167)..... 164

Table 6.4 Lattice constants and atom positions for the products of the reactions between $Li[(Ni_{0.5}Mn_{0.5})_xCo_{1-x}]O_2$ (x = 0.4, 0.7, 0.9, and 1) samples and EC/DEC in ARC experiments stopped at 290°C [shown in Figure 6.29]. Multi-phase Rietveld refinement was used. The space group used for the refinements is Fm3m (#225) for $[Li_qM_{1-q}]O$ rock-salt and M phases. "M" represents mixed transition metals (Ni, Co, and Mn). The Bragg R-factors are listed..... 167

Table 6.5 Lattice constants and atom positions for the products of the reactions between $Li[(Ni_{0.5}Mn_{0.5})_xCo_{1-x}]O_2$ (x = 0.4, 0.7, 0.9, and 1) samples and EC/DEC in ARC experiments stopped at 350°C [shown in Figure 6.33]. Multi-phase Rietveld refinement was used. The space group used for the refinements is Fm3m (#225) for $[Li_qM_{1-q}]O$ rock-salt and M phases. "M" represents mixed transition metals (Ni, Co, and Mn). The Bragg R-factors are listed..... 171

Table 6.6 Lattice constants and atom positions for the products of reactions between $Li[(Ni_{0.5}Mn_{0.5})_{0.4}Co_{0.6}]O_2$ and EC/DEC in ARC experiments stopped at different temperatures (shown in Figure 6.37). Multi-phase Rietveld refinement was used. The space groups used for the refinements were R-3m (#166) for Li_xMO_2 phase and Fd3m (#227) for $[Li_pM_{1-p}]_3O_4$ spinel, Fm3m (#225) for $[Li_pM_{1-p}]O$ rock-salt and M phases. "M" represents mixed transition metals (Ni, Co, and Mn). The Bragg R-factors are listed... 174

Table 6.7 The standard free energies of formation (ΔG_f°) of MCO_3 and MO compounds and their differences (ΔG_f) from reference [114]. M represents the transition metals (Mn, Co, and Ni)..... 178

Table 6.8 Lattice constants and atom positions of x $Li[Mn_{1/2}Ni_{1/2}]O_2$ • y $LiCoO_2$ • 1/3 $Li[Li_{1/3}Mn_{2/3}]O_2$ (x + y = 2/3) samples with different Co content (y = 1/12, 1/6, ¼, and 5/12) synthesized at 900°C or 1000°C from the Rietveld refinement of the XRD patterns. The space group used for the refinement was R-3m (#166). "u" represents the percentage of the Li site occupied by transition metal atoms (presumably Ni). The Bragg R-factors are listed..... 196

Abstract

The thermal stability of lithium-ion batteries has recently attracted attention for two major reasons. (1). Attempts to make large-size cells used in power tools, E-bikes and EVs. Large cells have lower surface area to volume ratios and hence heat dissipation is more problematic than 18650-size cells. Safety problems, therefore, for large cells are more serious. (2). Next generation high-capacity electrodes will increase the energy density of lithium-ion cells meaning even an 18650-size cell may face safety concerns.

This thesis presents studies of the thermal stability of electrode materials in electrolytes to understand their reactivity. A search for new positive electrode materials with high thermal stability was made.

The thermal stability of two common electrode materials ($Li_{0.81}C_6$ and $Li_{0.5}CoO_2$) in lithium-ion cells was studied by Accelerating Rate Calorimeter (ARC). $Li_{0.81}C_6$ has much lower reactivity with lithium bis(oxalato)borate (LiBOB) electrolyte compared to $LiPF_6$ electrolyte. It is not the case, however, for $Li_{0.5}CoO_2$. Oven tests of full $LiCoO_2$/C 18650-size cells with LiBOB or $LiPF_6$ electrolytes, confirmed the ARC results.

ARC was then used to study the reactivity of existing electrode materials. The thermal stability of a negative electrode material was found to increase with the binding energy of Li atoms hosted in the material. $Li_{0.5}VO_2$ (B) has a higher lithium binding energy (2.45 eV vs. Li) than $Li_{0.81}C_6$ (0.1 eV vs. Li) and $Li_7Ti_5O_{12}$ (1.55 eV) and it shows the highest thermal stability in EC/DEC among the three materials. The reactivity of two existing positive electrode materials, $LiMn_2O_4$ and $LiFePO_4$, was studied. Cell systems expected to be highly tolerant to thermal abuse were suggested: $LiFePO_4$/C or $Li_4Ti_5O_{12}$ in LiBOB electrolytes.

The system, x $Li[Ni_{1/2}Mn_{1/2}]O_2$ • y $LiCoO_2$ • z $Li[Li_{1/3}Mn_{2/3}]O_2$ ($x + y + z = 1$), was explored for new positive electrode materials with large capacity and high thermal stability. $Li[(Ni_{0.5}Mn_{0.5})_xCo_{1-x}]O_2$ ($0.4 \leq x \leq 0.7$) samples have excellent electrochemical properties and thermal stability and are being commercialized by industry. $Li[(Ni_{0.5}Mn_{0.5})_xCo_y(Li_{1/3}Mn_{2/3})_z]O_2$ ($1/12 \leq y \leq 1/4$, $1/6 \leq z \leq 1/3$) samples have high specific capacity (200 mA h g^{-1}), excellent cycling performance, and are safer than $LiCoO_2$. The materials are suggested for energy cells used in cell phones, laptops, and so on.

List of Abbreviations and Symbols used

a – lattice constant (Å)

A-E model – Avrami-Erofeev model

Ah – ampere-hour

ARC – Accelerating Rate Calorimeter

b – lattice constant (Å)

BET – Brunauer-Emmett-Teller

c – lattice constant (Å)

C_i – specific heat of substance i ($J\ K^{-1}\ g^{-1}$)

C_{Tot} – total heat capacity of reactant(s) plus sample holder ($J\ K^{-1}$)

C/n – a specific charge/discharge rate at which a charge/discharge process completes in n hours

$D°_{298}$ – bond energy ($kJ\ mol^{-1}$) at 298 K

DEC – diethyl carbonate ($C_5H_{10}O_3$)

DMC – dimethyl carbonate ($C_3H_6O_3$)

DSC – Differential Scanning Calorimeter

DTBP – di-t-butyl peroxide

E – binding energy of lithium atoms hosted in a material (eV)

e^- – electronic charge (C)

E_a – activation energy ($kJ\ mol^{-1}$)

E-bicycle – electrical bicycle

EC – ethylene carbonate ($C_3H_4O_3$)

EDS – Energy Dispersive Spectroscopy

EMC – ethyl methyl carbonate ($C_4H_8O_3$)

EPDM – ethylene propylene diene terpolymer

EV – electric vehicle

eV – electron volt

f – surface heat transfer coefficient

$\Delta G_f°$ – standard free energy of formation ($kJ\ mol^{-1}$)

ΔG_f – change in the standard free energy of formation (kJ mol^{-1})

GITT – Galvanostatic Intermittent Titration Test

h – heat evolved (J)

ΔH – heat evolved (J g^{-1})

ΔH_f° – standard enthalpy of formation (kJ mol^{-1})

HEV – hybrid electric vehicle

HWS – Heat-wait-search

K – Kelvin temperature

k – Arrhenius rate constant

k_B – Boltzmann constant

lb. – pound

$LiAsF_6$ – lithium hexafluoroarsenate

LIB – lithium ion battery

LIBD – Lithium-ion Battery Discussion on electrode materials

LiBETI – $LiN[SO_2C_2F_5]_2$

LiBOB – lithium bis(oxalato)borate ($LiBC_4O_8$)

Li_xC_6 – lithiated graphite. "x" represents the lithium content.

LMI – Liquid Metronics Inc.

$[Li_pM_{1-p}]O$ – a metal oxide having the rock-salt structure (space group Fm3m, #225) where "M" represents a mixture of transition metal atoms (Ni, Mn, Co, etc.) and "p" is the lithium content.

$[Li_pM_{1-p}]_3O_4$ – a metal oxide with the spinel structure (space group Fd3m, #227)

$LiPF_6$ – lithium hexafluorophosphate

$Li_{0.5}VO_2$ (B) – lithiated VO_2 (B)

M* – a mixture of Co and Ni

MCMB – mesocarbon microbeads

MFA – methyl difluoroacetate (CHF_2COOCH_3)

MFE – methyl fluorinated ethers

m_i – mass of substance i (g)

min. – minute

NFP – no flash point

NMP – n-methyl pyrrolidinone

Oct – octahedral site

PC – propylene carbonate ($C_4H_6O_3$)

PVDF – polyvinylidene difluoride

Q – specific capacity (mA h g^{-1})

r – probability of a turbostratic shift between adjacent graphene layers

R_{Bragg} – Bragg agreement factor in Rietveld refinement

S – area between the self-heating rate versus temperature curve and the x-axis (temperature) between 110°C and 180°C (K^2 min^{-1})

S cm^{-1} – conductivity unit

SEI – Solid Electrolyte Interface

SEM –Scanning Electron Microscopy

SHR – Self-Heating Rate (°C/min)

T – Temperature (°C)

ΔT – change in temperature (K)

t – time (minute)

Tet – tetrahedral site

TGA – Thermal Gravimetric Analysis

TIG – Tungsten Inert Gas

TMP – trimethyl phosphate

u – fraction of lithium sites occupied by transition metal atoms in lithium transition metal oxides

UL – Underwriters Laboratories

USD – United States Dollars

V – potential in volts

V_{av} – average oxidation state

VO_2 (B) – a phase of VO_2 having the space group C2/m ($^{\#}12$)

XPS – X-ray Photoelectron Spectroscopy

XRD – X-ray Diffraction

Y_{ic} – intensity calculated at point i in the X-ray diffraction pattern

Y_{io} – intensity observed at point i in the X-ray diffraction pattern

α – fractional degree of conversion

α_0 – fractional degree of conversion at t (time) = 0

β – angle between the *a* and *c* axes of a unit cell

β-MnO_2 – a phase of MnO_2 (space group $P4_2/mnm$, $^{\#}136$)

λ – wavelength (Å)

λ-MnO_2 – a phase of MnO_2 formed by delithiation of $LiMn_2O_4$ spinel

χ^2 – goodness of fitting parameter

γ – frequency factor (min^{-1})

μ – chemical potential (eV)

δ – constant in Newton's law of cooling

Acknowledgements

It has been my great pleasure to pursue my Ph.D in such a great group and in such an interesting field. There are lots of great people that I want to thank for their help during my studies at Dalhousie University. Their guidance and help were essential to the smooth completion of this thesis.

I would like to first thank my supervisor, Professor Jeff Dahn, for his constant encouragement and support. The most important for me is what I learned from him. As his student, I learned how a deep insight can be gained from a simple experiment, how experiments can be designed to test my ideas about science, and how a trend can be extracted from data. As a researcher, I learned that enthusiasm, dedication, hard work, and patience are necessary to be a great scientist. As a member in the Dahn-lab, I learned how important it is to gel the whole research group to move ahead.

Second, I would like to thank members of the Dahn-lab during the past three years. They are David, Hubert, Mike, Arman, Adam, Thorsten, Claudia, Lee, Jing, Brad, Vincent, Dean, Zhonghua, Zhaohui, Zhonghai, Jun, Tim, Luc, Severine, Shane, and many summer students, etc. It is great to work with you guys.

Third, I want to thank my supervisory committee members, Dr. Neil Burford, Dr. Mary Anne White, and Dr. Josef Zwanziger, for their support and guidance throughout my degree. Also, I thank Dr. Jean Burnell for helping me as graduate coordinator.

I also acknowledge the help from the staff in the Departments of Chemistry and Physics: Giselle, Gail, Shelley, Cheryl, Deanna, Barbara, Anne, Anne-Marie, Melissa, etc.

Finally, a big thanks to my family in China and to Zhuoran for their constant love and support.

Chapter 1 Introduction

1.1 Battery development

Lithium-ion batteries (LIBs) were first brought to market in 1991 by Sony Corp. (Japan). Since then LIBs have been used in consumer products as diverse as cellular phones, video cameras, notebook computers, portable minidisk players and others. LIBs have played a leading role in the portable secondary battery market in the recent decade because of their large energy density, higher voltage and longer lifetime compared to conventional battery systems.

Approximately 600 million cells for LIBs per year are currently produced. The rate of production is increasing by 13% per year [1]. Many of these cells are 18 mm in diameter by 65 mm in length (18650-size cylindrical type) and deliver about 2 Ah of charge [2]. However, large size LIBs for electric vehicles (EVs) are still unavailable because of safety concerns [3-12]. For an EV (no combustion engine), about 100 - 150 Ah are needed to supply the necessary energy and power to the car. Heat dissipation to the environment is not as effective when the surface area to volume ratio decreases, as would occur in 100 Ah cells as compared to a 2 Ah cell. In abuse situations, such as short circuit, overcharge, etc., the components of the cells begin to react and the temperature of 100 Ah cells would reach higher values than the temperature of 2 Ah cells because of the slower rate of heat dissipation.

The reactions between the components within lithium-ion batteries at elevated temperature are still not completely understood. An understanding of these reactions must be obtained so that safer cell components can be found and higher thermal stability of LIBs can be achieved.

1.2 Electrochemistry of lithium-ion batteries

A commercial lithium-ion cell usually contains a graphite negative electrode, a lithium transition metal oxide positive electrode ($LiMO_2$, where M is a transition metal, such as Co, Mn, Ni, etc.) and an organic electrolyte with a dissolved lithium salt (typically $LiPF_6$). During charge, lithium atoms are extracted from the positive electrode material and inserted into the negative electrode material. During discharge, the reverse process takes place, as shown in Figure 1.1. The basic electrochemistry of the cell is only

the transfer of lithium atoms between the two layered electrodes, the ions through the electrolyte and the corresponding electrons through the external current. The electrochemical charge/discharge reactions can be represented by the following equations [1-1] and [1-2],

For the positive electrode:

$$LiMO_2 \underset{\text{discharge}}{\overset{\text{charge}}{\rightleftharpoons}} Li_{1-x}MO_2 + xLi^+ + xe^-. \qquad [1\text{-}1]$$

For the negative electrode:

$$C + xLi^+ + xe^- \underset{\text{discharge}}{\overset{\text{charge}}{\rightleftharpoons}} Li_xC. \qquad [1\text{-}2]$$

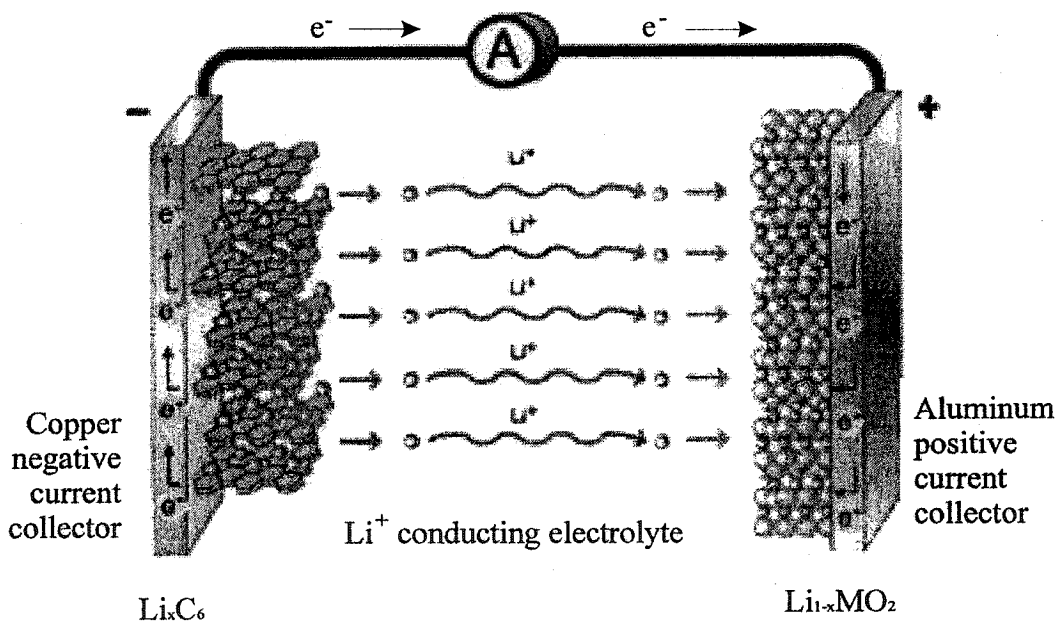

Figure 1.1 Schematic diagram of a commercialized lithium-ion cell during discharge [13]. Reprinted with permission from the authors.

The voltage of the electrochemical cell depends on the difference in the chemical potential of lithium atoms in the two electrode materials,

$$V = -\frac{(\mu_{positive} - \mu_{negative})}{e}, \qquad [1\text{-}3]$$

where $\mu_{positive}$ and $\mu_{negative}$ are the chemical potential of lithium atoms in the positive and negative electrode materials, respectively, and e is the magnitude of electron charge. The chemical potential of Li in lithium metal, μ_{Li}, is constant because it is composed a single phase. This chemical potential therefore serves as a reference for the chemical potential of lithium atoms in the electrode materials. The chemical potential of lithium in the electrodes may also be described in terms of the lithium atom binding energy, E, in the host, related simply to μ by $\mu = -E$ (μ_{Li} is used as a reference for both μ and E).

Figure 1.2 shows the lithium binding energies versus lithium metal of different electrode materials that will be discussed in the next section. For example, the lithium binding energy of a lithium atom in the $LiCoO_2$ positive electrode and in the Li_xC_6 negative electrode are approximately 4.2 eV and 0.1 eV vs. Li metal (Figure 1.2). This suggests a fully charged $LiCoO_2$/C cell has an output potential of approximately 4.1 V.

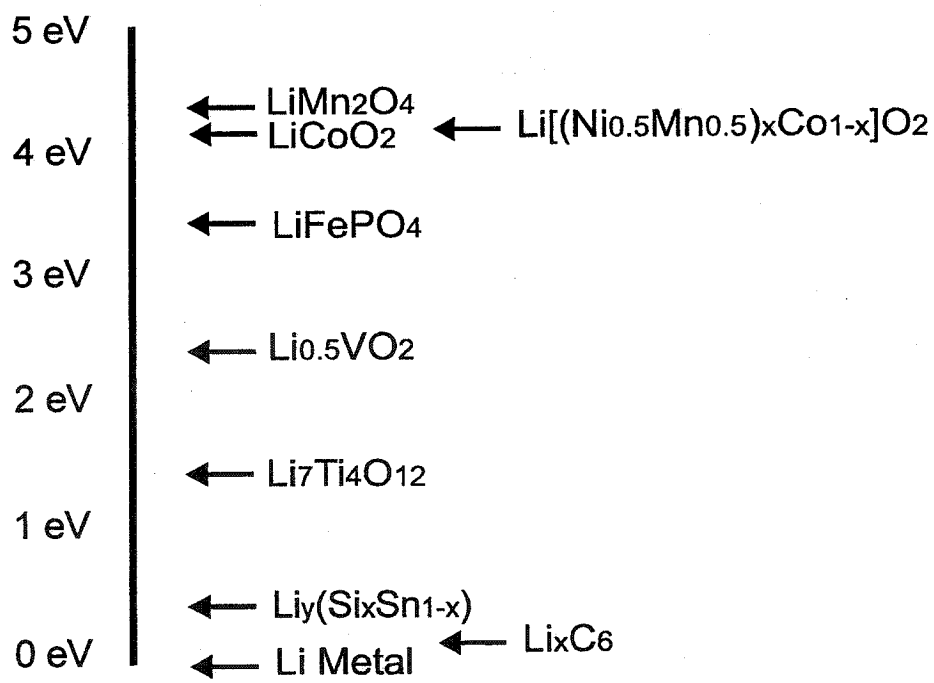

Figure 1.2 Binding energies of lithium in various lithium compounds versus lithium metal.

1.3 State of the art lithium-ion battery technology today

Battery manufacturers want to produce LIBs with higher energy density and improved safety characteristics. Recently, many new negative [14-20] and positive electrode materials [21-25] with higher capacity and better thermal stability have been characterized and some have been adopted to improve the electrochemical and safety performance of LIB technologies.

1.3.1 Negative electrode material development

In the early 1960s, primary cells with metallic lithium negative electrodes and non-aqueous electrolytes were successfully introduced into the market. The main benefits of these cells over conventional batteries with aqueous electrolytes were the high voltage, high energy density and low self-discharge rate [26]. In the 1980's much effort was expended developing secondary lithium batteries with lithium metal as a negative electrode. However, the poor safety of rechargeable cells incorporating lithium metal inhibited their further application.

In the 1980s graphite was first introduced as a negative electrode material [27]. Graphite has a low binding energy for lithium so that the combination of a graphite negative electrode with a high binding energy positive electrode, such as $LiCoO_2$, produces a cell having a high voltage. In addition, graphitic materials show a high degree of structural tolerance for reversible intercalation, which leads to good charge-discharge cycling performance [9, 28]. Today, most LIB manufacturers still use graphite as the negative electrode material [1].

The disadvantages of graphite are a low discharge capacity and a relatively low thermal stability [29]. The first discharge capacity of graphite is close to its theoretical capacity of 372 mA h g^{-1}. The plateau at around 0.8 V in the first discharge curve of graphite vs. lithium corresponds to the formation of a solid electrolyte interphase (SEI) between the negative electrode (Li_xC_6) and the electrolyte [30, 31]. The capacity loss in this process is called irreversible capacity because it can not be recovered in later cycles. The discharge capacity of graphite after the first cycle is around 330 mA h g^{-1}, which is much lower than alloy negative electrode materials such as SiSn [15, 32]. Richard *et al.* [29, 33-35] showed that an exothermic reaction can be detected (0.03°C/min slope

sensitivity used) between fully charged MCMB ($Li_{0.81}C_6$) and $LiPF_6$ EC/DEC electrolyte starting as low as 70°C by accelerating rate calorimetry (ARC).

Recently, many efforts have been made to search for new negative electrode materials with high capacity. Amorphous silicon has been tried by several groups [36-38] because of its high capacity of up to 4200 mA h g^{-1}. An amorphous silicon thin film electrode with a 150 nm thickness can cycle more than 1000 times while still retaining 90% capacity [39]. Tin is another attractive negative electrode material for LIBs again because of its high theoretical capacity of 980 mA h g^{-1} [30-44]. A SiSn alloy developed by 3M Corp. (USA) and Dalhousie University has a capacity of 800 mA h g^{-1} and its capacity retention is above 80% after 100 cycles. The application of these new negative electrode materials will significantly increase the energy density of LIBs.

Until now, alloy negative electrode materials with high capacity are still not commercially available for the following reasons: (1). Crystalline alloys generally have large irreversible capacity up to 200 mA h g^{-1}, which can not be recovered after the first cycle; (2). Crystalline alloys show poorer capacity retention during cycling than graphite. A large volume expansion of up to 250% after full lithiation can cause alloy particles to break into small parts, which causes loss of electrical contact and hence cycling capacity loss [45]; (3). Amorphous alloys have been designed to partially overcome the two disadvantages described above and they have lower irreversible capacity and better cycling performance [45, 46]. However it is difficult to economically mass-produce amorphous alloys which can react with substantial amounts of lithium; (4). Alloys also generally have a high potential (average around 0.3 ~ 0.4 V vs. Li), which decreases the output voltage of the Li-ion cell;

Another concern about alloy negative electrode materials is safety. Previously it was believed that increasing the energy density of LIBs decreases thermal stability. For example, a 2 Ah 18650-type cell from E-One Moli/Energy Ltd. passed a 150°C oven test whereas 2.4 Ah cells exhibit thermal runway forty minutes after they were put into a 150°C oven. Until now, no thermal stability data has been reported for 18650-size cells containing high capacity negative electrode materials.

1.3.2 Trends for positive electrode material development

$LiCoO_2$ was first proposed as a positive electrode material for LIBs in 1980 and has been used since then because of its favorable cycling, satisfactory stability, and ease of preparation in a high quality, ideal layered structure. Figure 1.3 shows the layered structure of $LiCoO_2$ based on close-packed oxygen layers. Li and Co cations are arranged into alternating layers between the oxygen planes.

Currently, LIB manufacturers still use $LiCoO_2$ as the positive electrode material in 18650 size cells. However the safety of $LiCoO_2$ is still a big concern for the application of large lithium-ion batteries in electric bicycles and electric vehicles (EVs). In addition, the price of Co has increased from approximately 7 USD/*lb.* in 2002 to nearly 23 USD/*lb.* in September 2004 in part because of the booming market for lithium-ion batteries [47]. Therefore, there has been a large effort in finding a replacement for $LiCoO_2$ to make lithium-ion batteries safer and cheaper as well.

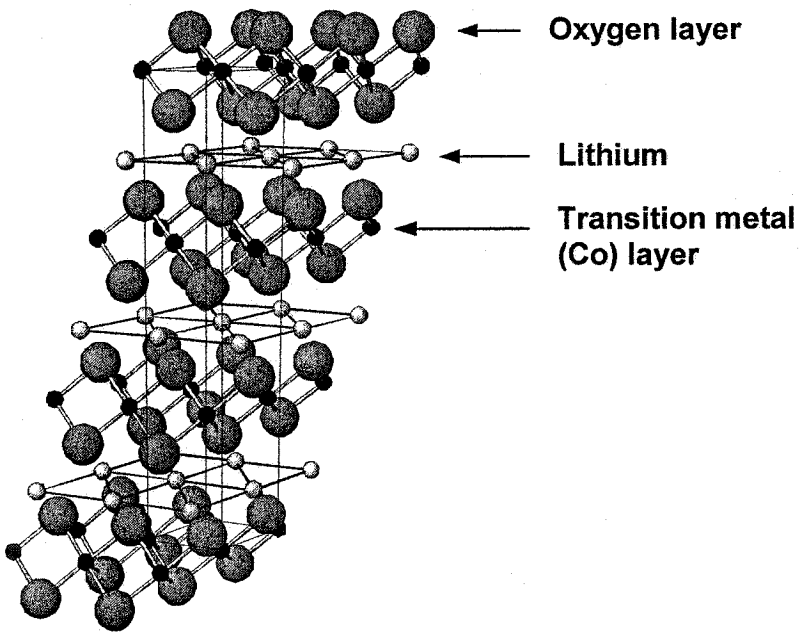

Figure 1.3 Layered structure of $LiCoO_2$.

$LiMn_2O_4$ with the spinel structure has become more and more attractive for EV applications because its delithiated structure (MnO_2) has a higher thermal stability than $Li_{0.5}CoO_2$ [48, 49]. The onset temperature for the reaction of 100 mg of charged $LiMn_2O_4$ with 100 mg of EC/DEC solvent is about 180°C as measured by ARC, which is 30°C

higher than the ARC onset temperature for charged $LiCoO_2$ in EC/DEC [50-52]. In addition, Mn has a much lower price than Co.

The main disadvantage of $LiMn_2O_4$ is its poor cyclability, which is considered to be due largely to the dissolution of manganese from the compound into the electrolyte during cycling [53, 54]. Doping $LiMn_2O_4$ with Al, Nb, and also excess Li effectively stabilizes the $LiMn_2O_4$ structure, improves its cycling performance, and also increases its thermal stability as measured by DSC [55-57]. Another disadvantage of $LiMn_2O_4$ is that its capacity, 120 mA h g^{-1}, is about 20 mA h g^{-1} lower than $LiCoO_2$ when charged to 4.2 V vs. lithium metal, which means that the energy density of cells made with $LiMn_2O_4$ is lower than the energy density of cells with $LiCoO_2$. This lower capacity has hindered the widespread introduction of $LiMn_2O_4$ as a positive electrode material for commercial cells. Recently, some lithium-ion battery producers, such as E-One Moli/Energy Ltd. (Canada), have started to make cells with $LiMn_2O_4$ as the positive electrode material for E-bicycle (electrical bicycle) applications [58].

$LiFePO_4$ is an another attractive cathode material for large size cells because it has even higher thermal stability than $LiMn_2O_4$ [59-61]. Pure $LiFePO_4$ has a relatively low electrical conductivity of around $10^{-7} \sim 10^{-9}$ S cm^{-1}, compared to the conductivity of $LiCoO_2$ of 10^{-3} S cm^{-1} [62]. Hence the rate capability of $LiFePO_4$ is not good as $LiCoO_2$. Much effort was expended improving the conductivity of $LiFePO_4$. Chiang *et al.* [63] tried to dope $LiFePO_4$ with 1% Nb, which improves the conductivity of $LiFePO_4$ to above 10^{-2} S cm^{-1} at room temperature. Armand [64] coated $LiFePO_4$ with only 0.2% carbon and a conductivity of 10^{-4} S cm^{-1} was achieved. Chen and Dahn [65] coated $LiFePO_4$ with carbon using a range of methods and the coated $LiFePO_4$ presented good cyclability and rate capability.

The stability of carbon-coated $LiFePO_4$ in the charged state was studied in EC/DEC solvents using ARC and no obvious exothermic signal appeared until 300°C [60]. The onset temperature of charged $LiFePO_4$ heated with $LiPF_6$ EC/DEC (1:2 by volume) electrolyte was found to be about 190°C, which is 30°C and 10°C higher than the ARC onset temperature of charged $LiCoO_2$ and charged $LiMn_2O_4$ in $LiPF_6$ EC/DEC electrolyte, respectively [51, 66]. It is possible that the exothermic signal from 220°C to 240°C in the ARC experiment of $LiFePO_4$ with $LiPF_6$ EC/DEC comes from the

decomposition of $LiPF_6$ salt in EC/DEC solvent because the ARC result of $LiPF_6$ EC/DEC alone shows a similar exothermic signal in the same temperature range.

The low tap density of carbon-coated $LiFePO_4$ has limited the comprehensive application of $LiFePO_4$ in the LIB industry. The tap density of 0.2% carbon-coated $LiFePO_4$ is only about 1.4 g cm^{-3}, which is much lower than the tap density of $LiCoO_2$, 2.5 g cm^{-3}. The lower tap density of $LiFePO_4$ leads to a lower volumetric energy density in LIBs than $LiCoO_2$. Despite this density issue, $LiFePO_4$ still is considered to be a candidate positive electrode material for EV applications because of its high thermal stability.

In 2001 Lu *et al.* [24, 67] and Ohzuku [25] first synthesized a series of new layered cathode materials, $Li[(Ni_{0.5}Mn_{0.5})_xCo_{1-x}]O_2$ ($0 < x \leq 1$), which can be regarded as solid solutions between $Li[Ni_{0.5}Mn_{0.5}]O_2$ and $LiCoO_2$ phases. $Li[(Ni_{0.5}Mn_{0.5})_xCo_{1-x}]O_2$ compounds have the same layered structure as $LiCoO_2$ (shown in Figure 1.3). There are three metal species in the transition metal layer, Mn, Co, and Ni. Lu and Dahn [67] found that some compounds in this series provided a high capacity of around 180 mA h g^{-1} when charged to 4.4 V vs. Li metal, together with good cyclability and rate capability. Jouanneau [21] modified the synthesis method for making $Li[(Ni_{0.5}Mn_{0.5})_{0.2}Co_{0.8}]O_2$ (x = 0.2) increasing its pellet density to 3.6 g cm^{-3}, which is close to the pellet density of $LiCoO_2$. MacNeil [23] found that the thermal stability of $Li[(Ni_{0.5}Mn_{0.5})_xCo_{1-x}]O_2$ in electrolyte increases substantially as x increases from 0 to 0.4. Even with small Ni and Mn concentrations of x = 0.2 in $Li[(Ni_{0.5}Mn_{0.5})_xCo_{1-x}]O_2$, there is an almost 80°C increase in the temperature of any significant exothermic activity as measured by Differential Scanning Calorimetry (DSC).

Our preliminary studies on the thermal stability of $Li[(Ni_{0.5}Mn_{0.5})_{0.2}Co_{0.8}]O_2$ shows that the onset temperature of reaction between charged $Li[(Ni_{0.5}Mn_{0.5})_{0.2}Co_{0.8}]O_2$ (4.2 V vs. Li) and $LiPF_6$ EC/DEC is around 200°C, which is even 10°C higher than the ARC onset temperature of charged $LiFePO_4$ in $LiPF_6$ EC/DEC electrolyte [60]. However, the details of the reaction between charged $Li[(Ni_{0.5}Mn_{0.5})_{0.2}Co_{0.8}]O_2$ and solvent or electrolyte at elevated temperature are still unknown. The structure, electrochemical properties, and thermal stability of $Li[(Ni_{0.5}Mn_{0.5})_{0.2}Co_{0.8}]O_2$ ($0 < x \leq 1$) materials will be

explored in this thesis. Furthermore, the thermal reaction sequence in EC/DEC solvent and $LiPF_6$ based electrolyte will be discussed.

As discussed in Section 1.3.1, the development of metal alloys (such as SiSn, etc.) as negative electrode materials can bring a huge capacity over 1000 mA h g^{-1} and also an average potential of 0.3 ~ 0.4 V versus Li. This pushes the development of positive electrode materials with higher capacity, higher voltage, and higher thermal stability.

Recently, solid solutions between Li_2MnO_3 ($Li[Li_{1/3}Mn_{2/3}]O_2$) and $LiMO_2$ (M = Co, $Mn_{0.5}Ni_{0.5}$, etc.) have been used to improve the electrochemical properties of positive electrode materials [67-77]. To design such a lithium transition metal oxide with a mixture of transition metals is complex. Consider the hypothetical compound $Li[Li_xM^1{}_yM^2{}_z...]O_2$ with M^1 and M^2 being transition metals. Here, the atoms within the brackets are designated to be in the "transition metal" layer and $x + y + z + \ldots = 1$. There are several guidelines that need to be met:

(1). The layer sequence should be lithium - oxygen - transition metal - oxygen - lithium ..... (some lithium atoms are allowed within the transition metal layers, but as little transition metal as possible should be allowed on the lithium planes). This ensures rapid diffusion in the lithium planes and hence good battery performance.

(2). To maximize capacity for lithium-ion cell applications, the lithium layers should be full, unless it is impossible to synthesize the desired layers with full alkali occupation.

(3). To make synthesis facile in air, the oxidation states of the transition metals should be those that they naturally adopt in air at synthesis temperature in the presence of the other cations.

(4). Normally, at least one of M^1, M^2, etc. should be able to be oxidized within the electrochemical window of the electrolyte.

These guidelines have been used to synthesize new positive electrode materials for Li-ion cells. In 1997, Numata [69, 78] synthesized a series of layered compounds, $Li[(Li_{1/3}Mn_{2/3})_xCo_{1-x}]O_2$ ($0 \leq x \leq 1$), which can be regarded as solid solutions between different ratios of $Li[Li_{1/3}Mn_{2/3}]O_2$ and $LiCoO_2$. The $Li[(Li_{1/3}Mn_{2/3})_xCo_{1-x}]O_2$ compounds meet all the above four rules. $Li[(Li_{1/3}Mn_{2/3})_xCo_{1-x}]O_2$ (x = 0.1, 0.2, and 0.3) samples showed good cycling performance and high rate capability but lower capacity than $LiCoO_2$ between 3.0 and 4.3 V [69, 78].

Lu and Dahn [70, 24] studied the solid solutions between $Li[Ni_{1/2}Mn_{1/2}]O_2$ and $Li[Li_{1/3}Mn_{2/3}]O_2$, which can be expressed as $Li[(Ni_{1/2}Mn_{1/2})_x(Li_{1/3}Mn_{2/3})_{1-x}]O_2$ ($0 < x \leq 1$). They found that $Li[(Ni_{1/2}Mn_{1/2})_x(Li_{1/3}Mn_{2/3})_{1-x}]O_2$ (x = 1/3, 1/2, 2/3, and 5/6) samples all displayed a plateau at about 4.5 V vs. lithium metal during the first charge, which was believed to correspond to oxygen loss concomitant with Li extraction. Subsequent to this plateau, the materials can reversibly cycle over 225 mA h g^{-1} (almost one Li atom per formula unit) between 2.0 V and 4.6 V [19]. However, the synthesized $Li[(Ni_{1/2}Mn_{1/2})_x(Li_{1/3}Mn_{2/3})_{1-x}]O_2$ cathode materials show a small particle size around 0.3 μm and relatively poor rate capability after traversing the O_2 loss plateau at room temperature. Furthermore, $Li[(Ni_{1/2}Mn_{1/2})_x(Li_{1/3}Mn_{2/3})_{1-x}]O_2$ cathodes charged to 4.8 V show relatively inferior thermal stability compared with $Li[(Ni_{1/2}Mn_{1/2})_xCo_{1-x}]O_2$ charged to 4.2 or 4.4 V [76].

Based on the prior studies that the rate capability of $Li[(Ni_{1/2}Mn_{1/2})_xCo_{1-x}]O_2$ positive electrode increases with Co content [79, 80], Co was added to $Li[(Ni_{1/2}Mn_{1/2})_x(Li_{1/3}Mn_{2/3})_{1-x}]O_2$ giving the $Li[(Ni_{1/2}Mn_{1/2})_xCo_y(Li_{1/3}Mn_{2/3})_z]O_2$ ($x + y + z = 1$) series of cathode materials, which lie within the $Li[Ni_{1/2}Mn_{1/2}]O_2 \bullet LiCoO_2 \bullet Li[Li_{1/3}Mn_{2/3}]O_2$ pseudo ternary system. These materials have a Li^+, Ni^{2+}, Mn^{4+}, and Co^{3+} cation mixture in the transition metal layer and meet the described four rules. We identified the effects of Co content (y) on the particle size, lattice constant, electrochemical performance, and thermal stability of the synthesized cathode materials as well. Cathode material candidates with high discharge capacity (over 200 mA h g^{-1} at C/6), excellent cycling performance, and acceptable thermal stability were found in this ternary system.

1.3.3 Salt

In lithium-ion batteries, a lithium salt also is important. A "good" lithium salt must meet the following requirements: (1) ability to form a stable solid electrolyte interphase (SEI); (2) electrochemical stability in a wide potential window; (3) acceptable solubility in alkyl carbonate organic solvents like EC, DMC, etc; (4) high conductivity in various nonaqueous solvent systems and (5) good cycling behaviour.

The lithium salts can be subdivided into fluorinated salts and non-fluorinated salts. Fluorinated salts include $LiPF_6$ [81], $LiAsF_6$ [82], $LiBF_4$ [83], $LiCF_3SO_3$, etc. At high temperatures, these salts can decompose to produce LiF:

$$LiPF_6 \rightarrow LiF + PF_5. \qquad [1\text{-}4]$$

$$LiAsF_6 \rightarrow LiF + AsF_5. \qquad [1\text{-}5]$$

The product, PF_5 for example, is a strong Lewis acid that can react easily with organic solvents such as EC [81] PC, etc. Furthermore, the labile P-F bond in PF_5 is highly susceptible to hydrolysis by any trace amounts of water present in the electrolyte releasing HF. These reactions can cause safety problems for LIBs. Richard showed that the onset temperature for discharged MCMB ($Li_{0.81}C_6$) is about 70°C in $LiPF_6$ EC/DEC and 50°C in $LiBF_4$ EC/DEC [35].

Although $LiPF_6$ is not a thermally stable salt, it is still the most successfully commercialized salt in LIB technology. For the graphite negative electrode, the formation of a LiF film from the decomposition of $LiPF_6$ salt on the Li_xC_6 surface can effectively inhibit further reaction between Li_xC_6 and electrolyte [35]. For the $Li_{0.5}CoO_2$ positive electrode, HF from the decomposition of $LiPF_6$ can polymerize with solvents, such as EC and PC protecting the positive electrode from further attack by reducing agents such as EC, DEC, PC, etc. The addition of $LiPF_6$ into EC/DEC solvent therefore increases the thermal stability of both the $Li_{0.81}C_6$ negative and $Li_{0.5}CoO_2$ positive electrodes [84-88].

Non-fluorinated salts, such as $LiClO_4$ and LiBOB, have recently received attention as alternative salts for LIBs [89,90]. The chlorine in $LiClO_4$ has a +7 oxidation state, which causes poor thermal stability for both LIB electrodes in the presence of $LiClO_4$ based electrolytes at high temperature [91].

Recently, the bis(oxalato)borate salt, LiBOB, has been proposed as a potential replacement for $LiPF_6$ [88-90, 92]. It meets the basic requirements for a salt to be used in lithium-ion cells outlined earlier. Furthermore, it gives better thermal stability than $LiPF_6$ in organic solvents [88-90]. Crystalline LiBOB is also much more stable than crystalline $LiPF_6$. For example, the TGA measurements made at Dalhousie have shown that crystalline LiBOB does not decompose until 300°C, however S.E. Sloop *et al.* [81] reported that only 60% of $LiPF_6$ remained after 200 minutes at 70°C in an isothermal TGA.

There have been few reports of the thermal stability of LiBOB-containing electrolytes with negative or positive electrodes. In this thesis, the thermal stability of lithiated MCMB in LiBOB EC/DEC is compared with that of lithiated MCMB in $LiPF_6$ EC/DEC using ARC and XRD measurements. The results show much improved thermal stability for lithiated MCMB in LiBOB EC/DEC electrolyte. However, the thermal stability of the Li_xCoO_2 electrode in LiBOB EC/DEC electrolyte is worse compared with $LiPF_6$-based electrolyte.

1.3.4 Solvent

The choice of solvent is another important factor that can affect the performance of the cells. For example, EC forms a SEI on the LiC_6 surface preventing direct contact between LiC_6 and the electrolyte and stabilizes the LiC_6 negative electrode while still allowing lithium ions to pass through [93]. However, graphite cannot cycle at all in $LiPF_6$ PC-based electrolyte because PC cointercalates causing exfoliation of graphitic anodes.

Preliminary ARC studies show that cyclic carbonate solvents, such as PC and EC, present higher thermal stability than linear carbonates like DMC and DEC. EC shows the best thermal stability among these carbonate solvents and DMC shows the worst thermal stability. The ARC onset temperature for reactions between $Li_{0.81}C_6$ and DMC is only 50°C [87].

An important direction to develop a thermally stable solvent for both $Li_{0.81}C_6$ and $Li_{0.5}CoO_2$ electrodes is to partially or totally displace traditional carbonate solvents with a series of new fluorinated carboxylic acid solvents. Using DSC, Yamaki *et al.* [94, 95] found that methyl difluoroacetate (MFA) has the highest thermal stability in this series of fluorinated carboxylic acids for both LiC_6 and Li_xCoO_2 electrodes. They also showed that the single solvent MFA electrolyte shows higher cycling efficiency for lithium metal than $LiPF_6$ EC/DMC, while the addition of MFA to EC/DMC could also improve the cycling efficiency of cells. XPS studies by Yamaki [95] showed that the formation of lithium acetate, which can not dissolve in the MFA solvent, effectively stabilizes both electrodes and improves thermal stability at elevated temperature.

Arai [96, 97] found that some methyl fluorinated ethers (MFE), such as CH_3-O-C_4F_9, are inflammable and have no flash point. The addition of fluorinated solvents into

electrolyte will definitely increase the thermal stability of positive electrode materials because the solvents will not be easily combusted by O_2 released from the decomposition of the charged positive electrode. A graphite/$LiCoO_2$ 18650 cylindrical cell with 1.0 M LiBETI ($LiN[SO_2C_2F_5]_2$) in MFE/EMC (ethyl methyl carbonate) (4:1 by volume) passed the nail penetration test without thermal runaway. The nail penetration test is one of the thermal abuse tests for lithium-ion batteries that will be described in Chapter 2.

The capacity of a graphite/$LiCoO_2$ 18650 cell with MFE based electrolyte, however, quickly faded from 1500 mA h to around only 250 mA h, compared to above 90% capacity retention of the cells with EC/EMC based electrolyte [97]. Further studies found that the low cyclability of graphite/$LiCoO_2$ 18650 cells containing MFE was due to the large resistance of the SEI on graphite in LiBETI MFE/EMC electrolyte. The addition of EC can significantly improve the cyclability of the cell because of a better SEI film is produced, however it is still apparently worse than the SEI produced by $LiPF_6$ EC/EMC electrolyte.

It is believed that a breakthrough in finding a thermally stable fluorinated solvent, which has equivalent electrochemical properties for both graphite and $LiCoO_2$ electrodes as an EC based solvent, will bring electric vehicles (EVs) or hybrid electric vehicles (HEVs) into the market.

1.3.5 Binder

A binder is used to hold the electrode particles together and to the current collector. The choice of binder perturbs the interface between the electrode and the electrolyte so that the choice of binder may affect the safety of lithium-ion batteries. In this report, the thermal stability of $Li_{0.81}C_6$ containing several different binders with electrolyte will be compared.

The first binder is ethylene propylene diene terpolymer (EPDM) obtained from Moli Energy Ltd. In the experiment, only 2% EPDM binder was added to the electrode. EPDM does not absorb any electrolyte (not swelled) and hence too much of it in the electrode mixture will cause the particles to be completely coated by this plastic which will prevent any electrochemical activity [35]. The EPDM binder is not used

commercially today by any manufacturer but it is a material that is significantly different from any of the other binders used, so it is worthy of study.

The other binder is polyvinylidene difluoride (PVDF), which is commonly used by LIB manufacturers. In contrast to EPDM, PVDF binder can be plasticized by electrolytes. Maleki *et al.* [98, 99] studied the stability of carbon-based negative electrodes with PVDF in electrolyte using ARC and he attributed the exothermic signal from 210°C to 300°C mainly to the reaction between PVDF binder and Li_xC_6. Maleki also showed that if 8% phenol-formaldehyde (PF) binder was used in the negative electrode mixture instead of PVDF, the released heat of the negative electrode (240 J g^{-1}) was nearly one-fifth of that of the PVDF electrode (1182 J g^{-1}).

In order to understand the effects of binders on thermal stability, MCMB negative electrodes with 1, 2, 4, 7, or 14% PVDF, 2% EPDM binder, or no binder were prepared and charged below 25 mV vs. lithium metal. The thermal stability of these electrodes was then compared using ARC.

1.3.6 Separator

A microporous separator is used to avoid the direct contact between the negative and positive electrodes while still allowing the lithium ions to pass easily. Currently, two major types of separators are used, polyethylene and polypropylene. The two polymers differ in their melting temperature (130°C and 150°C, respectively). When the melting point of the polymer is reached, the micropores in the separator melt and close, effectively stopping current flow. The lithium-ion cell can no longer operate due to the discontinuation of ion flow from one electrode to the other.

1.4 Introduction to the thermal stability of lithium-ion batteries

Strict safety guidelines have been developed for lithium ion batteries in order to protect consumers. In normal use, lithium-ion batteries are safe. However, under conditions of thermal (heating), mechanical (crushing), or electrical (short-circuit, overcharge) abuse, the charged electrodes of the lithium-ion battery, such as the $Li_{0.81}C_6$ negative electrode [85, 100, 101] and the $Li_{0.5}CoO_2$ positive electrode [8, 9, 86, 102], can react with organic solvents like EC, DEC, DMC, and PC, etc. at high temperature and

release heat. Under conditions of extreme abuse, this can result in cells emitting smoke or flame. Hence, in practical applications, the abuse tolerance of lithium-ion batteries in the charged state needs to be characterized.

The common abuse tests are described below:

(a) Oven test: this test simply involves placing the cell in a high temperature isothermal oven while its temperature is monitored. For consumer batteries, an oven temperature of 150°C is used.

(b) Short-circuit test: a low resistance (less than 5 mΩ) is connected across the terminals of the cell. The cell may be preheated. In this test, a high current flows through the battery generating heat within it. A typical 18650-size cell has an internal resistance of 50 mΩ, so most of the power is dissipated within the cell itself.

(c) Overcharge test: A constant current is forced through the cell until it reaches a limiting voltage near 10 V. Heat is generated by electrochemical reactions associated with decomposition of the cell electrolyte and by current flowing through the cell.

(d) Nail test: A nail is forced through a charged cell at a specified rate (such as 10 cm s^{-1}). When the nail penetrates the cell, the cell is internally shorted by the nail. Heat is then generated by current flowing through the cell, and by current flowing through the nail. This produces an internal local hot spot in the cell.

(e) Crush test: A round bar is used to press down on the charged cell until a short-circuit initiates. Heat is generated within the cell due to the discharge, and locally at the points where electrode pairs are physically shorted.

The oven test and the overcharge test can be more severe since additional energy is added to the cell. The nail and crush tests are more difficult to pass if overcharged cells are used. The nail, crush, and short-circuit tests are somewhat similar, but have significant differences. In these three tests, heat is generated by a rapid discharge of the cell. The short-circuit test allows the cell to discharge uniformly throughout the volume of the cell. The nail and crush tests create local hot spots in the cell.

Oven test results are generally quite reproducible. The oven tests of two commercially available lithium-ion cells are shown as an example to explain the oven test in detail.

1.4.1 Oven test

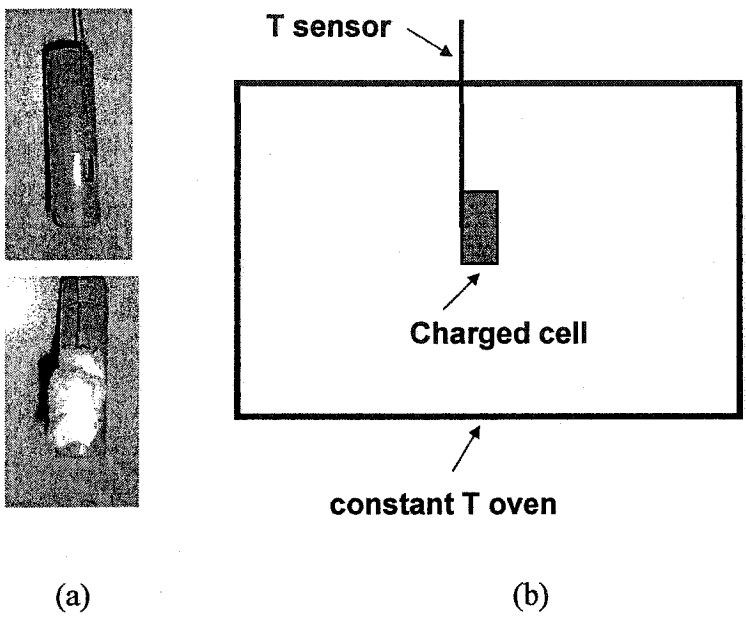

Figure 1.4 A thermocouple was attached to surface of an 18650-size cell charged to 4.2 V in (a). The cell then was put into a constant temperature oven.

An oven exposure test on a commercially available lithium-ion cell was previously done in Jeff Dahn's laboratory, in accordance with UL 1642 standards [103]. An 18650-size lithium-ion cell was fully charged to 4.2 V at a low rate of C/100 (100 hours for full charge). A thermocouple was strapped tightly to a region of the cell where part of the label (0.5 cm × 0.5 cm) had been removed with a sharp blade. The point of contact between the thermocouple and the cell was covered by alumina wool as shown in Figure 1.4a. The cell with attached thermocouple was then put into the center of a constant temperature oven shown in the schematic in Figure 1.4b. MCMB/1.0 M $LiPF_6$ EC:DEC/$LiCoO_2$ 18650 size cells were obtained from Moli Energy Ltd. (Canada). The heating profile of the cell (temperature vs. time) was studied The result is shown in Figure 1.5 [52]. In order to qualify as a safe cell according to the UL 1642 standard, the cell must survive a ten-minute exposure at 150°C without going into thermal runaway. Thermal runaway is the point where the exothermic reactions run out of control and result in the cell emitting smoke or flame.

Figure 1.5 shows that the cell began to self-heat because of the internal exothermic reactions as its temperature approached the 150°C oven temperature. The pressure buildup was sufficient to open the cell's pressure vent, causing a slight decrease in temperature, but this was not sufficient to stop the exothermic reactions. Then the cell proceeded into thermal runaway and ended with the cell venting with flames. This cell is not safe because it went into thermal runway about 11 minutes after it was placed in the 150°C oven. However, according to the UL 1642 standard, this is a safe cell since it did not go into runaway during the first 10 minutes after reaching 150°C.

Another oven test result for a MCMB/1.0 M $LiPF_6$ EC:DEC/$LiMn_2O_4$ 18650-size cell from Moli Energy Ltd. is shown in Figure 1.6 [52]. After the charged cell was put into a 150°C oven, there was an initial self-heating event that caused the cell temperature to increase above the 150°C oven temperature. The cell temperature then gradually decreased to the oven temperature because the small amount of heat generated by the exothermic reactions within the cell was efficiently transferred away. This cell is safe according to UL 1642.

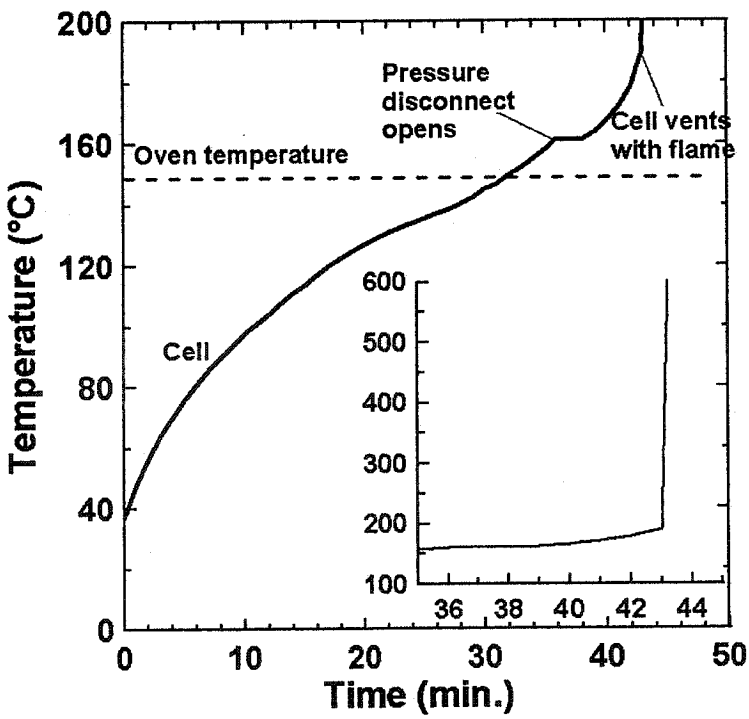

Figure 1.5 Measured oven exposure data for a commercial 18650-size cell [52]. Reprinted with permission from the author.

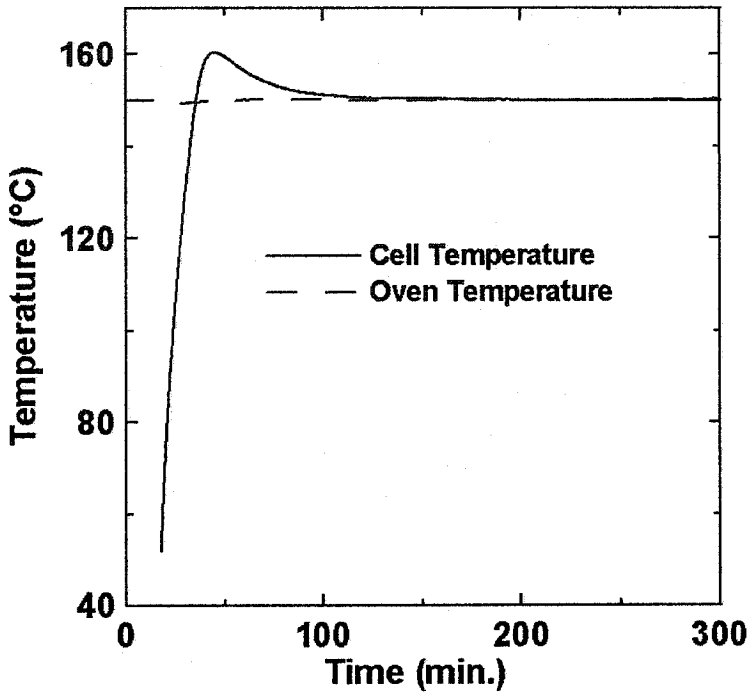

Figure 1.6 Oven exposure data for a MCMB/$LiMn_2O_4$ cell with 1.0 M $LiPF_6$ EC/DEC (1:2 by volume) electrolyte [52]. Reprinted with permission from the author.

The difference between the oven-test results in Figures 1.5 and 1.6 are mainly due to the different positive electrode materials used ($LiCoO_2$ in Figure 1.5 and $LiMn_2O_4$ in Figure 1.6). Charged $LiMn_2O_4$ has higher thermal stability than charged $LiCoO_2$ in lithium-ion batteries.

It is not convenient for university researchers to compare the thermal stability of different electrode materials, such as $LiCoO_2$ and $LiMn_2O_4$, using the oven-test on prototype 18650-size cells. Fortunately, the thermal stability of different electrode materials can be simply compared using calorimetry in the laboratory and only a few grams of electrode materials are needed to prepare samples for thermal tests.

1.4.2 Thermal tests for lithium-ion battery electrode materials in the laboratory

Lithium-ion battery researchers have used sensitive techniques such as thermal gravimetric analysis (TGA) and accelerating rate calorimetry (ARC) to test the thermal stability of the components of lithium-ion cells.

1.4.2.1 Thermal Gravimetric Analysis (TGA)

In a TGA measurement, the mass of a sample is measured as a function of temperature. A TGA study [48] on the stability of three cathode candidates (Li_xNiO_2, Li_xCoO_2, and $Li_xMn_2O_4$) demonstrated that upon heating in an inert atmosphere, the onset temperature for oxygen release (weight loss) was in the order of Li_xNiO_2< Li_xCoO_2< $Li_xMn_2O_4$. This indicates that $Li_xMn_2O_4$ presents higher thermal stability than the other two positive electrode materials because of its higher decomposition temperature. In order to precisely characterize the thermal reactivity between electrode materials and added electrolytes, a calorimeter is need, such as an accelerating rate calorimeter (ARC).

1.4.2.2 Accelerating Rate Calorimeter (ARC)

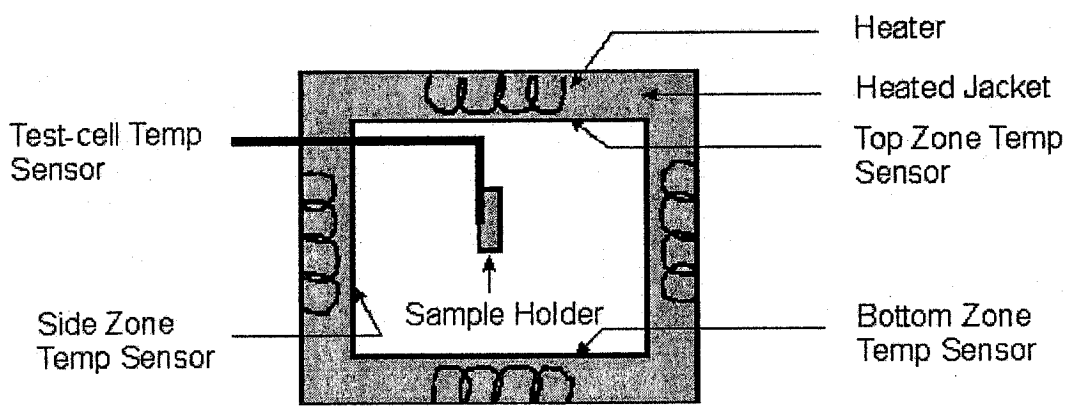

Figure 1.7 Schematic of an Accelerating Rate Calorimeter (ARC).

A simple schematic diagram of an Accelerating Rate Calorimeter is shown in Figure 1.7. One temperature sensor (a thermocouple) is attached to the surface of the sample holder to monitor the temperature of the sample with time. Heaters and sensors and a feedback circuit ensure the sample and jacket temperatures are very close. If the sample holder is heated by the heat released from internal reactions, a difference between the sample and jacket temperatures is detected. The heaters in the jacket then heat the jacket so it has the same temperature as the sample. Hence, there is no heat flow between the sample holder and the jacket. The sample holder is therefore maintained under

adiabatic conditions and it self-heats due to the exothermic reactions occurring within it. The temperature of the sample (T) is measured versus time (t) and the self-heating rate (dT/dt) vs. T is usually plotted.

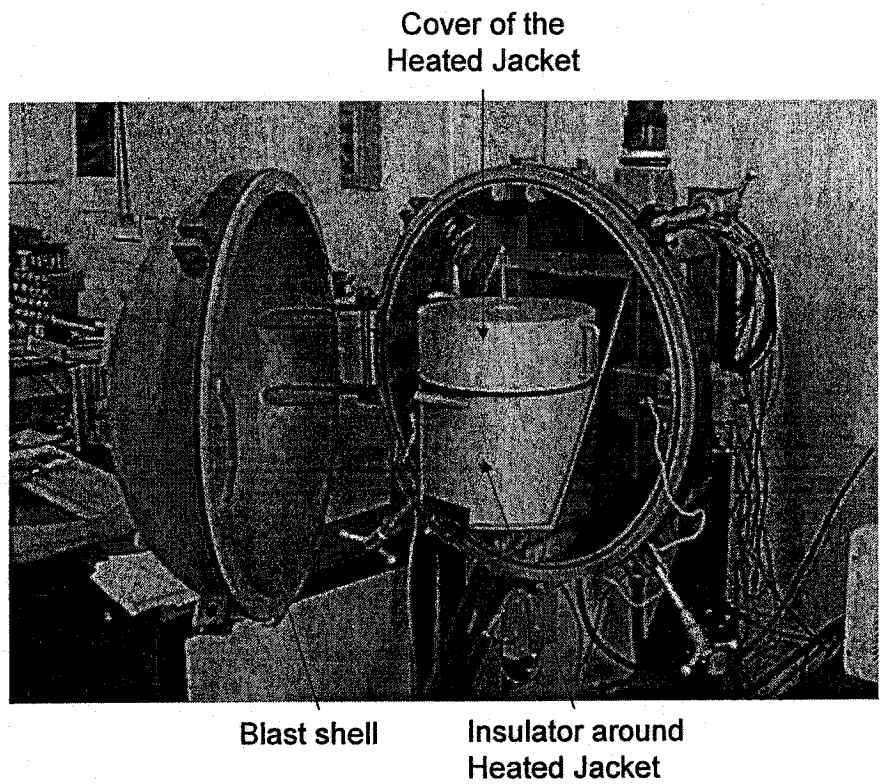

Figure 1.8 A picture of the ARC when the blast shell is open.

Figure 1.8 shows a picture of an ARC with its outside blast shell open. The blast shell is added mainly for safety protection because the ARC is usually used to study the thermal instability of explosives [104]. When the cover is lifted up, there is a thermocouple (type N) suspended in the center of the jacket and an ARC sample tube is hooked on the tip of the thermocouple as shown in Figure 1.9. There are heaters and thermocouples located in the top, bottom, and side zones around the jacket, which can not be seen in this picture.

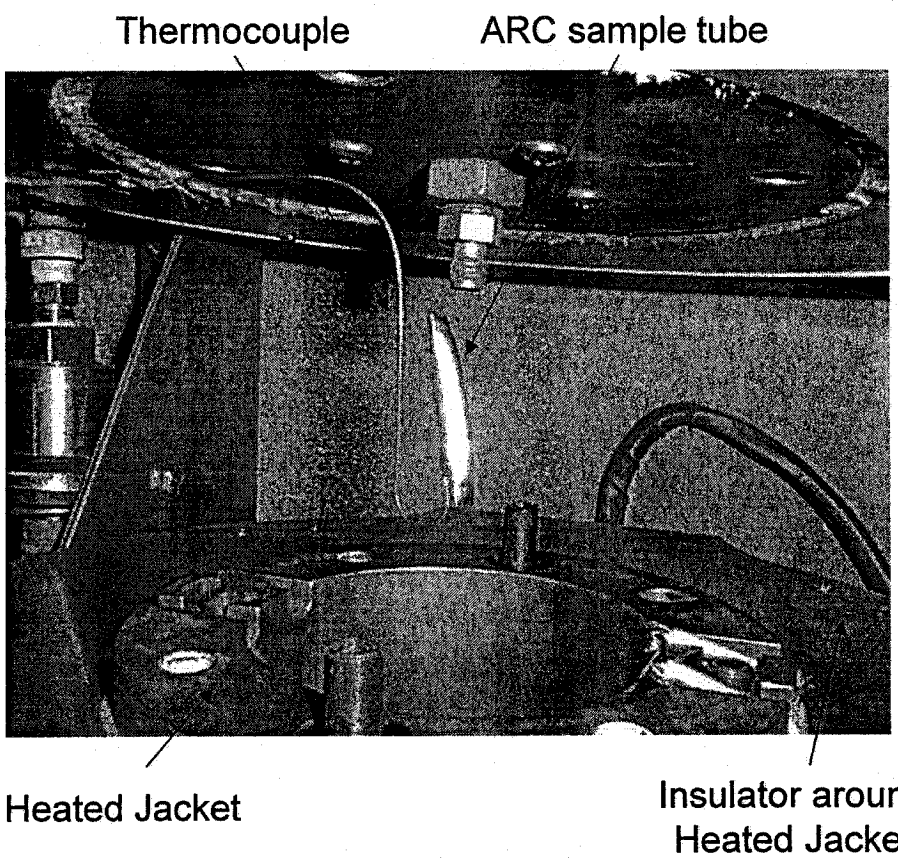

Figure 1.9 An ARC sample tube hooked on the tip of the sample thermocouple in the center cavity of the jacket.

The ARC sample holder was made from a 6.35 mm (0.250") outer diameter stainless steel (type 304) seamless tube having a wall thickness of 0.015 mm (0.006") (MicroGroup, Medway, Mass.). The stainless steel tubing was cut into 39.1 mm (1.540") long pieces shown in Figure 1.10a. A Canadian dime is shown in Figure 1.10 to indicate the size of stainless steel tubing. The sample tubing was sonicated in acetone solution two times for cleaning and then dried in a 100°C oven overnight. One end of the tubing was flattened and then welded inside an argon filled glove box using Tungsten Inert Gas (TIG) welding with a Miller Maxstar 91 ARC welder, equipped with a Snap Start II high frequency ARC starter. A small piece of stainless steel foil was attached to the surface of the tubing for hooking the thermal sensor in the ARC experiment. The sample holder (b) in Figure 1.10 was obtained. A known amount of electrode material, such as $Li_{0.81}C_6$ or $Li_{0.5}CoO_2$, and solvent or electrolyte was then added to the tube (b) in an argon-filled

glove box. The other end of the tube was clamped and welded shut with the sample held in a large copper block as a heat sink [105]. TIG welding was performed under a flow of argon and essentially melted the end of the tube together. Then the sample holder in Figure 1.10c was ready for the ARC experiment.

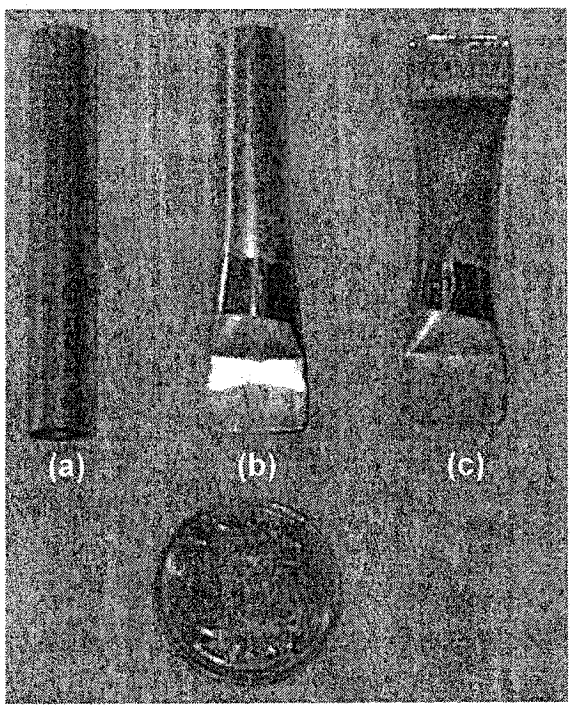

Figure 1.10 ARC tubes for ARC experiments.

Accelerating Rate Calorimetry of the decomposition of di-t-butyl peroxide (DTBP) is used as a simple example of typical ARC results. DTBP was chosen for the first ARC experiment because it is widely studied as a cetane improver in diesel fuels and thus its chemical decomposition has been studied extensively [106]. Various kinetic parameters, E_a (activation energy) and γ (reaction frequency), have been characterized depending on the method used for studies but all have concluded a first-order decomposition mechanism for DTBP [107, 108]. The self-heating rate versus temperature of DTBP was fitted to extract the kinetic parameters of its thermal decomposition. The resulting kinetic parameters were then compared with literature results to test the accuracy of the ARC measurement. The result will be shown later in this section.

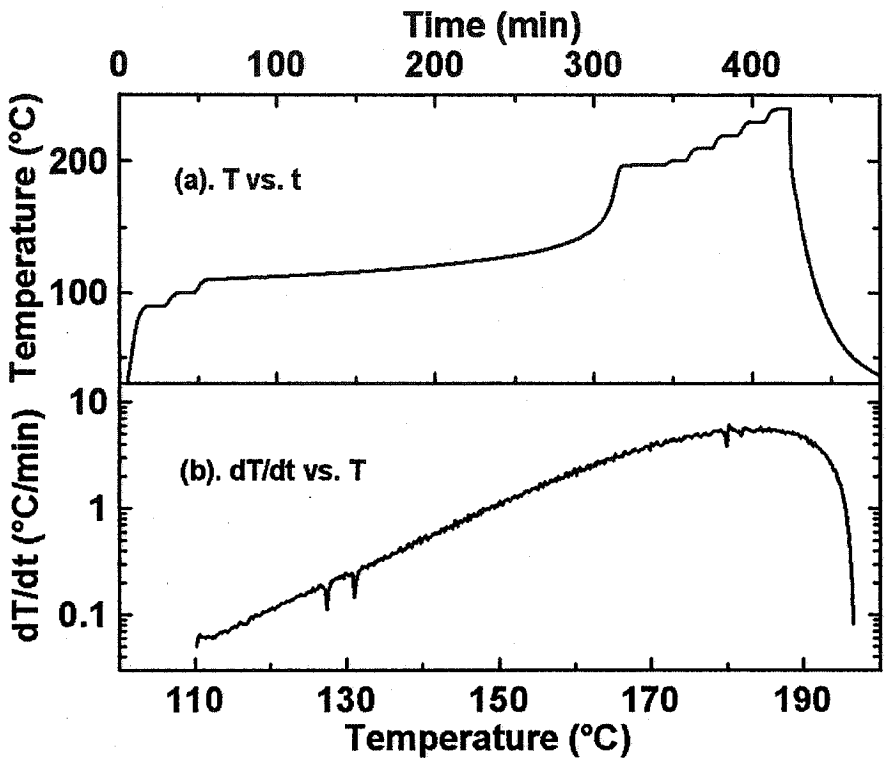

Figure 1.11 ARC curves of 50 mg DTBP started at 90°C. Temperature vs. time in panel (a) and self-heating rate (SHR) vs. temperature in panel (b).

Figure 1.11a shows the temperature (T) versus time (t) for 50 mg of DTBP heated in the ARC. Figure 1.11b shows the self-heating rate (dT/dt) versus temperature (T). In this experiment, the starting temperature was set to be 90°C, the slope sensitivity was 0.03°C/min, the stop temperature was 350°C, the searching time was 10 minutes, and the temperature step was 10°C. When the ARC experiment started, the computer-controlled heater shown in Figure 1.9 heated both jacket and sample holder up to the starting temperature of 90°C. Once the temperature of the sample reached 90°C, the computer measured the self-heating rate (SHR) of the sample using the temperature sensor attached. If the SHR of the sample holder at this temperature is lower than the slope sensitivity of 0.03°C/min during the 10 minutes search time, the heater heats up the jacket and sample a further 10°C to 100°C. When the temperature of the jacket and the sample holder reaches 100°C, the computer measured the SHR again. If the SHR is larger than 0.03°C/min, the computer tracks the exothermic reactions versus time and temperature

under adiabatic conditions. This process continues until the stop temperature (usually 350°C) is reached.

In this ARC experiment, when the sample was heated to 110°C, the SHR from the exothermic decomposition of di-t-butyl peroxide (DTBP) was about 0.06°C/min (higher than 0.03°C/min) as shown in Figure 1.11b. Then the computer started to track the exothermic reaction until the depletion of the DTBP reactant inside the holder at around 197°C. During the tracking process from 110°C to 197°C, the heater heated the jacket to maintain adiabatic conditions (no heat flow to or from the sample).

The tubes before and after the ARC experiment in Figure 1.11 are shown in Figure 1.12a and c, respectively. After the ARC experiment, both ends of the ARC tube expanded (Figure 1.12c) because of the high pressure caused by the decomposition reaction of DTBP at high temperature. The data in Figure 1.11b show two downward spikes near 130°C, which correspond to the sequential expansion of the two ends of the sample tube. This expansion leads to instantaneous cooling, and a brief lowering of the self-heating rate. Another DTBP sample was run and stopped at 130°C, which is exactly between the two temperatures where the spikes occurred. After cooling, this ARC tubing was taken out of the ARC and is shown in Figure 1.12b, where only one end of the tubing has expanded after the first spike. Therefore, in the ARC experiments reported here, the downward spikes correspond to the sequential expansion of the ends of the tubing.

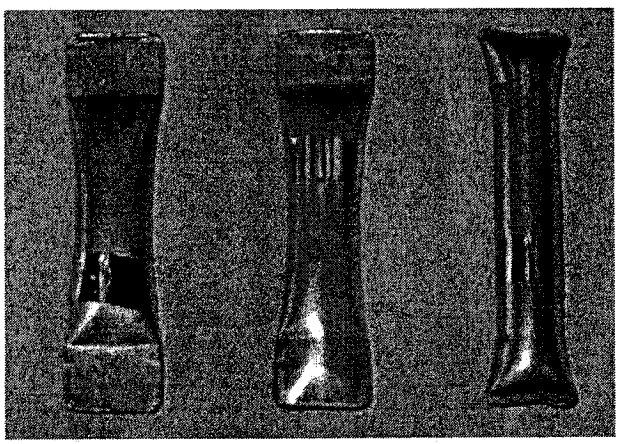

(a) (b) (c)

Figure 1.12 ARC tube (a) before ARC, (b) in the middle of the ARC experiment around 130°C (between the two spikes in Figure 1.11b), and (c) after ARC.

Simple calculations were conducted to simulate the ARC profile of reacting or decomposing samples. For a first order reaction, such as DTBP decomposition, the reaction rate is proportional to the amount of the remaining reactant,

$$\frac{d\alpha}{dt} = k(1-\alpha), \qquad [1\text{-}6]$$

$$k = \gamma \exp(-\frac{E_a}{k_B T}), \qquad [1\text{-}7]$$

where α is the fractional degree of conversion of the reactant, $d\alpha/dt$ is the reaction rate, k is the Arrhenius rate constant, γ is the pre-exponential factor, E_a is the reaction activation energy, k_B is the Boltzmann constant, and t is the reaction time (minutes). Here it is assumed that γ is temperature-independent.

In an ARC experiment, the self-heating rate (SHR) is given by

$$\frac{dT}{dt} = \frac{h}{C_{Tot}} \frac{d\alpha}{dt}, \qquad [1\text{-}8]$$

where h (J) is the total heat which can be evolved by the sample due to the reaction and C_{Tot} (J K^{-1}) is the total heat capacity of the reactants and the sample holder. h/C_{Tot} is the temperature rise (ΔT) from the onset temperature to the end of the exothermic reaction.

Combining equations [1-6], [1-7], and [1-8], gives,

$$\frac{dT}{dt} = \frac{h}{C_{Tot}} \gamma \exp(\frac{-E_a}{k_B T})(1-\alpha). \qquad [1\text{-}9]$$

Based on formula [1-9], the ARC result of DTBP decomposition in Figure 1.11b was fitted to extract the activation energy (E_a). The fitted curve is indicated by a dashed line in Figure 1.13.

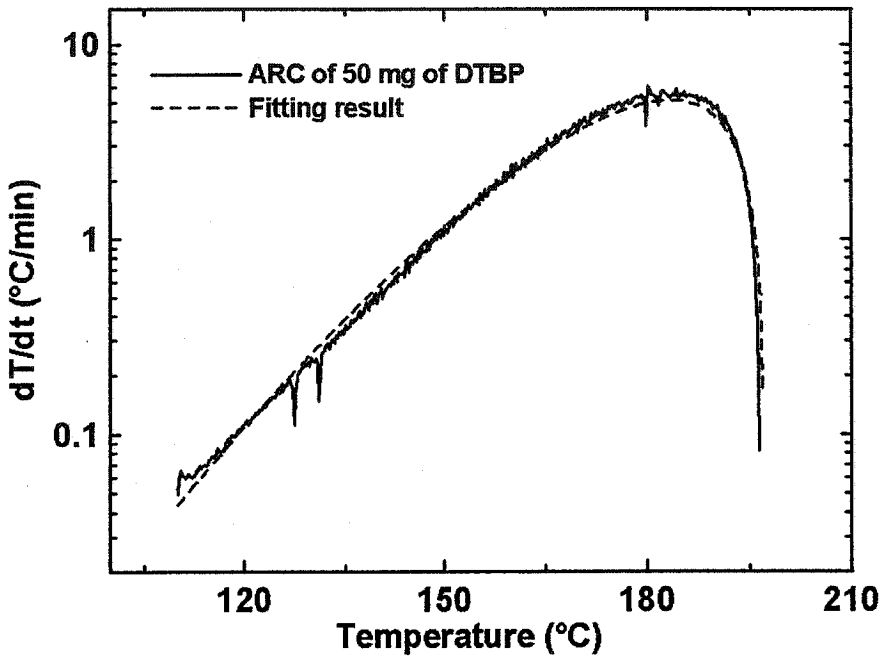

Figure 1.13 Self-heating rate versus temperature for 50 mg of DTBP (solid line) and the fitted result (dashed line) where $\alpha_0 = 0.001$, $\gamma = 4.9\times10^{14}$ min^{-1}, $E_a = 132$ kJ mol^{-1}, $\Delta T = 87$ K.

From the best-fit to the ARC curve, the activation energy E_a was determined to be about 132±10 kJ mol^{-1} and reaction frequency (γ) is around 4.9×10^{14} min^{-1}, which are close to literature values [105, 107, 108] (E_a is between 125 and 150 kJ mol^{-1} and γ ranges from 10^{14} to 10^{16} min^{-1}). This strongly suggests that ARC can be used to accurately characterize exotherms from the thermal reaction of samples inside ARC tubes. In this thesis, a known amount of charged negative or positive electrode materials, such as 100 mg of $Li_{0.81}C_6$ or $Li_{0.5}CoO_2$, and a known amount of solvent or electrolyte was added to the ARC tube to study their thermal reactivity.

The temperature rise (ΔT) of the ARC result in Figure 1.13 is approximately 87 K. The specific heat capacities of ARC tube and DTBP are about 0.46 J K^{-1} g^{-1} and 2.3 J K^{-1} g^{-1} [108], respectively. The masses of ARC tube and DTBP used in this ARC test are about 0.95 g and 0.05 g, respectively. The total heat capacity (C_{Tot}) of the ARC sample tube is calculated to be 0.95 × 0.46 (J K^{-1}) + 0.05 × 2.3 (J K^{-1}) = 0.55 J K^{-1}. Therefore, the heat (ΔH) released from the decomposition of DTBP is calculated to be 960 J g^{-1}, which is close to 916 ± 12% J g^{-1} measured by DSC in reference [105].

Usually, three parameters are used to quantify the thermal stability of samples studied. The first one is the onset temperature, which is the starting temperature where the sample SHR becomes higher than the slope sensitivity set point. The higher the onset temperature, the safer the sample inside the ARC tubing. The second important parameter is the total temperature rise, ΔT, which is related to h, the total heat released from the reaction of the sample, by $\Delta T = h/C_{Tot}$. Usually a lower ΔT means a smaller total heat released and therefore represents a safer sample. The last parameter is the SHR at a certain temperature. A lower SHR for the sample at the same temperature means slower heat release indicating a safer sample.

1.4.3 Prediction of oven test behavior of full lithium-ion cells from ARC results

As described above, the oven and ARC tests are two different techniques for assessing thermal-stability of lithium-ion batteries. The oven test is used to measure the thermal stability of full lithium-ion cells whereas ARC is used to measure the thermal reactivity between a single electrode material, such as the $Li_{0.81}C_6$ negative electrode or the $Li_{0.5}CoO_2$ positive electrode, and solvents or electrolytes.

In this thesis, the thermal stability of both $Li_{0.81}C_6$ and $Li_{0.5}CoO_2$ electrodes in two different electrolytes, $LiPF_6$ and LiBOB in EC/DEC, was studied using ARC. A qualitative prediction was then made for the oven test behavior of graphite/$LiCoO_2$ 18650-size cells, with $LiPF_6$ or LiBOB based electrolyte. This prediction later was verified by oven test experiments of such cells obtained from Moli Energy Ltd. and is reported in Chapter 3 of this thesis.

1.5 Scope of this thesis

Single electrode material ($Li_{0.81}C_6$ or $Li_{0.5}CoO_2$) tests by ARC correlated well with oven tests of full-size lithium ion cells (described in Chapter 3). Therefore, it was concluded that ARC is an excellent technique to study the thermal stability of electrode materials in LIBs. The thermal stability of different negative and positive electrode materials in various solvents and electrolytes was characterized in order to identify battery systems with high thermal stability.

In Chapter 4, the thermal stability of three negative electrode materials with different lithium binding energies ($Li_{0.81}C_6$ 0.1 eV, $Li_7Ti_5O_{12}$ 1.55 eV, and $Li_{0.5}VO_2$ 2.45 eV vs. Li metal) in EC/DEC solvent and in $LiPF_6$/LiBOB based electrolytes were compared. The steps in the thermal reactions were explored.

Chapter 5 focuses on the thermal-stability investigations of two existing positive electrode materials (spinel $LiMn_2O_4$ and olivine $LiFePO_4$) that are more thermally stable than $LiCoO_2$. The reasons for their high thermal stability are discussed. From the research results in Chapter 5, two battery systems with high thermal stability stand out, C or $Li_4Ti_5O_{12}$/LiBOB EC:DEC/$LiFePO_4$.

Chapter 6 describes studies on the synthesis, structure, electrochemical properties, and thermal stability of a new class of positive electrode materials the $Li[Ni_{1/2}Mn_{1/2}]O_2$ • $LiCoO_2$ • $Li[Li_{1/3}Mn_{2/3}]O_2$ pseudoternary system, based on the four described guidelines. A simple $Li[Ni_{1/2}Mn_{1/2}]O_2$ • $LiCoO_2$ binary system, which can be expressed as $Li[(Ni_{1/2}Mn_{1/2})_xCo_{1-x}]O_2$, was chosen to be studied first. In Section 6.1, a series of $Li[(Ni_{1/2}Mn_{1/2})_xCo_{1-x}]O_2$ (x = 0.2, 0.4, 0.7, 0.9, and 1) samples were synthesized and their electrochemical properties and thermal stabilities are investigated. The best positive electrode candidates in terms of rate capability and thermal stability were found to be $Li[(Ni_{1/2}Mn_{1/2})_xCo_{1-x}]O_2$ with $0.4 \leq x \leq 0.7$

Section 6.2 describes another binary system, $Li[Ni_{1/2}Mn_{1/2}]O_2$ • $Li[Li_{1/3}Mn_{2/3}]O_2$, which can be expressed as $Li[(Ni_{1/2}Mn_{1/2})_x(Li_{1/3}Mn_{2/3})_{1-x}]O_2$ ($0 < x \leq 1$). Three $Li[(Ni_{1/2}Mn_{1/2})_x(Li_{1/3}Mn_{2/3})_{1-x}]O_2$ samples (x = 1/6, 1/2, and 5/6) were synthesized at 900°C. The electrochemical properties and thermal stabilities of the samples were studied.

Based on the results on the two binary systems (Sections 6.1 and 6.2), nine different compositions in the $Li[Ni_{1/2}Mn_{1/2}]O_2$ • $LiCoO_2$ • $Li[Li_{1/3}Mn_{2/3}]O_2$ pseudo ternary system were chosen for further study. Positive electrode candidates with high capacity (over 200 mA h g^{-1}), excellent cycling performance (about 97% capacity retention for 70 cycles between 2.5 V and 4.6 V at C/6) and good thermal stability (higher thermal stability than $LiCoO_2$) were found in this pseudoternary system, as described in Section 6.3.

Conclusions and suggestions for future work are presented in Chapter 7.

Chapter 2. Experimental section

This section explains the synthesis of electrode materials, electrode preparation, cell construction, and sample rinsing, as well as the experimental techniques used like X-ray diffraction (XRD), scanning electron microscopy (SEM), and BET surface area analysis.

2.1 Synthesis of electrode materials

Synthesis of negative electrode materials [$Li_4Ti_5O_{12}$ and VO_2 (B)] and new layered positive electrode materials will be described in this section.

2.1.1 $Li_4Ti_5O_{12}$

$Li_4Ti_5O_{12}$ was prepared by heating a mixture of TiO_2 (99%+, Sigma) and a stoichoimetric amount of $LiOH \bullet H_2O$ (98%+, Aldrich) at 800°C for 4 hours in air. A 5% molar excess of Li was used to compensate for the possible loss of Li during the heating process. The involved reaction is

$$5TiO_2 + 4LiOH \bullet H_2O \rightarrow Li_4Ti_5O_{12} + 6H_2O. \qquad [2\text{-}1]$$

The synthesized $Li_4Ti_5O_{12}$ sample was characterized by SEM, BET, and XRD, which will be described in Section 4.1.

2.1.2 VO_2 (B)

VO_2 (B) is a particular phase of VO_2 having the space group C2/m ($^{\#}12$), which can be obtained from the decomposition of NH_4VO_3 under an argon atmosphere at 350°C for 20 hours. The corresponding reaction is [109]:

$$6NH_4VO_3 \rightarrow 6VO_2\ (B) + 6H_2O + 4NH_3 + N_2. \qquad [2\text{-}2]$$

The synthesized VO_2 (B) sample was characterized by SEM, BET, and XRD, which will be described in Section 4.2.

2.1.3 New positive electrode materials in the $xLi[Ni_{1/2}Mn_{1/2}]O_2 \bullet yLiCoO_2 \bullet zLi[Li_{1/3}Mn_{2/3}]O_2$ pseudoternary system ($x + y + z = 1$)

Based on the four guidelines for developing novel layered cathodes [Section 1.3.2], layered compounds in the $xLi[Ni_{1/2}Mn_{1/2}]O_2 \bullet yLiCoO_2 \bullet zLi[Li_{1/3}Mn_{2/3}]O_2$ pseudoternary system, which can be expressed as $Li[(Ni_{1/2}Mn_{1/2})_xCo_y(Li_{1/3}Mn_{2/3})_z]O_2$, were synthesized. These compounds have a similar layered structure to $LiCoO_2$ shown in Figure 1.3 in Chapter 1. There is a mixture of Li, Ni, Co, and Mn cations in the transition metal layer.

$LiOH \cdot H_2O$ (98%+, Aldrich), $CoSO_4 \cdot 7H_2O$ (99%+, Sigma), $NiSO_4 \cdot 6H_2O$ (98%, Alpha Aesar), and $MnSO_4 \cdot H_2O$ (Fisher Scientific) were used as starting materials. $M(OH)_2$ (M is a mixture of Ni, Co, and Mn transition metals) was prepared by coprecipitation as described by the first step of the "mixed hydroxide" method [24]. A 100 ml aqueous solution of the transition metal sulfates (MSO_4 total concentration equal to 1.0 M) was dripped into 250 ml of a stirred solution of 1.0 M LiOH, using an electronic metering pump (LMI, Milton Roy), with a constant speed and stroke leading to 1 hour of co-precipitation. The pH was controlled to be approximately 14 by maintaining constant LiOH concentration during the co-precipitation process. This should cause the precipitation of $M(OH)_2$ (M = Ni, Co, and Mn) with a homogeneous cation distribution. The beaker containing the starting transition metal sulfate solution and the pump tubes were washed with distilled water for 15 min to ensure that all the transition metal sulfates were added to the LiOH solution. The precipitate was filtered out and washed five times with additional distilled water to remove the residual salts (LiOH, SO_4^{2-} ions, or formed Li_2SO_4). The precipitate was dried in a 120°C oven overnight and ground for 5 minutes in an automatic grinder. Then, the dried precipitate was mixed with a stoichoimetric amount of $LiOH \cdot H_2O$ and ground for approximately 15 min. After grinding, pellets about 5 mm thick were pressed and fired in alumina crucibles in air by the following heating procedure.

First, the pellets were heated to 750°C at a rate of 4°C/min and then soaked at that temperature for 2 hours. The pellets then were heated to 900°C, 1000°C, or 1100°C, as desired, at 4°C/min and soaked for 3 hours. After that, the pellets were cooled to room

temperature at 4°C/min and the pellets were ground into powder. The resulting powder then was passed through a 50-μm sieve.

2.2 Electrode preparation for ARC or electrochemical tests

2.2.1 Electrodes with PVDF binder

2.2.1.1 Thin film electrodes for electrochemical tests

Thin film electrodes were made to test their electrochemical properties. In almost all the cells for electrochemical testing, electrodes with PVDF binder were made. The process of making the thin film electrodes is described below.

About 500 mg of the active electrode material, such as MCMB, $LiCoO_2$, or $LiFePO_4$, was mixed with 40 mg Super-S carbon black (MMM Carbon, Belgium), 400 mg of 10% polyvinylidene difluoride (PVDF) solution in n-methyl pyrroldinone (NMP), and 750 mg of NMP in a 5 ml vial. Five small stainless steel balls were put into this vial. The vial was shaken intensely by hand until a homogeneous electrode slurry was obtained, which takes approximately 20 mins. The slurry was poured onto the electrode substrate, copper foil for the negative electrode or aluminum foil for the positive electrode, then a 0.28 mm (0.011") notch bar was used to spread the slurry in a uniform layer. The electrode was then dried in a 100°C oven overnight. Usually the mass loading of the active material was around 8 mg cm^{-2}.

2.2.1.2 Pellet electrodes for ARC

One ARC experiment requires approximately 100 mg of active electrode material. It is therefore impractical to use the thin film electrodes for ARC experiments. Usually, the mass of a pellet electrode used for the ARC is a few hundred milligrams. A few grams of active electrode material were mixed with 7% by mass, each of Super S carbon black, PVDF (10% in NMP), and excess NMP to make a slurry, following the same procedures as in 2.2.1.1. After drying the electrode slurry at 120°C overnight, the electrode powder was slightly ground in a mortar and then passed through a 300 μm sieve. A certain amount of electrode powder was then placed in a stainless steel die to which 13.8 Mpa (2000 psi) was applied to produce an approximately 1 mm thick pellet electrode.

Figure 2.1a shows a picture of a positive electrode pellet. A 2325-size coin cell [23 mm diameter and 2.5 mm thickness, Figure 2.1b] was constructed using the positive electrode pellet and a MCMB pellet sized to balance the capacity of both electrodes. After being treated electrochemically, this positive electrode was used for an ARC test. The cell construction and ARC sample preparation will be introduced in Sections 2.3 and 2.4.

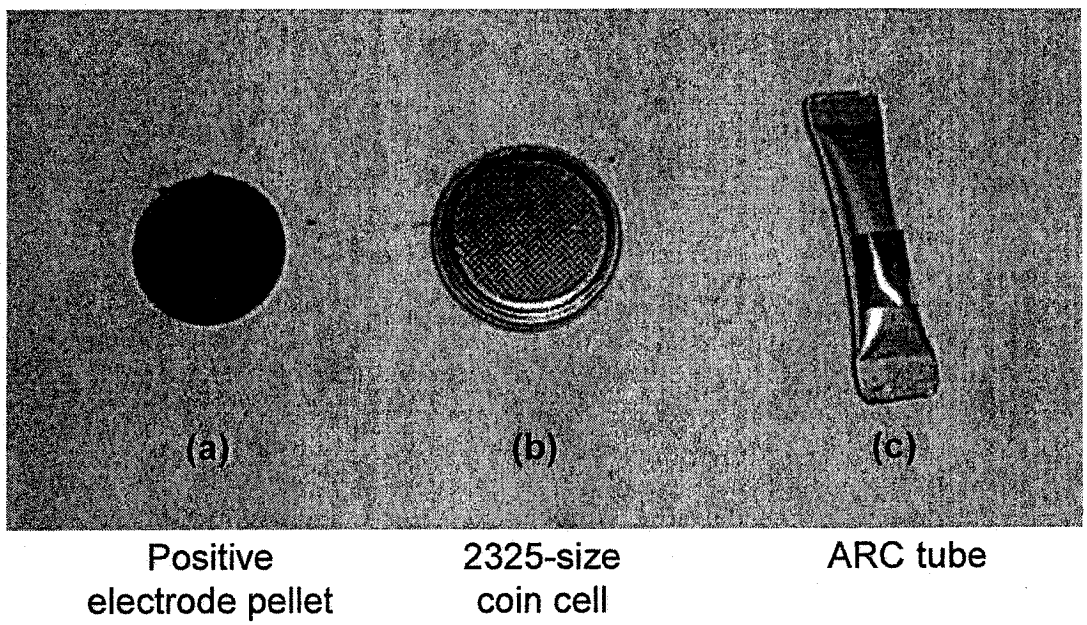

Figure 2.1 Pictures of a positive electrode pellet (a), 2325-size coin cell (b), and an ARC tube (c).

The amount of positive electrode material and MCMB used in the pellets depends on the charging capacity of the positive electrode material, which varies with the material itself and the charging voltage. For example, if 700 mg of $LiCoO_2$ $Li[(Ni_{0.5}Mn_{0.5})_{0.2}Co_{0.8}]O_2$, and $LiFePO_4$ electrodes are charged to 4.2 V, 4.2 V, and 3.8 V vs. Li metal, respectively, the amounts of MCMB used were around 280 mg, 280 mg, and 320 mg to balance the capacity of both electrodes. Assuming a first charge (lithiation) capacity of 350 mA h g^{-1} for MCMB and capacities of 140, 140 and 160 mA h g^{-1} for $LiCoO_2$ at 4.2 V, $Li[(Ni_{0.5}Mn_{0.5})_{0.2}Co_{0.8}]O_2$ at 4.2 V and $LiFePO_4$ at 3.8 V, these masses lead to coulometrically balanced cells.

2.2.2 Pellet electrodes with EPDM binder

Some MCMB-based pellet electrodes were built with 2% ethylene propylene diene terpolymer (EPDM) in order to study the thermal behavior of the MCMB electrode with different binders, such as EPDM or PVDF. A solution of 2% EPDM in cyclohexane was prepared. The electrode slurry was prepared by combining, by mass, 7% Super S carbon black, 2% EPDM (2% EPDM in cyclohexane), MCMB, and excess cyclohexane solvent. After the slurry was well mixed, the slurry was spread into a shallow 20 cm × 30 cm glass tray, which was heated by a hot plate. The temperature of the hot plate was set to 85°C, which is higher than the boiling point of cyclohexane (80°C). During drying, the slurry was stirred using a glass rod. In about half an hour the electrode mixture was dry. After drying the electrode mixture completely in an oven at 70°C overnight, the electrode mixture was lightly ground in a mortar. The powder was then passed through a 300 μm sieve and pressed into pellet electrodes as described in 2.2.1.2.

2.2.3 Powder electrodes without binder

In order to compare the thermal stability of MCMB with and without binder, MCMB electrodes were also prepared without binder. These electrodes contained 7% Super S carbon black and 93% MCMB. Additional pressure was applied to the electrodes and the lithium foil to ensure good electric contact between the small MCMB particles. The cell construction for electrodes without binder will be described in Section 2.3.3.

2.3 Cell construction for different electrodes

2.3.1 Cell construction for thin-film electrodes

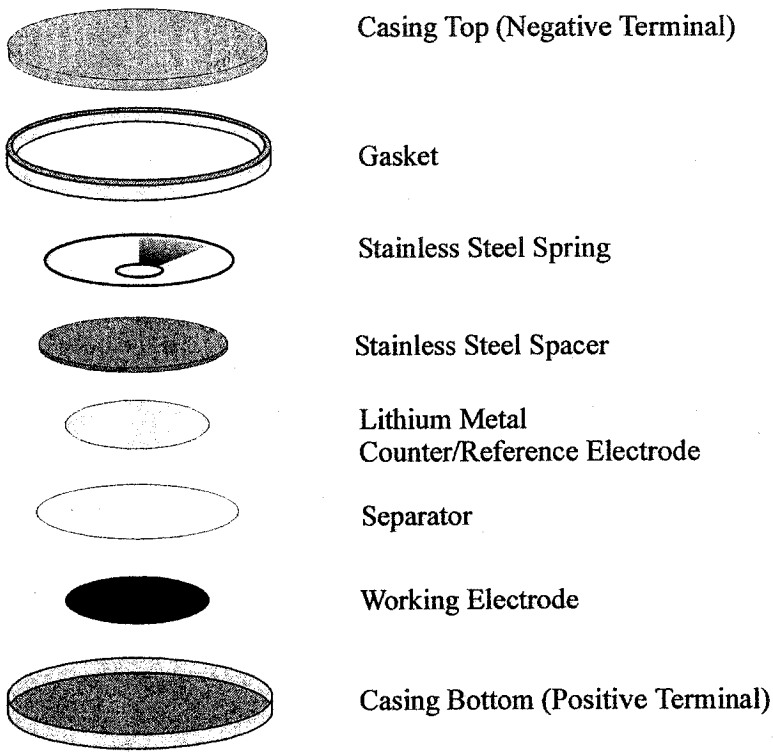

Figure 2.2 Construction of 2325 lithium coin cell used for electrochemical testing.

The electrochemical cells were assembled from the parts shown in Figure 2.2 in an argon-filled glove box. The 2325 cell [shown in Figure 2.1b] had stainless steel top and bottom casings. The prepared electrode was placed in the center of the bottom casing and the desired electrolyte, usually 1.0 M $LiPF_6$ EC/DEC (1:2, vol:vol, Mitsubishi Chemicals) was added. A polypropylene separator (Celgard 2502, Celanese) was placed above the electrode. Then the negative film electrode was put on the top of the separator. The negative film electrode used depended on the particular cell type. For example, if a single electrode was investigated, a lithium foil electrode (125 μm thick, 1.3 cm diameter, FMC) was usually used as a reference. A stainless steel spacer and spring were added to maintain pressure on the electrode stack. The cell top, on which there is a polypropylene gasket, was then placed and the cell was crimped shut, sealing the electrodes from the

environment. When the electrochemical cells were removed from the argon-filled glove box, stainless steel tabs were welded onto the two sides of the cells for electrical contact.

2.3.2 Cell construction for pellet electrodes

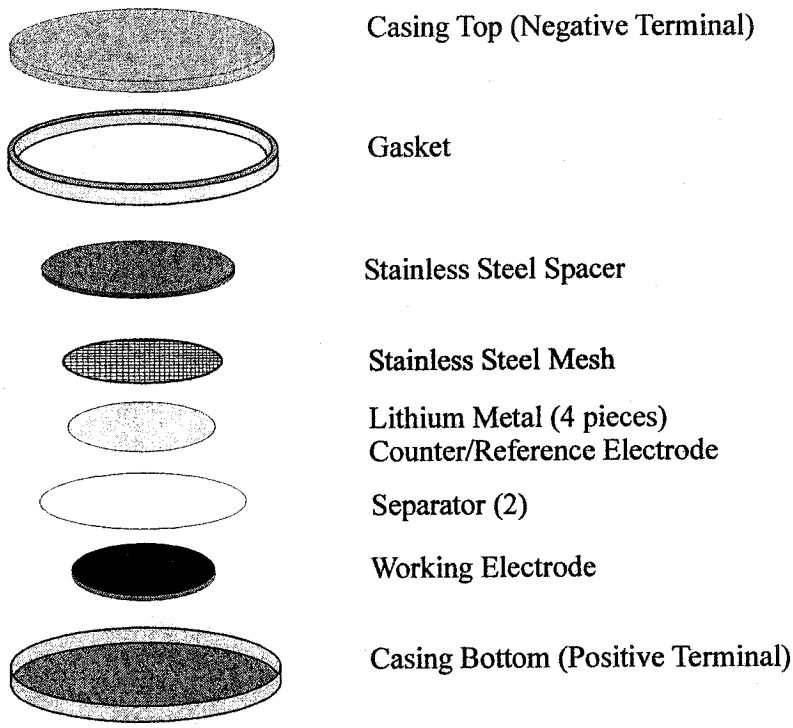

Figure 2.3 Construction of 2325 lithium coin cell with MCMB pellet electrode [52]. Reprinted with permission from the author.

The construction for cells with pellet negative or positive electrodes is different. For negative MCMB pellet electrodes, the cell assembly procedure is simply shown in Figure 2.3. The pellet electrode was placed in the center of the bottom casing with enough $LiPF_6$ EC/DEC electrolyte to wet the pellet electrode completely. A stainless steel mesh (1 mm mesh, 125 μm thick) was added on top of four pieces of 125 μm thick lithium foil to maintain electrical contact with all of the lithium foils. Then a stainless steel spacer was then added above the mesh to provide pressure on the electrodes of the cell. Finally, the cell top, with the polypropylene gasket, was attached and the cell was crimped shut to seal it from the outside environment.

The cells with the MCMB pellet electrodes were fully discharged to below 25 mV versus lithium metal and allowed to equilibrate for one week or more. Then the cells were transferred to the glove box for ARC sample preparation, which is described in Section 2.4.

For the positive pellet electrode, the assembly procedure is shown in Figure 2.4. This is almost the same as the ARC negative electrode assembly, except that a MCMB pellet was used as the counter electrode instead of lithium foil and no stainless steel mesh and spacer were used.

The positive pellet electrodes were charged to different voltages based on the type of active material or experimental design.

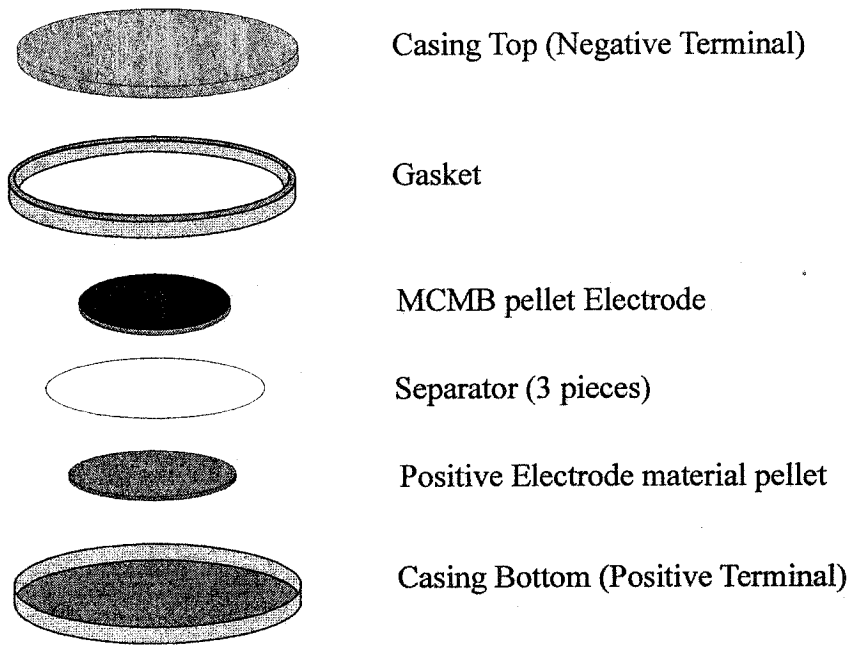

Figure 2.4 Construction of 2325 lithium coin cell with a positive electrode material.

2.3.3 Cell construction for MCMB powder electrode without binder

The cell construction for a MCMB powder electrode without binder is shown in Figure 2.5. Four lithium foils (125 μm thick and 1.5 cm diameter of each) were put into the center of the casing bottom. 1.0 M $LiPF_6$ EC/DEC electrolyte was added to wet the lithium electrode and then one polypropylene separator was placed on top of the lithium electrode. A plastic sleeve was placed on the top of the separator and then around 0.9 g

MCMB powder with 7% Super S carbon black was put into the plastic sleeve. Enough 1.0 M $LiPF_6$ EC/DEC was added again to wet the MCMB powder electrode. Then a stainless steel plate and spring were added to apply pressure to the powder. Finally, the cell top, a piece of stainless steel, was placed and three screws were used to tighten the cell.

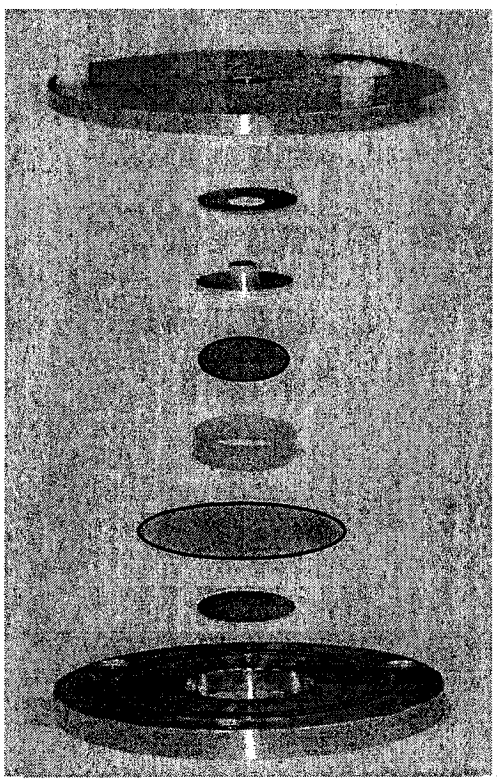

Figure 2.5 Construction of lithium cell with MCMB powder electrode without binder.

The MCMB powder electrode was discharged by connecting the positive and negative ends of the cell with a 100 Ω resistor until the voltage of the cell dropped below 100 mV. Then the cell was shorted directly for five days until the open circuit cell voltage was below 25 mV. Finally, the cell was transferred into the glove box and the lithiated MCMB was recovered and rinsed with DMC.

2.4 Rinsing procedure for electrodes to be studied by ARC

MacNeil *et al.* [50] developed a rinsing procedure to remove the original electrolyte, usually $LiPF_6$ EC/DEC, from the charged $LiCoO_2$ positive electrode and the

same rinsing method was used in this thesis. The XRD patterns of charged $LiCoO_2$ before and after the rinsing procedure are virtually identical. ARC studies of both rinsed and unrinsed samples show similar results [50, 52]. This demonstrates that the rinsing procedure changes neither the bulk structure nor the thermal behavior of charged $LiCoO_2$.

The recovered negative electrode (pellet or powder) was lightly ground and then rinsed four times using DMC by MacNeil's rinsing method [50, 87]. The waste DMC solution for each rinse was stored in a 3 ml vial. These four vials with waste DMC solution were dried and the white residue in the four vials weighed approximately 50, 16, 5, and 2 mg respectively. The residue is believed to be $LiPF_6$ and EC. This implies that the original electrolyte ($LiPF_6$ EC/DEC) can be predominantly removed from the electrode material after rinsing four times with DMC. XRD patterns of lithiated MCMB before and after rinsing (Figure 2.6) show that rinsing did not change the XRD pattern of $Li_{0.81}C_6$.

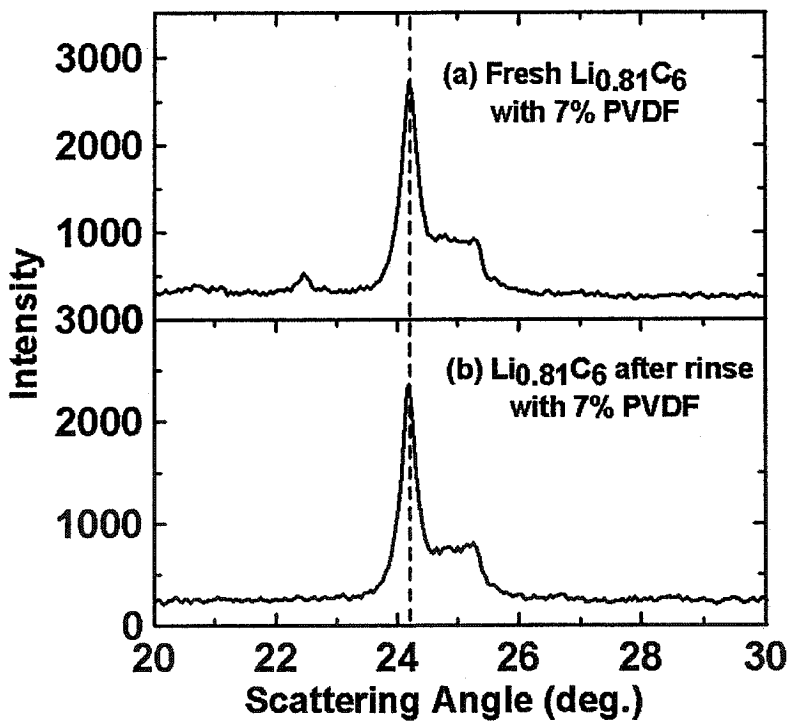

Figure 2.6 XRD patterns of lithiated MCMB ($Li_{0.81}C_6$) with 7% PVDF binder before (a) and after the rinsing procedure (b).

2.5 Other techniques

2.5.1 Electrochemical Test System

Cells were tested using a computer controlled constant-current charger system obtained from Moli Energy Ltd. (1990). The temperature of the cells can be adjusted and is 30.0 ± 0.1°C unless specified. The current used for the electrochemical testing was selected based on the active mass and type of material in the electrodes, which will be described for each specific experiment.

2.5.2 Scanning Electron Microscopy (SEM)

Two scanning electron microscopes, a JSM-35CF from JEOL Ltd. and a S-4700 from Hitachi, were used to study the morphology of different electrode materials.

2.5.3 Powder X-ray Diffraction

Powder X-ray diffraction is the main technique used to identify the crystalline structure of each sample under study in this thesis. A Siemens D500 diffractometer equipped with a copper target X-ray tube and a diffracted beam monochromator was used for the diffraction measurements. The emitted X-rays utilized were the Cu $K_{\alpha 1}$ (λ = 1.54051 Å) and Cu $K_{\alpha 2}$ (λ = 1.54433 Å). The divergence and anti-scatter slits used were set both at 0.5°, while the receiving slit was set at 0.2 mm, which gives an instrument resolution of about 0.15°. The X-ray tube was powered to 40 kV at 30 mA.

Two different kinds of samples were prepared for XRD measurements: (1) newly synthesized electrode materials to identify their structure and lattice constants and (2) samples before and after ARC measurements in order to study the steps of the reaction between electrode materials and electrolytes or solvents. Different sample holders were used for the two different types of samples.

The holder for the new electrode material samples was typically made in-house from a stainless steel plate. The sample was put in a well in the center. Occasionally, when there was insufficient powder to fill the well, a zero-background holder was used. The zero-background holder was made by fixing a single crystal of silicon cleaved to expose the (510) face to a stainless steel backplate. The (510) plane of silicon has a geometrical structure factor of zero and therefore does not scatter X-rays to the detector.

Small quantities of powder (around 5 ~ 10 mg) were adhered to this surface by applying 2 or 3 drops of acetone solution. The holder was then agitated to evenly spread the attached powder. After drying, the powder remains lightly adhered to the surface of the XRD holder.

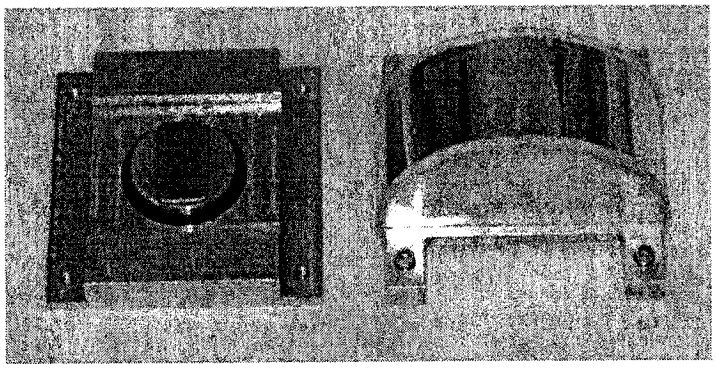

(a) (b)

Figure 2.7 XRD sample holder for air and moisture sensitive samples.

The second type of samples is charged electrode materials before/after ARC measurement. After cooling to room temperature, the ARC sample tubes were taken into a helium-filled glove box and the sample inside ARC tube was recovered. The samples were possibly air and moisture sensitive so that a specially designed air-sensitive sample holder shown in Figure 2.7 was used to prevent air exposure during the diffraction measurement [110]. A layer of aluminized mylar was sealed to the semi-circular frame. A small amount of sample was placed on a zero-background silicon wafer and a few drops of DMC solution were used to spread the sample uniformly on the silicon wafer. During an XRD measurement, X-rays can pass through the mylar layer to reach the sample but air cannot. The XRD sample holders were then placed into the diffractometer mount such that the surface of the sample holder is coincident with the goniometer center.

2.5.3.1 Rietveld Refinement

Diffraction patterns were fitted using Rietveld's refinement method to extract important physical parameters of a measured sample, such as lattice constants (*a*, *b*, and *c*), atom positions, and so on [23, 111]. In this method the results of a step-scan X-ray diffraction measurement are fit by the function below,

$$Y_{ic} = Y_{ib} + \sum_{\xi} \sum_{k} G_{ik} I_k , \qquad [2\text{-}3]$$

where Y_{ic} is the intensity calculated at point i in the diffraction pattern, Y_{ib} is the background intensity, G_{ik} is a normalized peak profile function, an I_k is the intensity of the k^{th} Bragg reflection. The second summation is carried out over all reflections, k, contributing to the point i in the pattern and the first summation is carried out over all of the phases, ξ, present in the sample.

The calculated XRD peak shape adopts a pseudo-Voigt function, which has a Lorentzian component and Gaussian component. The fit attempts to minimize the goodness of fitting parameter, χ^2:

$$\chi^2 = \frac{1}{N-P} \sum [\frac{(Y_{io} - Y_{ic})^2}{Y_{ic}}]. \qquad [2\text{-}4]$$

The Bragg agreement factor (R_{Bragg}) is calculated as:

$$R_{Bragg} = \frac{\sum |I_{ko} - I_{kc}|}{\sum |I_{ko}|}. \qquad [2\text{-}5]$$

In the two equations above, the subscripts o and c refer to the observed and calculated quantities, respectively, I_k is the integrated intensity of the k^{th} reflection, Y_i is the magnitude of the i^{th} point in the pattern, N is the number of points in the profile, and P is the number of parameters in the fit. The parameter R_{Bragg} is usually used to evaluate whether the fit is reasonable or not.

The diffraction pattern of samples containing several phases can also be fitted by Rietveld's refinement method. This method was used to identify co-existing phases in samples after ARC experiments and extract the lattice constants of the phases (Chapter 6). In order to show the validity of this multi-phase Rietveld refinement method, one experiment was designed as follows. About 1.5 g of $LiCoO_2$ (obtained from Moli Energy Ltd., Canada) was ground with 1.0 g of Si (Aldrich) for about 15 minutes. The XRD pattern of the mixed sample was taken and is shown in Figure 2.8 along with the two-phase Rietveld refinement results [phase (I) $LiCoO_2$ and phase (II) Si]. The R_{Bragg} factors for the refinements of $LiCoO_2$ and Si phases are 3.7 and 6.0, respectively. Table 2.1 compares the lattice constants of $LiCoO_2$ and Si from the refinements and from the

literature. The results in Figure 2.8 and Table 2.1 strongly show the validity of the multi-phase Rietveld refinement method to identify co-existing phases in mixed phase samples.

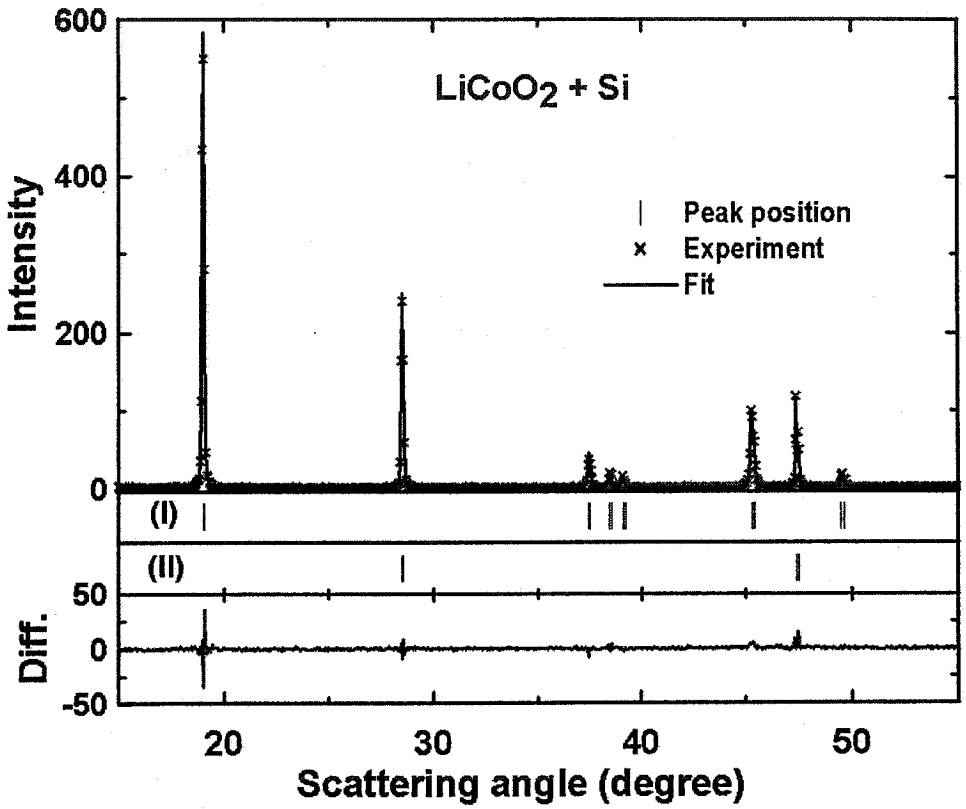

Figure 2.8 XRD pattern and the corresponding two-phase Rietveld refinement of the $LiCoO_2$ (phase I) and Si (phase II) sample.

Table 2.1 Comparison of lattice constants of $LiCoO_2$ and Si phases from two-phase Rietveld refinements and from the literature.

Phases	Lattice constant from XRD refinement	Lattice constant from references
$LiCoO_2$	a = b = 2.8175 Å c = 14.0572 Å	a = b = 2.8168 Å; c = 14.0544 Å Reference [23]
Si	a = b = c = 5.4331 Å	a = b = c = 5.4307 Å Reference [112]

2.5.4 Surface Area Measurement

Single-point Brunauer-Emmett-Teller (BET) surface area measurements were performed on electrode materials using a Micromeritics Flowsorb II 2300 surface area analyzer. In this thesis, single-point BET surface area measurements were conducted to measure the surface area of electrode materials. The amount of N_2 gas from a mixture of N_2 in He (3:7 by volume) adsorbed as a monolayer of atoms at 77 K on the surface of the sample is a measure of its surface area. Before testing, the sample was placed in a U-shaped glass tube, weighed, and degassed at 150°C under a N_2/He gas mixture for about 1.5 ~ 2 hours. The glass tube was then immersed in liquid N_2 for adsorption and after that, in a beaker filled with tap water for desorption at room temperature. The adsorption or desorption was considered complete when the change of the BET result was less than 0.02 m^2 g^{-1}. Usually, the surface area difference between adsorption and desorption is smaller than 0.1 m^2. The final surface area result was taken from the desorption data of the single-point BET measurement.

Chapter 3. Baseline studies of the thermal stability of $LiCoO_2$/MCMB cells

Today, most lithium-ion battery producers still use MCMB and $LiCoO_2$ as negative and positive electrode materials, respectively. This chapter focuses on thermal-stability studies of single electrodes, charged MCMB ($Li_{0.81}C_6$) and $LiCoO_2$ ($Li_{0.5}CoO_2$) using ARC, and full 18650-size cells ($LiCoO_2$/MCMB) by the oven test. For a particular set of electrode materials and electrolyte, the ARC and the oven test results are in good agreement. It is concluded that ARC is an excellent technique to study the thermal stability of single electrode materials in LIBs.

3.1 ARC studies

3.1.1 MCMB

The effects of the cell components, such as the binder, solvent, and salt, on the thermal stability of the MCMB negative electrode were studied using ARC and XRD and are described in this section. A SEM image of the MCMB (Moli Energy Ltd.) used is shown in Figure 3.1. The average particle size of the MCMB is approximately 20 μm.

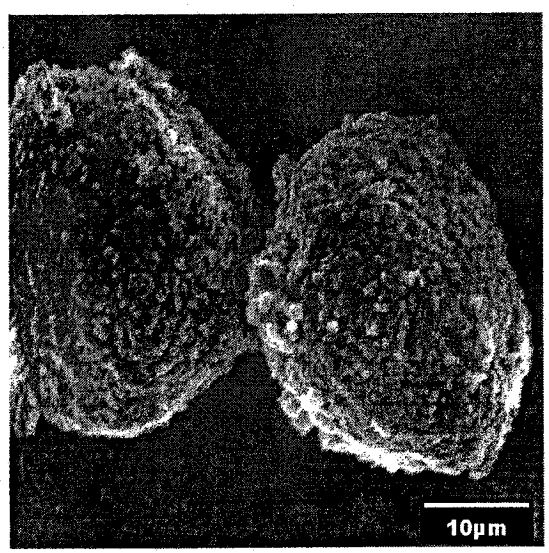

Figure 3.1 A SEM image of the MCMB sample used (average particle size of about 20 μm).

3.1.1.1 Lithium intercalated graphite

Figure 3.2 shows diagrams of the staged phases of Li intercalated graphite. Stage-n order is a sequence of n graphite sheets and one lithium-intercalated layer. Stage-1 order is fully lithiated graphite and the corresponding compound is LiC_6. Stage-2 order is half-lithiated graphite and the corresponding compound is LiC_{12}.

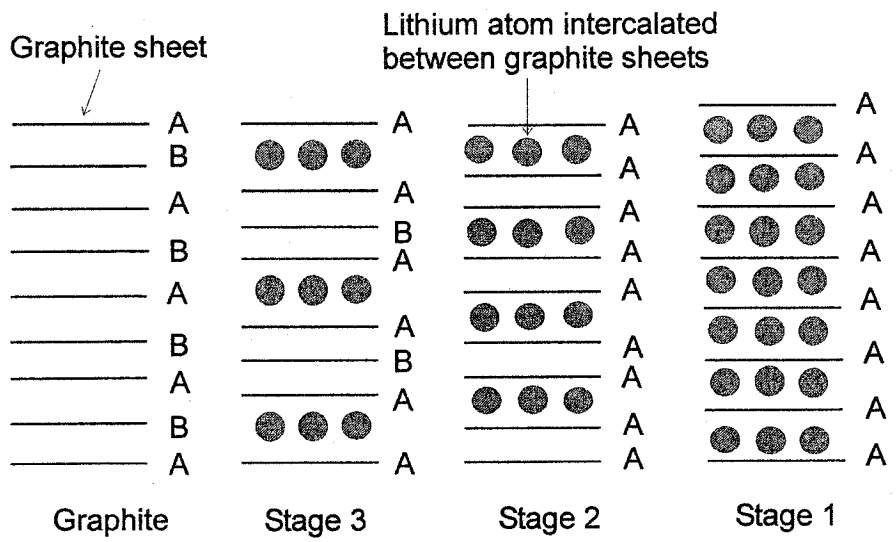

Figure 3.2 A schematic diagram of the staged phases of Li intercalated graphite. "A" and "B" represent graphite sheets. Sheet "B" shifts relative to the adjacent sheet, "A", by a distance of $(3)^{-1/2}a$ in the [010] reciprocal lattice direction. a is the in-plane graphite lattice constant.

Figure 3.3 shows XRD patterns taken of (a) MCMB, (b) fresh $Li_{0.81}C_6$ and (c) rinsed $Li_{0.81}C_6$ with 2% EPDM binder. Panel (a) shows that the (002) Bragg peak of MCMB is at approximately 26.5°. The XRD pattern for fully lithiated MCMB in panel (b) contains a peak at 24.25°, which corresponds to the stage-1 phase (LiC_6), and a shoulder at around 25.25°. This XRD shoulder corresponds to small regions of stage-2 phase (LiC_{12}), which form because some adjacent graphene sheets cannot accommodate Li due to turbostratic misalignment [113].

The diffraction pattern of rinsed $Li_{0.81}C_6$ (2% EPDM) is shown in Figure 3.3c. By comparison to Figure 3.3b the diffraction pattern of $Li_{0.81}C_6$ remains unchanged during

rinsing. Thus it is believed that the DMC rinsing procedure does not change the bulk structure and hence the lithium content, x, of Li_xC_6.

The lithium content in the samples described by Figure 3.3c can be estimated from the intensity of the XRD peaks. The fitting of the both XRD peaks (LiC_6 and LiC_{12} phases) in Figure 3.3c is shown in Figure 3.4. It is assumed that the amounts of LiC_6 and LiC_{12} are proportional to their corresponding peak areas. The calculated x in Li_xC_6 is about 0.81. The lithium content can also be obtained by the following equation,

$$x = 1 - r, \qquad [3\text{-}1]$$

where r is probability of a turbostratic shift between adjacent graphene layers of MCMB, which is about 0.19 for this sample of MCMB [113].

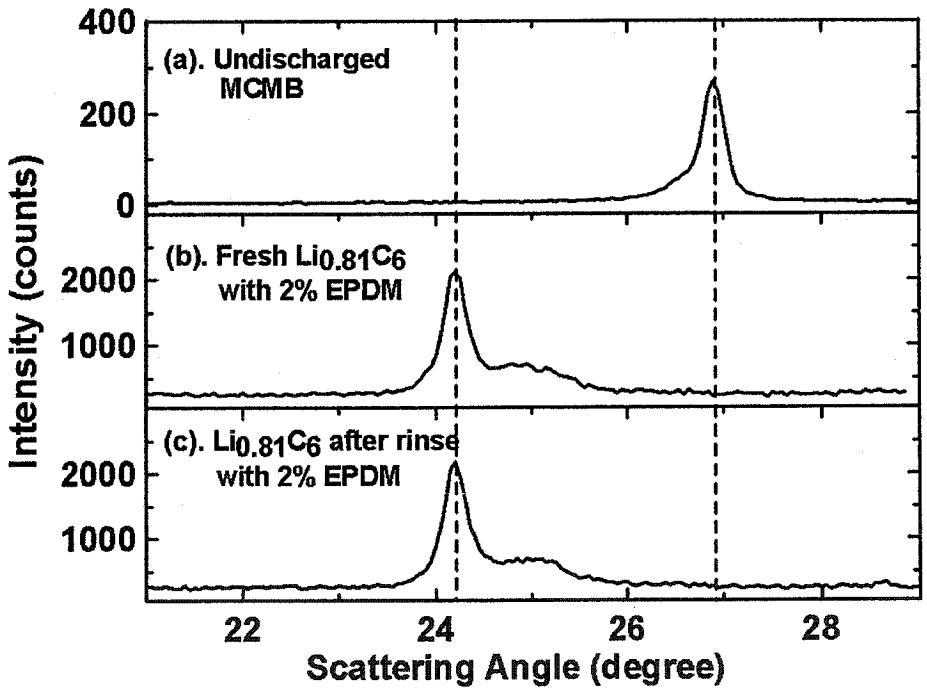

Figure 3.3 XRD patterns of (a) MCMB and (b) $Li_{0.81}C_6$ with 2% EPDM before or (c) after the DMC rinse.

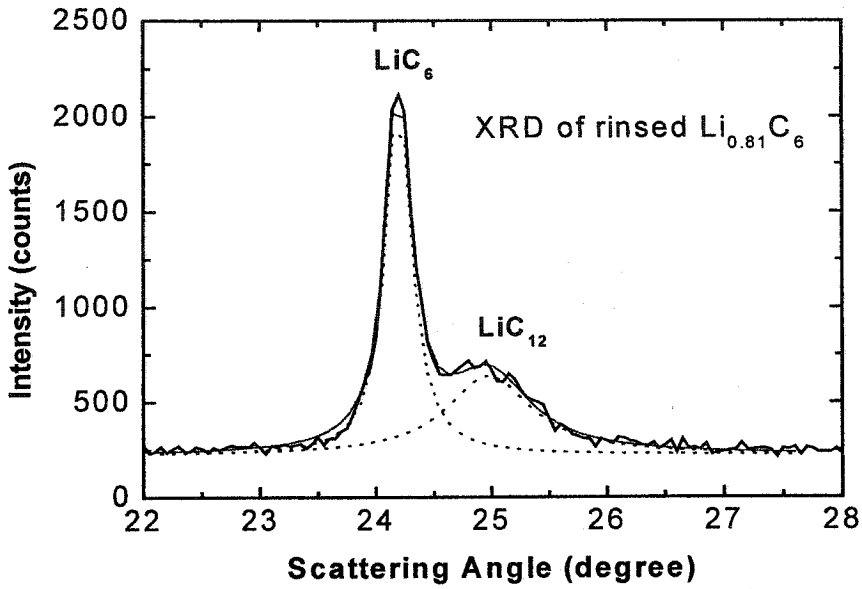

Figure 3.4 Fitting the Bragg peaks from the LiC_6 and LiC_{12} phases in the XRD pattern of rinsed $Li_{0.81}C_6$.

3.1.1.2 Reactivity of $Li_{0.81}C_6$ with EPDM and PVDF binders

Figure 3.5a shows the self-heating rate (SHR) of 200 mg of rinsed $Li_{0.81}C_6$ containing 2% EPDM versus temperature. The sample was initially heated to 90°C before the search for exothermic behaviour began. Almost no heat was released by this sample in the temperature range between 90°C and 350°C. This means that $Li_{0.81}C_6$ does not react significantly with EPDM binder in this temperature range.

Figure 3.5b shows the self-heating rate versus temperature of 50 mg of rinsed $Li_{0.81}C_6$ (2% EPDM) mixed with 35 mg PVDF binder. The sample was initially heated to 90°C prior to searching for exothermic behaviour. The SHR in panel b between 250°C and 302°C is due to the exothermic reaction between $Li_{0.81}C_6$ and PVDF binder. Since PVDF contains F and EPDM does not, it is likely that a reaction to produce LiF as a product occurs. The temperature rise, ΔT, for this reaction is around 52 K. The heat, h, released from this reaction is given by

$$h = \Delta T * C_{Tot}, \qquad [3\text{-}2]$$

where C_{Tot} is the total heat capacity of the entire sample ($Li_{0.81}C_6$, PVDF binder, plus stainless steel ARC tube). For the ARC sample in Figure 3.5b, the total heat capacity is calculated as

$$C_{Tot} = \sum_i c_i m_i = 1.0\frac{J}{gK} m_{LiC} + 0.46\frac{J}{gK} 0.93g + 1.1\frac{J}{gK} m_{pvdf}, \quad [3\text{-}3]$$

where m_{LiC} is the mass of $Li_{0.81}C_6$ in grams in this ARC experiment, m_{pvdf} is the mass of PVDF binder in grams in the ARC tube, and 0.93 g is the mass of the stainless steel ARC tube. A specific heat of 1.0 J K^{-1} g^{-1} was used for $Li_{0.81}C_6$, 1.1 J K^{-1} g^{-1} for PVDF binder, and 0.46 J K^{-1} g^{-1} for stainless steel [114, 117]. Therefore the total heat (h) of the reaction is calculated to be 26.8 J. The $Li_{0.81}C_6$ electrode contains 2% EPDM and 7% Super S carbon black. Therefore the heat (ΔH) of the reaction between $Li_{0.81}C_6$ and PVDF per gram of $Li_{0.81}C_6$ is given by,

$$\Delta H = \text{h/mass of } Li_{0.81}C_6, \quad [3\text{-}4]$$

which is about 590 J g^{-1}. Using a similar calculation, the heat (ΔH) per gram of lithium is approximately 8080 J g^{-1}.

Du Pasquier *et al.* [115] suggested a possible reaction mechanism between lithium and PVDF as follows:

$$\text{-}(CH_2 - CF_2)_n\text{-} + n\,Li \rightarrow n\,LiF + \text{-}(CH = CF)_n\text{-} + n/2\,H_2. \quad [3\text{-}5]$$

There is excess PVDF compared to that needed for a stoichiometric reaction for the sample described by Figure 3.5b. The heat (ΔH) observed by Du Pasquier was 1220 J g^{-1}, approximately two times that obtained from Figure 3.5b. This difference will be discussed later.

Panel 3.5c shows the SHR of 3.0 mg of lithium metal mixed with 30 mg of PVDF. For the experiment described by Figure 3.5b, the amount of lithium contained in the $Li_{0.81}C_6$ sample was about 3.3 mg. The temperature rise (ΔT) in Figure 3.5c is approximately 50 K, which is similar to the temperature rise of 52 K in Figure 3.5b. The heat capacity of lithium metal is 3.5 J K^{-1} g^{-1} [114, 117]. The calculated heat (ΔH) for the reaction of lithium metal with PVDF is approximately 7600 J g^{-1} of lithium, which is close to the heat (ΔH) of 8080 J g^{-1} of lithium for the reaction between $Li_{0.81}C_6$ and PVDF shown in Figure 3.5b.

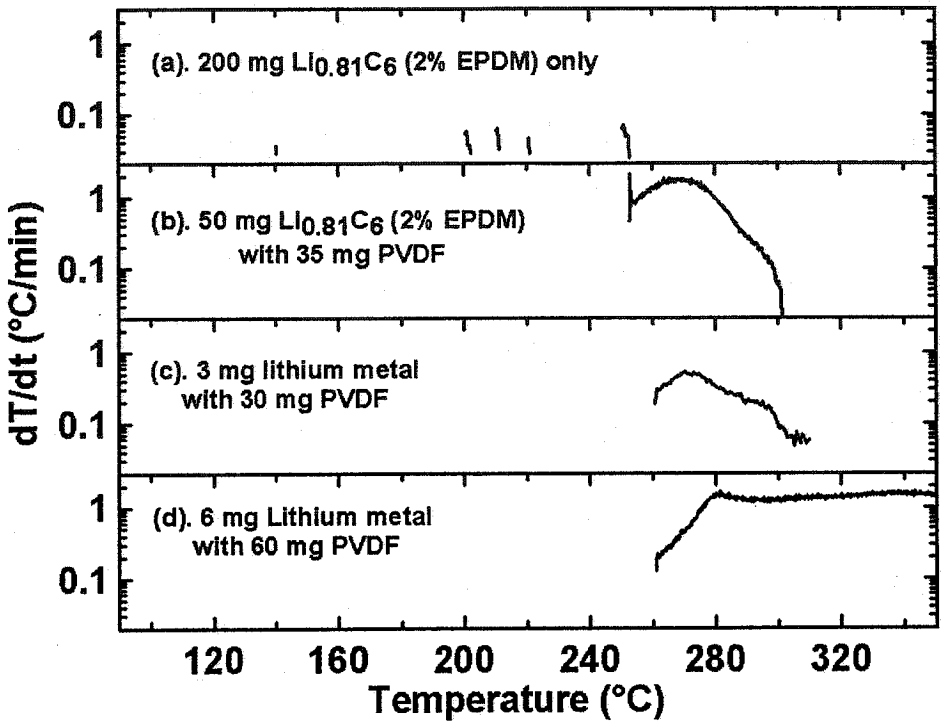

Figure 3.5 Self-heating rate versus temperature for 200 mg $Li_{0.81}C_6$ with 2% EPDM binder (a), 50 mg $Li_{0.81}C_6$ (2% EPDM) with 35 mg PVDF (b), 3 mg lithium metal with 30 mg PVDF (c), and 6 mg lithium metal with 60 mg PVDF (d). All the experiments were started at 90°C.

Figure 3.5d shows the self-heating rate versus temperature of 6 mg lithium metal reacting with 60 mg PVDF heated to 90°C. The amount of lithium metal used in the experiment reported in Figure 3.5d is twice the 3 mg lithium used in Figure 3.5c. The heat (ΔH) released from the reaction between lithium and PVDF in Figure 3.5d should be twice the heat released from the sample described in Figure 3.5c. It is assumed that the total heat capacities (C_{Tot}) are the same for the samples described in Figures 3.5c and d because the majority of the heat capacity comes from the 0.93 g ARC tube. Therefore, the temperature rise (ΔT) in Figure 3.5d should be approximately 100 K, which is twice the temperature rise in Figure 3.5c. The detectable exothermic reaction in Figure 3.5d started at 260°C and should finish at 360°C. This experiment was stopped at 350°C, the highest temperature suggested for the ARC, where the reaction of lithium with binder had unfortunately not yet finished.

3.1.1.3 Reactions between $Li_{0.81}C_6$ and solvents or electrolytes

The reaction between the $Li_{0.81}C_6$ negative electrode and DMC, DEC, EC, or EC/DEC solvents before and after the addition of $LiPF_6$ salt were compared using ARC. The effects of the concentration of $LiPF_6$ and LiBOB in EC/DEC solvent on the thermal stability of $Li_{0.81}C_6$ were also studied. The reaction between $LiPF_6$/LiBOB EC/DEC mixed electrolytes and $Li_{0.81}C_6$ are also discussed in this section. For the experiments here, the $Li_{0.81}C_6$ negative electrode contained 7% PVDF and 7% Super S carbon black.

Figure 3.6 shows the self-heating rate versus temperature of 100 mg of rinsed $Li_{0.81}C_6$ reacting with 100 mg of the different solvents, DMC, DEC, EC, or the EC/DEC mixture, as well as $LiPF_6$-based electrolytes in each solvent. The data for the solvent are given by the dashed lines and for the $LiPF_6$-containing electrolyte by the solid lines. DMC shows the lowest thermal stability with respect to $Li_{0.81}C_6$ of all the solvents. A SHR of 0.6°C/min for the reaction between $Li_{0.81}C_6$ and DMC was measured at a starting temperature of 90°C. This means that an exothermic signal existed at lower temperatures than 90°C. Another ARC sample, the same as the sample in Figure 3.6a, was run with a starting temperature of 40°C. It was found that the detectable onset temperature for the reaction of $Li_{0.81}C_6$ with DMC was 50°C.

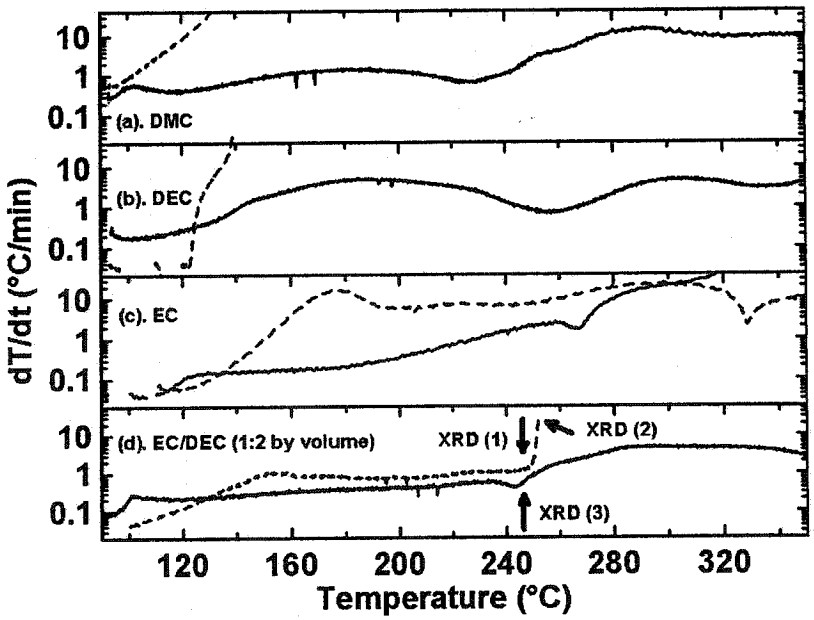

Figure 3.6 Self-heating rate versus temperature for $Li_{0.81}C_6$ reacting with different solvents, DMC (a), DEC (b), EC (c), or EC/DEC (d) indicated with dashed lines or 1.0 M $LiPF_6$ in these solvents indicated with solid lines.

The SHR of $Li_{0.81}C_6$ with DMC in Figure 3.6a or DEC in Figure 3.6b increases quickly with temperature and both samples went into thermal runaway even at low temperatures around 135°C. However, EC can effectively stabilize the protective passivating film on $Li_{0.81}C_6$ and higher thermal stability was achieved as shown in Figure 3.6c. Figure 3.6 also shows that the addition of $LiPF_6$ salt into EC or DEC solvent decreased the thermal stability of $Li_{0.81}C_6$ in the range from 90°C to 120°C probably because of the decomposition of $LiPF_6$ as follows [81]:

$$LiPF_6(solvated) \rightarrow LiF(s) + PF_5(solvated). \qquad [3\text{-}6]$$

The product, PF_5, is a strong Lewis acid that can react easily with organic solvents such as EC, PC, etc., releasing heat. Therefore, the addition of the salt into the solvents decreased the thermal stability of $Li_{0.81}C_6$ in the lower temperature range. With the increase of temperature, more and more LiF is probably incorporated in the SEI on Li_xC_6, which effectively inhibits the reactivity of Li_xC_6. Hence, the thermal stability of $Li_{0.81}C_6$ improved with the addition of $LiPF_6$ salt into these solvents in the higher temperature region from approximately 130°C to 300°C (Figure 3.6).

Two ARC experiments involving 100 mg $Li_{0.81}C_6$ mixed with 100 mg EC/DEC were run. One of these was the same sample as in Figure 3.6d. The experiments were stopped at 243°C and 253°C, respectively. One experiment was therefore stopped before the thermal runaway shown in Figure 3.6d and the other was stopped after the thermal runaway. After cooling, both ARC tubes were transferred to an argon-filled glove box. The ARC tubes were opened and the samples inside the ARC tubes were recovered. XRD patterns for both samples are shown in Figures 3.7a and b. Figure 3.7a shows the existence of the stage-2 phase together with some stage-1 phase and delithiated MCMB. For this sample, x in Li_xC_6 is calculated to be about 0.5. About half of the lithium in $Li_{0.81}C_6$ was consumed due to the reaction between $Li_{0.81}C_6$ and EC/DEC to apparently produce Li-alkyl carbonate [30, 116], which cannot be detected by XRD. Figure 3.7b shows that the products of $Li_{0.81}C_6$ heated with EC/DEC after the thermal runaway are mainly delithiated MCMB and Li_2CO_3.

The corresponding reaction of $Li_{0.81}C_6$ with EC/DEC described in Figure 3.6d at elevated temperature can therefore be divided into two main processes (Figure 3.8):

(1). Between 90 and 243°C, $Li_{0.81}C_6$ reacts with EC/DEC to form Li alkylcarbonate and Li_xC_6 where $x<0.81$;

(2). Above 243°C, Li_xC_6, Li alkylcarbonate, and EC/DEC react to produce Li_2CO_3 and ethylene.

It is interesting to note that once Li_2CO_3 forms, thermal runaway apparently begins. The overall thermal reaction between $Li_{0.81}C_6$ with EC/DEC can be given by (using EC as an example):

$$2Li + C_3H_4O_3 \rightarrow C_2H_4 + Li_2CO_3, \qquad [3\text{-}7]$$

where the Li deintercalates from the carbon to react with the solvent [116].

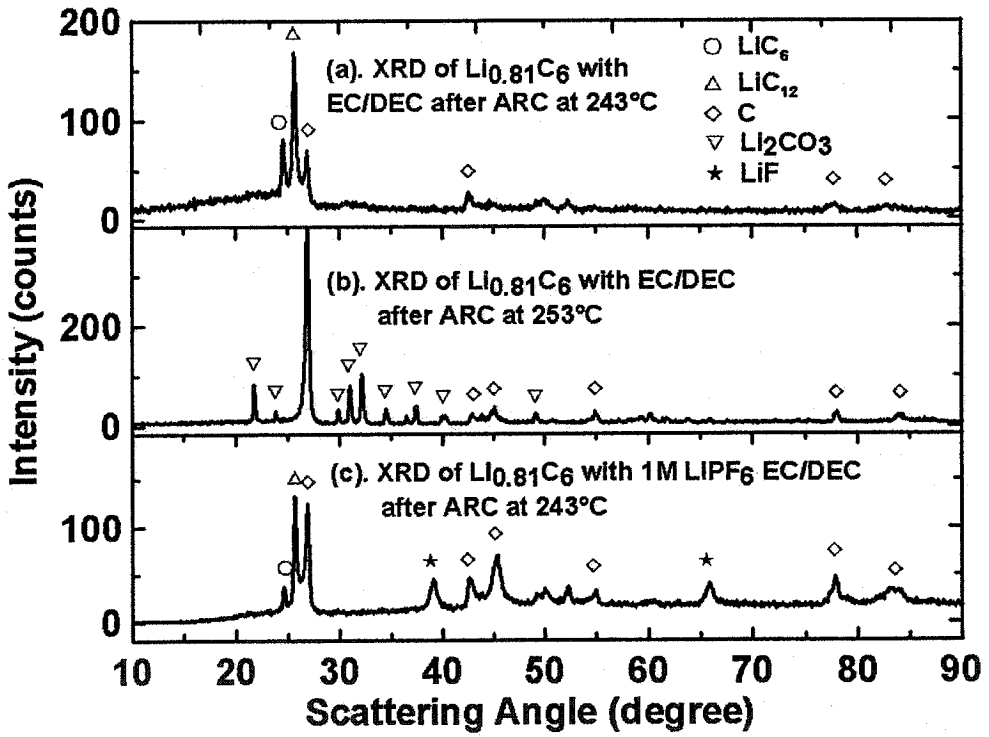

Figure 3.7 XRD patterns of $Li_{0.81}C_6$ ARC samples after reacting with EC/DEC solvent stopped at 243°C (a) or 253°C after the thermal runaway (b) and with 1.0 M $LiPF_6$ EC/DEC electrolyte stopped at 243°C (c).

Figure 3.7c shows the XRD pattern of the products from the reaction of $Li_{0.81}C_6$ with 1.0 M $LiPF_6$ EC/DEC stopped at 243°C. This data should be compared with Figure 3.7a where the products of the reaction of $Li_{0.81}C_6$ with EC/DEC at the same temperature are shown. Figure 3.7c shows the existence of LiF. The addition of the $LiPF_6$ salt changes

the reaction path of $Li_{0.81}C_6$ and apparently produces a surface film dominated by LiF rather than Li alkylcarbonate at temperatures below 240°C. This apparently increases the thermal stability of $Li_{0.81}C_6$ in electrolyte compared to solvent.

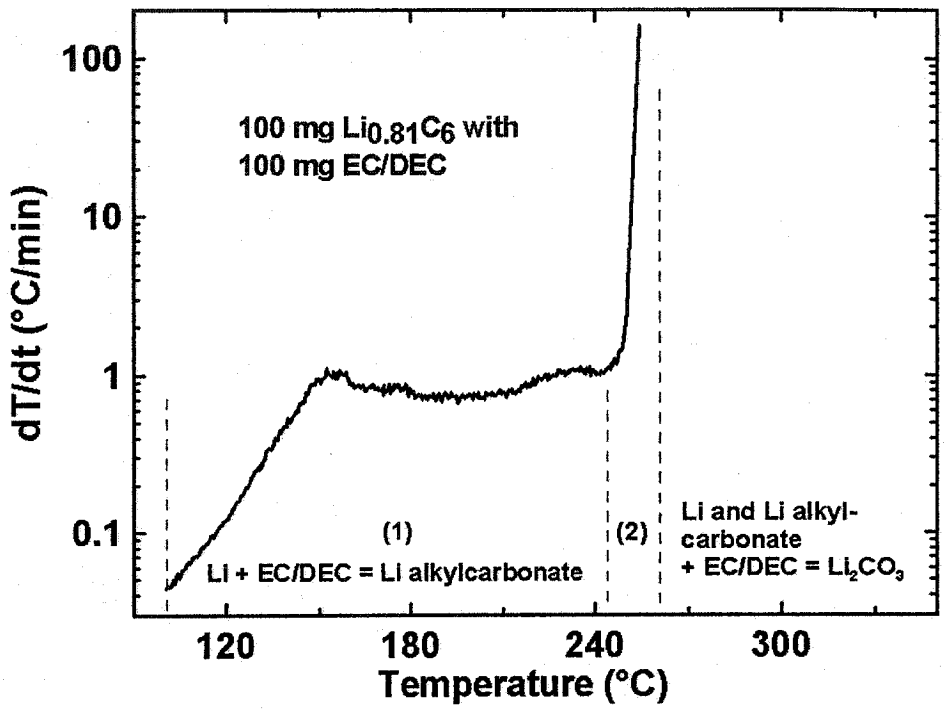

Figure 3.8 Proposed reaction sequence between $Li_{0.81}C_6$ and EC/DEC solvent during the temperature range between 90 and 260°C correlated to ARC results.

In order to characterize the enthalpy (ΔH) of reaction [3-7], one needs to measure the temperature change that corresponds to the entire reaction between $Li_{0.81}C_6$ and EC/DEC. In Figure 3.8, a large part of reaction was not monitored because of the thermal runaway. Therefore, further samples were prepared with smaller amounts of reactants. In one test, 50 mg of both $Li_{0.81}C_6$ and EC/DEC was used and in another, 35 mg of both $Li_{0.81}C_6$ and EC/DEC was used. The ARC results are shown in Figure 3.9. Thermal runaway still occurred for the 50 mg sample in Figure 3.9a. However, the entire exotherm could be measured for the 35 mg sample as shown in Figure 3.9b. The temperature rise (ΔT_1), as indicated by the sum of the four temperature rises indicated by the arrows in Figure 3.9b, for this reaction is about 137 K. The heat, h_1, released from this reaction is

calculated as 71 J using the method described in Section 3.1.1.2. The enthalpy change of the reaction, therefore, is approximately -215 kJ mol^{-1} of lithium.

The heat of reaction can be estimated using tabulated enthalpy of formations for EC (ΔH_f^o = -683 kJ mol^{-1}), DEC (ΔH_f^o = -681 kJ mol^{-1}), Li_2CO_3 (ΔH_f^o = -1216 kJ mol^{-1}) and ethylene (ΔH_f^o = +52 kJ mol^{-1}) [117]. For reaction [3-7], ΔH^o is found to be approximately -240 kJ mol^{-1} of Li. Of course, the reaction under study does not occur under standard conditions of either temperature or pressure. Nevertheless, the agreement between experiment and the theoretical estimate is within 15%.

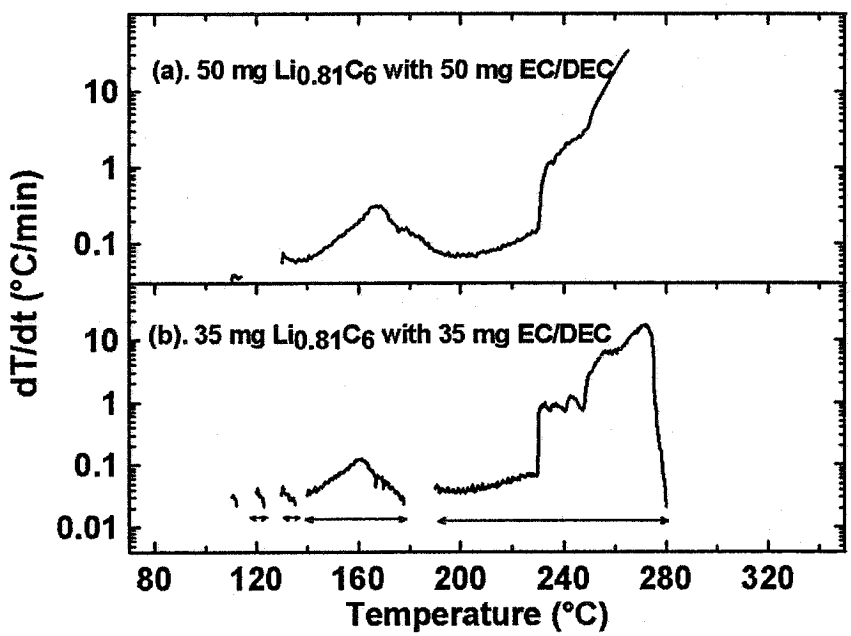

Figure 3.9 SHR vs. T of 50 mg of $Li_{0.81}C_6$ reacting with 50 mg of EC/DEC in panel (a) and 35 mg of $Li_{0.81}C_6$ reacting with 35 mg of EC/DEC (b). The ARC sample was initially heated to 90°C.

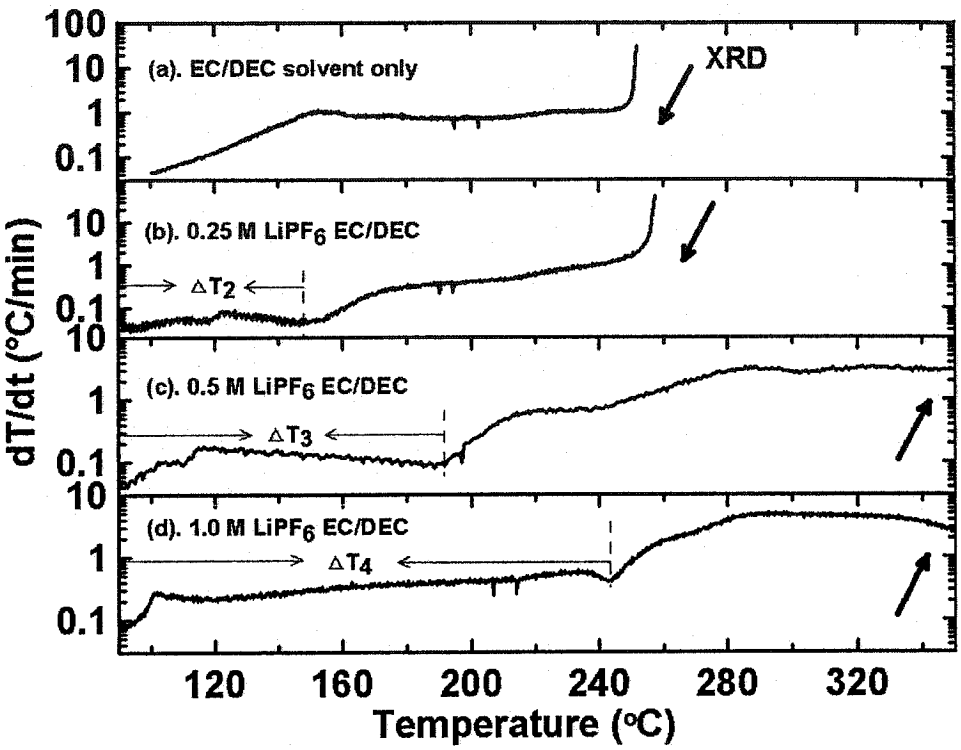

Figure 3.10 Self-heating rate versus temperature for 100 mg of $Li_{0.81}C_6$ with the same amount of EC/DEC (a) or 0.25 M (b), 0.5 M (c), or 1.0 M $LiPF_6$ EC/DEC electrolyte (d), heated initially to 90°C.

In order to learn more about the effects of $LiPF_6$ salt in EC/DEC solvent on the thermal stability of $Li_{0.81}C_6$, the concentration of $LiPF_6$ EC/DEC was varied between 0 and 1.0 M and corresponding ARC results measured. Figure 3.10 shows these results. As the concentration of $LiPF_6$ in EC/DEC increased from 0.25 M, 0.5 M, to 1.0 M, the temperature rise (ΔT) for the first peak in the ARC response of $Li_{0.81}C_6$ in $LiPF_6$ EC/DEC increased from approximately ΔT_2 = 59 K (b), ΔT_3 = 100 K (c), to ΔT_4 = 154 K (d), respectively. The first ARC peak in Figure 3.10 is probably due to the exothermic reaction between $Li_{0.81}C_6$ and PF_5 (resulting from $LiPF_6$) so that the temperature rise for the first peak is approximately proportional to the initial concentration of $LiPF_6$ salt in EC/DEC solvent.

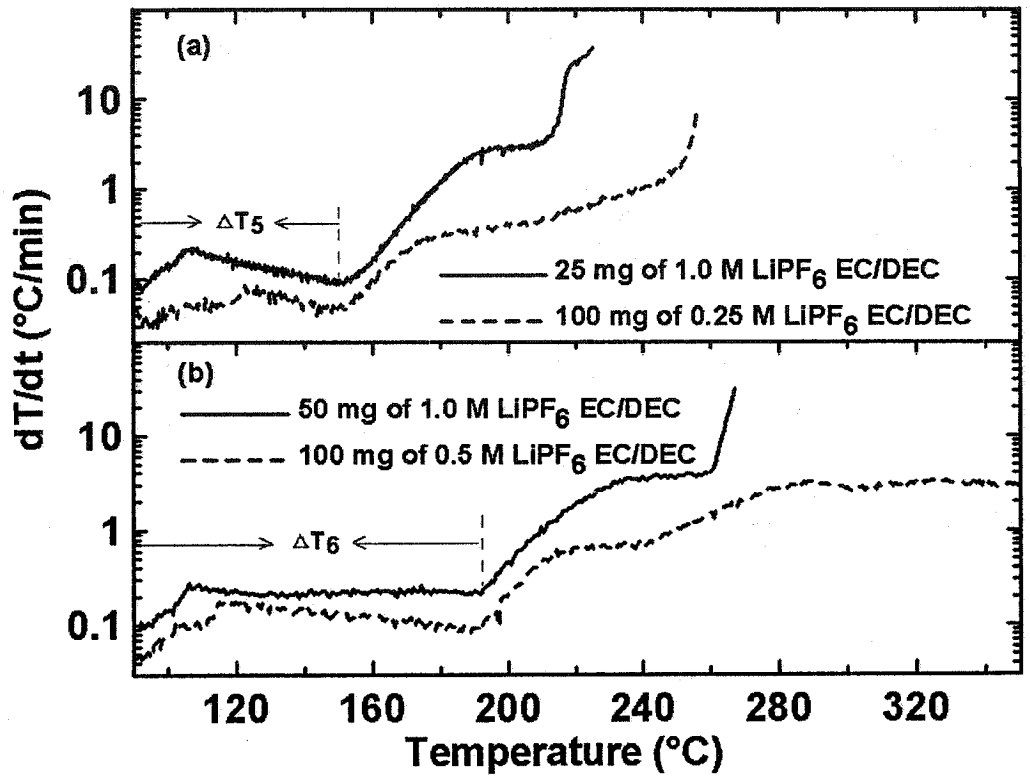

Figure 3.11 Self-heating rate versus temperature for 100 mg of $Li_{0.81}C_6$ with 25 (panel a) or 50 mg (panel b) of 1.0 M $LiPF_6$ EC/DEC in solid line. Self-heating rate versus temperature for 100 mg of $Li_{0.81}C_6$ with 100 mg of 0.25 M and 0.5 M $LiPF_6$ EC/DEC shown in (a) and (b), respectively, in the dashed line for comparison.

ARC experiments on 100 mg of $Li_{0.81}C_6$ heated with either 25 mg or 50 mg of 1.0 M $LiPF_6$ EC/DEC were conducted to study the reaction sequence between $Li_{0.81}C_6$ and PF_5 (Figure 3.10). The results are shown in Figures 3.11a and b as the solid lines. The dashed lines show similar results but for 100 mg of $Li_{0.81}C_6$ reacting with 100 mg of either 0.25 M or 0.5 M $LiPF_6$ EC/DEC, taken from Figures 3.10b and c, for comparison. Figure 3.11a clearly shows that the temperature rise (ΔT_5) of the first ARC peak for 100 mg of $Li_{0.81}C_6$ reacting with either 25 mg of 1.0 M $LiPF_6$ EC/DEC (solid line) or 100 mg of 0.25 M $LiPF_6$ EC/DEC (dashed line) is about 59 K in both cases. This is simply because 25 mg of 1.0 M $LiPF_6$ EC/DEC and 100 mg of 0.25 M $LiPF_6$ EC/DEC contain similar amounts of $LiPF_6$ salt, which thermally reacts with $Li_{0.81}C_6$ releasing a similar amount of heat. Similarly, the ARC temperature rises (ΔT_6) for 100 mg of $Li_{0.81}C_6$ with

50 mg of 1.0 M $LiPF_6$ EC/DEC or 100 mg of 0.5 M $LiPF_6$ are both about 100 K as shown in Figure 3.11b.

It is interesting to observe from Figures 3.10 and 3.11 that the SHR of $Li_{0.81}C_6$ in $LiPF_6$ EC/DEC electrolyte significantly increases after the reaction between $Li_{0.81}C_6$ and PF_5 completes. The XRD patterns of the samples after completion of the ARC experiments described in Figure 3.10 were measured.

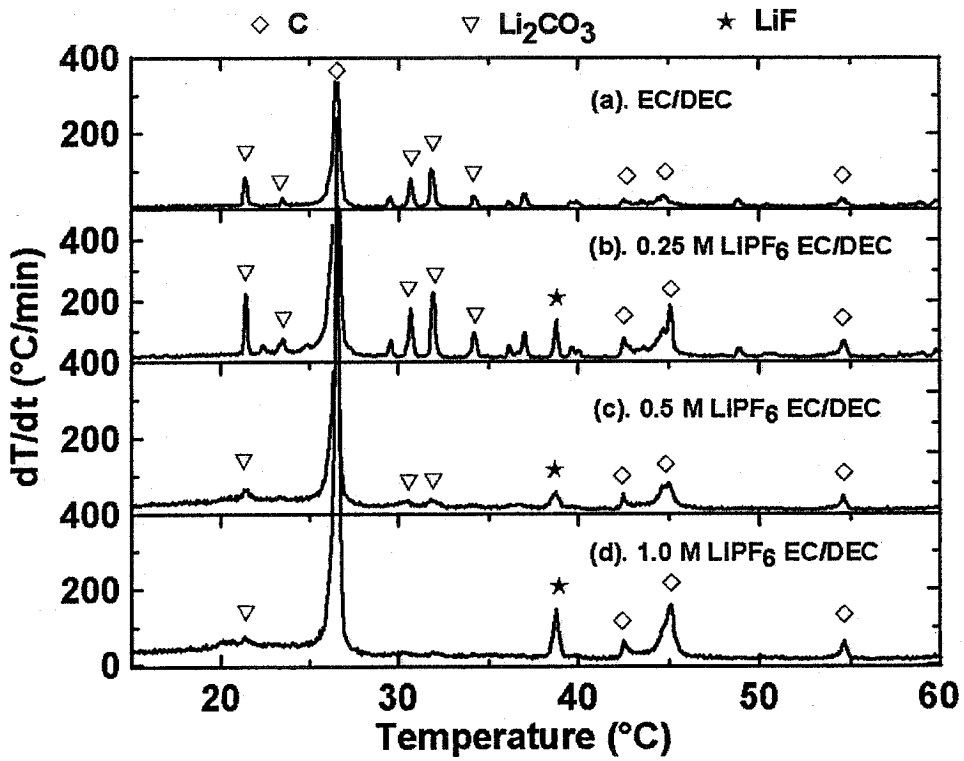

Figure 3.12 XRD patterns of $Li_{0.81}C_6$ ARC samples after reacting with EC/DEC solvent and different concentrations of $LiPF_6$ in EC/DEC shown in Figure 3.10. Figure 3.12a is the same as Figure 3.7b.

Figures 3.12b, c, d, and e show the XRD patterns of the products from the reactions between $Li_{0.81}C_6$ and $LiPF_6$ EC/DEC with different concentrations (0.25 M, 0.5 M, and 1.0 M, respectively) after ARC tests. Figure 3.12a shows the XRD patterns of the products from the reaction between $Li_{0.81}C_6$ and EC/DEC solvent at 253°C, which is the same as the XRD pattern in Figure 3.7b. The main products from the reaction between $Li_{0.81}C_6$ and $LiPF_6$ EC/DEC are LiF, Li_2CO_3, and C. This suggests that, after reacting

with PF_5, Li_xC_6 thermally reacts with EC/DEC to produce Li_2CO_3. More Li_2CO_3 is produced in 0.25 M $LiPF_6$ EC/DEC (Figure 3.12b) than in 0.5 M or 1.0 M $LiPF_6$ EC/DEC (Figures 3.12c and d). The masses of $LiPF_6$ EC/DEC electrolyte used in the ARC tests in Figure 3.11 are the same (around 100 mg). The $LiPF_6$ EC/DEC electrolyte with a higher concentration (such as 1.0 M in Figure 3.10d) contains a larger amount of $LiPF_6$ salt, which releases more PF_5 that reacts with $Li_{0.81}C_6$. Therefore, in a higher concentration of $LiPF_6$ EC/DEC electrolyte, less $Li_{0.81}C_6$ is left to react with EC/DEC producing Li_2CO_3. The observations suggest a step-wise reaction sequence between $Li_{0.81}C_6$ and $LiPF_6$ EC/DEC electrolyte described as follows.

(1) $Li_{0.81}C_6$ starts reacting with PF_5 to produce LiF as shown in Figure 3.12. The LiF incorporates into the SEI on Li_xC_6 forming a passivating film on Li_xC_6, which effectively inhibits the reactivity of Li_xC_6.

(2) After the depletion of PF_5, the remaining Li_xC_6 reacts with EC/DEC producing Li_2CO_3 (Figure 3.12).

In Figure 3.11, it is observed that the SHR of the $Li_{081}C_6$ sample remains constant or even decreases with temperature during its reaction with PF_5. It is possibly because, as the temperature increases, more LiF is produced and the passivating film containing LiF becomes thicker, which inhibits the further reaction between Li_xC_6 and electrolyte. After depletion of PF_5, the Li in Li_xC_6 diffuses through the passivating film and then thermally reacts with EC/DEC forming Li_2CO_3 (Figure 3.12).

Figure 3.13 shows the self-heating rate versus temperature for $Li_{0.81}C_6$ in different concentrations of LiBOB EC/DEC heated initially to 90°C. As the LiBOB concentration increases the onset temperature shows a corresponding increase, from 100°C for 0 M to about 200°C for 0.8 M LiBOB. Apparently, a more stable passivating film is formed on $Li_{0.81}C_6$ in higher concentrations of LiBOB EC/DEC [118]. In fact, the addition of only 0.2 M LiBOB in EC/DEC can greatly improve the thermal stability of $Li_{0.81}C_6$.

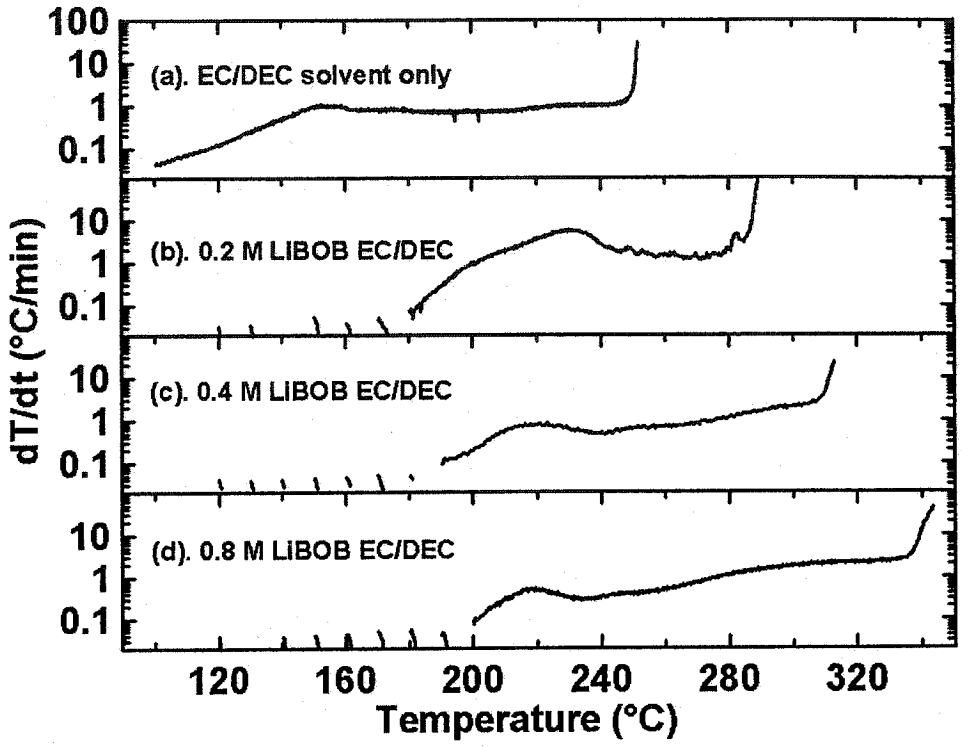

Figure 3.13 Self-heating rate versus temperature for 100 mg of $Li_{0.81}C_6$ with the same amount of EC/DEC (a) or 0.2 M (b), 0.4 M (c), or 0.8 M LiBOB EC/DEC electrolyte (d), heated initially to 90°C.

Figure 3.14 shows the SHR versus temperature for samples of $Li_{0.81}C_6$ immersed in 1.0 M $LiPF_6$ EC/DEC and in 0.8 M LiBOB EC/DEC, where the samples were first forced to 120°C at 10°C/min before the exotherms were monitored. The sample with the $LiPF_6$ electrolyte has sustained rapid self-heating that carries on, without delay, into the next exotherm, while the LiBOB sample does not. This experiment clearly shows the safety advantage of the LiBOB salt over $LiPF_6$ in EC/DEC solvents for the lithiated MCMB negative electrode.

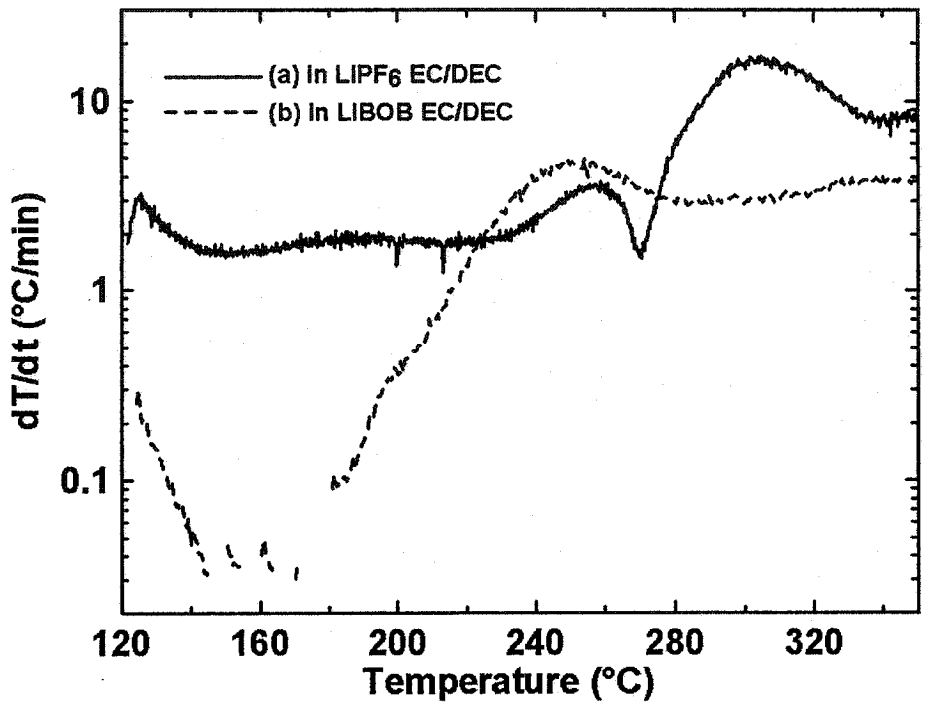

Figure 3.14 Comparison of the self-heating rate versus temperature of approximately 100 mg lithiated MCMB in two different electrolytes. In this case the samples were forced to 120°C at 10°C/min before the exotherms were monitored: (a) 100 mg $LiPF_6$ EC/DEC, and (b) 100 mg LiBOB EC/DEC.

Since the $LiPF_6$ salt can increase the thermal stability of the $Li_{0.5}CoO_2$ positive electrode but LiBOB cannot [86] and a small amount of LiBOB in EC/DEC, such as 0.2 M, can effectively stabilize the $Li_{0.81}C_6$ negative electrode, ARC experiments on $Li_{0.81}C_6$ in $LiPF_6$/LiBOB EC/DEC mixed electrolytes were conducted. Figure 3.15 shows the self-heating rate versus temperature of $Li_{0.81}C_6$ in different compositions of $LiPF_6$/LiBOB EC/DEC mixed electrolytes. As the $LiPF_6$ concentration decreases from 1.0 M (a), 0.75 M (b), 0.5 M (c) to 0.25 M (d), the temperature increase (ΔT) of the first peak in the ARC response, mainly attributed to the reaction of $Li_{0.81}C_6$ with PF_5, decreased from 154 K, 119 K, 74 K, to 23 K, respectively. These results suggest that an optimization of mixed $LiPF_6$/LiBOB electrolytes focused on the safety of $LiCoO_2$/MCMB cells would be worthwhile.

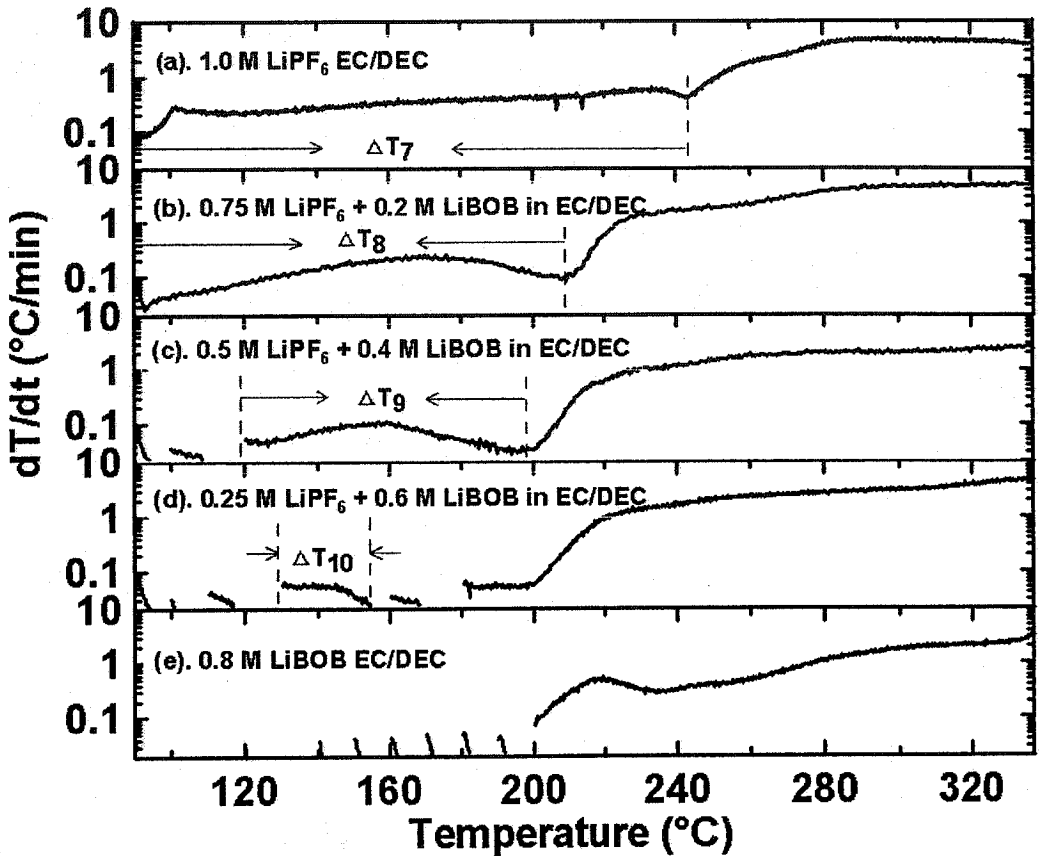

Figure 3.15 Self-heating rate versus temperature for 100 mg $Li_{0.81}C_6$ (7% PVDF) with 100 mg $LiPF_6$/LiBOB EC/DEC mixed electrolytes heated initially to 90°C.

3.1.1.4 Effects of binder on the thermal stability of $Li_{0.81}C_6$ in $LiPF_6$ EC/DEC electrolyte

Figure 3.16 shows the self-heating rate of 100 mg $Li_{0.81}C_6$ containing 2% binder, (PVDF in panel a and EPDM in panel b) reacting with 100 mg 1.0 M $LiPF_6$ EC/DEC initially heated to 90°C. The ARC curves in panels a and b are similar because the heat evolved arises mainly from the thermal reaction between $Li_{0.81}C_6$ and electrolyte. A small amount of binder in $Li_{0.81}C_6$ (such as 2%) does not apparently significantly affect the thermal behavior of the negative electrode in $LiPF_6$ EC/DEC electrolyte.

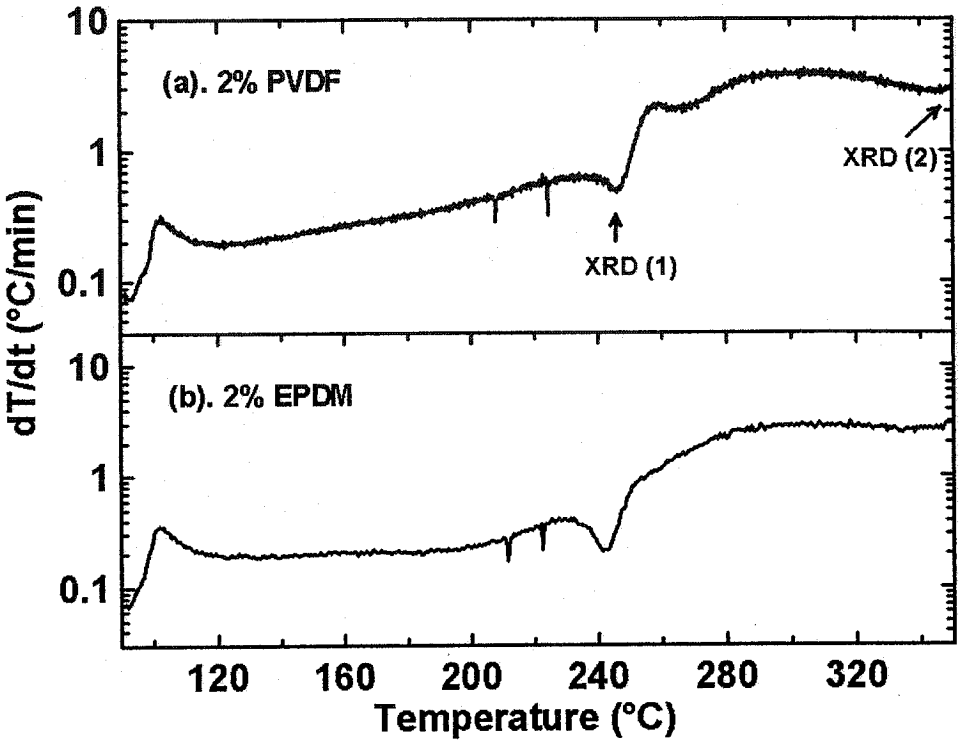

Figure 3.16 Self-heating rate versus temperature for 100 mg $Li_{0.81}C_6$ with 2% PVDF (a) or 2% EPDM (b) heated in 100 mg 1.0 M $LiPF_6$ EC/DEC electrolyte.

Figure 3.17 shows the XRD patterns collected after the experiment indicated in Figure 3.16a. Figure 3.17a shows the XRD pattern for the 100 mg of $Li_{0.81}C_6$ sample containing 2% PVDF heated with 1.0 M $LiPF_6$ EC/DEC till 250°C. Figure 3.17b shows the XRD pattern for $Li_{0.81}C_6$ containing 2% PVDF after the ARC run to 350°C. Figure 3.17a shows the Bragg peaks from delithiated MCMB as the majority peak with a small amount of Stage-2 LiC_{12} and Stage-1 LiC_6. Figure 3.17b shows only Bragg peaks for delithiated MCMB and no LiC_6 or LiC_{12}. The lithium content in the samples described by Figure 3.17a and b were calculated to be $x = 0.25$ and $x = 0$, respectively.

At a temperature of about 250°C, $Li_{0.81}C_6$ starts to react with PVDF (Figure 3.5b) but not with EPDM (Figure 3.5a). The self-heating rate versus temperature of $Li_{0.81}C_6$ with 2% PVDF binder (Figure 3.16a) and 2% EPDM binder (Figure 3.16b) as well as the electrolyte are similar above 250°C. This suggests that the SHR signals in Figure 3.16a above 250°C arise mostly from the reaction of $Li_{0.25}C_6$ with $LiPF_6$ EC/DEC electrolyte,

not with PVDF. Du Pasquier *et al.* [115] apparently incorrectly attributed the exothermic peaks in the DSC of $Li_{0.85}C_6$ with $LiPF_6$ EC:DMC (vol:vol = 2:1) electrolyte at above 250°C to the reaction between $Li_{0.85}C_6$ with PVDF. Therefore, the heat (ΔH) of 1220 J g^{-1} for the reaction of $Li_{0.85}C_6$ with PVDF proposed by Du Pasquier *et al.* is probably incorrect.

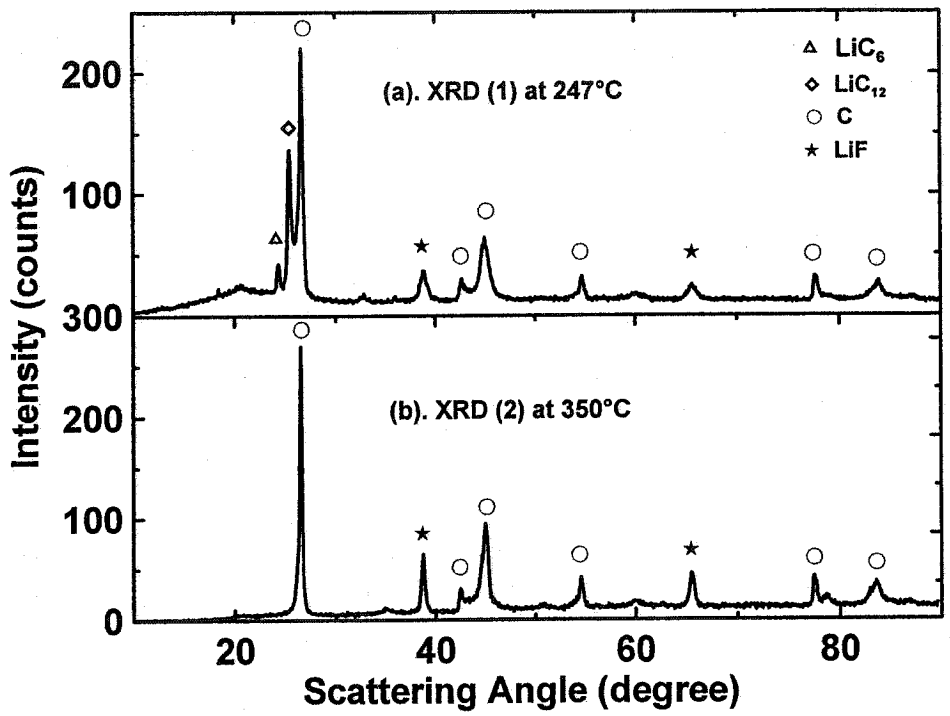

Figure 3.17 XRD patterns of ARC samples stopped at 247°C (a) or 350°C (b) for 100 mg $Li_{0.81}C_6$ reacted with 100 mg 1.0 M $LiPF_6$ EC/DEC electrolyte heated initially to 90°C.

Figure 3.18 shows the self-heating rate of 100 mg $Li_{0.81}C_6$ electrode material containing various amount of PVDF binder from 1% (a), 2% (b), 3.5% (c), 7% (d), to 14% (e) reacting with 100 mg 1.0 M $LiPF_6$ EC/DEC initially heated to 90°C. The shapes of the ARC curves for these samples are similar. This suggests that PVDF plays a minor role in the self-heating of the $Li_{0.81}C_6$ electrode in 1.0 M $LiPF_6$ electrolyte, in contrast to literature reports [115].

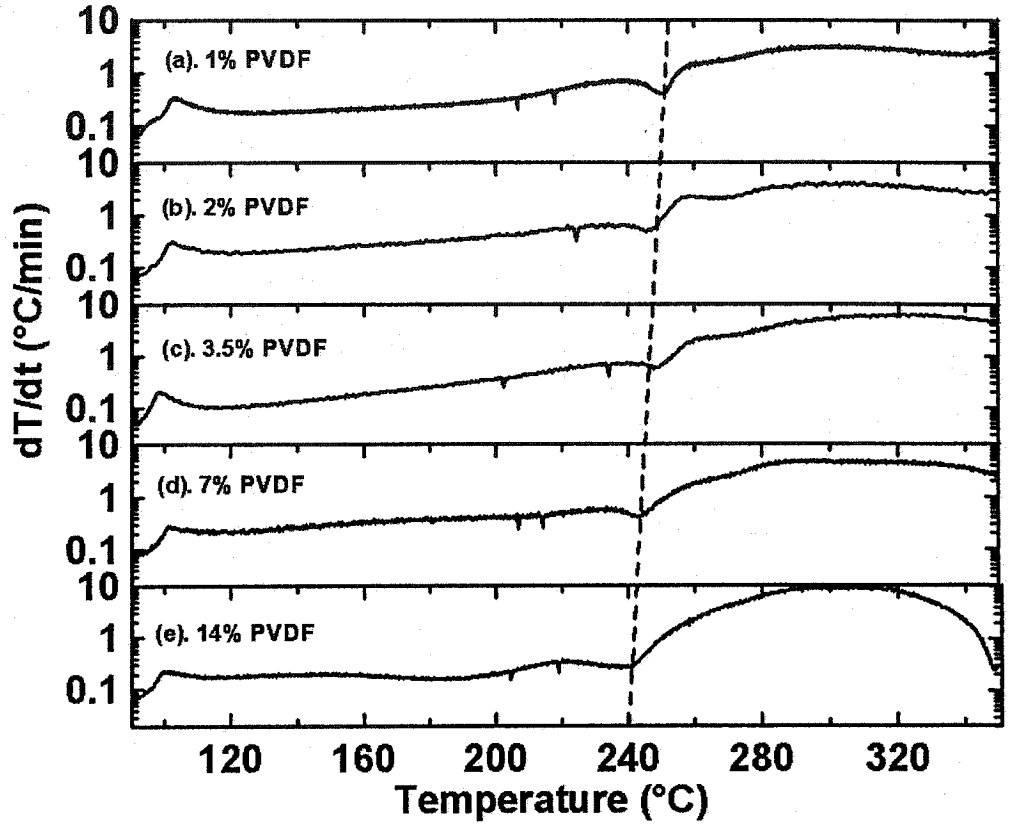

Figure 3.18 Self-heating rate versus temperature for 100 mg of $Li_{0.81}C_6$ containing 1% (a), 2% (b), 3.5% (c), 7% (d), and 14% PVDF (e) heated with 100 mg 1.0 M $LiPF_6$ EC/DEC electrolyte.

3.1.2 $LiCoO_2$

At this time, $LiCoO_2$ is the most successfully commercialized positive electrode material in LIBs and still is extensively used by most LIB manufacturers. The thermal stability of charged $LiCoO_2$ with different particle sizes (approximately 0.8 μm, 2 μm, and 5 μm) was compared using ARC. The thermal reaction sequence between $Li_{0.5}CoO_2$ and EC/DEC was characterized by ARC combined with XRD. Since electrolyte containing the new salt LiBOB shows much higher thermal stability than $LiPF_6$-based electrolyte for $Li_{0.81}C_6$ negative electrode material, the thermal stability of $Li_{0.5}CoO_2$ was studied in both $LiPF_6$ or LiBOB-based electrolytes.

3.1.2.1 SEM images of $LiCoO_2$ with different particle size

Figure 3.19 shows SEM images of the three different types of $LiCoO_2$ used in this study. The particle sizes are approximately 0.8 μm, 2 μm, and 5 μm, respectively. These samples are named $LiCoO_2$ (1), $LiCoO_2$ (2) and $LiCoO_2$ (3), respectively [samples (1) and (2) obtained from FMC Corp. and sample (3) from Moli Energy Ltd.]. The BET surface areas of these samples are 0.71, 0.36, and 0.10 $m^2 g^{-1}$, respectively.

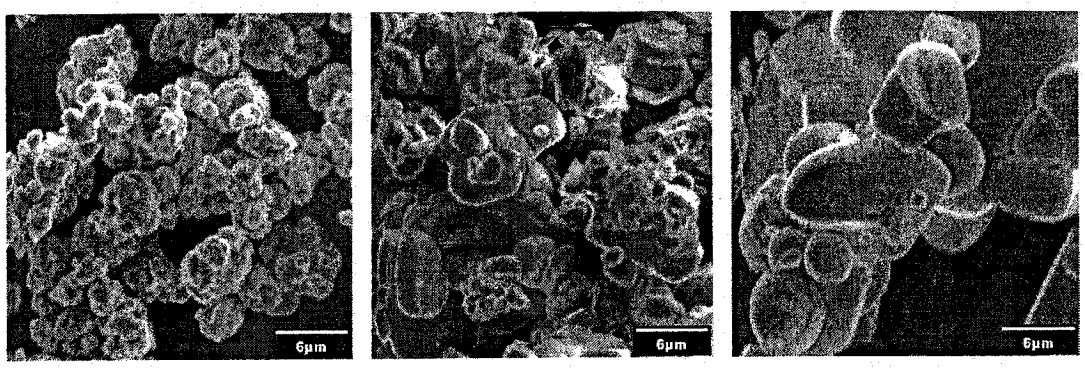

$LiCoO_2$ (1) **$LiCoO_2$ (2)** **$LiCoO_2$ (3)**

Figure 3.19 SEM pictures of three $LiCoO_2$ materials with different particle sizes (diameters of approximately 0.8 μm, 2 μm, and 5 μm, respectively).

3.1.2.2 Binder

Figure 3.20 shows the self-heating rate versus temperature of 200 mg rinsed $Li_{0.5}CoO_2$ with 7% PVDF binder. The mini-exothermic self-heating reactions at 180°C and 280°C are probably due to the reaction of $Li_{0.5}CoO_2$ with a small amount of residual $LiPF_6$ EC/DEC electrolyte soaked into the PVDF binder. The ARC test of $Li_{0.5}CoO_2$ in Figure 3.20 suggests that $Li_{0.5}CoO_2$ does not react significantly with PVDF.

3.1.2.3 Effects of particle size of $LiCoO_2$ on its thermal stability

Figure 3.21 shows the SHR vs. temperature (T) for 100 mg of the three $Li_{0.5}CoO_2$ samples heated in 100 mg of EC/DEC solvent. The ARC measurement of $Li_{0.5}CoO_2$ in panel (a) was stopped at 213°C because of the high possibility that the ARC tube containing the 0.8 μm $Li_{0.5}CoO_2$ would explode at high temperature. Sample $Li_{0.5}CoO_2$ (1) in panel (a) has the lowest onset temperature (110°C) and shows the worst thermal

stability among the three samples. Samples $Li_{0.5}CoO_2$ (2) and $Li_{0.5}CoO_2$ (3) have the same onset temperature of 150°C and show similar self-heating behavior.

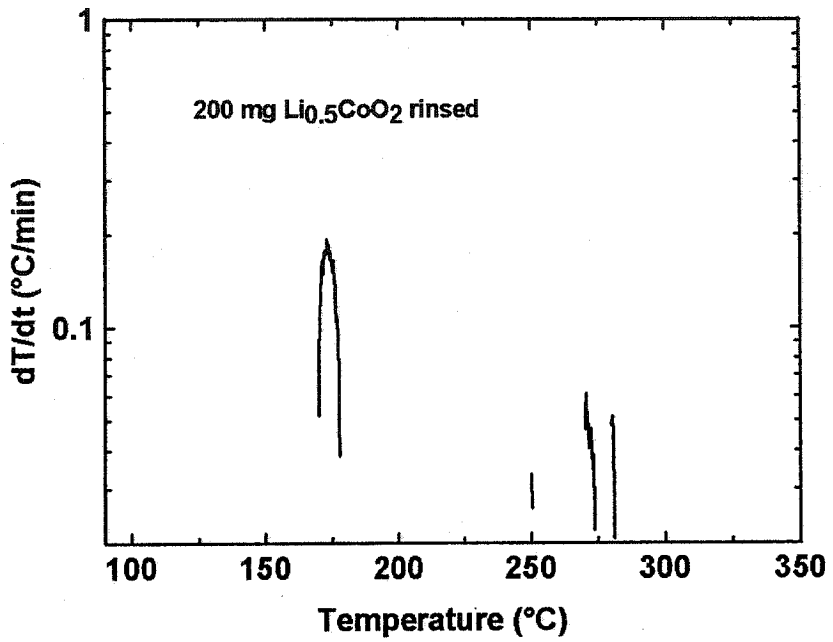

Figure 3.20 Self-heating rate versus temperature of 200 mg rinsed $Li_{0.5}CoO_2$ heated initially to 90°C.

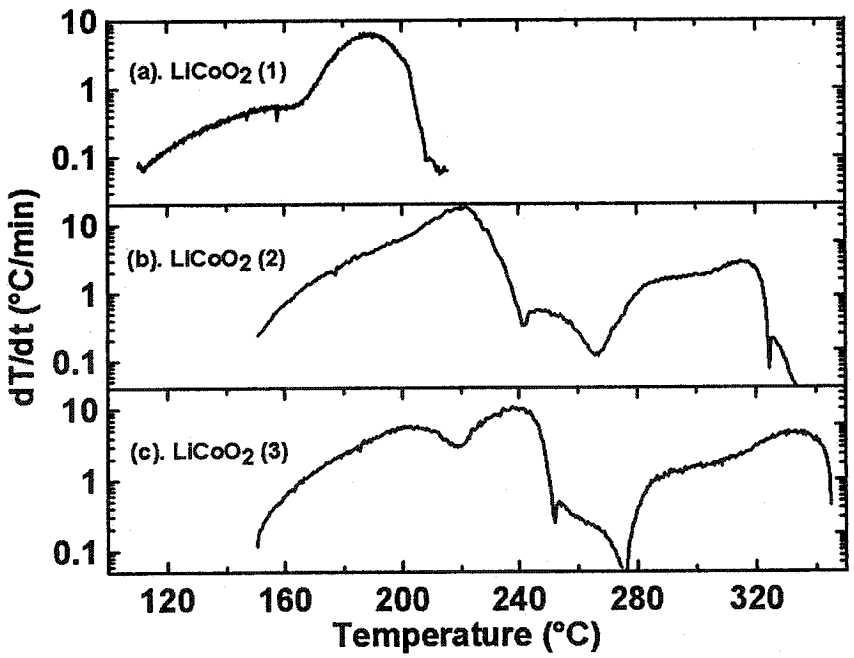

Figure 3.21 Self-heating rate versus temperature for the three $Li_{0.5}CoO_2$ samples reacting with EC/DEC solvent heated initially to 110°C.

Figure 3.22 shows the self-heating rate vs. temperature for 100 mg of the three $Li_{0.5}CoO_2$ samples heated with the same mass of 1.0 M $LiPF_6$ EC/DEC electrolyte. The samples were first heated to 110°C in the ARC before a search for exothermic behavior began. Again, $Li_{0.5}CoO_2$ sample (1), with a particle size of approximately 0.8 μm, shows the worst thermal stability with $LiPF_6$ EC/DEC electrolyte. In the temperature range between 170 and 210°C, the self-heating rate for $Li_{0.5}CoO_2$ sample (2) is about double that of $Li_{0.5}CoO_2$ (3), presumably because of its smaller particle size.

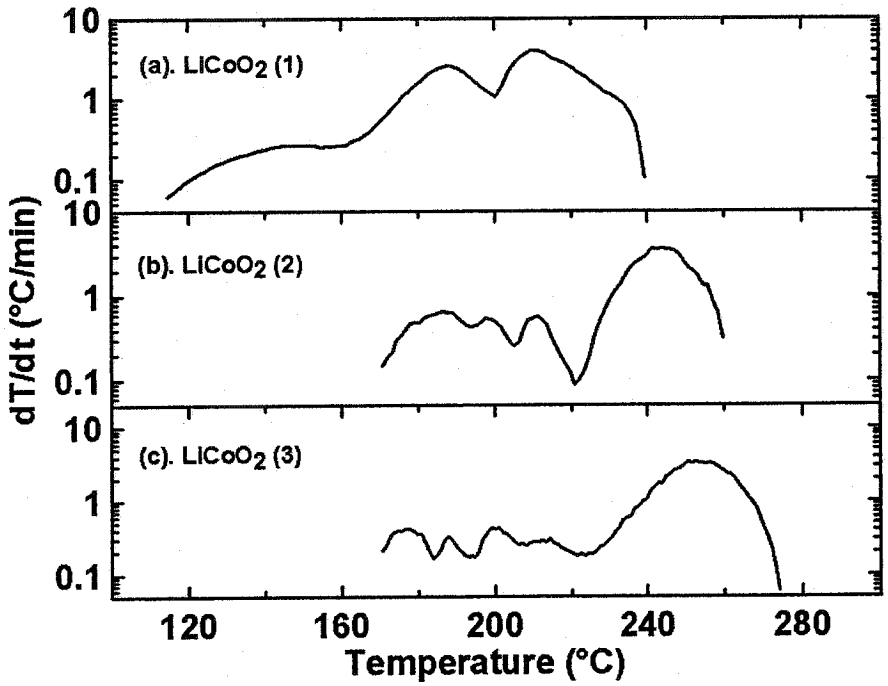

Figure 3.22 Self-heating rate versus temperature for the three $Li_{0.5}CoO_2$ samples with 1.0 M $LiPF_6$ EC/DEC heated initially to 110°C.

3.1.2.4 Changes to the mass ratio of charged $Li_{0.5}CoO_2$ and EC/DEC solvent.

Typically approximately 100 mg $Li_{0.5}CoO_2$ mixed with 100 mg EC/DEC solvent or electrolyte was used in the ARC experiments. The maximum amount of oxygen released from the decomposition of 100 mg $Li_{0.5}CoO_2$ is about 0.1/(2×94.5) mole when $Li_{0.5}CoO_2$ is completely reduced to Co metal by the following reaction [84, 86]:

$$2\ Li_{0.5}CoO_2 \rightarrow LiCoO_2 + Co + O_2. \qquad [3\text{-}8]$$

100 mg EC ($C_5H_{10}O_3$) or 100 mg DEC ($C_3H_4O_3$) can consume at most 0.1×6/118 mole or 0.1×2.5/88 mole of O_2, respectively, at high temperature. The combustion reactions are as follows:

$$2\ C_5H_{10}O_3 + 12\ O_2 \rightarrow 10\ CO_2 + 10\ H_2O \text{ and} \qquad [3\text{-}9]$$

$$2\ C_3H_4O_3 + 5\ O_2 \rightarrow 6\ CO_2 + 4\ H_2O. \qquad [3\text{-}10]$$

By comparing the amount of oxygen released from 100 mg of $Li_{0.5}CoO_2$ and that needed to react with 100 mg of EC or DEC, there is excess EC/DEC solvent compared to that needed to reduce $Li_{0.5}CoO_2$ to Co metal in the ARC experiments. When the mass of $Li_{0.5}CoO_2$ is maintained at 100 mg and the amount of EC/DEC solvent increases from 100 mg, 150 mg, to 200 mg, the total heat released from the combustion reactions, *h*, should be the same, because the amount of $Li_{0.5}CoO_2$ (the source of oxygen) does not change. Therefore, an increase in the amount of solvent should reduce the temperature rise, ΔT, of the reaction process. The temperature rise for a single reaction process is given by

$$\Delta T = h/C_{Tot}, \qquad [3\text{-}11]$$

where C_{Tot} is the total heat capacity of the entire sample (electrode material, solvent, plus stainless steel ARC tube). The total heat capacity for the ARC sample is

$$C_{Tot} = \sum_i c_i m_i = 1.0\frac{J}{gK} m_{cat} + 0.46\frac{J}{gK} 0.93g + 1.5\frac{J}{gK} m_{sol}, \qquad [3\text{-}12]$$

where m_{cat} is the mass of cathode in grams in the ARC tube, and m_{sol} is the mass of solvent or electrolyte in grams in the ARC tube, and 0.93 g is the mass of the stainless steel ARC tube. A specific heat of 1.0 J K^{-1} g^{-1} was used for $Li_{0.5}CoO_2$ [119-121], 1.5 J K^{-1} g^{-1} for EC/DEC solvent [117], and 0.46 J K^{-1} g^{-1} for stainless steel [114].

Figure 3.23 shows the self-heating rate vs. temperature for 100 mg $Li_{0.5}CoO_2$ (1) with 100 mg (a), 150 mg (b), and 200 mg EC/DEC solvent (c) initially heated to 110°C. The temperature rises, ΔT_{11} for 100 mg EC/DEC, ΔT_{12} for 150 mg EC/DEC, and ΔT_{13} for 200 mg EC/DEC, are 103 K, 92 K, and 78 K, respectively as indicated in Figure 3.23. The total heat capacities for the three ARC samples are approximately 0.68 J K^{-1}, 0.75 J

K^{-1} and 0.83 J K^{-1}, respectively. The total heats for these three ARC runs are given by equation [3-11] and turn out to be close, 70 J, 69 J, and 65 J, respectively.

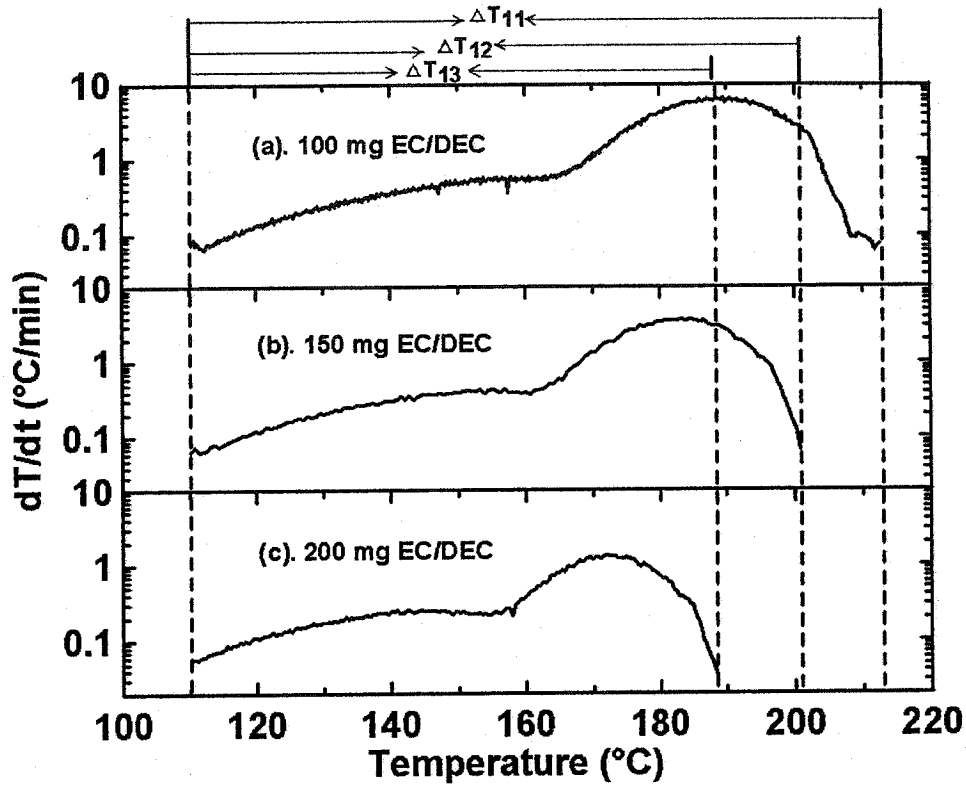

Figure 3.23 Self-heating rate versus temperature for 100 mg of $Li_{0.5}CoO_2$ (1) in 100 mg (a), 150 mg (b), or 200 mg EC/DEC solvent (c) heated initially to 110°C

Figure 3.24 shows the self-heating rate versus temperature for 100 mg $Li_{0.5}CoO_2$ (3) with different amounts of EC/DEC solvent initially heated to 110°C. The onset temperatures for all three ARC runs are 150°C. The temperature rises for the first two exothermic processes decrease from about approximately 103°C to 93°C to 81°C when the mass of EC/DEC solvent used increases from 100 mg (a), to 150 mg (b), to 200 mg (c). These results are very close to the results shown in Figure 3.23.

In order to identify the reaction process between $Li_{0.5}CoO_2$ and EC/DEC, another ARC experiment as shown in Figure 3.24a was performed and stopped at approximately 253°C at which point the first two reaction processes had finished. Then, this sample and the sample that had self-heated to 350°C were recovered and their XRD patterns were taken. Figure 3.25a shows that the main products from the reaction between $Li_{0.5}CoO_2$

and EC/DEC solvent for the reaction stopped at 253°C are $LiCoO_2$ and CoO. This result is in agreement with MacNeil and Dahn's [84] ARC studies, which indicated that the first two peaks in the self-heating rate versus temperature response are from combustion of solvent with oxygen from the reduction of $Li_{0.5}CoO_2$ to Co_3O_4 and then to CoO at elevated temperature. The reactions are (EC for example):

$$30Li_{0.5}CoO_2 + 2C_3H_4O_3 \rightarrow 15LiCoO_2 + 5Co_3O_4 + 6CO_2 + 4H_2O, \quad [3\text{-}13]$$

$$10Co_3O_4 + 2C_3H_4O_3 \rightarrow 30CoO + 6CO_2 + 4H_2O. \quad [3\text{-}14]$$

With the presence of sufficient reducing agent, EC/DEC solvent, the CoO can then be reduced to Co metal as shown in Figure 3.24b. The reaction is:

$$10CoO + 2C_3H_4O_3 \rightarrow 10Co + 6CO_2 + 4H_2O. \quad [3\text{-}15]$$

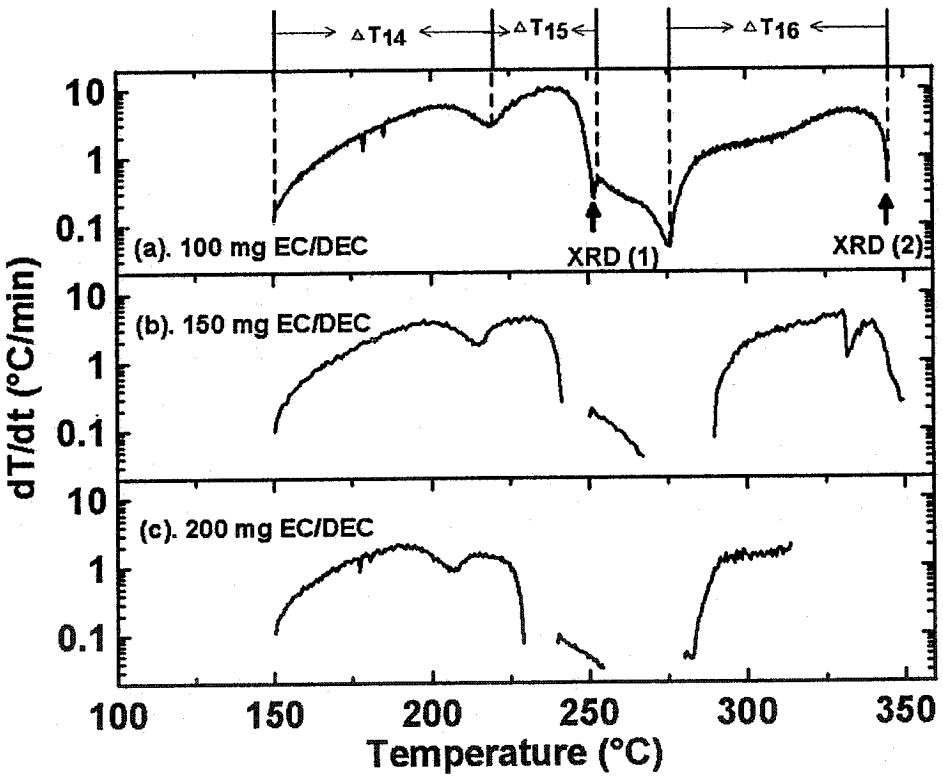

Figure 3.24 Self-heating rate versus temperature for 100 mg $Li_{0.5}CoO_2$ (3) in 100 mg (a), 150 mg (b), or 200 mg EC/DEC solvent (c) heated initially to 110°C.

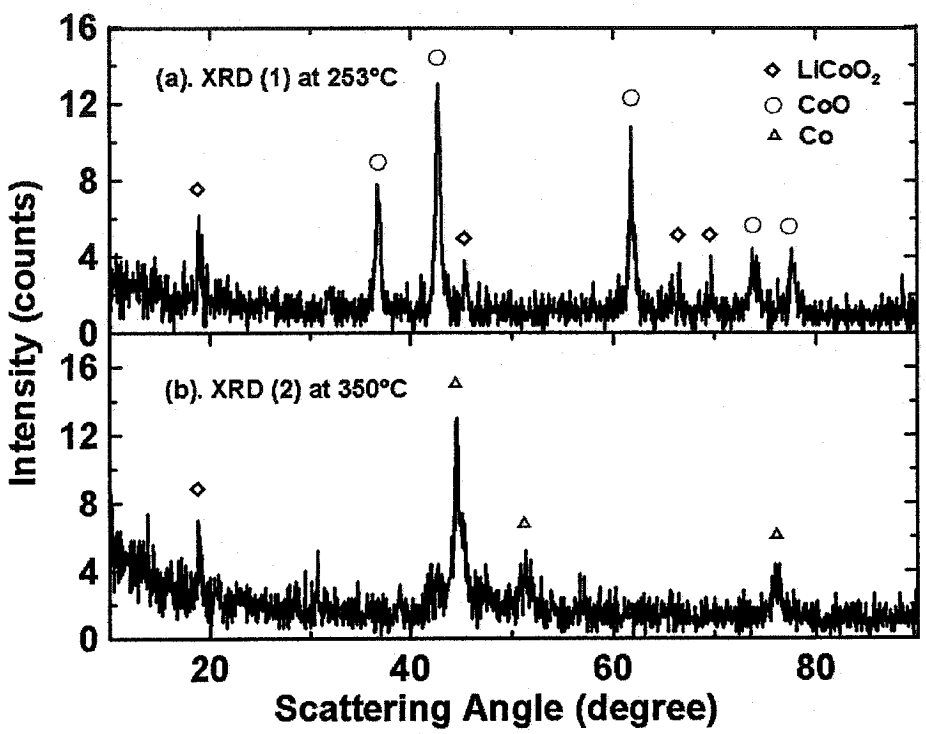

Figure 3.25 XRDs of ARC samples stopped at 253°C or 350°C for 100 mg $Li_{0.5}CoO_2$ (3) reacted with 100 mg EC/DEC solvent heated initially to 110°C.

The temperature increases, ΔT_{14}, ΔT_{15}, and ΔT_{16}, for the three reaction processes described by equations [3-13], [3-14], and [3-15] are approximately 69 K, 34 K, and 68 K, respectively, as shown in Figure 3.24a. The heat capacity of the ARC sample tube containing 100 mg $Li_{0.5}CoO_2$ cathode material, 100 mg EC/DEC, and 930 mg stainless steel is about 0.68 J K^{-1}, as mentioned before. The XRD result in Figure 3.25 suggests that there is excess solvent in this ARC tube because Co metal is formed at 350°C. Therefore, the heats released in these three reaction processes are about 0.68 × 69 J, 0.68 × 34 J, and 0.68 × 68 J, respectively. The amount of active $Li_{0.5}CoO_2$ in 100 mg of electrode material is 100 × (1.00-0.14) mg, to account for the presence of binder (7% by weight) and carbon black (7% by weight). Therefore, the exothermic heats based on the cathode weight for the three processes are approximately 550 J g^{-1}, 270 J g^{-1}, and 540 J g^{-1}, respectively. The total heat released from the three steps together (from $Li_{0.5}CoO_2$ to Co metal) is calculated to be 1360 J g^{-1} of $Li_{0.5}CoO_2$, 142 kJ mol^{-1} of $Li_{0.5}CoO_2$ or 284 kJ

mol^{-1} of O_2 combusted. This value is pretty close to MacNeil and Dahn's result who obtained 1160±450 J g^{-1} of $Li_{0.5}CoO_2$ [84]. Yamaki et al. [5] obtained the exothermic heat of reduction of $Li_{0.5}CoO_2$ in 1.0 M $LiPF_6$ EC/DEC electrolyte and found 1000±250 J g^{-1}, by DSC. It is not clear whether this result corresponds only to reactions [3-13] and [3-14] above, or to all of the reactions from [3-13] to [3-15]. Nevertheless, it is close to the results shown above for either case.

3.1.2.5 Effects of salts on the thermal stability of $Li_{0.5}CoO_2$

Figure 3.26 shows the self-heating rate versus temperature of $Li_{0.5}CoO_2$ (1) in EC/DEC solvent or in the electrolytes, 1.0 M $LiPF_6$ EC/DEC or 0.8 M LiBOB EC/DEC. In the low temperature range from approximately 110°C to 160°C, the addition of $LiPF_6$ salt decreases the reactivity of $Li_{0.5}CoO_2$ compared to EC/DEC solvent only. This suppression of reactivity is caused by the polymerization of ethylene carbonate solvent by HF from the decomposition of $LiPF_6$ on the surface of $Li_{0.5}CoO_2$, which improves the stability of $Li_{0.5}CoO_2$ at elevated temperature [84, 86]. There is no corresponding suppression in the case of LiBOB EC/DEC. This result is perhaps a consequence of the high stability of LiBOB in this temperature range.

Figure 3.27 shows the self-heating rate versus temperature for $Li_{0.5}CoO_2$ (3) in EC/DEC solvent or in EC/DEC containing the different salts, $LiPF_6$ and LiBOB, heated to 110°C. The reactivity of $Li_{0.5}CoO_2$ (3) with EC/DEC is observed to be inhibited by the addition of salt $LiPF_6$ at elevated temperature, which is in agreement with reference [60]. LiBOB EC/DEC exhibits worse stability with $Li_{0.5}CoO_2$ than $LiPF_6$ EC/DEC, or even EC/DEC only. This result is demonstrated by the lowest detectable onset temperature of 120°C for $Li_{0.5}CoO_2$ reacting with LiBOB EC/DEC.

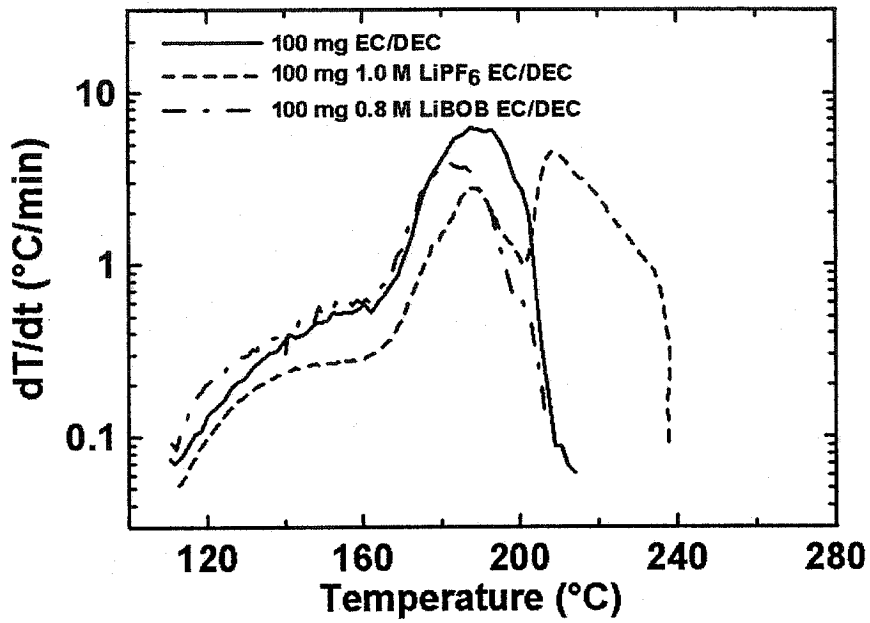

Figure 3.26 Self-heating rate versus temperature for 100 mg of $Li_{0.5}CoO_2$ (1) reacting with the same amount of EC/DEC, 1.0 M $LiPF_6$ EC/DEC or 0.8 M LiBOB EC/DEC heated initially to 110°C.

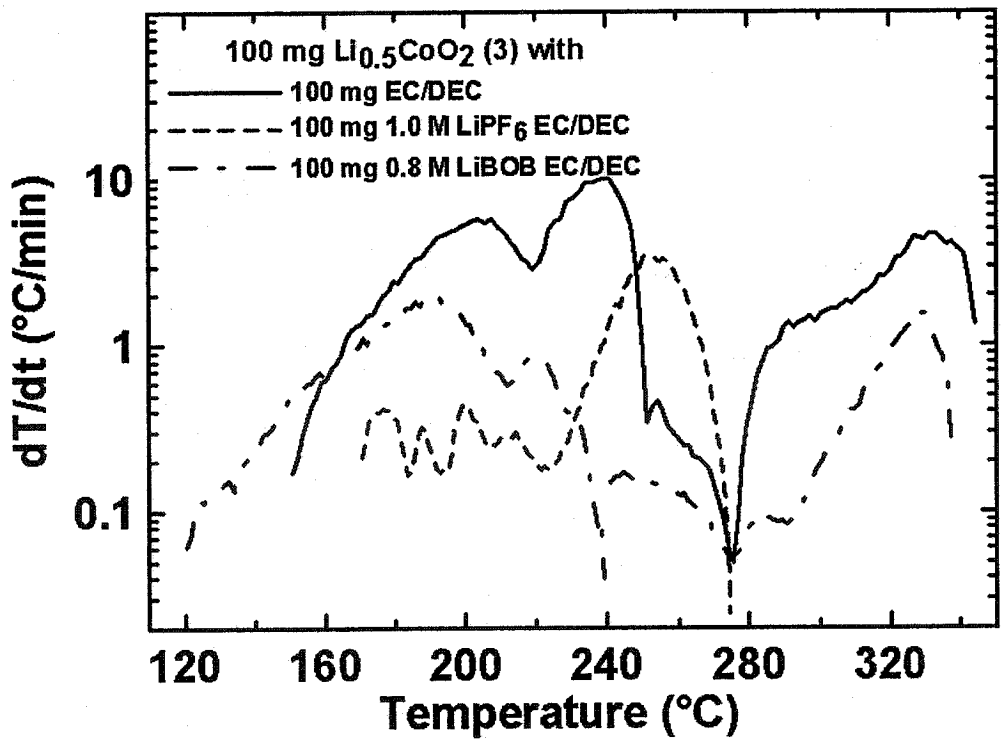

Figure 3.27 Self-heating rate versus temperature for 100 mg of $Li_{0.5}CoO_2$ (3) in 100 mg of EC/DEC or EC/DEC containing the salts, $LiPF_6$ and LiBOB, heated initially to 110°C.

Figure 3.28 compares the self-heating rate versus temperature of $Li_{0.5}CoO_2$ (3) in the electrolytes, $LiPF_6$ EC/DEC and LiBOB EC/DEC, or in EC/DEC solvent. These experiments were made by first heating the sample initially to a higher temperature of 150°C. The exotherm for the sample with LiBOB EC/DEC electrolyte is well underway at 150°C since the initial self-heating rate is approximately 0.7°C/min. For the sample with EC/DEC solvent, the self-heating rate is only 0.07°C/min at 150°C. Therefore, it is concluded that $Li_{0.5}CoO_2$ has lower stability in LiBOB EC/DEC than in $LiPF_6$ EC/DEC or in EC/DEC solvent, whether forced to 110°C or to a higher temperature of 150°C.

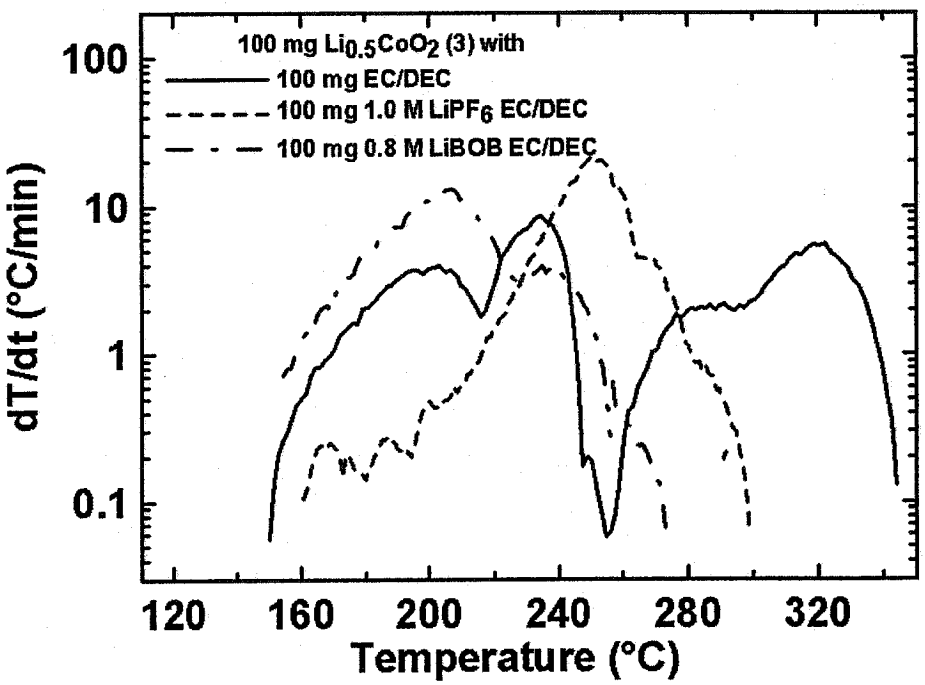

Figure 3.28 Self-heating rate versus temperature for 100 mg of $LiCoO_2$ (3) in the same amount of EC/DEC or EC/DEC containing the salts, $LiPF_6$ and LiBOB, heated initially to 150°C.

3.1.3 Prediction of oven test behavior of full cells (graphite/$LiCoO_2$) based on ARC results on $Li_{0.81}C_6$ and $Li_{0.5}CoO_2$

The thermal stabilities of charged MCMB ($Li_{0.81}C_6$) and $LiCoO_2$ ($Li_{0.5}CoO_2$) in $LiPF_6$ and LiBOB based electrolytes, were compared in this chapter using ARC. For the $Li_{0.81}C_6$ negative electrode material, LiBOB EC/DEC shows much higher thermal stability than $LiPF_6$ based electrolyte, with no significant thermal reaction between

$Li_{0.81}C_6$ and LiBOB EC/DEC electrolyte until 170°C compared to a 90°C ARC onset temperature in $LiPF_6$ EC/DEC (Figure 3.10). For $Li_{0.5}CoO_2$ [sample (3), 5μm size] positive electrode material, however, LiBOB EC/DEC shows a lower ARC onset temperature of 120°C compared with a 170°C onset temperature in $LiPF_6$ based electrolyte (Figure 3.26).

From the ARC studies, the following predictions are made about the oven test behavior of graphite/$LiPF_6$ or LiBOB EC:DEC/$LiCoO_2$ 18650-size cells, charged to 4.2 V (where $Li_{0.81}C_6$ and $Li_{0.5}CoO_2$ are obtained):

(1). In an oven with a constant T (130°C ~ 150°C), an 18650 cell with $LiPF_6$ EC/DEC electrolyte will release a significant amount of heat in the low temperature range (90°C to 120°C) from the thermal reaction between $Li_{0.81}C_6$ with $LiPF_6$ based electrolyte. An 18650 cell with LiBOB based electrolyte, however, will not show any significant exotherm over this temperature range because there are no exotherms from the reactions between both $Li_{0.81}C_6$ and $Li_{0.5}CoO_2$ electrodes and LiBOB EC/DEC below 120°C.

(2). At high temperature (T≥130°C), an 18650 cell with LiBOB based electrolyte will show higher thermal reactivity than a cell with $LiPF_6$ EC/DEC because LiBOB EC/DEC is much more thermally reactive than $LiPF_6$ EC/DEC for the $Li_{0.5}CoO_2$ electrode.

The oven test results obtained on 18650 cells with $LiPF_6$ or LiBOB based electrolytes are shown in Section 3.2.

3.2 Oven tests on Lithium-ion cells (graphite/$LiCoO_2$)

A number of 18650-size cells were obtained from E-One/Moli Energy Ltd. (Canada). The negative and positive electrode materials were MCMB (20 μm particle size) and $LiCoO_2$ (5 μm), respectively, the same materials used in the ARC measurements in Section 3.1. Four different electrolytes were adopted in these cells, 1.0 M $LiPF_6$ EC/DEC, 0.6 M LiBOB EC/DEC and two mixed electrolytes, 0.3 M LiBOB + 0.5 M $LiPF_6$ EC/DEC and 0.2 M LiBOB + 0.67 M $LiPF_6$ EC/DEC. Before oven testing, the cells were charged to 4.2 V using a low charging rate of C/100. Two different oven temperatures were chosen, 140°C and 130°C.

3.2.1 140°C oven test

Figure 3.29 shows temperature versus time profiles for MCMB/$LiCoO_2$ 18650 cells (4.2 V) containing 1.0 M $LiPF_6$ EC/DEC and 0.6 M LiBOB EC/DEC placed into a 140°C oven. There are two data sets shown for each situation, which demonstrate the excellent repeatability of the test. Figure 3.29 shows that the cells with LiBOB electrolyte (dashed line) heat more slowly to the oven temperature than do the cells with $LiPF_6$ electrolyte (solid line), but then the former go into thermal runaway. In the low temperature region (below 130°C), the heat production is dominated by the negative electrode/electrolyte reaction and the LiBOB cells show less heat production, as expected from the ARC results. In the high temperature region (above 130°C) the positive electrode/electrolyte reaction becomes important (as shown by Figure 3.29) and the LiBOB cells show larger heat production that leads to thermal runaway.

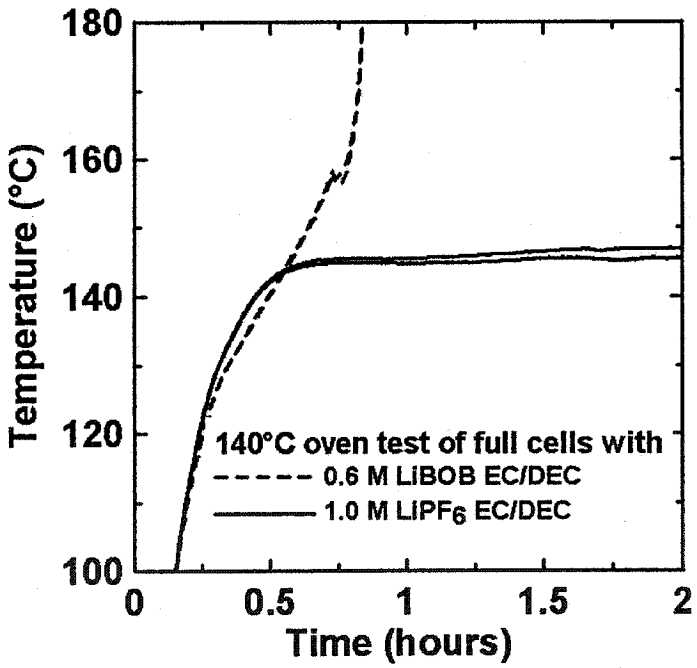

Figure 3.29 Temperature vs. time for 18650 Li-ion cells (4.2 V) in the 140°C oven test. Data for four cells are shown, two with 1.0 M $LiPF_6$ EC/DEC electrolyte and two with 0.6 M LiBOB EC/DEC electrolyte.

The impact of the positive and negative electrode reactions can be better separated if the oven test result is plotted as dT/dt versus T. Based on Newton's law of cooling

[122, 123], for a sample at temperature T, without internal heat generation, placed in an oven at temperature, T_o, it is expected that

$$dT/dt = \delta f (T_o - T), \qquad [3\text{-}16]$$

where f is the surface heat transfer coefficient and δ is a constant. δ is related to the mass, surface area, and specific heat capacity of the 18650-size cell. This assumes a uniform temperature within the sample placed in the oven, which implies a high thermal conductivity of the sample. Figure 3.30 shows experimental results for dT/dt versus T for a solid stainless steel cylinder machined to be the same size as an 18650 cell, placed in a 140°C oven. dT/dt decreases linearly to zero at the oven temperature as expected based on equation [3-16]. By contrast, if there were heat production within the cylinder, then equation [3-16] would not be perfectly obeyed.

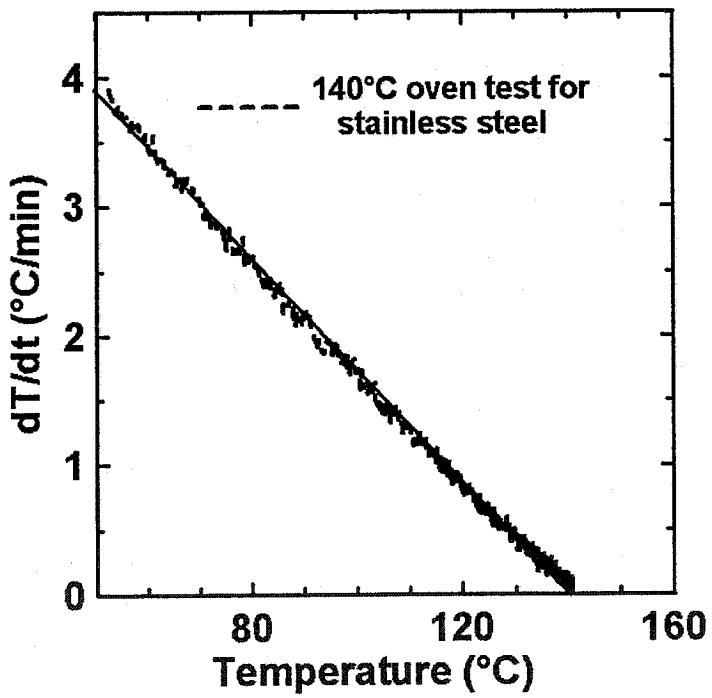

Figure 3.30 Heating rate, dT/dt vs. temperature, T, for a stainless steel cylinder placed in a 140°C oven to demonstrate the validity of Newton's law.

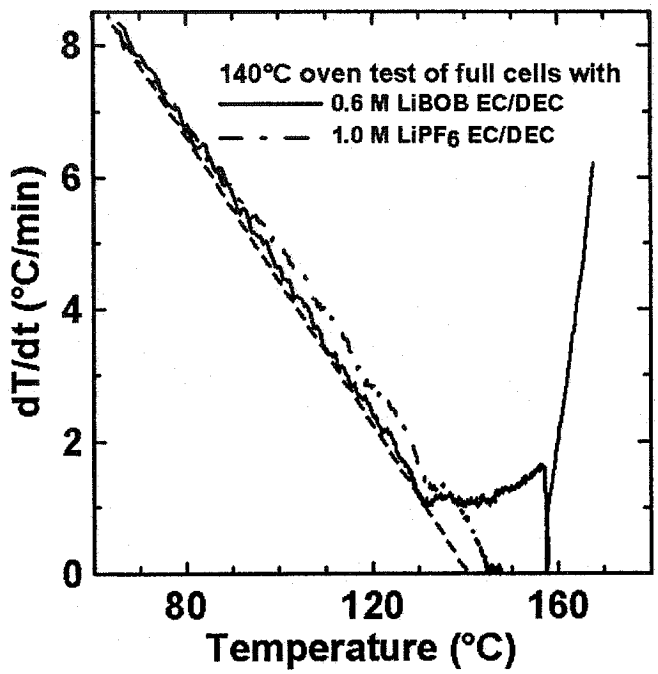

Figure 3.31 The data of Figure 3.29 replotted as dT/dt vs. T. The dashed line indicates a cell with no internally generated heat.

Figure 3.31 shows the data in Figure 3.29 replotted as dT/dt versus T for the 18650 cells containing LiBOB and $LiPF_6$ electrolytes. The straight short-dashed line in Figure 3.31 was drawn from the data near 70°C, where no heat production is occurring based on ARC measurements, to the oven temperature and represents the path these cells would follow if there were no internal heat generation at all. By comparing the data sets to this line, one can easily observe:

(1). The cell containing $LiPF_6$ electrolyte generates heat between about 80 and 120°C because the self-heating rate is larger than that expected based on Newton's law. This is due to the negative electrode/electrolyte reaction as clearly shown in Figure 3.15. This observation is in good agreement with the prediction (1) in Section 3.1.3;

(2). The cell containing LiBOB electrolyte generates almost no heat between 80 and 120°C because the self-heating rate matches that of Newton's law. This is expected based on the lack of negative electrode/electrolyte reactivity (Figure 3.15) and positive electrode/electrolyte reactivity (Figure 3.27) in this temperature range, which agrees well with prediction (1) in Section 3.1.3;

(3). The cell containing LiBOB electrolyte generates substantial heat above 130°C and this is exactly where the positive electrode/electrolyte reaction begins powerfully as shown in Figure 3.27. This proves prediction (2) described in Section 3.1.3.

It is very clear that the oven test results of the 18650 cells are qualitatively predicted from the thermal stability measurements of single electrode materials, $Li_{0.81}C_6$ or $Li_{0.5}CoO_2$, with electrolytes using ARC. This clearly shows that ARC is an excellent technique to study the thermal stability of electrode materials used in LIBs.

ARC results in Section 3.1.1.3 showed that LiBOB electrolyte presents higher thermal stability than $LiPF_6$ electrolyte for $Li_{0.81}C_6$ but lower thermal stability for $Li_{0.5}CoO_2$. We then consider whether there are possible advantages to adding a small amounts of LiBOB into $LiPF_6$ EC/DEC, a mixed electrolyte, from a safety standpoint. Figure 3.15 compares the SHR vs. T for $Li_{0.81}C_6$ reacting with EC/DEC based electrolytes containing 1.0 M $LiPF_6$, 0.75 M $LiPF_6$ + 0.2 M LiBOB, 0.5 M $LiPF_6$ + 0.4 M LiBOB and 0.8 M LiBOB as measured using the ARC. The addition of LiBOB clearly and dramatically slows the reactivity of the negative electrode in the 80 - 170°C temperature range.

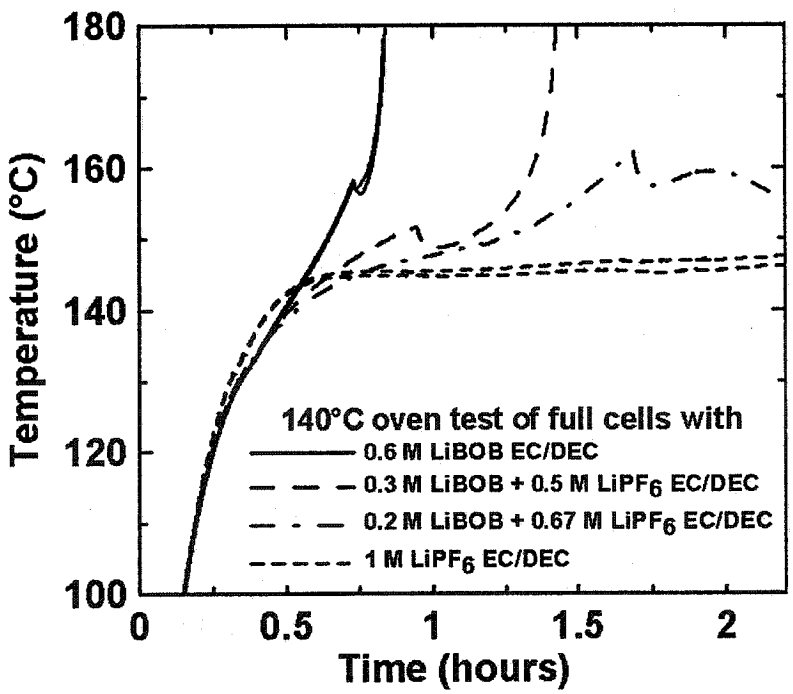

Figure 3.32 Temperature vs. time for 18650 Li-ion cells (4.2 V) in the 140°C oven test. Data for six cells are shown, with the electrolytes indicated in the legend.

Figure 3.32 shows oven exposure tests (140°C) for 18650 cells (4.2 V) with 0.6 M LiBOB EC/DEC, 1.0 M $LiPF_6$ EC/DEC, or mixed electrolytes, 0.3 M LiBOB + 0.5 M $LiPF_6$ EC/DEC and 0.2 M LiBOB + 0.67 M $LiPF_6$ EC/DEC as indicated. As expected, the addition of LiBOB slows the heating rate below the oven temperature due to a decrease in negative electrode/electrolyte reactivity. However, as the LiBOB concentration increases from 0.2, 0.3, to 0.6 M in $LiPF_6$ EC/DEC, the cell temperature increases faster at high temperatures (T >140°C) due to an increase in the thermal reactivity between the $Li_{0.5}CoO_2$ electrode and LiBOB based electrolyte.

3.2.2 130°C oven test

Figure 3.33 shows oven exposure tests (130°C) for 18650 cells (4.2 V) containing 0.6 M LiBOB EC/DEC, 1.0 M $LiPF_6$ EC/DEC, or mixed electrolyte, 0.3 M LiBOB + 0.5 M $LiPF_6$ EC/DEC and 0.2 M LiBOB + 0.67 M $LiPF_6$ EC/DEC. Figure 3.34 shows plots of dT/dt vs. T for the oven test results of the cells with LiBOB and $LiPF_6$ based electrolyte shown in Figure 3.33. The results in Figure 3.33 and 3.34 mirror those in Figure 3.32 and 3.31, respectively. That is, the LiBOB cell generated very little heat below 130°C due to the low rate of the negative electrode/electrolyte reactions and the $LiPF_6$ cell shows heat generation in the 80 - 130°C range due to the negative electrode/electrolyte reactions. The LiBOB cell shows substantial heat generation above 130°C due to the onset of the positive electrode/electrolyte reactions. These results clearly prove the predictions based on ARC studies of $Li_{0.81}C_6$ and $Li_{0.2}CoO_2$ in $LiPF_6$ or LiBOB based electrolytes.

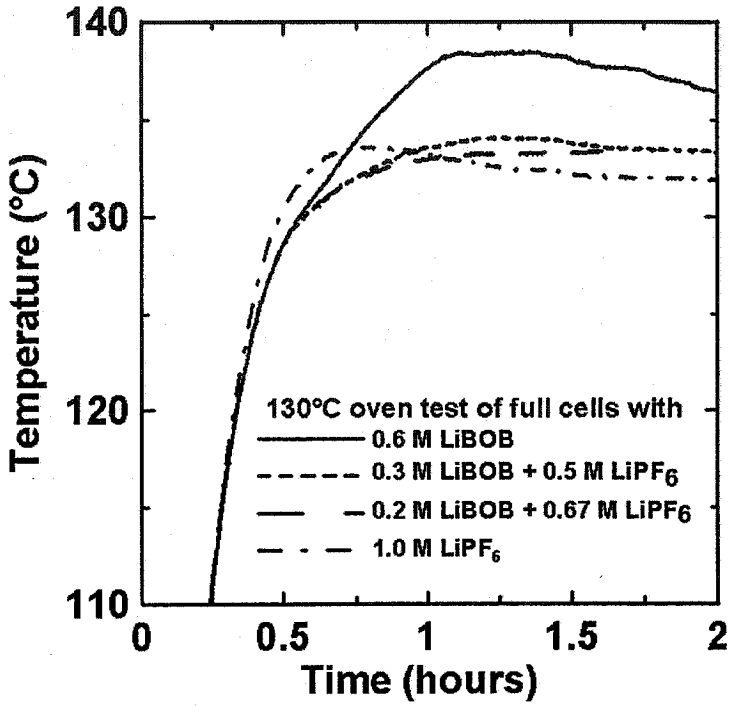

Figure 3.33 Temperature vs. time for 18650 cells (4.2 V) in the 130°C oven test.

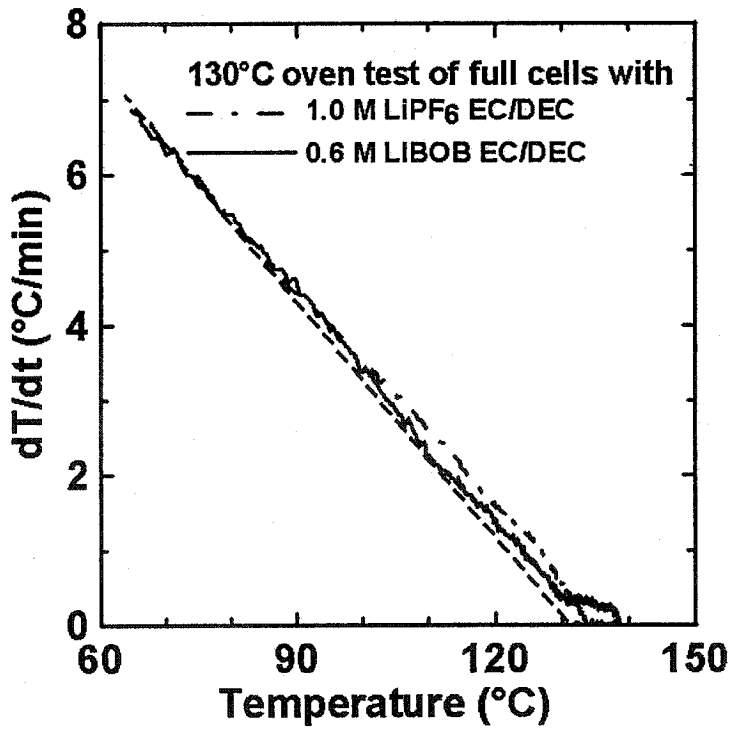

Figure 3.34 The data of Figure 3.33 replotted as dT/dt vs. T. The dashed line indicates a cell with no internally generated heat.

The oven test results for 18650 Li-ion cells clearly show that ARC measurements of the thermal stability of single electrode materials can be used to successfully qualitatively understand the oven test behavior of full size lithium-ion cells. This gives us confidence to use the ARC technique to study the thermal stability of different negative and positive electrodes. The results will be reported from Chapter 4 to Chapter 6.

Chapter 4 Thermal stability studies on negative electrode materials with different lithium binding energies

The thermal stability of three different negative electrode materials with different lithium binding energies was compared using ARC. The lithium binding energies for $Li_{0.81}C_6$, $Li_7Ti_5O_{12}$ [124, 125], and $Li_{0.5}VO_2$ (B) [126, 127] are 0.1 eV, 1.55 eV, and 2.45 eV versus lithium metal, respectively, as shown in Figure 4.1. ARC combined with XRD was used to explore the reaction mechanism of these negative electrode materials in EC/DEC solvent or in different electrolytes and study the impact of changes to the lithium binding energy on thermal stability. The reactions between $Li_{0.81}C_6$ and solvents or electrolytes were shown in Chapter 3. This chapter reports the ARC studies of $Li_7Ti_5O_{12}$ and $Li_{0.5}VO_2$ (B). The thermal stability of $Li_{0.81}C_6$, $Li_7Ti_5O_{12}$, and $Li_{0.5}VO_2$ (B) is compared.

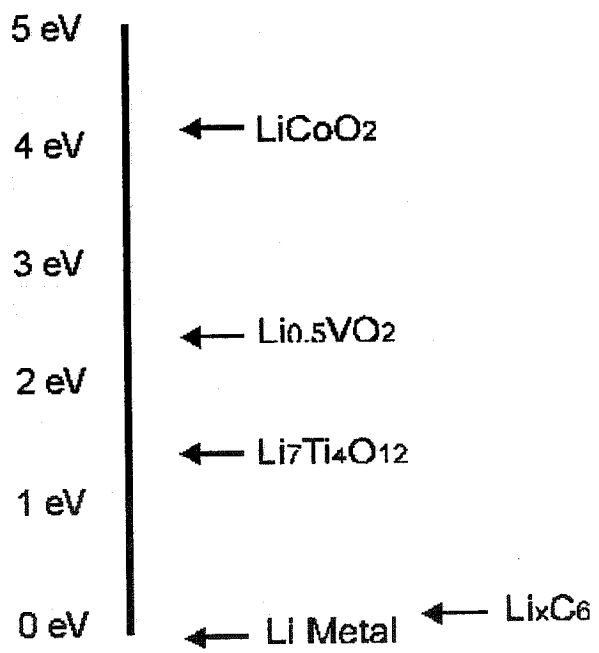

Figure 4.1 Binding energies of lithium atoms in various lithium compounds versus lithium metal.

Figure 4.2 shows the potential (V) versus specific capacity (mA h g^{-1}) for Li/VO_2 (B), $Li_4Ti_5O_{12}$, or MCMB coin cells during the first cycle. Figure 4.2a was obtained from

reference [126], where $LiPF_6$ PC/EC (1:1 by volume) was used as electrolyte. The discharge occurs at approximately 0.1 V, 1.55 V, and 2.5 V vs. Li for MCMB, $Li_4Ti_5O_{12}$, and VO_2 (B) electrodes, respectively. At the end of the discharge process, fully lithiated $Li_{0.81}C_6$, $Li_7Ti_5O_{12}$, and $Li_{0.5}VO_2$ phases are formed.

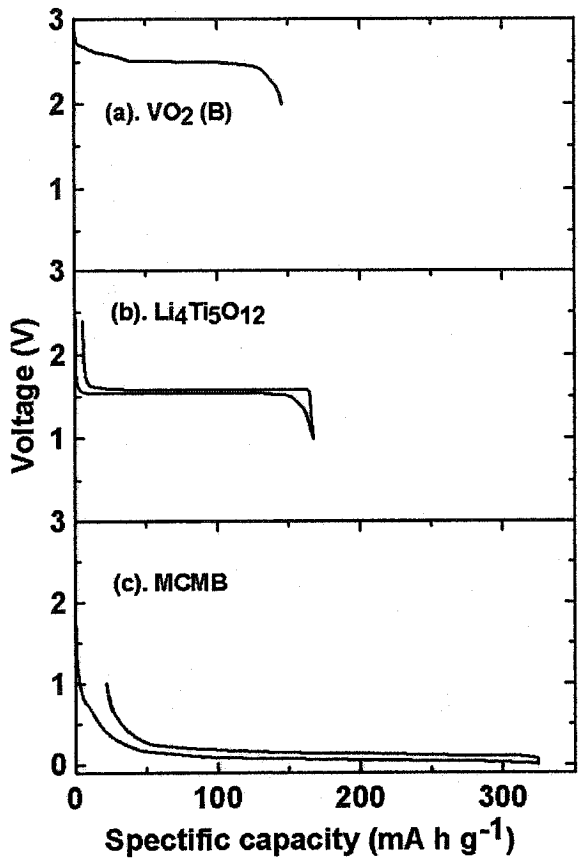

Figure 4.2 The potential (V) versus specific capacity (mA h g^{-1}) for Li/VO_2 (B), Li/$Li_4Ti_5O_{12}$, and Li/MCMB coin cells during the first cycle.

4.1 $Li_7Ti_5O_{12}$

$Li_4Ti_5O_{12}$ is called a "zero-strain insertion material" because its lattice constants do not change appreciably during insertion of lithium at 1.55 V vs. Li. The reaction is

$$1/3\ Li_4Ti_5O_{12} + Li^+ + e^- \rightarrow 1/3\ Li_7Ti_5O_{12}. \qquad [4\text{-}1]$$

Ohzuku *et al.* [125] cycled $Li_4Ti_5O_{12}$ vs. Li in 1.0 M $LiClO_4$ EC/DEC (1:1 by volume) electrolyte at a current density of 0.17 mA cm^{-2} and found almost no capacity loss after 100 cycles. Ohzuku attributed the excellent capacity retention of $Li_4Ti_5O_{12}$ to its zero insertion strain and suggested it could be used as a negative electrode in safe and long-

life rechargeable batteries. Nakahara *et al.* [128] showed that $Li_4Ti_5O_{12}$ with a primary particle size of 0.7 μm attained a capacity of 165 mA h g^{-1} when charged and discharged at a 1C rate and retained 99% of its initial capacity after 100 cycles. Although the cycling of $Li_4Ti_5O_{12}$ has been well studied, there has been little published on the reactivity of $Li_7Ti_5O_{12}$ with electrolyte at elevated temperature.

A $Li_4Ti_5O_{12}$ sample was synthesized by the method described in Section 2.1.1. Figure 4.3 shows a SEM image of the synthesized $Li_4Ti_5O_{12}$ sample indicating an average particle size around 0.3 μm. The specific surface area determined by single point BET was approximately 3.1 m^2 g^{-1}.

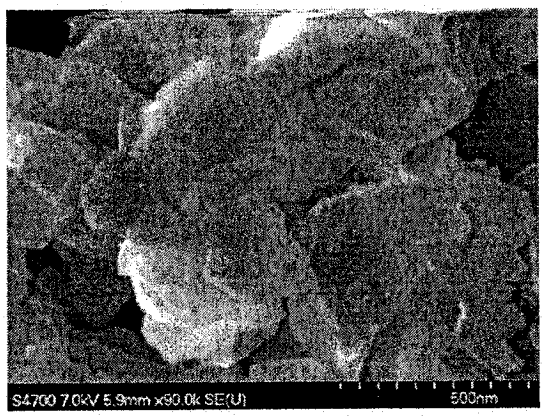

Figure 4.3 SEM micrograph of synthesized $Li_4Ti_5O_{12}$ having a particle size of approximately 0.3 μm.

For the ARC measurements, 150 mg of $Li_7Ti_5O_{12}$ was used instead of 100 mg (100 mg of $Li_{0.81}C_6$ was usually used in ARC experiments) based on the following considerations. The theoretical specific capacity is 175 mA h g^{-1} for $Li_4Ti_5O_{12}$ and 0.81*372 mA h g^{-1} = 301 mA h g^{-1} for MCMB (r = 0.19 and 372 mA h g^{-1} for graphite). In order to maintain the same number of moles of lithium as in 100 mg of $Li_{0.81}C_6$, the amount of $Li_7Ti_5O_{12}$ used in the ARC sample should be 100*301/175 mg = 172 mg. An amount of 150 mg $Li_7Ti_5O_{12}$ was used in this thesis.

Figure 4.4 shows the SHR vs. T for 150 mg of $Li_7Ti_5O_{12}$ reacting with 100 mg of EC/DEC solvent in panel (a), 100 mg of 0.8 M LiBOB EC/DEC in panel (b) and 1.0 M $LiPF_6$ EC/DEC in panel (c). The ARC samples were initially heated to 90°C, as indicated

by the solid lines or to 160°C by the dashed lines. XRD patterns of $Li_7Ti_5O_{12}$ taken after the ARC experiment are shown in Figure 4.5. $Li_7Ti_5O_{12}$ reacts with EC/DEC, producing $Li_4Ti_5O_{12}$ and Li_2CO_3. The main reaction can be expressed as (in the case of EC):

$$2Li_7Ti_5O_{12} + 3C_3H_4O_3 \rightarrow 3C_2H_4 + 3Li_2CO_3 + 2Li_4Ti_5O_{12}. \qquad [4\text{-}2]$$

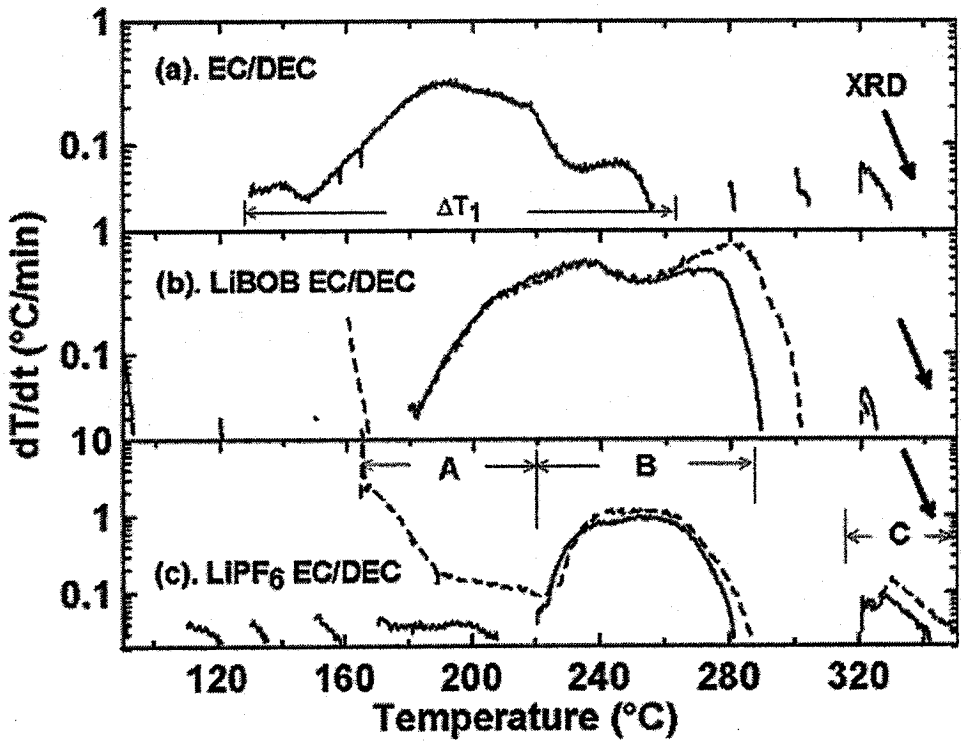

Figure 4.4 The self-heating rate versus temperature of 150 mg of $Li_7Ti_5O_{12}$ reacting with 100 mg of EC/DEC in panel (a), 100 mg 0.8 M LiBOB EC/DEC (b), and 100 mg of 1.0 M $LiPF_6$ EC/DEC (c). The samples for the ARC experiments were initially heated to 90°C (solid lines) or forced to a higher temperature of 160°C (dashed lines).

This is similar to the thermal reaction of $Li_{0.81}C_6$ with EC/DEC solvent described by reaction [3-6] in Chapter 3. The temperature rise (ΔT_1) shown in Figure 4.4a is about 130 K and hence the enthalpy of reaction [4-2] is approximately –110 kJ mol^{-1} of Li that reacts. This is much less than the enthalpy of reaction between $Li_{0.81}C_6$ and EC/DEC (–215 kJ mol^{-1} of Li), presumably because the Li atoms in $Li_7Ti_5O_{12}$ are at a lower chemical potential (by around 1.5 eV or 144 kJ mol^{-1}) than the Li atoms in $Li_{0.81}C_6$. This

suggests that the exotherm released from the reaction of a negative electrode material with EC/DEC solvent is related to the binding energy of Li in this material in the charged state. Theoretically, negative electrode materials with a higher lithium binding energy will release a smaller amount of heat during reaction with EC/DEC solvent. This is because: (1) the material with a higher lithium binding energy has a lower lithium atom chemical potential; (2) the main products after the reaction between negative electrodes and EC/DEC are mainly Li_2CO_3 and C_2H_4; and (3) the heat released is related to the enthalpy difference between the reactants and products. As shown above, this is the case for $Li_{0.81}C_6$ (0.1 eV Li binding energy) and $Li_7Ti_5O_{12}$ (1.55 eV) electrodes. Thermal studies of another negative electrode material, $Li_{0.5}VO_2$ (B) with a Li binding energy of 2.45 eV, will be presented in Section 4.2.

The SHR vs. T for 150 mg of $Li_7Ti_5O_{12}$ reacting with 100 mg of 0.8 M LiBOB EC/DEC in Figure 4.4b shows a temperature rise around 130 K that is close to ΔT_1 due to the reaction with EC/DEC in Figure 4.4a. The products after $Li_7Ti_5O_{12}$ reacts with LiBOB EC/DEC are also $Li_4Ti_5O_{12}$ and Li_2CO_3 as indicated in Figure 4.5b. The LiF existing in Figures 4.5a and b is believed to come from the original $LiPF_6$ EC/DEC electrolyte during preparation of ARC samples, which apparently was swollen in the PVDF binder and could not be removed completely by the rinsing procedure.

The SHR vs. T for 150 mg of $Li_7Ti_5O_{12}$ reacting with 100 mg of 1.0 M $LiPF_6$ EC/DEC is shown in Figure 4.4c. There are some weak exothermic signals between 110°C to 210°C for $Li_7Ti_5O_{12}$ initially heated to 90°C (solid line) in $LiPF_6$ EC/DEC. In order to explore the impact of these "mini-exotherms", an ARC sample of $Li_7Ti_5O_{12}$ in $LiPF_6$ EC/DEC was initially forced to 160°C and then the resulting exotherm was followed as indicated by the dashed line in Figure 4.4c. The "mini-exotherms" in the dashed curve of Figure 4.4c basically add up to create a new ARC peak when the sample is forced to a starting temperature of 160°C.

The addition of $LiPF_6$ to the EC/DEC solvent slows the reaction of both negative electrode materials as shown by comparison of Figures 4.4a and c. The XRD pattern in Figure 4.5c shows the main products LiF, Li_2CO_3 and $Li_4Ti_5O_{12}$ with a small amount of TiO_2 after the reaction between $Li_7Ti_5O_{12}$ and $LiPF_6$ EC/DEC. LiF is believed to come from the reaction between deintercalated Li with PF_5 and of course from the

decomposition of $LiPF_6$ as well. The small amount of TiO_2 possibly comes from the reaction between $Li_4Ti_5O_{12}$ after Li-detercalation and $LiPF_6$ EC/DEC electrolyte, which corresponds to region C indicated in Figure 4.4c. The proposed reaction mechanism for the production of TiO_2 will be later tested by a designed experiment.

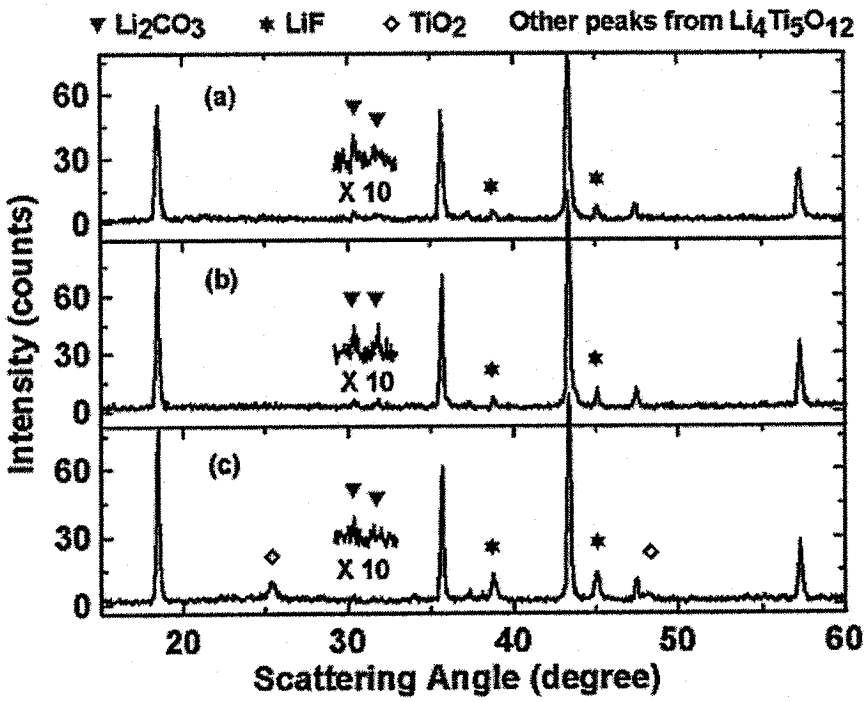

Figure 4.5 XRD patterns of the products of $Li_7Ti_5O_{12}$ after reacting with EC/DEC in panel (a), LiBOB EC/DEC (b), and $LiPF_6$ EC/DEC (c) at 350°C in ARC measurements as shown in Figure 4.4.

In order to understand how $Li_7Ti_5O_{12}$ reacts with $LiPF_6$ EC/DEC to produce LiF, it is worth considering the number of moles of the possible reactants in the samples as listed in Table 4.1. It is believed that $LiPF_6$ decomposes according to $LiPF_6 \rightarrow LiF + PF_5$ and then the PF_5 reacts **first** with the available lithium to make LiF and other products. This LiF on the surface of the electrode particles slows down the reaction. If this is the case, Table 4.1 shows that about 47% of the available Li in $Li_7Ti_5O_{12}$ can react with fluorine to make LiF. The exotherms in Figure 4.4c have been divided into two regions marked on Figure 4.4c. The region, A, is where the intercalated Li reacts with F from PF_5 and the region, B, is where the intercalated Li reacts with the solvents producing

Li_2CO_3 as shown in Figure 4.5c. Notice that region A in Figure 4.4c represents about 50% of the temperature rise, suggesting it could correspond to the fluorine reaction. As shown later in this section, the temperature rise of region A depends on the amount of $LiPF_6$ in the ARC tube, strongly suggesting that region A corresponds to the reaction of Li with F from PF_5. Either the molarity or the mass of electrolyte added to the ARC tube can adjust the amount of $LiPF_6$.

Table 4.1 Number of moles of reactants in the ARC samples used.

Material and amount	Number of moles of reactive species	Number of moles of reactive atom or group
100 mg $Li_{0.81}C_6$ composite (7% PVDF binder)	8.9×10^{-4} mol Li	8.9×10^{-4} mol Li
35 mg $Li_{0.81}C_6$ composite (2% EPDM binder)	3.3×10^{-4} mol Li	3.3×10^{-4} mol Li
150 mg $Li_7Ti_5O_{12}$ composite (7% PVDF)	8.1×10^{-4} mol Li reacting to form $Li_4Ti_5O_{12}$	8.1×10^{-4} mol Li
100 mg EC/DEC	9.6×10^{-4} mol total of EC and DEC	9.6×10^{-4} mol CO_3
35 mg EC/DEC	3.4×10^{-4} mol total of EC and DEC	3.4×10^{-4} mol CO_3
100 mg 1.0 M $LiPF_6$ EC/DEC	7.7×10^{-5} mol PF_5 from $LiPF_6 \rightarrow PF_5 + LiF$	3.8×10^{-4} mol F (from PF_5)
100 mg 0.5 M $LiPF_6$ EC/DEC	4.5×10^{-5} mol PF_5 from $LiPF_6 \rightarrow PF_5 + LiF$	2.3×10^{-4} mol F (from PF_5)
50 mg 1.0 M $LiPF_6$ EC/DEC	3.9×10^{-5} mol PF_5 from $LiPF_6 \rightarrow PF_5 + LiF$	1.9×10^{-4} mol F (from PF_5)

An ARC experiment involving 150 mg of $Li_7Ti_5O_{12}$ reacting with 100 mg of **0.5** M $LiPF_6$ EC/DEC was run and the result is shown in Figure 4.6a. The sample was initially forced to 160°C, compared to the results for the same electrode material in 100 mg of 1.0 M $LiPF_6$ in Figure 4.6b. The latter curve is the same as the dashed line in Figure 4.4c. The results clearly show that as the amount of $LiPF_6$, and hence resulting PF_5, in the sample is reduced, so is the temperature rise associated with region A. Correspondingly, the size of region B is increased in Figure 4.6a, because more lithium is available to react with the solvents once the PF_5 is used up. Table 4.2 gives the temperature rises in the regions A and B for the two experiments. The temperature rise in

region A decreased by about a factor of two, from 66 K to 38 K when the electrolyte molarity was decreased by a factor of two, suggesting that region A is caused by the reaction between PF_5 and intercalated Li. Finally, notice that Table 4.1 predicts that about 1/2 and 1/4 of the intercalated Li, respectively, could react with the PF_5 generated from the $LiPF_6$ in 1.0 M and 0.5 M electrolyte. The results in Figure 4.6 provide clear evidence that the intercalated lithium first reacts with F from PF_5, and then with the solvents, once all the available PF_5 has been used up.

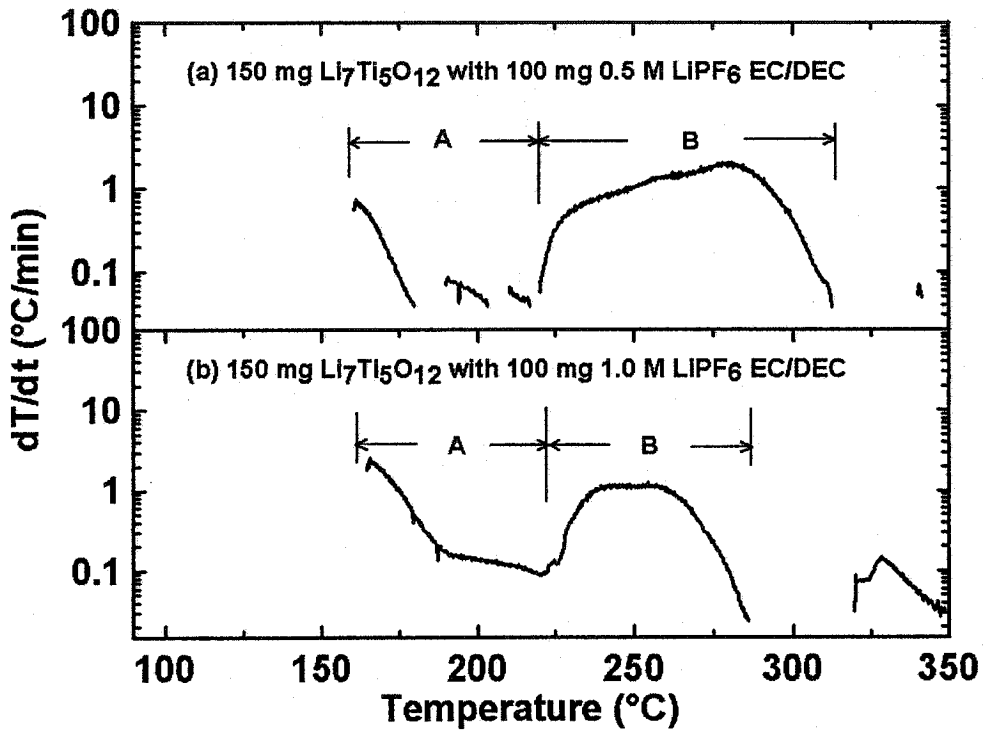

Figure 4.6 Self-heating rate versus temperature for 150 mg of $Li_7Ti_5O_{12}$ reacting with 100 mg 0.5 M $LiPF_6$ EC/DEC in panel (a) or 100 mg 1.0 M $LiPF_6$ EC/DEC in panel (b) both forced to 160°C.

Table 4.2 Temperature rises in the reaction between 150 mg $Li_7Ti_5O_{12}$ and 100 mg 1.0 M $LiPF_6$ EC/DEC or 100 mg 0.5 M $LiPF_5$ EC/DEC.

Electrolyte Molarity (M)	ΔT - region A (K)	ΔT - region B (K)	Sum: $\Delta T_A+\Delta T_B$ (K)
0.5	38.3	92.2	130.5
1.0	66.0	65.0	131.0

The XRD pattern of $Li_7Ti_5O_{12}$ after its reaction with 100 mg of 0.5 M $LiPF_6$ EC/DEC is shown in Figure 4.7. The Bragg peaks from Li_2CO_3 in Figure 4.7 are more pronounced than in Figure 4.5c, where the reaction was with 100 mg of 1.0 M $LiPF_6$ EC/DEC electrolyte. This can be explained using Table 4.1. The amount of PF_5 in 100 mg of 0.5 M and 1.0 M $LiPF_6$ EC/DEC in Table 4.1 is about 4.5×10^{-5} mol and 7.7×10^{-5} mol, which will consume approximately 28% and 47% of the available Li in 150 mg $Li_7Ti_5O_{12}$, respectively. The remaining available Li then reacts with EC/DEC solvent to produce lithium alkyl carbonate, and then lithium carbonate. In the latter case, there is insufficient lithium to drive the reaction to Li_2CO_3. However, in the former case, with only 100 mg of 0.5 M $LiPF_6$ EC/DEC electrolyte, there is enough lithium to convert most of the solvent to Li_2CO_3 and hence it is easily observed in Figure 4.7.

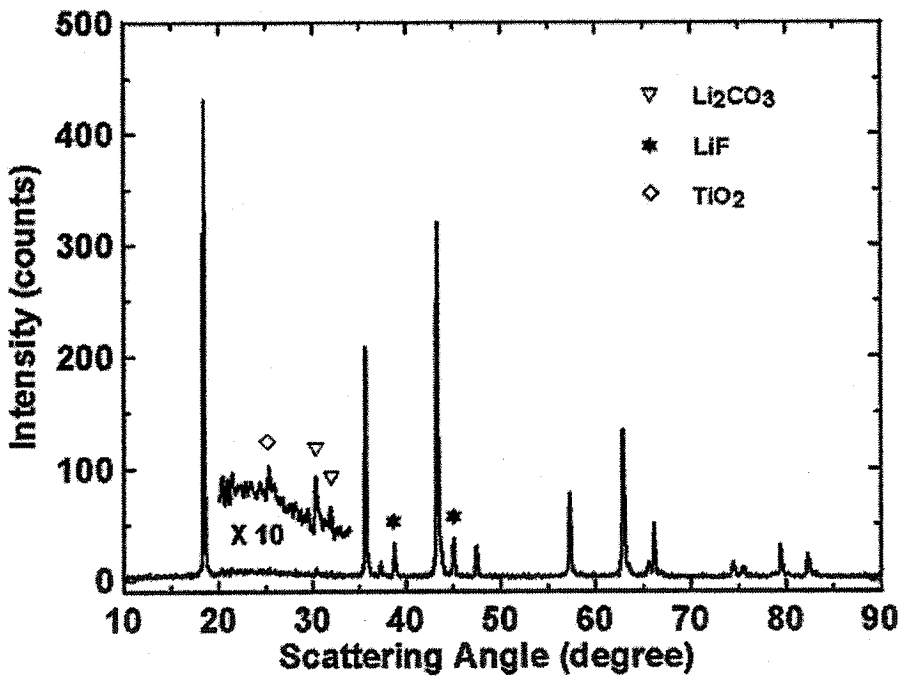

Figure 4.7 XRD patterns of the products of the reaction of 150 mg of $Li_7Ti_5O_{12}$ with 100 mg of 0.5 M $LiPF_6$ EC/DEC electrolyte.

In order to identify the reaction route for TiO_2 formation, another two ARC experiments were designed: (1) $Li_4Ti_5O_{12}$ (uncharged) with EC/DEC; and (2) $Li_4Ti_5O_{12}$ (uncharged) with $LiPF_6$ EC/DEC shown in Figures 4.8a and b, respectively. The ARC

result of $Li_7Ti_5O_{12}$ reacting with $LiPF_6$ EC/DEC was added in panel (c) for comparison. The XRD patterns of all the three ARC samples are plotted in Figures 4.9a, b, and c, respectively. There is almost no exotherm in the SHR vs. T of $Li_4Ti_5O_{12}$ reacting with EC/DEC (Figure 4.8a) indicating that uncharged $Li_4Ti_5O_{12}$ is thermally stable as expected and can not react with EC/DEC (Figure 4.9a). However, the SHR vs. T of $Li_4Ti_5O_{12}$ reacting with $LiPF_6$ EC/DEC electrolyte shows an exotherm starting from 320°C. Substantial amounts of TiO_2 and LiF are observed in Figure 4.9b. Clearly, the PF_5 from the decomposition of $LiPF_6$ is capable of extracting Li from $Li_4Ti_5O_{12}$ to make LiF. TiO_2 is a natural decomposition product because Ti can not be oxidized beyond the +4 oxidation state in which it is already formed in $Li_4Ti_5O_{12}$. This reaction process corresponds to the region C in Figure 4.4c.

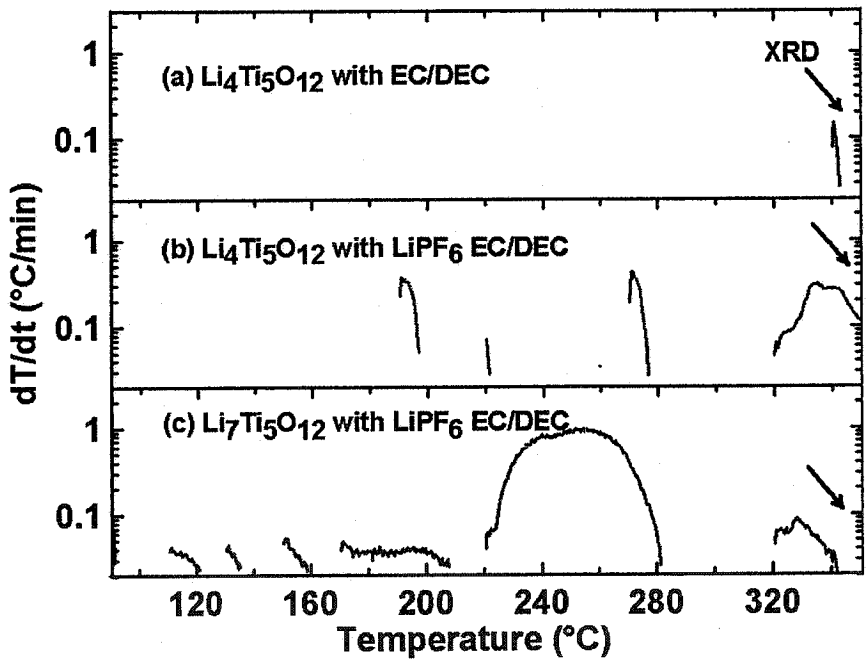

Figure 4.8 Self-heating rate versus temperature of 150 mg of uncharged $Li_4Ti_5O_{12}$ with 100 mg EC/DEC in panel (a), or 100 mg of 1.0 M $LiPF_6$ EC/DEC (b). Figure 4.8c shows the SHR vs. T for 150 mg of $Li_7Ti_5O_{12}$ reacting with 100 mg of 1.0 M $LiPF_6$ EC/DEC. The ARC samples were initially heated to 90°C.

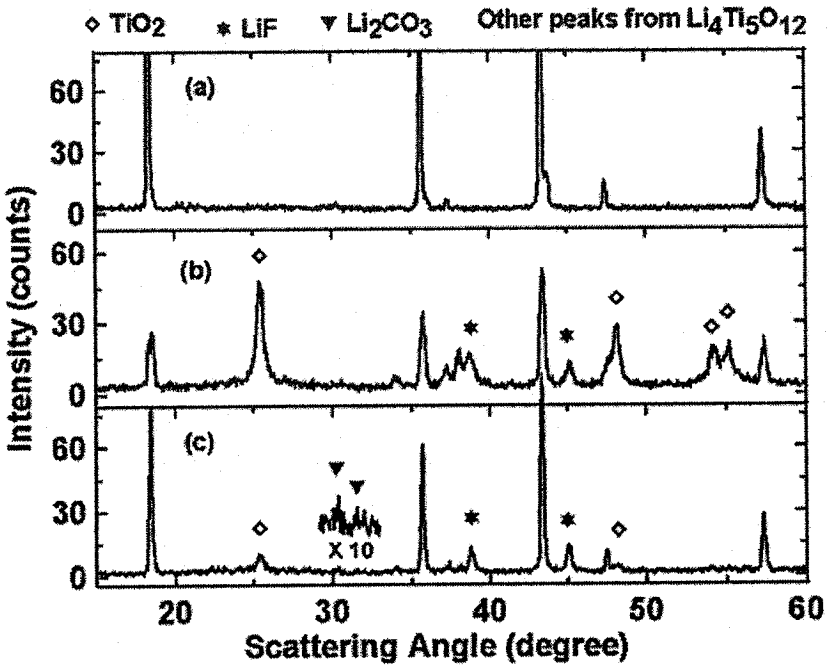

Figure 4.9 XRD patterns of the products of $Li_4Ti_5O_{12}$ after reacting with EC/DEC in panel (a) or $LiPF_6$ EC/DEC (b) at 350°C. Figure 4.9c shows the XRD patterns of the products from the reaction between $Li_7Ti_5O_{12}$ and $LiPF_6$ EC/DEC at 350°C. The ARC data are shown in Figure 4.8.

4.2 $Li_{0.5}VO_2$ (B)

$Li_{0.5}VO_2$ (B) was chosen as the third negative electrode material to study the effects of lithium binding energy. The reasons for this choice are listed below:

(1). The lithium binding energy of $Li_{0.5}VO_2$ (B) is around 2.45 eV vs. lithium metal, which is significantly different from the lithium binding energy of $Li_7Ti_5O_{12}$, 1.55 eV.

(2). The discharge curve of VO_2 (B) at 2.45 V is flat showing a two-phase region between VO_2 (B) and $Li_{0.5}VO_2$ (B).

(3). The synthesis of VO_2 (B) is relatively simple. VO_2 (B) can be obtained from the decomposition of NH_4VO_3 under an argon atmosphere at 350°C, which is described in Section 2.1.2.

$Li_{0.5}VO_2$ (B) was obtained by discharging VO_2 (B) at 2.45 V vs. Li metal as follows:

$$2VO_2\ (B) + Li^+ + e^- \rightarrow 2Li_{0.5}VO_2\ (B). \qquad [4\text{-}3]$$

$Li_{0.5}VO_2$ (B) adopts the monoclinic structure (Space group C2/m, #12) shown in Figure 4.10. It is a three-dimensional array of corner-shared VO_6 octahedral [129, 130].

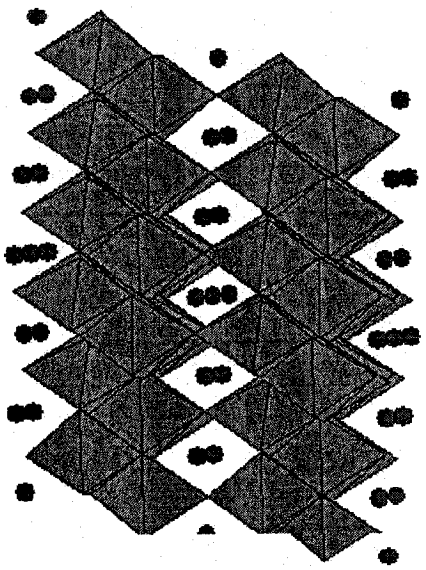

Figure 4.10 The $Li_{0.5}VO_2$ (B) structure (Space group C2/m, #12). It is based on a three-dimensional array of corner-shared VO_6 octahedra. ("•" represents lithium atoms).

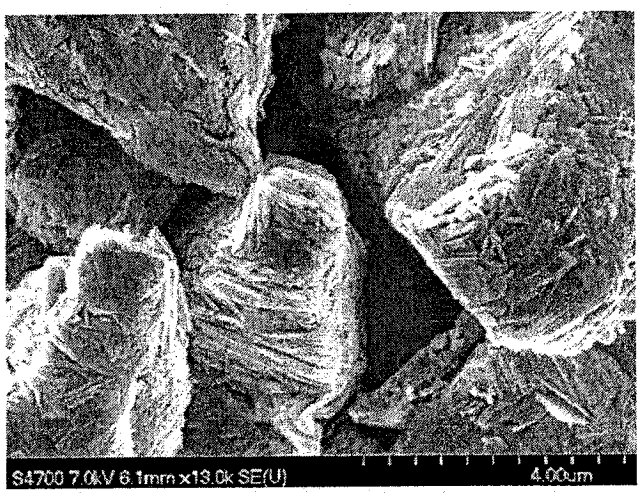

Figure 4.11 SEM micrograph of VO_2 (B) having an average particle size about 5 μm.

A SEM micrograph of synthesized VO_2 (B) shown in Figure 4.11 indicates an average particle size around 5 μm. The BET surface area of VO_2 (B) is around 8.9 $m^2\ g^{-1}$.

XRD patterns of synthesized VO_2 (B) and the fitted curve using Rietveld refinement are shown in Figure 4.12. The refinement results are shown in Table 4.3.

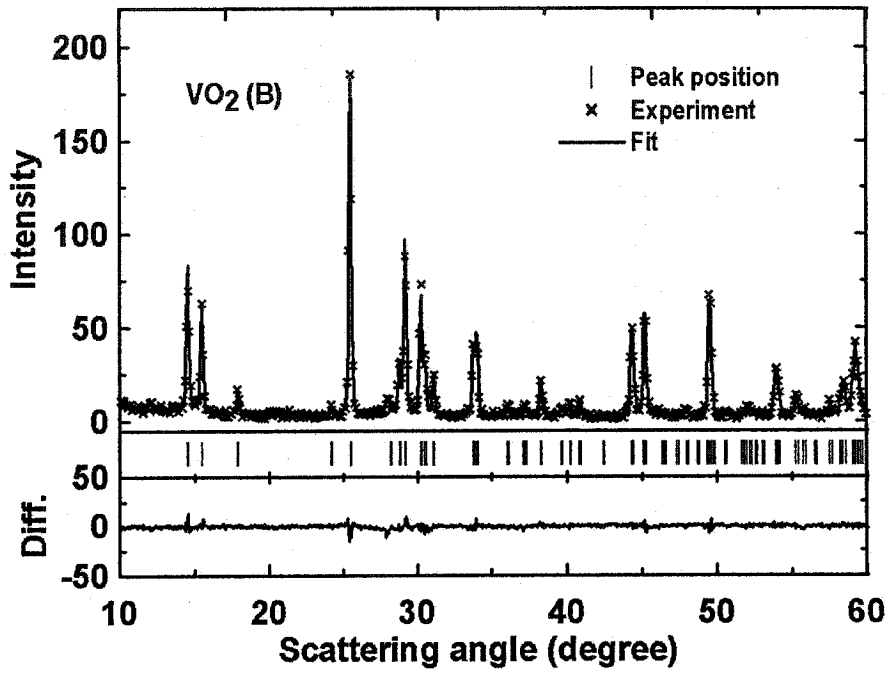

Figure 4.12 X-ray diffraction (XRD) pattern of the synthesized VO_2 (B) sample and the fit using Rietveld refinement.

Table 4.3 Lattice constants and atom positions for the synthesized VO_2 (B) sample from the XRD refinement. The space group used for the refinement was C2/m ($^{\#}12$). The Bragg R-factor is listed.

	Synthesized VO_2 (B) sample		
	$\beta = 106.97°$		
	a (Å)	*b* (Å)	*c* (Å)
	12.0673(3)	3.6892(2)	6.4212(2)
	x	y	z
V_1	0.8036(6)	0	0.7369(2)
V_2	0.9023(3)	0	0.3102(5)
O_1	0.8640(7)	0	0.9953(7)
O_2	0.7334(1)	0	0.3410(9)
O_3	0.9390(3)	0	0.6459(8)
O_4	0.6310(6)	0	0.6970(8)
R_{Bragg}	3.5%		

Starting atomic coordinates for VO_2 (B) were taken from reference [131].

$Li_{0.5}VO_2$ (B) was obtained and its XRD pattern is shown in Figure 4.13b. The XRD pattern of VO_2 (B) is shown in Figure 4.13a for comparison. The theoretical capacity of VO_2 (B) was calculated to be 161 mA h g^{-1} from reaction [4-3], which is close to the capacity of $Li_4Ti_5O_{12}$ (175 mA h g^{-1}). In the ARC measurements, therefore, 150 mg of $Li_{0.5}VO_2$ (B) was used to maintain a similar amount of Li to the $Li_{0.81}C_6$ and $Li_7Ti_5O_{12}$ samples.

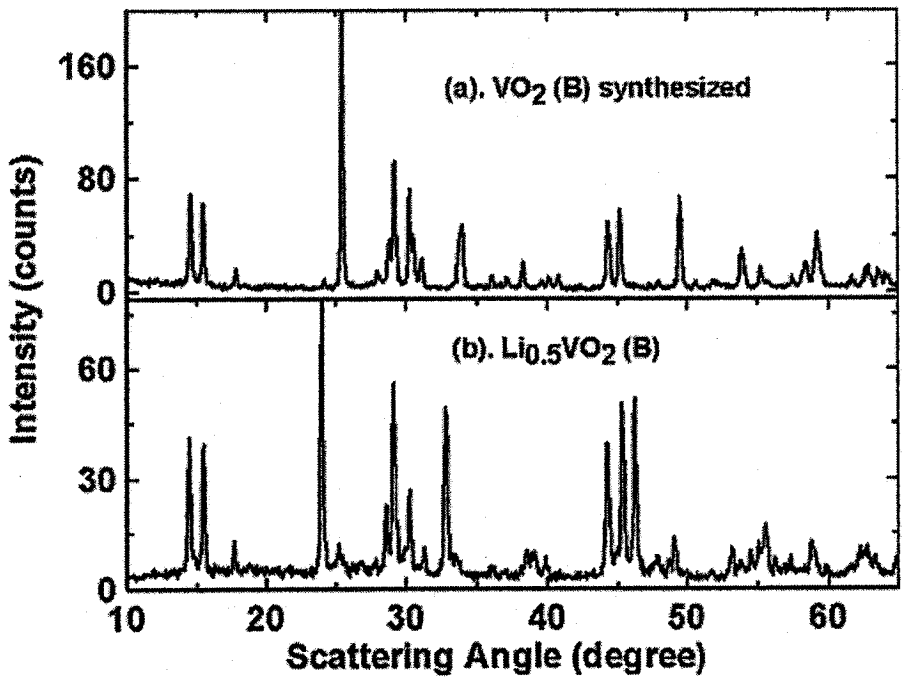

Figure 4.13 The XRD pattern of $Li_{0.5}VO_2$ (B) in panel (b). The XRD pattern of VO_2 (B) is shown in Figure 4.13a for comparison.

Figure 4.14 shows the SHR vs. T for 150 mg of $Li_{0.5}VO_2$ (B) reacting with 100 mg EC/DEC solvent in panel (a), 100 mg of 1.0 M $LiPF_6$ EC/DEC (b) and 100 mg of 0.8 M LiBOB EC/DEC (c). The ARC sample was initially heated to 90°C as indicated by a solid line or to 160°C as indicated by a dashed line. XRD patterns of $Li_{0.5}VO_2$ (B) taken after the ARC experiment at 350°C are shown in Figure 4.15. The main products from $Li_{0.5}VO_2$ (B) reacting with EC/DEC shown in Figure 4.15a or LiBOB EC/DEC in Figure 4.15b are Li_2CO_3 and V_2O_3. It is easy to understand that Li_2CO_3 comes from deintercalated Li reacting with EC/DEC at high temperature producing Li_2CO_3:

$$4Li_{0.5}VO_2\ (B) + C_3H_4O_3 \rightarrow C_2H_4 + Li_2CO_3 + 4VO_2\ (B). \qquad [4\text{-}4]$$

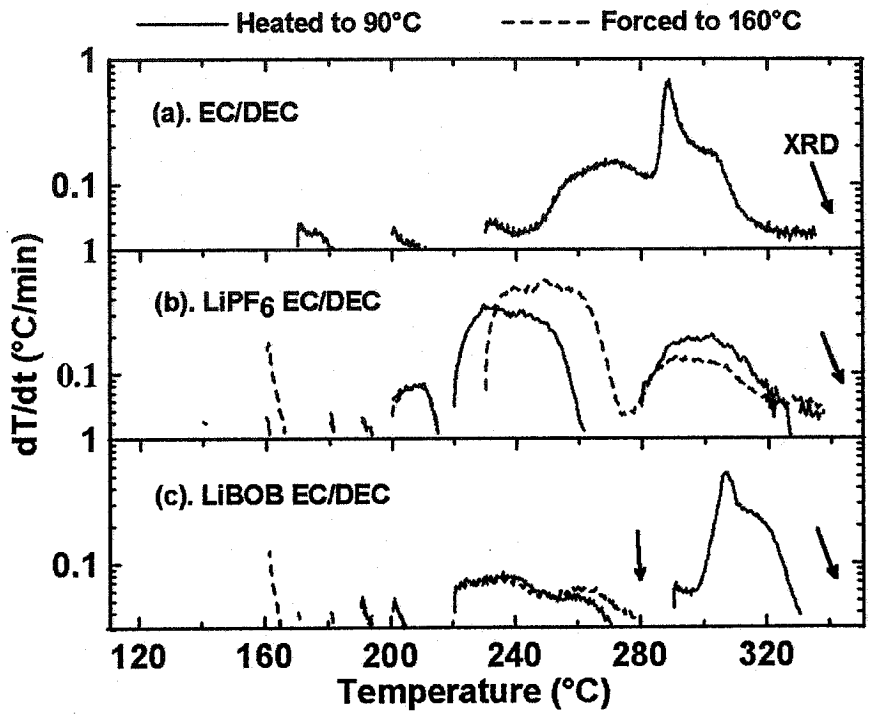

Figure 4.14 The self-heating rate versus temperature of 150 mg of $Li_{0.5}VO_2$ (B) reacting with 100 mg of EC/DEC panel (a), 100 mg of 0.8 M LiBOB EC/DEC (b), and100 mg of 1.0 M $LiPF_6$ EC/DEC (c). The ARC experiments were initially heated to 90°C (solid lines) or forced to a higher temperature of 160°C (dashed lines).

It is possible that the VO_2 (B) produced in reaction [4-4] decomposes into V_2O_3 (shown in Figure 4.15) and O_2 that combusts the EC/DEC solvent, releasing further heat in the ARC measurements, as seen in Figure 4.14. The thermal reaction of $Li_{0.5}VO_2$ (B) in LiBOB EC/DEC (Figure 4.14c) obviously contains two processes, one from 220°C to 280°C the other one from 290°C to 340°C. Two ARC samples in Figure 4.14c were stopped at 280°C and 340°C, respectively. XRD patterns of the two samples are shown in Figures 4.16b and c. The XRD pattern of VO_2 (B) is shown in panel (a) for comparison. The main products from the reaction of $Li_{0.5}VO_2$ (B) with LiBOB EC/DEC before 280°C [process (1)] are VO_2 (B) and Li_2CO_3 shown in Figure 4.16b, which strongly support the reaction mechanism [4-4]. In process (2) from 290°C to 340°C, the main product is V_2O_3

shown in Figure 4.16c. Therefore, the thermal reaction in process (2) is as follows (EC for example):

$$20VO_2\,(B) + 2C_3H_4O_3 \rightarrow 6CO_2 + 4H_2O + 10V_2O_3. \qquad [4\text{-}5]$$

The temperature rises for processes (1) and (2), shown in Figure 4.17, are approximately 60 K (ΔT_1) and 42 K (ΔT_2), respectively. Hence the enthalpy of reaction [4-4] in process (1) is approximately –54 kJ mol^{-1} of Li, which is much lower than the enthalpy of $Li_7Ti_5O_{12}$ or $Li_{0.81}C_6$ thermally reacting with EC/DEC to produce Li_2CO_3, - 110 kJ mol^{-1} and - 215 kJ mol^{-1} of Li, respectively. These results show that the negative electrode materials with higher lithium binding energy (lower chemical potential of Li) release a smaller amount of heat during reaction with EC/DEC solvent.

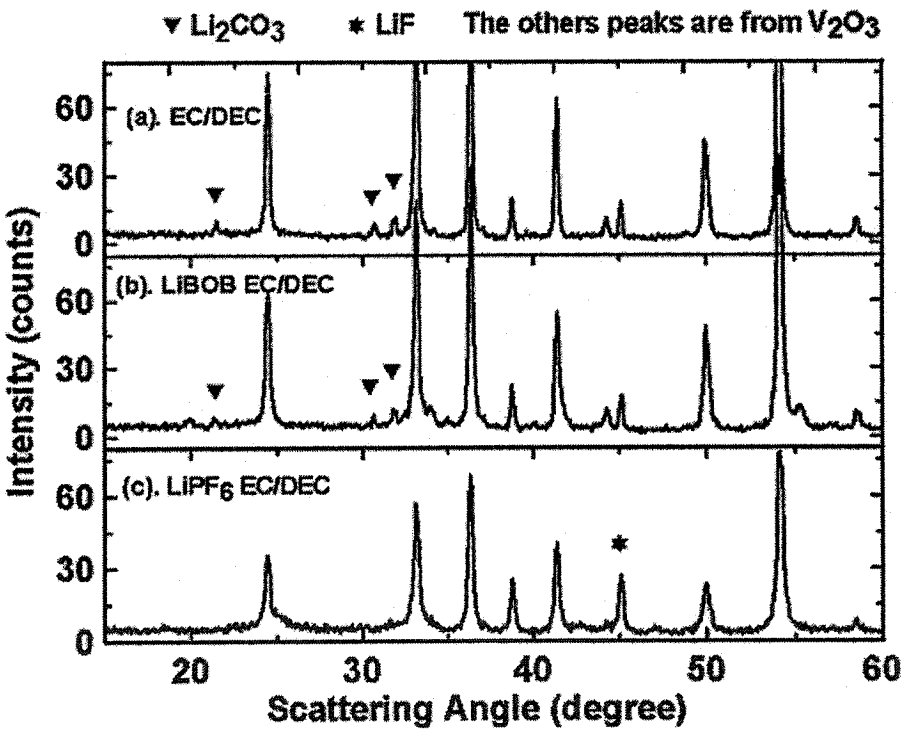

Figure 4.15 XRD patterns of the products of $Li_{0.5}VO_2$ (B) after reacting with EC/DEC in panel (a), LiBOB EC/DEC (b), and $LiPF_6$ EC/DEC (c) at 350°C in ARC measurements as shown in Figure 4.14.

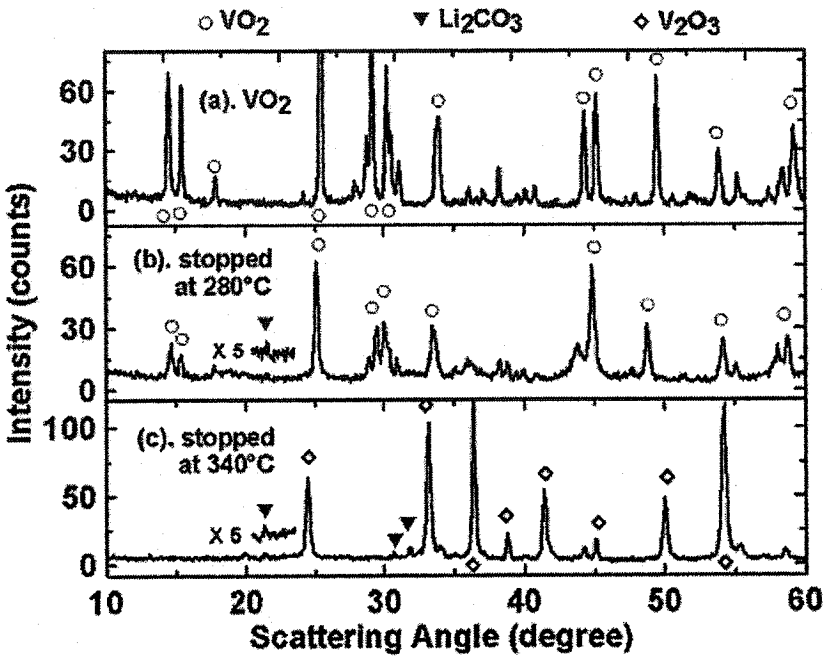

Figure 4.16 The XRD patterns of the products from the reactions between $Li_{0.5}VO_2$ (B) and LiBOB EC/DEC electrolyte in ARC measurements stopped at 280°C in panel (b) or 340°C in panel (c). The ARC results are shown in Figure 4.14c. The XRD pattern of VO_2 (B) is added into Figure 4.16a for comparison.

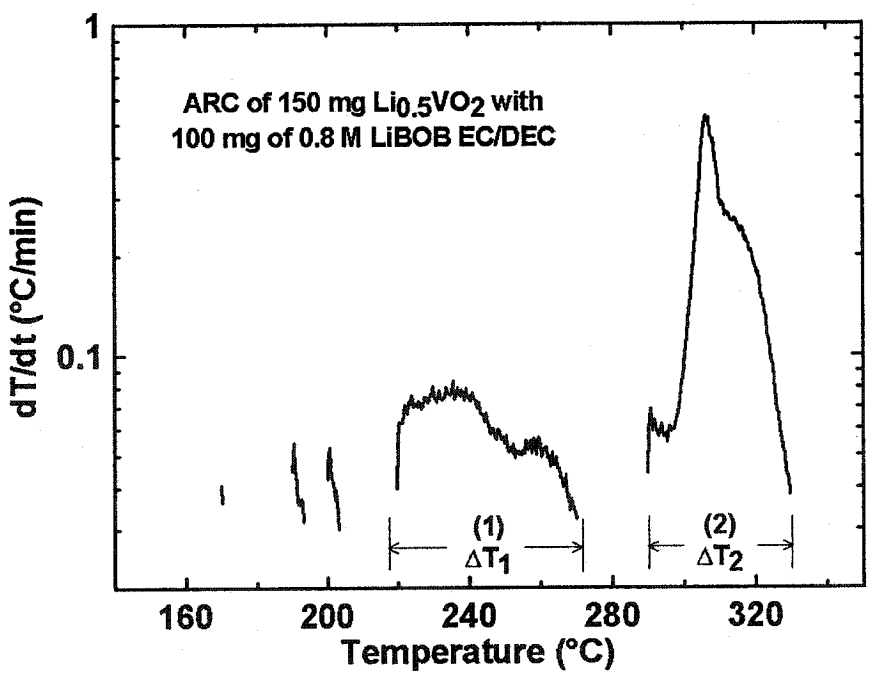

Figure 4.17 The two processes involved in the reaction between VO_2 (B) and LiBOB EC/DEC electrolytes in the ARC measurements (Figure 4.14c).

4.3 Thermal stability-comparison of $Li_{0.81}C_6$, $Li_7Ti_5O_{12}$, and $Li_{0.5}VO_2$ (B)

$Li_{0.81}C_6$, $Li_7Ti_5O_{12}$, and $Li_{0.5}VO_2$ (B) have Li binding energies of 0.1 eV, 1.55 eV, and 2.45 eV, respectively. Their thermal stability is compared in this section.

4.3.1 EC/DEC solvent

Figure 4.18 shows the SHR vs. T of $Li_{0.81}C_6$, $Li_7Ti_5O_{12}$, and $Li_{0.5}VO_2$ (B) reacting with EC/DEC solvent initially heated to 90°C (solid line). The ARC onset temperature for $Li_{0.81}C_6$, $Li_7Ti_5O_{12}$, and $Li_{0.5}VO_2$ (B) in EC/DEC is approximately 100°C, 130°C, and 230°C, respectively. This suggests that $Li_{0.5}VO_2$ (B) with a high Li binding energy (2.45 eV) has much higher thermal stability than $Li_{0.81}C_6$ (0.1 eV) and $Li_7Ti_5O_{12}$ (1.55 eV).

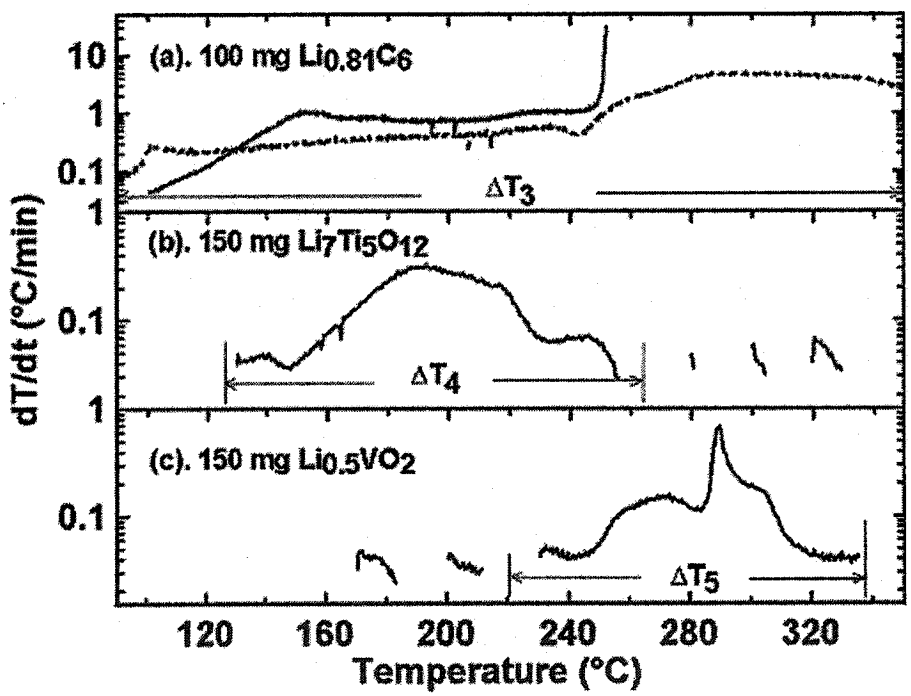

Figure 4.18 The self-heating rate vs. temperature for 100 mg of EC/DEC reacting with 100 mg of $Li_{0.81}C_6$ in panel (a), 150 mg of $Li_7Ti_5O_{12}$ (b), or $Li_{0.5}VO_2$ (B) in panel (c) shown in solid lines. The dashed line in Figure 4.18a shows the SHR vs. T of 100 mg of $Li_{0.81}C_6$ reacting with 100 mg of 1.0 M $LiPF_6$ EC/DEC.

The temperature rises (ΔT) for the ARC tests are used to compare the heat released from the reactions between $Li_{0.81}C_6$, $Li_7Ti_5O_{12}$, or $Li_{0.5}VO_2$ (B) and EC/DEC producing Li_2CO_3 and deintercalated materials [C, $Li_4Ti_5O_{12}$, and VO_2 (B)]. The temperature rise for the adiabatic reaction of 150 mg of $Li_7Ti_5O_{12}$ with 100 mg of EC/DEC is approximately 140 ± 16 K (ΔT_4) shown in Figure 4.18b. The temperature rise (ΔT_5) from the reaction of $Li_{0.5}VO_2$ (B) with EC/DEC (Figure 4.18c) includes two process, (1) production of Li_2CO_3 together with VO_2 (B) and (2) O_2 from the decomposition of VO_2 (B) combusting EC/DEC. The temperature rise due to the Li from Li-intercalated anodes reacting with EC/DEC solvent is to be compared. Therefore, temperature rise ΔT_1 (65 ± 10 K) in Figure 4.17, is used, which corresponds to process (1) [equation 4-4] of the reaction between $Li_{0.5}VO_2$ (B) and EC/DEC.

The temperature rise for the adiabatic reaction of $Li_{0.81}C_6$ with EC/DEC is unknown because the ARC went into thermal runaway. Therefore, an ARC curve for 100 mg of $Li_{0.81}C_6$ reacting with 100 mg of 1.0 M $LiPF_6$ EC/DEC was added to Figure 4.18a and indicated with a dashed line. Its temperature rise (ΔT_3) is approximately 285 ± 20 K.

Actually, the temperature rise for 100 mg of $Li_{0.81}C_6$ reacting with 100 mg of EC/DEC can be calculated. Figure 3.9 in Chapter 3 shows that the temperature rise for the adiabatic reaction of 35 mg of $Li_{0.81}C_6$ with 35 mg of EC/DEC is around 137 K. The heat capacity of the 930 mg ARC tube together with 35 mg of $Li_{0.81}C_6$ and EC/DEC is calculated to be 0.515 J K^{-1}. The released heat is 137*0.515 J = 70.5 J. 100 mg of $Li_{0.81}C_6$ reacting with EC/DEC will release a heat of 70.5*100/35 J = 200 J. Similarly, the heat capacity of an ARC tube together with 100 mg of $Li_{0.81}C_6$ and the same amount of EC/DEC is around 0.678 J K^{-1}. Therefore, the temperature rise for the adiabatic reaction of 100 mg of $Li_{0.81}C_6$ with 100 mg of EC/DEC should be around 200/0.678 K = 295 K. This value agrees with the range of 285 ± 20 K, which was estimated from Figure 4.18a.

Therefore, the temperature rises for adiabatic reaction of 100 mg of $Li_{0.81}C_6$, 150 mg of $Li_7Ti_5O_{12}$, and 150 mg of $Li_{0.5}VO_2$ (B) with EC/DEC are around 285 ± 20 K, 140 ± 16 K, and 65 ± 10 K, respectively. The corresponding thermal reaction can be concluded as (EC as example):

$$2LiA + C_3H_4O_3 \rightarrow 2A + Li_2CO_3 + C_2H_4, \qquad [4\text{-}6]$$

where A represents electrode materials before lithiation, such as C, $Li_4Ti_5O_{12}$, and VO_2 (B). The released heat (ΔH) is approximately 215 ± 16 kJ, 110 ± 13 kJ, and 54 ± 8 kJ per mol of Li for $Li_{0.81}C_6$, $Li_7Ti_5O_{12}$, and $Li_{0.5}VO_2$ electrodes, respectively.

Figure 4.19 shows the potential (vs. Li) of charged negative electrode materials versus the heat released, ΔH (per mole of Li), for $Li_{0.81}C_6$, $Li_7Ti_5O_{12}$, and $Li_{0.5}VO_2$ (B) materials in the adiabatic reaction with EC/DEC solvent. There is a linear relationship between the potential and the heat. The curve intercepts with the y-axis at around 3.3 V. This means that if the potential of a Li-intercalated electrode material is higher than 3.3 V vs. Li, this material will not thermally react with EC/DEC to release any heat under 350°C. In practice, this is right. For example, $LiFePO_4$, $LiCoO_2$, and $LiMn_2O_4$ have an average lithium binding energy of 3.5 V, 4.2 V, and 4.1 V, respectively. They are all thermally stable in EC/DEC solvent.

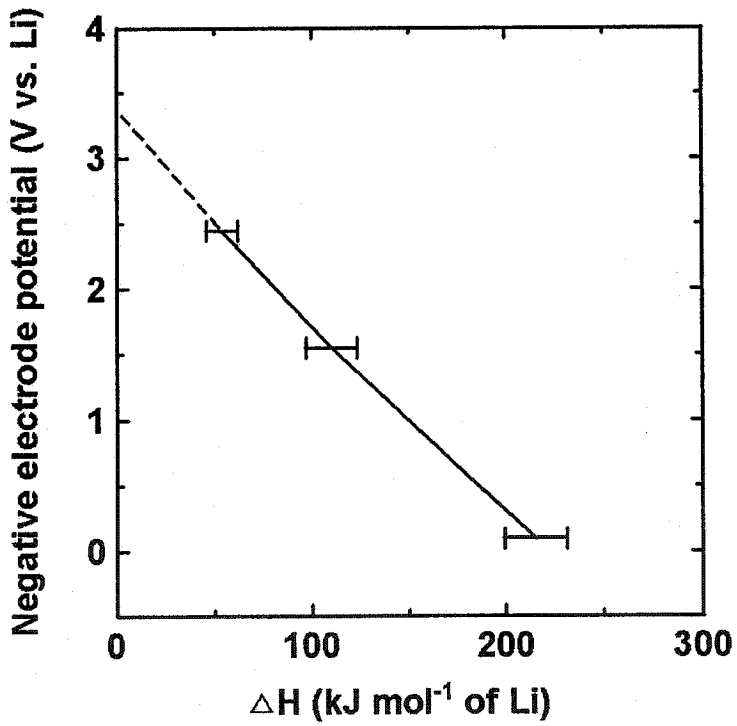

Figure 4.19 The potential (vs. Li) of charged negative electrode materials versus the heat released, ΔH (per mole of Li), for $Li_{0.81}C_6$, $Li_7Ti_5O_{12}$, and $Li_{0.5}VO_2$ (B) materials reacting with EC/DEC in the ARC measurements (Figure 4.18).

4.3.2 $LiPF_6$ and LiBOB based electrolyte

Figure 4.20 shows the SHR vs. T of $Li_{0.81}C_6$, $Li_7Ti_5O_{12}$, and $Li_{0.5}VO_2$ (B) reacting with $LiPF_6$ EC/DEC electrolyte initially heated to 90°C. $Li_{0.5}VO_2$ (B) clearly shows higher thermal stability than $Li_{0.81}C_6$ and $Li_7Ti_5O_{12}$.

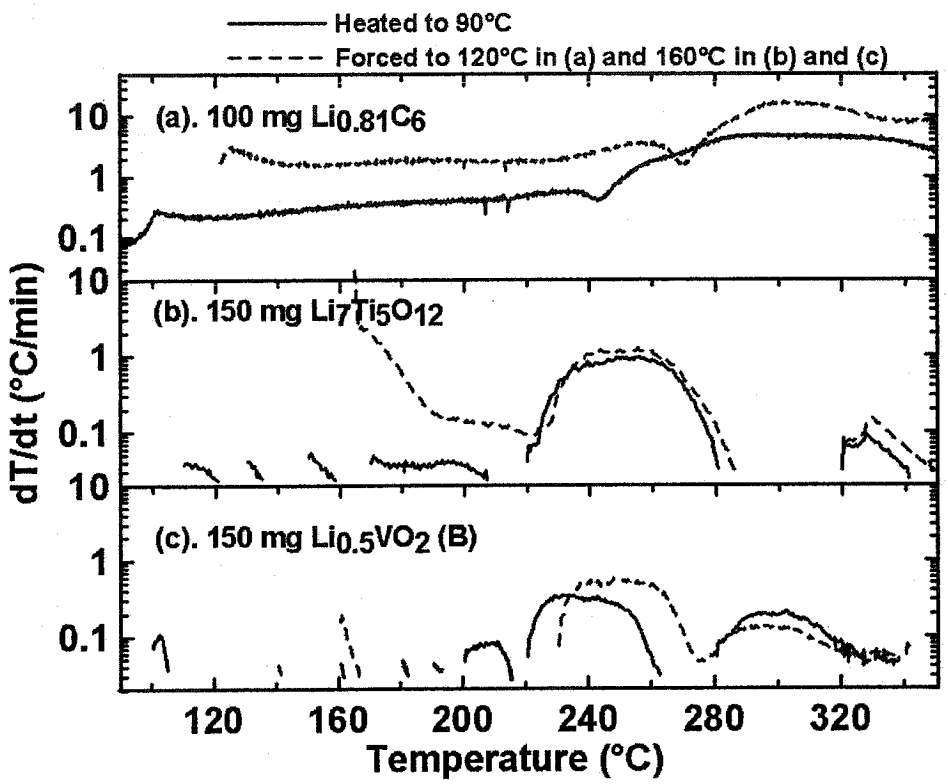

Figure 4.20 The SHR vs. T for 100 mg of 1.0 M $LiPF_6$ EC/DEC reacting with 100 mg of $Li_{0.81}C_6$, 150 mg of $Li_7Ti_5O_{12}$, and $Li_{0.5}VO_2$ (B) shown in panels a, b, and c, respectively. The ARC samples were initially heated to 90°C (solid lines) or forced to a higher temperature of 120°C (dashed line in panel a) or 160°C (dashed lines in panels b and c).

The SHR vs. T for the three negative electrodes in LiBOB EC/DEC are shown in Figure 4.21. ARC samples initially heated to 90°C are indicated with solid lines. The dashed lines indicate samples initially heated to 120°C for $Li_{0.81}C_6$ in panel (a) and 160°C for $Li_7Ti_5O_{12}$ (b) and $Li_{0.5}VO_2$ (B) (c). LiBOB EC/DEC clearly shows thermal advantages for $Li_{0.81}C_6$ over $LiPF_6$ EC/DEC that were described in Chapter 3. However, when the lithium binding energy of the negative electrode material increases, the thermal advantage of LiBOB over $LiPF_6$ is not significant any more. For example, the thermal

reactions of $Li_7Ti_5O_{12}$ or $Li_{0.5}VO_2$ (B) in $LiPF_6$ or LiBOB based electrolytes start from similar temperatures as shown in Figures 4.20 and 4.21. This suggests that when the lithium binding energy of negative electrode material increases to some extent, their thermal stability cannot be significantly improved by changing salt. The thermal-stability results for $Li_{0.81}C_6$, $Li_7Ti_5O_{12}$, $Li_{0.5}VO_2$ (B) are compared in Table 4.4

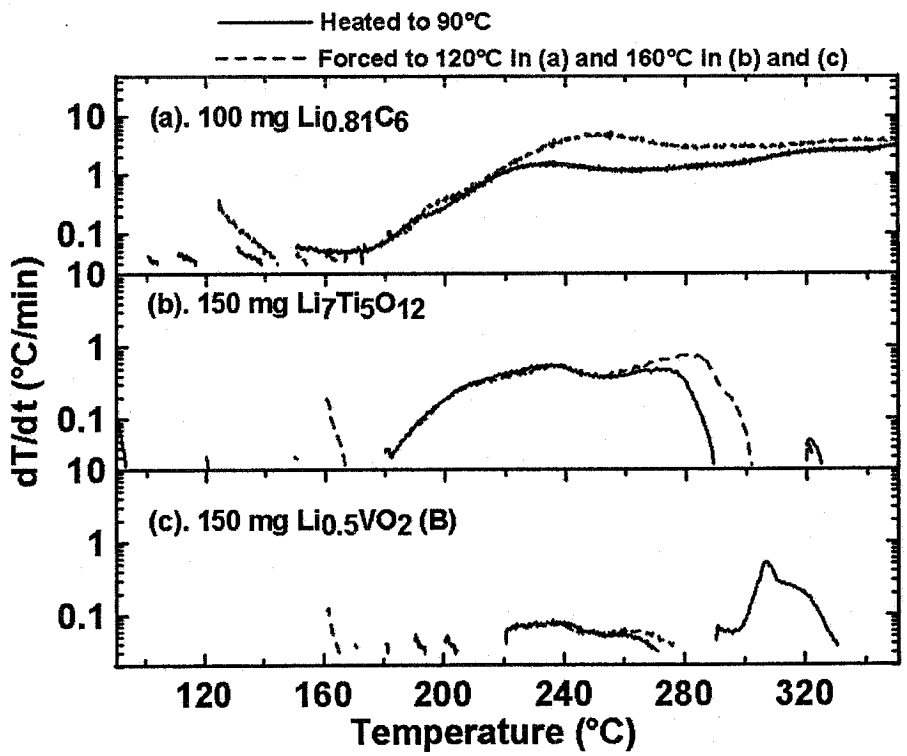

Figure 4.21 The SHR vs. T of 100 mg of 0.8 M LiBOB EC/DEC reacting with 100 mg of $Li_{0.81}C_6$, 150 mg of $Li_7Ti_5O_{12}$, and $Li_{0.5}VO_2$ (B) shown in panels a, b, and c, respectively. The ARC samples were initially heated to 90°C (solid lines) or forced to a higher temperature of 120°C (dashed line in panel a) or 160°C (dashed lines in panels b and c).

Table 4.4 Comparison of three different negative electrode materials, MCMB, $Li_4Ti_5O_{12}$, and VO_2 (B) with different lithium binding energies.

Negative electrode materials	MCMB	$Li_4Ti_5O_{12}$	VO_2 (B)
Particle size (μm)	25	0.3	5
BET surface area ($m^2\ g^{-1}$)	0.8	3.1	8.9
Li binding energy (eV) vs. Li metal	0.1	1.55	2.45
Discharged state	$Li_{0.81}C_6$	$Li_7Ti_5O_{12}$	$Li_{0.5}VO_2$
Theoretical discharge capacity (mA h g^{-1})	310	175	160
Mass in ARC in mg (discharged anode material : solvent or electrolyte)	100:100	150:100	150:100
Onset T with EC/DEC (°C)	100	130	230
Temperature rise with EC/DEC (ΔT, K)	Around 295 from 35/35 in Figure 3.9	140 ± 16	65 ± 10 only process (1)
Products after ARC to 350°C with EC/DEC by XRD	MCMB + Li_2CO_3	$Li_4Ti_5O_{12}$ + Li_2CO_3	V_2O_3 + Li_2CO_3
Onset T with 1.0 M $LiPF_6$ EC/DEC (°C)	80	220	220
Temperature rise with 1.0 M $LiPF_6$ EC/DEC (ΔT, K)	280	150	65 only process (1)
Products after ARC to 350°C with 1.0 M $LiPF_6$ EC/DEC	LiF + MCMB	$Li_4Ti_5O_{12}$, TiO_2, LiF, and Li_2CO_3	V_2O_3 + LiF + Li_2CO_3

Chapter 5 Existing alternate positive electrode materials ($LiMn_2O_4$ and $LiFePO_4$)

$LiMn_2O_4$ and $LiFePO_4$ are very attractive positive electrode materials for large batteries used in E-bike, EV and HEV applications mainly because of their high thermal stability. $LiMn_2O_4$ adopts the spinel structure (Space group Fd3m, #227) shown in Figure 5.1. It is made up of a cubic close-packed oxygen array with three-dimensional array of edge-shared MnO_6 octahedra [132]. $LiFePO_4$ adopts an olivine structure shown in Figure 5.2 (Space group Pnma, #62) with a hexagonally-closed packed oxygen array where there are corner-shared FeO_6 octahedra and PO_4 tetrahedra. The lithium atom binding energies of $LiMn_2O_4$ and $LiFePO_4$ are approximately 4.1 eV and 3.5 eV vs. Li metal [133, 134].

Figure 5.3 shows the potential (V) versus specific capacity (mA h g^{-1}) for $Li/LiMn_2O_4$ and $Li/LiFePO_4$ coin cells during the first cycle. The first charge process happens at approximately 4.1 V and 3.5 V vs. Li for the $LiMn_2O_4$ and $LiFePO_4$ electrodes, respectively. In this chapter, the thermal stabilities of charged $LiMn_2O_4$ and $LiFePO_4$ are studied and their reaction sequences are characterized by ARC and XRD.

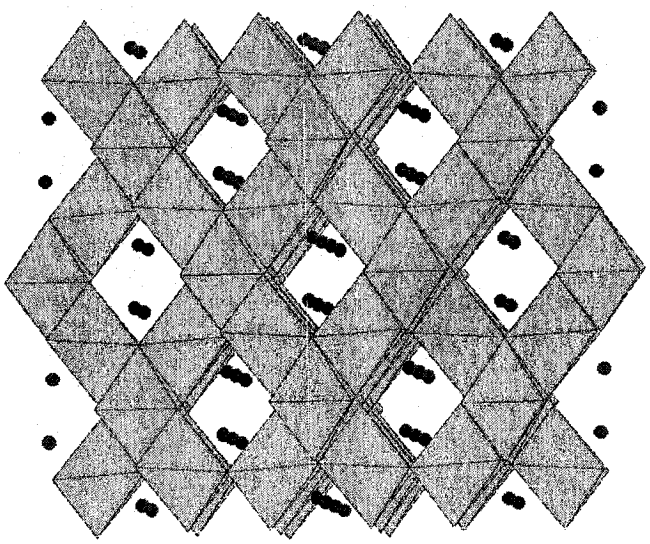

Figure 5.1 The $LiMn_2O_4$ spinel structure (Space group Fd3m, #227). It is based on a cubic close-packed oxygen array with edge-shared MnO_6 octahedra ("•" represents lithium atoms).

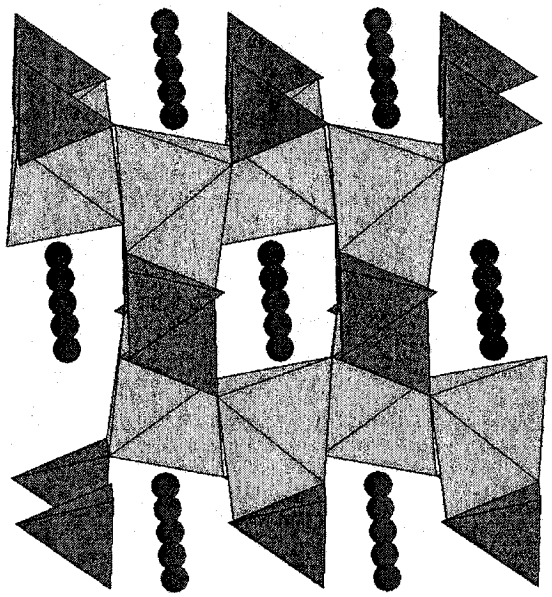

Figure 5.2 The $LiFePO_4$ olivine structure (Space group Pnma, #62) It is based on a hexagonal-close packed oxygen array with corner-shared FeO_6 octahedra and PO_4 tetrahedra ("●" represents lithium atoms).

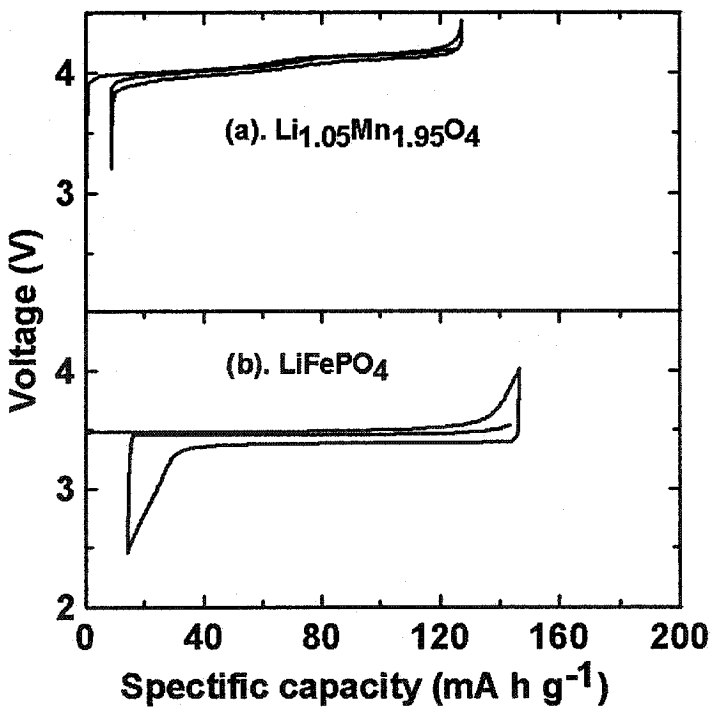

Figure 5.3 The potential (V) versus specific capacity (mA h g^{-1}) for Li/$LiMn_2O_4$ and Li/$LiFePO_4$ coin cells during the first cycle.

5.1 $LiMn_2O_4$ with the spinel structure

It has been shown that adding excess lithium to the octahedral site of the $LiMn_2O_4$ with the spinel structure helps maintain capacity for many cycles [133, 135]. The amount of excess lithium is represented with x in the formula $Li_{1+x}Mn_{2-x}O_4$ [or written as $Li_{Tet}(Li_xMn_{2-x})_{Oct}O_4$, where Tet and Oct designate the tetrahedral and octahedral sites in the spinel structure]. Adding too much excess Li, x, reduces the capacity of the electrode because the amount of lithium which can be removed during the charging process is only 1-3x per formula unit, which can be calculated as below. For the material with a formula of $Li_{1+x}Mn_{2-x}O_4$, the average oxidation state (V_{av}) of the Mn cation is:

$$V_{av} = [2\times4-(1+x)]/(2-x) = (7-x)/(2-x). \qquad [5\text{-}1]$$

When $Li_{1+x}Mn_{2-x}O_4$ is fully charged, the Mn cation is oxidized to +4 and the amount of lithium, n, that can be removed during the charge process is calculated to be:

$$n = (4-V_{av}) \times(2-x). \qquad [5\text{-}2]$$

Solving [5-1] and [5-2] gives n = 1-3x. References 133 and 135 show that $Li_{1+x}Mn_{2-x}O_4$ samples with $x\approx0.05$ give a reasonable discharge capacity around 120 mA h g^{-1} and good cyclability.

A $Li_{1+x}Mn_{2-x}O_4$ (x = 0.05) sample was obtained from Chemetals Inc. (USA). $Li_{1.05}Mn_{1.95}O_4$ is simply written as $LiMn_2O_4$ in the later sections of this chapter for convenience. Figure 5.4 shows a SEM micrograph of the $LiMn_2O_4$ sample indicating that it has an average particle size of approximately 10 μm. The BET surface area of the $LiMn_2O_4$ sample was measured to be 0.6 m^2 g^{-1}. Figure 5.5 shows the X-ray diffraction (XRD) pattern and corresponding Rietveld refinement of the $LiMn_2O_4$ sample.

λ-MnO_2 was obtained by charging $LiMn_2O_4$ to 4.4 V vs. Li metal as follows:

$$\tfrac{1}{2}\ LiMn_2O_4 \rightarrow \tfrac{1}{2}\ Li^+ + \lambda\text{-}MnO_2 + \tfrac{1}{2}\ e^-. \qquad [5\text{-}3]$$

The theoretical capacity of $LiMn_2O_4$ is about 148 mA h g^{-1} calculated from reaction [5-3]. Considering that there is 5% excess lithium in the Mn site in $LiMn_2O_4$, the theoretical capacity of this sample is around $148\times(1-3\times5\%)$ = 126 mA h g^{-1}. The fully delithiated $LiMn_2O_4$ with the spinel structure should be written as $Li_{1-(1-3x)}(Li_xMn_{2-x})O_4$ [or $Li_{3x}(Li_xMn_{2-x})O_4$]. Therefore, delithiated $Li_{1.05}Mn_{1.95}O_4$ will be $Li_{0.15}(Li_{0.05}Mn_{1.95})O_4$. The Rietveld refinement results for $LiMn_2O_4$ before and after charge are shown in Table 5.1.

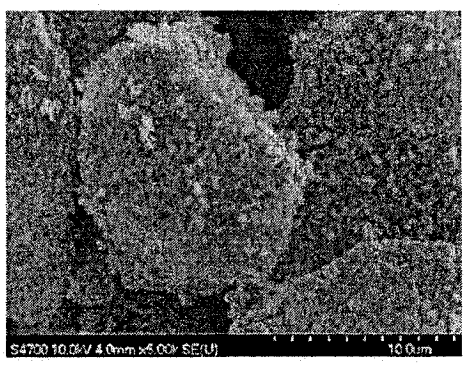

Figure 5.4 SEM micrograph of $LiMn_2O_4$ having a particle size of approximately 10 μm.

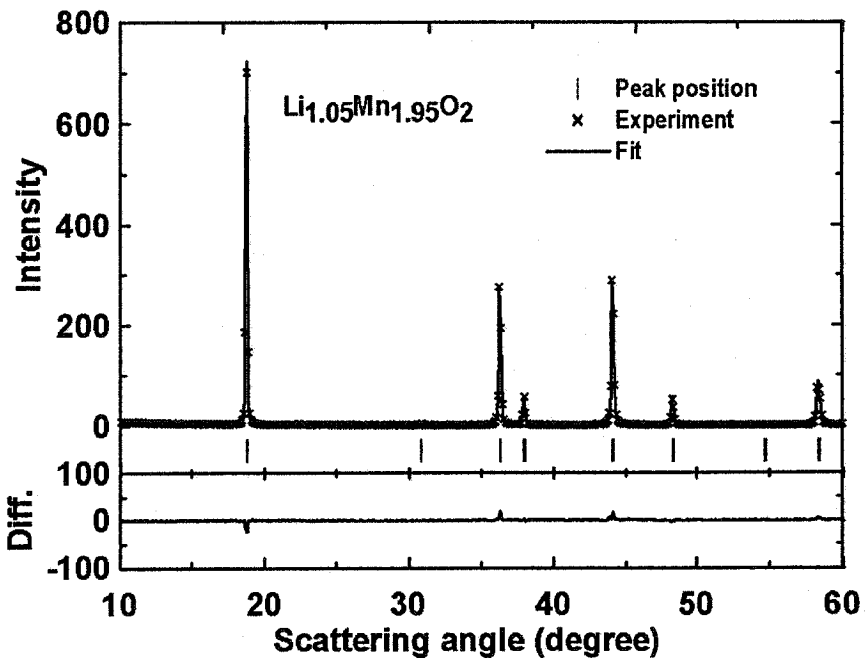

Figure 5.5 X-ray diffraction (XRD) pattern and the corresponding Rietveld refinement of the $LiMn_2O_4$ sample.

The lattice constant of $Li_{0.15}(Li_{0.05}Mn_{1.95})O_4$ obtained from $LiMn_2O_4$ charged to 4.4 V vs. Li is about 8.06 Å, in good agreement with literature values of 8.07 Å for fully charged $LiMn_2O_4$ (x = 0.05) reported by Yang *et al.* [136]. The fully charged $LiMn_2O_4$ (x = 0.05) adopts the same structure as λ-MnO_2, which is the fully delithiated phase of $LiMn_2O_4$ (x = 0). In the later sections of this chapter, the fully charged $LiMn_2O_4$ (x = 0.05) phase is written as λ-MnO_2 for convenience.

Table 5.1. Lattice constants of $LiMn_2O_4$ before and after charging to 4.4 V vs. Li. The space group used for this refinement was Fd3m (#227). The Bragg R-factors are listed.

	$Li_{1.05}Mn_{1.95}O_4$	$Li_{1.05}Mn_{1.95}O_4$ charged to 4.4 V vs. Li $Li_{0.15}[Li_{0.05}Mn_{1.95}]O_4$
a (Å)	8.2321(9)	8.0626(5)
O position	0.2599(6), 0.2599(6), 0.2599(6)	0.2526(7), 0.2526(7), 0.2526(7)
R_{Bragg}	2.5 %	4.2 %

5.1.1 Reaction sequence in EC/DEC

Figure 5.6 shows the SHR vs. T for 100 mg of λ-MnO_2 sample initially heated to 110°C. A detectable exothermic reaction began at approximately 230°C and stopped at around 252°C. The temperature rise (ΔT) is about 22 K. The XRD pattern of the λ-MnO_2 sample after the ARC measurement is shown in Figure 5.7b. [Figure 5.7a shows the XRD pattern of λ-MnO_2 for comparison]. The λ-MnO_2 phase transforms into the β-MnO_2 phase during the ARC experiment as shown in Figure 5.7b. This phase transformation starts at approximately 230°C, which is in good agreement with reference [137].

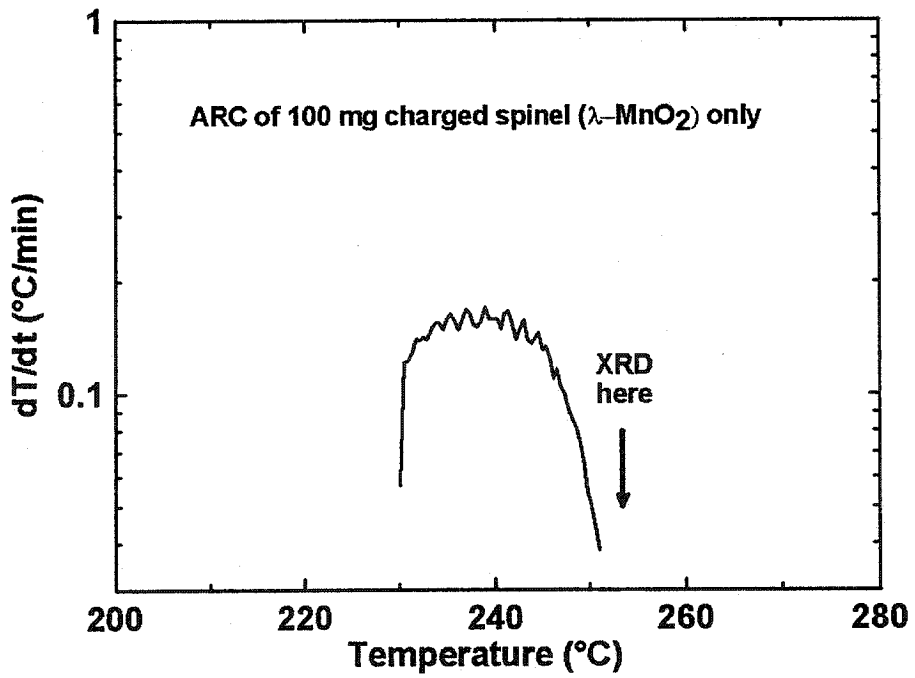

Figure 5.6 Self-heating rate versus temperature for 100 mg of λ-MnO_2 initially heated to 110°C.

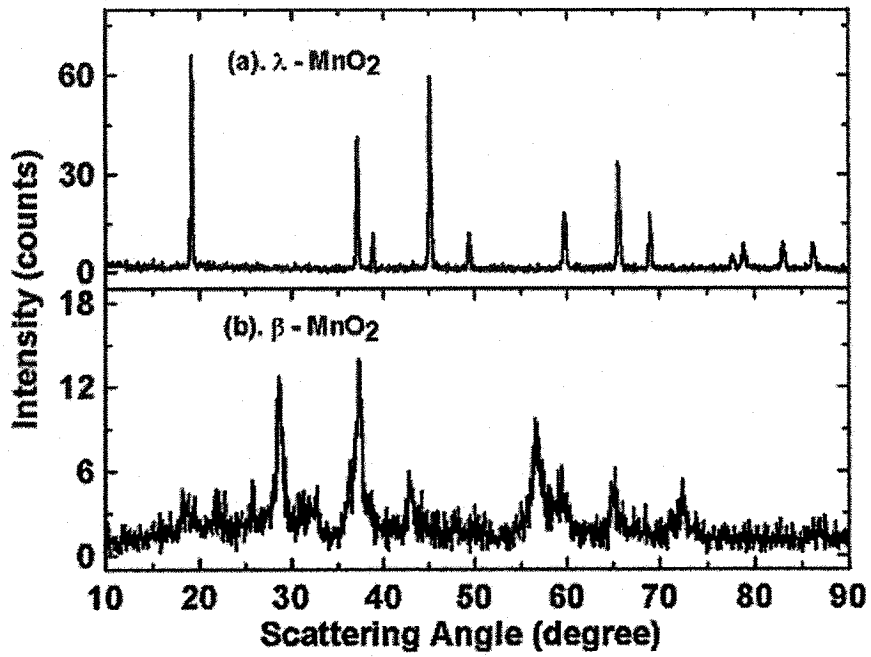

Figure 5.7 X-ray diffraction (XRD) pattern of λ-MnO_2 in panel (a) for comparison. Panel (b) shows the XRD pattern of λ-MnO_2 after the ARC measurement up to 260°C.

The heat, h, released during the phase transition from λ-MnO_2 to β-MnO_2 can be calculated. The total heat capacity of the entire sample (electrode material plus stainless steel ARC tube) is about 0.53 J K^{-1}. Hence, h is 22 K × 0.53 J K^{-1} = 11.6 J. The λ-MnO_2 sample contained 7% by weight of each of PVDF binder and Super S carbon black by mass. The heat released during the phase transition from λ-MnO_2 to β-MnO_2 shown in reaction [5-4] is 12±1 kJ mol^{-1}:

$$\lambda\text{-}MnO_2 \rightarrow \beta\text{-}MnO_2. \qquad (\Delta H = 12\pm1 \text{ kJ mol}^{-1}) \qquad [5\text{-}4]$$

Figure 5.8a shows the SHR vs. T for 100 mg of λ-MnO_2 reacting with 100 mg of EC/DEC initially heated to 110°C (solid line). The exothermic reaction between λ-MnO_2 and EC/DEC starts at 190°C, which is higher than the 150°C onset temperature of 100 mg $Li_{0.5}CoO_2$ (5 μm particle size, 4.2 V) in EC/DEC. This confirms that λ-MnO_2 has a higher thermal stability than $Li_{0.5}CoO_2$.

The experiment described in Figure 5.8a went into thermal runaway at around 220°C. In order to obtain the complete ARC curve of λ-MnO_2 reacting with EC/DEC

solvent, both the amounts of λ-MnO_2 and EC/DEC solvent were decreased to 20 mg and the resulting ARC curve is shown as Figure 5.8b (solid line). The experiment proceeded till 350°C even though no significant exotherms were detected. The temperature rise ΔT, in Figure 5.8b is about 39 K. The main exotherm between charged $LiMn_2O_4$, $LiNiO_2$, and $LiCoO_2$ electrodes reacting with EC/DEC solvent comes from the combustion of solvent by O_2 released from the cathode during decomposition [5, 84, 86]. Even if all the oxygen in 20 mg of λ-MnO_2 could be released during heating in the ARC experiment, 20 mg of EC/DEC is still in excess for the combustion reaction with the released O_2 by a simple calculation [86]. This suggests that the combustion reaction in the ARC experiments in Figure 5.8b is complete. If the amount of λ-MnO_2 is decreased from 20 mg to 15 mg and the amount of EC/DEC is maintained the same, the temperature rise, ΔT, should decrease by approximately one fourth. This expectation assumes that the total heat is proportional to the amount of λ-MnO_2 and the total heat capacity does not change significantly.

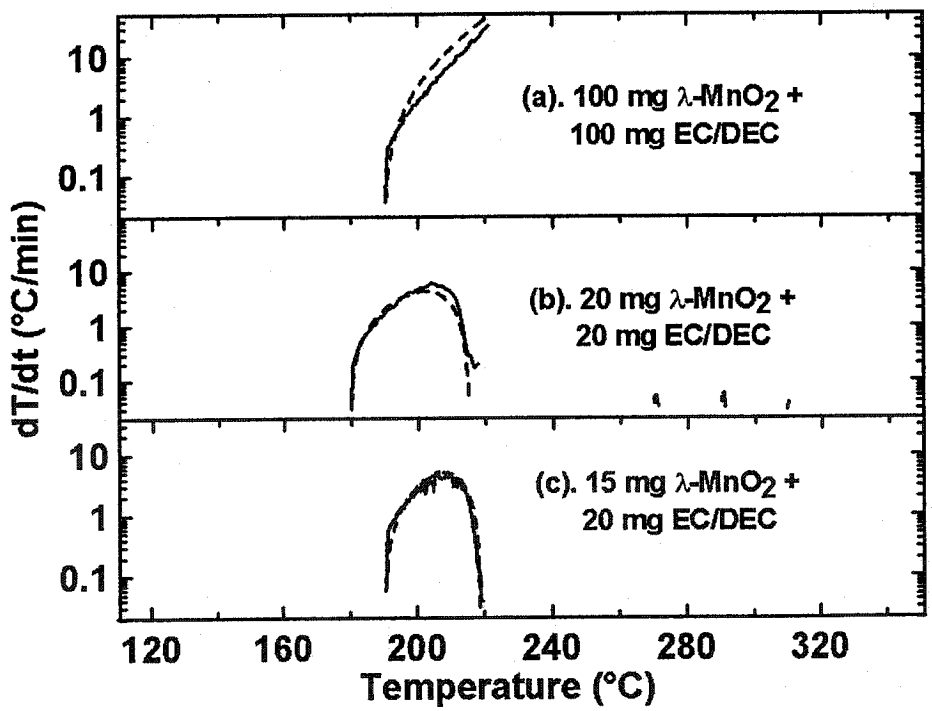

Figure 5.8 ARC curves (solid line) and fits (dashed line) for 100 mg of λ-MnO_2 reacting with 100 mg EC/DEC in panel (a), 20 mg of λ-MnO_2 with 20 mg EC/DEC (b), and 15 mg of λ-MnO_2 with 20 mg EC/DEC (c).

Figure 5.8c shows the SHR vs. T for 15 mg of λ-MnO_2 heated with 20 mg of EC/DEC. The temperature rise in Figure 5.8c is about 30 K, which is close to 75% of the temperature rise, 39 K, of the ARC experiment in Figure 5.8b. The exotherm in Figure 5.8c displays a heat of approximately 14.2 J or 96 kJ mol^{-1} of λ-MnO_2.

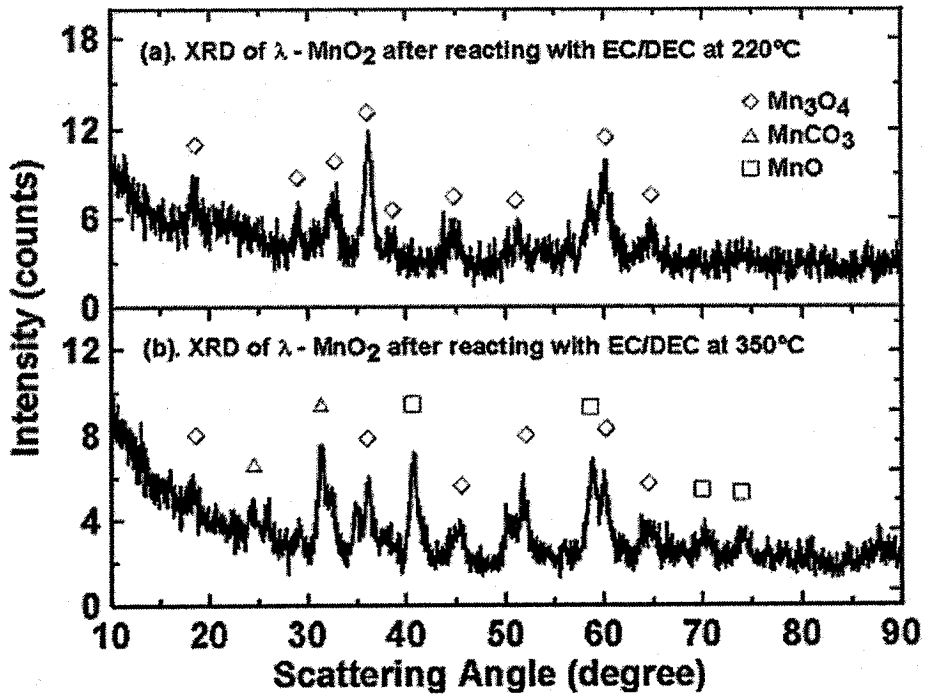

Figure 5.9 X-ray diffraction (XRD) patterns of ARC samples of 15 mg of λ-MnO_2 with 20 mg EC/DEC stopped at 220°C in panel (a) and 20 mg of λ-MnO_2 with 20 mg EC/DEC stopped at 350°C in panel (b).

The XRD patterns of the products after the adiabatic reaction stopped at 220°C (Figure 5.8c) and at 350°C (Figure 5.8b) were taken and are shown in Figures 5.9a and b, respectively. Figure 5.9a shows that λ-MnO_2 reacts with EC/DEC producing Mn_3O_4 at 220°C. At 350°C, the products are the mixtures of three phases, Mn_3O_4, $MnCO_3$ and MnO, as shown in Figure 5.9b. Therefore, reaction sequences between λ-MnO_2 and EC/DEC are described as follow (EC as example):

Process (1) from 180°C to 220°:

$$15\lambda\text{-}MnO_2 + 2C_3H_4O_3 \rightarrow 5Mn_3O_4 + 6CO_2 + 4H_2O, \qquad [5\text{-}5]$$

and (2) above 220°C:

$$Mn_3O_4 + C_3H_4O_3 \rightarrow MnCO_3 + MnO + CO_2 + H_2O. \qquad [5\text{-}6]$$

Reaction [5-6] has not been balanced here since the ratio between $MnCO_3$ and MnO in the final product is unknown. The heat released during the second process is insignificant, ($\Delta T \approx 3$ K) as indicated by the solid line above 220°C in Figure 5.8b. In process (1) the temperature rise, ΔT, in Figure 5.8c, is approximately 30 K. Around 4.9×10^{-5} mol of O_2 was released from the decomposition 15 mg of λ-MnO_2, which quickly combusts EC/DEC as indicated by reaction [5-5]. The released heat, therefore, is calculated to be approximately 290 kJ per mole of O_2 for process (1).

In Chapter 3, the thermal reaction between $Li_{0.5}CoO_2$ and EC/DEC was clearly described. $Li_{0.5}CoO_2$ follows a step-wise decomposition reaction to Co_3O_4, CoO, and finally Co metal while releasing O_2, which reacts immediately with EC/DEC. The resulting exotherm is about 142 kJ mol^{-1} of $Li_{0.5}CoO_2$ or 284 kJ mol^{-1} of O_2 that combusts EC/DEC. By comparing the thermal reaction between $Li_{0.5}CoO_2$ or λ-MnO_2 and EC/DEC solvent, two main conclusions are drawn:

(1). λ-MnO_2 shows higher thermal stability than $Li_{0.5}CoO_2$. The heat of the reaction when λ-MnO_2 reacts with EC/DEC is approximately 96 kJ mol^{-1} of λ-MnO_2. The analogous heat for $Li_{0.5}CoO_2$ is about 142 kJ mol^{-1}.

(2). The heat released from the reaction between EC/DEC solvent and λ-MnO_2 or $Li_{0.5}CoO_2$ depends on the amount of O_2 supplied by decomposition of the electrode materials in the presence of EC/DEC. This heat is approximately 280 ~ 290 kJ mol^{-1} of O_2 for both electrodes.

5.1.2 Reaction kinetics

ARC has been used to obtain the kinetic parameters, such as the activation energy (E_a, kJ mol^{-1}) and the reaction frequency (γ, min^{-1}) for simple reactions [128]. MacNeil *et al.* [138] studied the reactions between $Li_{0.5}CoO_2$ and EC/DEC solvent and obtained the kinetic parameters (E_a = 124 kJ mol^{-1} and $\gamma = 1.48 \times 10^{13}$ min^{-1}). The same method was used here to try to fit the ARC curves of λ-MnO_2 reacting with EC/DEC in the first process [5-5] and to probe its reaction kinetics.

5.1.2.1 Activation energy (E_a)

The reaction order for reaction [5-5] is unknown. It is common to write:

$$\frac{d\alpha}{dt} = k(T)f(\alpha), \qquad [5\text{-}7]$$

where t is the time, T is the temperature, and α is the fractional degree of conversion of reactants ($0 \leq \alpha \leq 1$), k(T) is the rate constant, and f(α) represents the reaction model.

Combining equations [1-7] and [1-8], gives,

$$\frac{dT}{dt} = \Delta T * \gamma * e^{-(E_a / k_B T)} f(\alpha). \qquad [5\text{-}8]$$

Taking the natural logarithm of both sides gives

$$\ln(\frac{dT}{dt}) = \ln[\Delta T * \gamma * f(\alpha)] - \frac{E_a}{k_B T}. \qquad [5\text{-}9]$$

Hence, a plot of the natural logarithm of the initial self-heating rate (*i. e.* when $\alpha \approx 0$) versus 1/T (an Arrhenius plot) has a slope related to the activation energy, E_a, of the process. Figure 5.10 shows the initial SHR (°C/min) vs. 1000/T for 20 mg λ-MnO_2 reacting with the same amount of EC/DEC initially heated to different temperatures, 180°C, 200°C, 210°C, and 220°C, respectively. E_a was found to be approximately 143 kJ mol^{-1}.

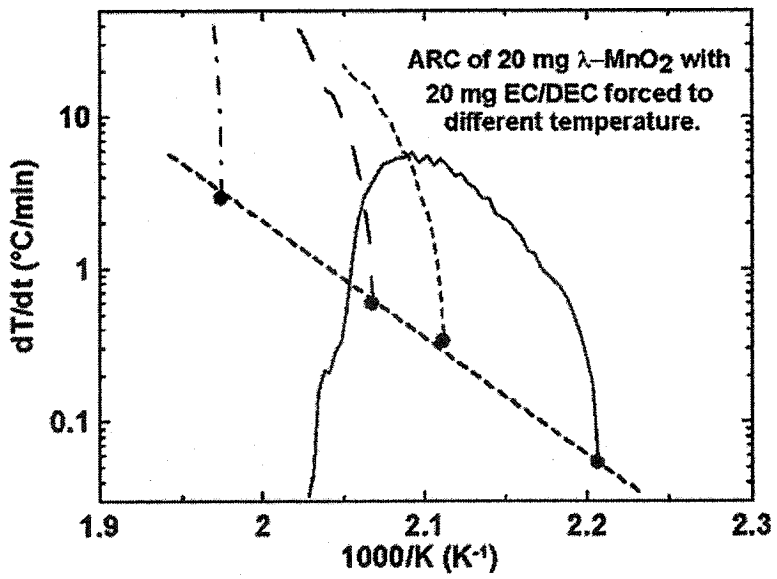

Figure 5.10 Self-heating rate vs. 1000/T (in K^{-1}) of 20 mg of λ-MnO_2 reacting with 20 mg EC/DEC initially forced to different temperature, 180°C, 200°C, 210°C, and 220°C, respectively. The initial points of the experiments ($\alpha_0 \approx 0$) are indicated with black circles.

5.1.2.2 Fitting ARC curves using E_a

In Section 1.4.2, a first order reaction model was used to successfully fit the ARC curve of DTBP decomposition. The kinetic parameters, reaction frequency (γ) and activation energy (E_a), for this reaction were extracted. In order to fit the ARC result for λ-MnO_2 reacting with EC/DEC, the reaction model, $f(\alpha)$, needs to be determined.

Several typical reaction models for thermal decomposition of solid materials are listed in Table 5.2. Model (1) is the first order reaction model. Avrami-Erofeev (A-E) models (2, 3, and 4) have been successfully used in kinetic analyses of many solid phase decomposition reactions, phase transformations, and for the recrystallization of alloys [139]. In A-E models, it is assumed that nucleus formation process is the rate-determining step during the solid phase reactions [139]. The nucleation process involves conversion of a small volume of reactant into a stable particle of product and continued reaction (growth) occurs preferentially at the interfacial zone of contact between these two phases. Sites for the initiation of reaction are widely regarded as occurring exclusively at reactant surfaces [139]. The different exponent, p, applied to the $(-\ln(1-\alpha))$ term in models (2), (3), and (4) represents the nucleation process occurring in one, two, and three dimensions [139].

Table 5.2 Several typical reaction models for thermal decomposition of solids [139].

No.	Reaction model	$d\alpha/dt =$	$k\alpha^m(1-\alpha)^n(-\ln(1-\alpha))^p$		
			m	n	p
1	First order	$k(1-\alpha)$	0	1	0
2	Avrami-Erofeev (I)	$k(1-\alpha)(-\ln(1-\alpha))^{1/2}$	0	1	½
3	Avrami-Erofeev (II)	$k(1-\alpha)(-\ln(1-\alpha))^{2/3}$	0	1	2/3
4	Avrami-Erofeev (III)	$k(1-\alpha)(-\ln(1-\alpha))^{3/4}$	0	1	3/4
5	Autocatalytic	$k\alpha(1-\alpha)$	1	1	0
6	Full model	$k\alpha^m(1-\alpha)^n(-\ln(1-\alpha))^p$	-	-	-

For example, A-E models (Table 5.2) have been widely used in kinetic studies of the thermal decomposition of transition metal oxalates [140-142]. Malecka *et al.* [143] successfully used the A-E model (p = 0.5) to fit the decomposition of CoC_2O_4 in TGA experiments in a helium atmosphere (finally producing Co metal around 400°C). Later in 2003, Malecka *et al.* [144] studied the thermal decomposition of MnC_2O_4 in a helium atmosphere and fitted the result with an A-E model (p = 0.47) (the final product was MnO).

It is very interesting to note that the final product from the thermal decomposition of CoC_2O_4 is pure Co metal but MnO for MnC_2O_4. This difference is possibly attributed to the difference in bond strength between the transition metals and oxygen (listed in Table 5.3). The bond energy between Mn and O in MnO is around 402 kJ mol^{-1}, which is higher than the bond energy between Co and O (around 384 kJ mol^{-1}) [114]. Actually the decomposition process of MC_2O_4 (M is a transition metal, such as Mn, Co, Ni, etc) can be divided into two steps as follows:

Process (1): $MC_2O_4 \rightarrow MO + CO + CO_2$ and [5-10]

Process (2): $MO + CO \rightarrow M + CO_2$. [5-11]

The occurrence of process (2) depends on the ability of CO here to reduce MO to M. For example, MC_2O_4 (M = Ti, Cr, or Mn in the first row of the transition metal in the periodic table) thermally decompose to produce MO in an inert gas atmosphere. Their M-O bond energies are relatively high (672 kJ mol^{-1} for Ti-O, 429 kJ mol^{-1} for Cr-O, and 402 kJ mol^{-1} for Mn-O bond, see Table 5.3) and the thermal decomposition of the oxalates stops after process (1). By contrast, MC_2O_4 (M = Co, Ni, or Cu) thermally decomposes into M metal in inert gas. Their M-O bond energies are only 384 kJ mol^{-1} for Co, 382 kJ mol^{-1} for Ni, and 269 kJ mol^{-1} for Cu.

Table 5.3 The energies ($D°_{298}$, kJ mol^{-1}) of the chemical bonds in diatomic molecules of transition metal oxides (MO) at 298 K [114].

Bond energy	Sc-O	Ti-O	V-O	Cr-O	Mn-O	Fe-O	Co-O	Ni-O	Cu-O
$D°_{298}$	681	672	626	429	402	390	384	382	269

In the ARC experiments, $Li_{0.5}CoO_2$ and λ-MnO_2 electrodes were reduced by EC/DEC solvent instead of CO producing Co metal and MnO (together with $MnCO_3$ and Mn_3O_4), respectively, which are similar to the thermal decomposition reactions of CoC_2O_4 and MnC_2O_4. Based on the similar reduction reactions, it is possible that the A-E model can also be used to analyze the adiabatic reactions of $Li_{0.5}CoO_2$ and λ-MnO_2 electrodes with EC/DEC solvents.

In 2001, MacNeil *et al.* successfully fitted the SHR vs. T for $Li_{0.5}CoO_2$ reacting with EC/DEC solvent using an A-E model [145], an autocatalytic model [138], and a general reaction model listed in Table 5.2. In this section, the SHR vs. T (Figure 5.8b) for 20 mg of λ-MnO_2 reacting with 20 mg of EC/DEC was fitted using models 2-6 in Table 5.2. The best fit was achieved by minimizing the goodness of fit parameter, χ^2, which is defined here as follows:

$$\chi^2 = \frac{1}{N}\sum_{n=1}^{N}\frac{[dT/dt_{\exp} - dT/dt_{cal}]^2}{dT/dt_{\exp}}, \qquad [5\text{-}12]$$

where dT/dt_{exp} and dT/dt_{cal} represent the experimental and calculated self-heating rate (SHR), respectively. The best fit curves are plotted in Figures 5.11b, c, d, e, and f for the A-E models (2), (3), and (4), the autocatalytic model (5), and the full model (6), respectively, listed in Table 5.2. The fitting results are shown in Table 5.4. Obviously, the fit using the full model with m = 0.75, n = 1.49, and p = 0.52 shows the lowest χ^2 and therefore the best fit is achieved. The full model for the best fitting is

$$f(\alpha) = k\alpha^{0.75}(1-\alpha)^{1.49}(-\ln(1-\alpha))^{0.52}. \qquad [5\text{-}13]$$

Then this model was used to simultaneously fit the three ARC curves plotted in Figure 5.8. The fit results are listed in Table 5.5 and best-fit ARC curves are plotted in Figure 5.8 with dashed lines. The ARC results in Figures 5.8b and 5.8c were described well and both reactions were complete. The adiabatic reaction between 100 mg of λ-MnO_2 and 100 mg of EC/DEC proceeded to thermal runaway and the calculated curve predicted this trend.

Table 5.4 Fitting the ARC results for 20 mg of λ-MnO_2 reacting with 20 mg of EC/DEC solvent using the models described in Table 5.2.

Model	γ ($\times 10^{15}$ min^{-1})	α_0	m	n	p	χ^2
Model 2	1.80	0.001	0	1	½	0.42
Model 3	1.74	0.001	0	1	2/3	0.61
Model 4	1.75	0.01	0	1	3/4	0.49
Model 5	3.09	0.01	1	1	0	0.17
Model 6 (full model)	4.28	0.02	0.75	1.49	0.52	0.06

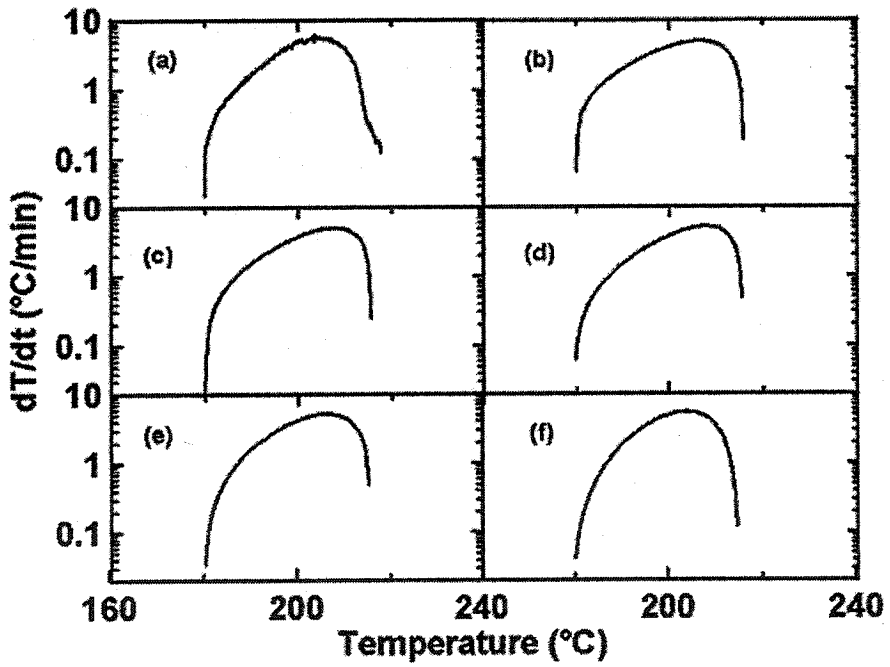

Figure 5.11a The self-heating rate versus temperature for 20 mg λ-MnO_2 reacting with 20 mg of EC/DEC. Figures 5.11b, c, d, e, and f show the best fit SHR vs. T curves calculated using the reaction models 2, 3, 4, 5, and 6 in Table 5.4, respectively.

Table 5.5 Fitting the ARC results for different amounts of λ-MnO_2 reacting with EC/DEC (shown in Figure 5.8) using model 6 described in Table 5.2.

ARC experiments	$\gamma = 4.28\times10^{15}$ min^{-1}; m = 0.75; n = 1.49; p = 0.52		
	ΔT (K)	α_0	χ^2
(1) 15 mg of λ-MnO_2 + 20 mg of EC/DEC	28	0.02	0.19
(2) 20 mg of λ-MnO_2 + 20 mg of EC/DEC	36	0.02	0.06
(3) 100 mg of λ-MnO_2 + 100 mg of EC/DEC	110	0.01	2.62

The extracted kinetic parameters from the ARC results are very useful information. Hatchard *et al.* [51] used the kinetic parameters for the thermal reactions between $Li_{0.5}CoO_2$ or $Li_{0.81}C_6$ with EC/DEC to build up a mathematical model of oven exposure tests for lithium-ion cells. This model predicts the oven-test behavior of MCMB/$LiCoO_2$ cells very well. A similar model could now be built for the oven test for MCMB/$LiMn_2O_4$ cells. The oven tests in Figures 1.5 and 1.6 show that MCMB/$LiMn_2O_4$ cells have higher thermal stability than MCMB/$LiCoO_2$ cells. It is simply because the charged $LiMn_2O_4$ (λ-MnO_2) has higher thermal stability than $Li_{0.5}CoO_2$.

5.1.3 Thermal stability in $LiPF_6$ or LiBOB based electrolyte

Figure 5.12 shows the SHR vs. T for 100 mg of λ-MnO_2 reacting with the same amount of 1.0 M $LiPF_6$ EC/DEC (solid line) or 0.8 M LiBOB EC/DEC (dashed line). Figure 5.12 clearly shows that λ-MnO_2 exhibits higher thermal stability in $LiPF_6$-based electrolyte than in LiBOB EC/DEC and the onset temperatures are about 160°C and 120°C, respectively. By comparing the ARC curves with solid lines in Figure 5.8a and Figure 5.12, it was observed that the addition of $LiPF_6$ into EC/DEC solvent decreases the thermal stability of λ-MnO_2. This is believed to be a result of the instability of $LiPF_6$ during the heating process at around 160°C.

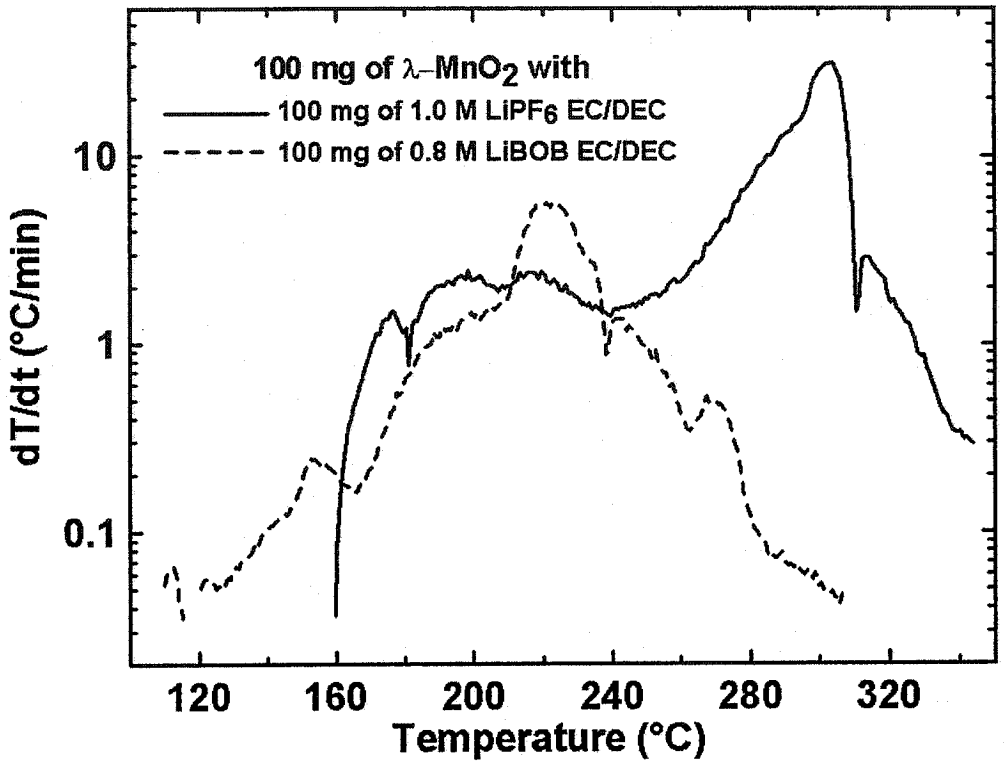

Figure 5.12 Self-heating rate versus temperature for 100 mg of λ-MnO_2 reacting with the same amount of 1.0 M $LiPF_6$ EC/DEC (solid line) or 0.8 M LiBOB EC/DEC electrolyte (dashed line) initially heated to 110°C.

λ-MnO_2 starts to react with LiBOB EC/DEC electrolyte at around 120°C (dashed line in Figure 5.12). Figure 3.27 also shows that the exothermic reaction between $Li_{0.5}CoO_2$ and LiBOB EC/DEC starts at 120°C. The adiabatic reaction between 100 mg of $Li_{0.5}NiO_2$ and the same amount of 0.8 M LiBOB EC/DEC was measured (not shown here). The exothermic reaction starts at 120°C ~ 130°C. The addition of LiBOB into EC/DEC reduces the thermal stability of λ-MnO_2, $Li_{0.5}CoO_2$, and $Li_{0.5}NiO_2$ electrodes. The reason for this still is unknown.

The adiabatic reaction of 100 mg of 0.8 M LiBOB EC/DEC was measured and is shown in Figure 5.13, which is plotted as T (°C) vs. t (minute) (similar to Figure 1.11a). Figure 5.13 shows that there is no exothermic signal during the heating of LiBOB EC/DEC electrolyte up to 350°C. There is no obvious reason that the addition of LiBOB into EC/DEC should decrease the thermal stability of charged lithium transition metal oxide electrode materials.

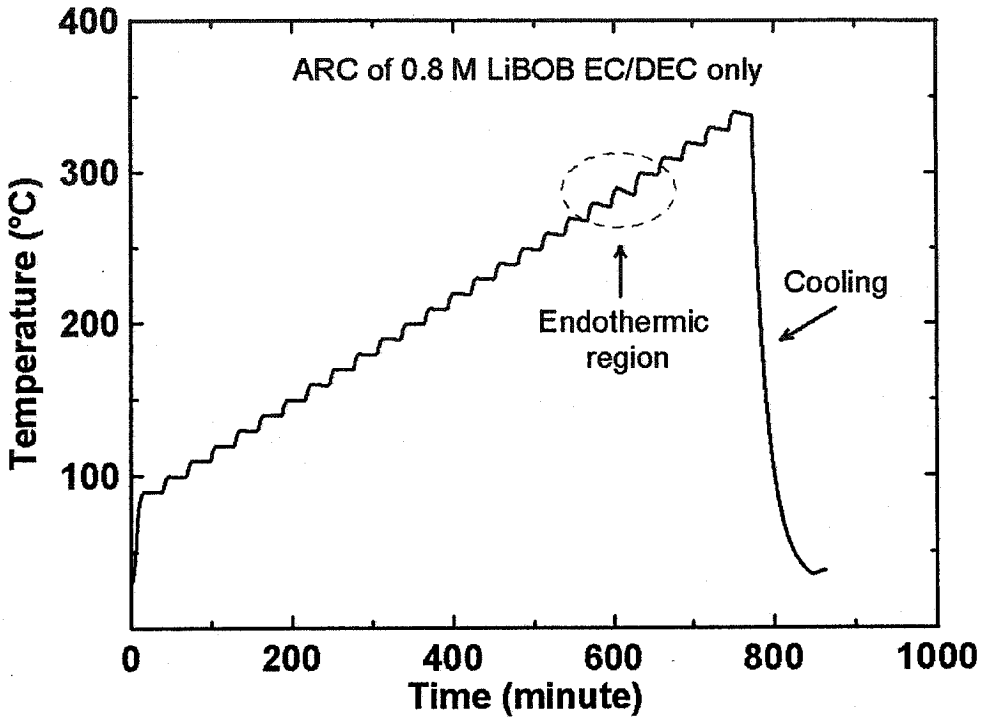

Figure 5.13 Heat-wait-search results [temperature (°C) versus time (minutes)] for 100 mg of 0.8 M LiBOB EC/DEC initially heated to 90°C. A dashed circle indicates an endothermic region.

5.2 Olivine $LiFePO_4$

$LiFePO_4$, which has an olivine structure, is an attractive positive electrode material for LIBs because of its higher stability and low cost. $LiFePO_4$ (triphylite) is a mineral that exists in nature. Pure $LiFePO_4$ is an insulator, which has a relatively low electrical conductivity between $10^{-7} \sim 10^{-9}$ S cm^{-1}. Carbon-coated $LiFePO_4$ can have a conductivity up to 10^{-4} S cm^{-1} [64].

Three different kinds of carbon-coated $LiFePO_4$ with different particle size were obtained from Hydro-Quebec, Canada. Figure 5.14 shows SEM micrographs of the three $LiFePO_4$ samples indicating that they have primary particle sizes of about 3 μm, 7 μm and 15 μm, respectively. The specific surface areas determined by single point BET of the three $LiFePO_4$ samples are 23.9 m^2 g^{-1}, 17.2 m^2 g^{-1}, and 10.8 m^2 g^{-1}, respectively. There are smaller particles in each of the samples on the surface of the larger particles. In order to study the composition of these small particles and the uniformity of the carbon coated on $LiFePO_4$, a few energy dispersive spectroscopy (EDS) dot maps of $LiFePO_4$ (3 μm-size sample) were taken and are shown in Figure 5.15. Figure 5.15a shows the SEM image of a particle having many small particles around 0.1 μm dotted on its surface. The EDS dot maps for C, Fe, O, and P are shown in Figures 5.15b, c, d, and e, respectively. The SEM image and the dot maps of C, Fe, O, and P are similar. This suggests that the small particles shown in panel (a) are $LiFePO_4$ and that the carbon is evenly coated on $LiFePO_4$.

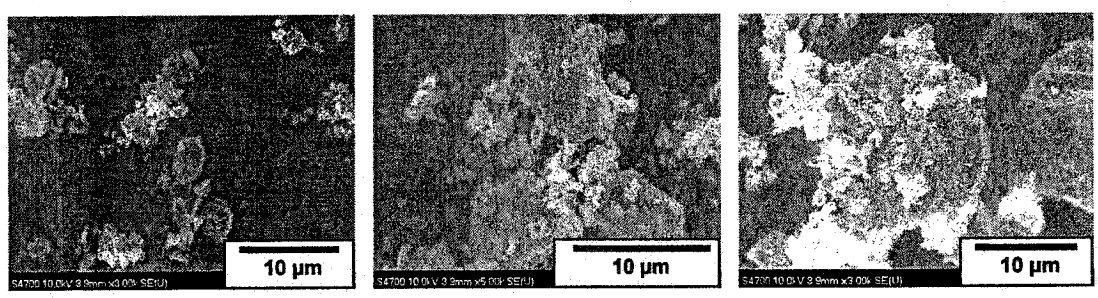

Figure 5.14 SEM micrographs of three carbon-coated $LiFePO_4$ samples having different particle sizes. From the images it can be observed that the diameters of the primary particles are approximately 3, 7, and 15 μm, respectively.

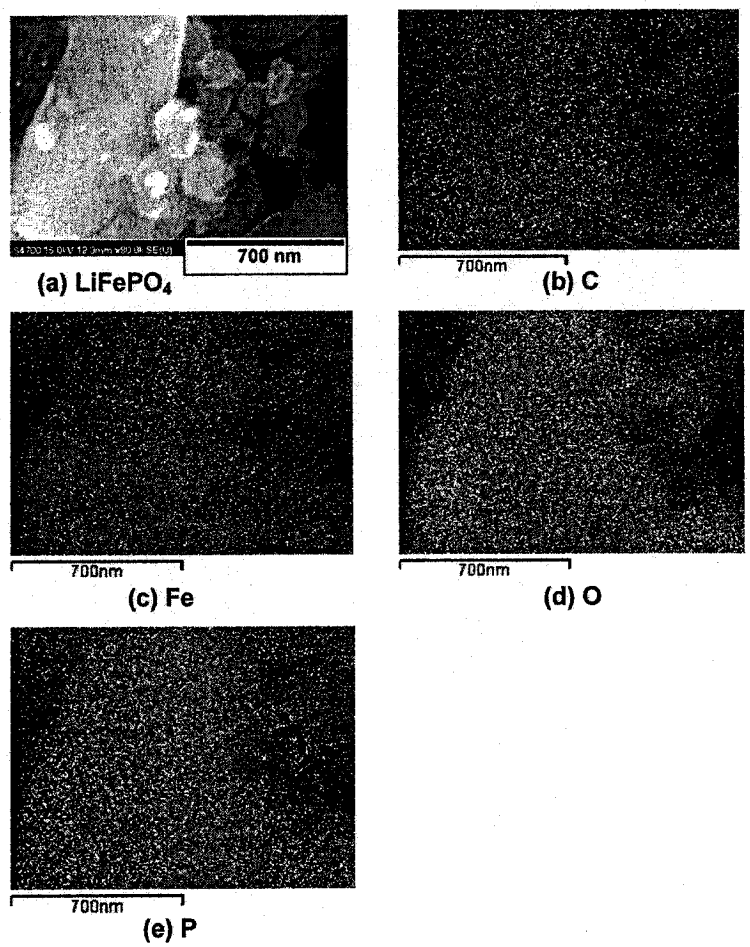

Figure 5.15a The SEM image of a particle having many small particles around 0.1 μm dotted on its surface. The EDS dot maps for C, Fe, O, and P are shown in Figures 5.15b, c, d, and e, respectively. The SEM image and the dot maps of C, Fe, O, and P are similar.

5.2.1 Charged $LiFePO_4$ ($FePO_4$)

$FePO_4$ was obtained by charging $LiFePO_4$ to 3.8 V vs. Li metal as follows:

$$LiFeO_4 \rightarrow Li^+ + FePO_4 + e^-. \qquad [5\text{-}14]$$

The theoretical capacity of $LiFePO_4$ is approximately 170 mA h g^{-1} calculated from reaction [5-14].

Figure 5.16 shows the XRD pattern of $LiFePO_4$ (15 μm) without binder charged to 3.8 V vs. Li metal (in the special cell for powder electrodes shown in Figure 2.5) and its Rietveld refinement as an olivine-type $FePO_4$ single phase. [The XRD pattern and refinement of the starting $LiFePO_4$ material (15 μm) are not shown here]. The lattice constants and atom positions for $LiFePO_4$ (15 μm) before and after delithiation are given in Table 5.6 and agree well with those in reference [146]. Figure 5.16 shows that the delithiation is almost complete, even though a powdered electrode without binder was used in the special cell. There are impurity peaks at about 25.7°, 29.5°, and 35.6°, which are in the positions of some of the strongest Bragg peaks of the $LiFePO_4$ starting material. A small amount of $LiFePO_4$ impurity in the predominantly $FePO_4$ phase is not believed to influence the accelerating rate calorimeter results that follow.

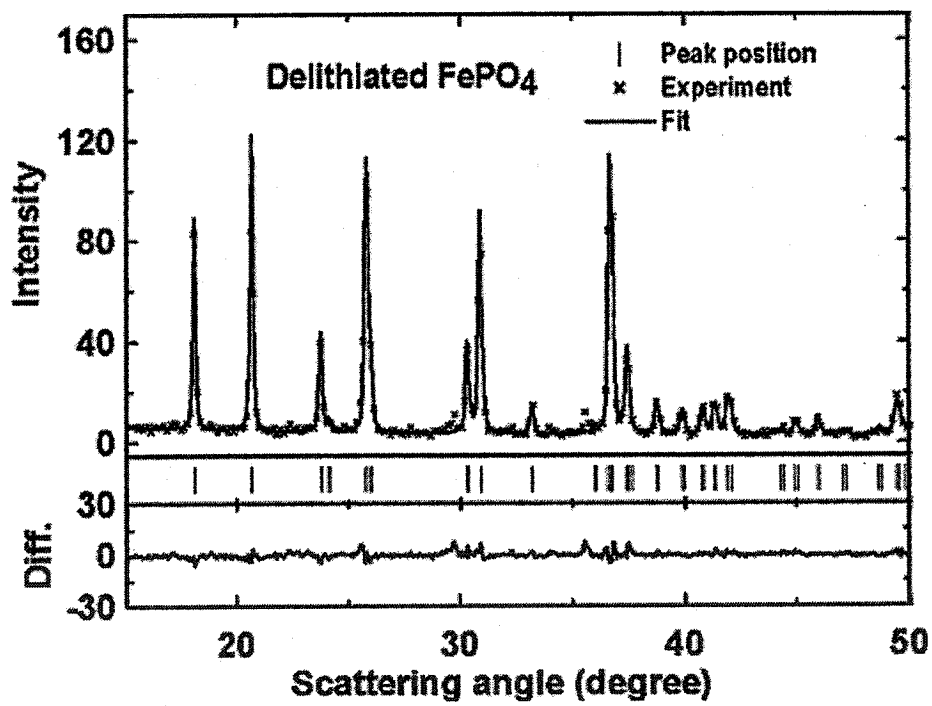

Figure 5.16 XRD pattern of $LiFePO_4$ (15 μm) charged in the special cell (Figure 2.5) without binder to 3.8 V vs. Li metal and its single-phase Rietveld refinement using the $FePO_4$ structure given in Table 5.6.

Table 5.6 Lattice constants and atom positions for 15 μm particle size $LiFePO_4$ and the same material charged to 3.8 V ($FePO_4$) vs. Li/Li^+. The electrochemical cell used to charge the $LiFePO_4$ is shown in Figure 2.5 and there was no binder used in the $LiFePO_4$ electrode (see text). The space group used for the refinement was Pnma (#62). The Bragg R-factors are listed.

	$LiFePO_4$			$FePO_4$		
	a (Å)	*b* (Å)	*c* (Å)	*a* (Å)	*b* (Å)	*c* (Å)
	10.3379(3)	6.0112(2)	4.6973(2)	9.8177(2)	5.7901(2)	4.7810(2)
	x	y	z	x	y	z
Li	0	0	0	-	-	-
Fe	0.2812(3)	¼	0.9716(7)	0.2737(3)	¼	0.9511(7)
P	0.0956(7)	¼	0.4179(6)	0.0933(8)	¼	0.3999(5)
O_1	0.0974(11)	¼	0.7403(8)	0.1165(5)	¼	0.7085(9)
O_2	0.4534(5)	¼	0.2056(10)	0.4465(9)	¼	0.1676(7)
O_3	0.1621(4)	0.0534(8)	0.2861(12)	0.1640(5)	0.0455(6)	0.2490(6)
R_{Bragg}	3.2%			3.7%		

Starting atomic coordinates for $LiFePO_4$ and $FePO_4$ were taken from reference [146].

5.2.2 Thermal stability

Figures 5.17a, b and c show the self-heating rate (SHR) versus temperature for 100 mg of delithiated $LiFePO_4$ (7% PVDF binder) having particle sizes of 3, 7, and 15 μm heated with 100 mg of EC/DEC solvent, respectively. All three charged $LiFePO_4$ samples show high thermal stability with EC/DEC solvent and their onset temperatures for exothermic reaction are greater than 300°C. This is about 150°C higher than the onset temperature of $Li_{0.5}CoO_2$ (5 μm size) reacting with EC/DEC [84, 86]. As the primary particle size of $LiFePO_4$ increases from 3 μm to 15 μm, the self-heating rate at the same temperature decreases. However, the shape of the self-heating rate versus temperature curves for the three samples is almost the same. The self-heating process for the three ARC measurements seems to include two processes, one between 300°C and 320°C and the other starting at 320°C. The latter process did not finish by 350°C, the suggested upper-limit temperature of ARC, at which these experiments were stopped.

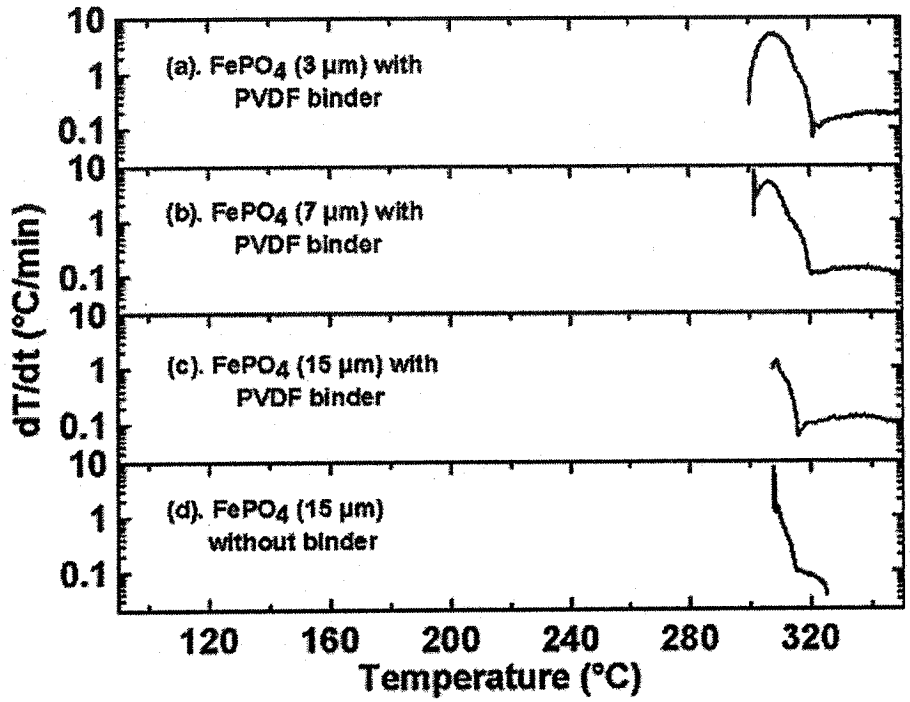

Figure 5.17 Self-heating rate versus temperature for 100 mg of delithiated $LiFePO_4$ (7% PVDF binder) having a primary particle size of 3 µm in panel (a), 7 µm (b) and 15 µm (c), respectively, heated with 100 mg of EC/DEC solvent. Panel (d) shows the self-heating rate versus temperature for 100 mg of delithiated $LiFePO_4$ (15 µm) without binder heated with EC/DEC solvent.

There is a possibility that one of the two processes observed in Figures 5.17a, b, and c could be caused by the PVDF binder. Figure 5.17d shows the results of an identical experiment made on a sample of the 15-µm delithiated $LiFePO_4$ without binder. The self-heating rate versus temperature profile in Figure 5.17d contains only the first reaction process. This suggests that the second reaction process only occurs in the presence of PVDF binder and may be caused by it in some way. After the ARC experiments in Figures 5.17a, b, and c, the ARC samples were opened in an argon filled glove box and XRD patterns were taken with the samples protected from air. In each case the XRD patterns [not shown] changed radically from that shown in Figure 5.16 to a pattern that may represent a new phase of $FePO_4$. The first exothermic process may therefore be associated with the heat released in this solid-solid phase transformation.

Figures 5.18a, b, and c show the SHR vs. T of 100 mg of charged $LiFePO_4$ (3 μm, 7 μm and 15 μm) incorporating 7% PVDF binder, respectively, heated with 100 mg of 1.0 M $LiPF_6$ EC/DEC (solid line) or 100 mg of 0.8 M LiBOB EC/DEC electrolyte (dashed line). Compared to Figure 5.17, with the addition of $LiPF_6$ to EC/DEC solvent, the thermal stability of delithiated $FePO_4$ becomes worse and the onset temperature is approximately 190°C for all three $LiFePO_4$ materials. The effect of the particle size of $LiFePO_4$ on its thermal stability in electrolyte is imperceptible, in contrast to $Li_{0.5}CoO_2$ [86]. The exothermic signal for charged $LiFePO_4$ reacting with $LiPF_6$ EC/DEC between 190 and 235°C is not present when only EC/DEC solvent is used [Figure 5.17], suggesting that this exotherm is caused by the $LiPF_6$ salt. In order to investigate this, Figure 5.18d shows the self-heating rate versus temperature for 100 mg of 1.0 M $LiPF_6$ EC/DEC, without $FePO_4$. The self-heating rate versus temperature in Figure 5.18d is similar to, but not identical to, those in Figures 5.18a, b, and c for $FePO_4$ in 1.0 M $LiPF_6$ EC/DEC, suggesting that $FePO_4$ may play some role.

Figures 5.18 a, b, and c show that the self-heating rate versus temperature profiles for the three $LiFePO_4$ samples reacting with 0.8 M LiBOB EC/DEC electrolyte are similar. The exothermic signal between 240 and 290°C probably results from a LiBOB-related reaction, since this reaction is not present when LiBOB is not included (Figure 5.17). Compared to $LiPF_6$-based electrolyte, LiBOB-based electrolyte shows higher thermal stability with charged $LiFePO_4$. This result is in agreement with reference [60]. Finally, a 100 mg sample of 0.8 M LiBOB EC/DEC alone was heated in the ARC to see whether the exothermic signal between 240 and 290°C would be observed. This experiment showed no detectable reactivity (Figure 5.13) throughout the entire temperature range investigated (100 - 350°C). This suggests that the reactivity observed between LiBOB electrolyte and $FePO_4$ does involve the $FePO_4$.

The results in Figures 5.17 and Figure 5.18 show that the thermal stability of delithiated $LiFePO_4$ in EC/DEC solvent or in electrolyte is not substantially affected by its particle size. However, the situation is totally different for $Li_{0.5}CoO_2$ as described in Section 3.1.2. This difference can be explained from the different reaction mechanism between delithiated $FePO_4$ or $Li_{0.5}CoO_2$ with solvents or electrolytes. In EC/DEC solvent, for example, the small exotherm of $FePO_4$ (Figure 5.17) is caused by a phase transition

that is not affected by the surface area of $FePO_4$. Therefore, the thermal stabilities for the $FePO_4$ samples with different particle sizes (3 μm, 7 μm, and 15 μm) are similar in EC/DEC solvent (Figure 5.17). The thermal reaction of $Li_{0.5}CoO_2$ can be described as a combustion reaction between O_2 from the decomposition of the $Li_{0.5}CoO_2$ sample and EC/DEC. The reaction happens on the surface of $Li_{0.5}CoO_2$ sample. A $Li_{0.5}CoO_2$ sample with a smaller particle size will have a shorter O_2 diffusion path and a larger area of contact with EC/DEC solvent. This obviously causes higher reactivity of $Li_{0.5}CoO_2$ with smaller particle size in EC/DEC. The thermal-stability measurement of $Li_{0.5}CoO_2$ samples with different particle sizes (0.8 μm, 2 μm, and 5 μm) in Section 3.1.2 supports this explanation.

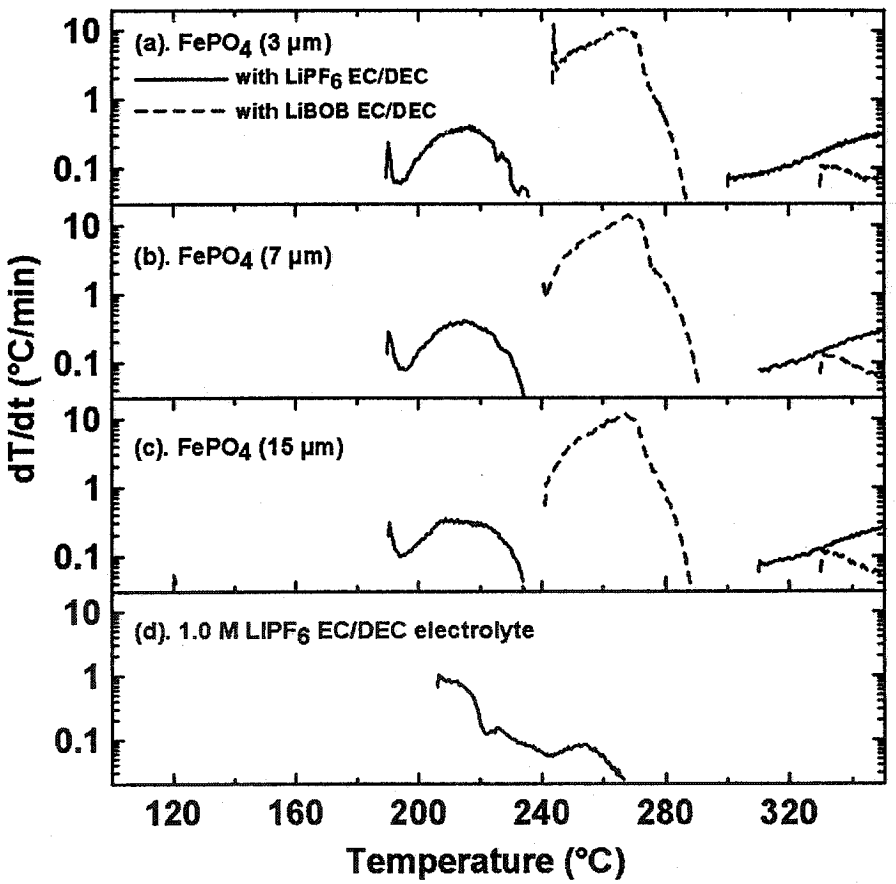

Figure 5.18 Self-heating rate versus temperature of 100 mg of charged $LiFePO_4$ (3 μm, 7 μm, and 15 μm) containing 7% PVDF binder, respectively, heated with 100 mg of 1.0 M $LiPF_6$ EC/DEC (solid line) or 100 mg of 0.8 M LiBOB EC/DEC electrolyte (dashed line).

Table 5.7 Comparison of three positive electrode materials, $LiCoO_2$, $LiMn_2O_4$, and $LiFePO_4$.

Positive electrode materials	$LiCoO_2$ Sample (3)	$LiMn_2O_4$	$LiFePO_4$ Sample (3)
Particle size (μm)	5	20	15
BET surface area ($m^2\ g^{-1}$)	0.1	0.6	10.8
Voltage charged (V vs. Li metal)	4.2	4.4	3.8
Discharged state	$Li_{0.5}CoO_2$	λ-MnO_2	$FePO_4$
Theoretical discharge capacity (mA h g^{-1})	140	148	170
Mass in ARC in mg (discharged cathode material : solvent or electrolyte)	100:100	100:100	100:100
Onset T with EC/DEC (°C)	150	190	300
Temperature rise with EC/DEC (ΔT, K)	190±10	Thermal runaway, calculated to be (90±10)	Around 20
Products after ARC with EC/DEC by XRD	Co metal and $LiCoO_2$	Mn_3O_4, $MnCO_3$ and MnO	Possibly a new phase of $FePO_4$
Main exothermic reaction	Combustion of EC/DEC by O_2	Combustion of EC/DEC by O_2	Phase transition (?)
Heat (kJ per mol of cathode)	Around 142	Around 96	Around 15
Heat (kJ per mol of O_2)	Around 284	Around 290	
Onset T with 1.0 M $LiPF_6$ EC/DEC (°C)	160 ~170	160 ~170	Around 190
Onset T with 0.8 M LiBOB EC/DEC (°C)	120	120	240
Thermal stability affected by particle size	Yes	Yes (?)	No

Prior studies in Section 3.1.1 showed that the reactivity of charged MCMB ($Li_{0.81}C_6$) with LiBOB-based electrolytes is substantially reduced compared to $LiPF_6$-based electrolytes. Therefore, one Li-ion battery system that will have very high tolerance to thermal or electrical abuse is suggested here. $LiFePO_4$/LiBOB EC:DEC/graphite cells will be very safe.

5.3 Thermal-stability comparisons of $LiMn_2O_4$ and $LiFePO_4$ with $LiCoO_2$

The thermal stabilities of $LiMn_2O_4$, $LiFePO_4$, and $LiCoO_2$ are compared in Table 5.7. $LiMn_2O_4$ shows a higher thermal stability than $LiCoO_2$ [sample (3) in Chapter 3 with an average particle size of 5 μm]. The thermal reaction between charged $LiMn_2O_4$ (λ-MnO_2) and EC/DEC starts from 190°C, compared to 150°C for $Li_{0.5}CoO_2$ in EC/DEC (Section 3.1.2). Charged $LiFePO_4$ ($FePO_4$) shows the highest thermal stability among the three electrode materials, showing no obvious SHR signal until 300°C in EC/DEC solvent.

Chapter 6. Layered positive electrode materials in the pseudoternary system, $xLi[Ni_{1/2}Mn_{1/2}]O_2 \bullet yLiCoO_2 \bullet zLi[Li_{1/3}Mn_{2/3}]O_2$ $(x + y + z = 1)$

The purpose of this chapter is to explore positive electrode materials in the $xLi[Ni_{0.5}Mn_{0.5}]O_2 \bullet yLiCoO_2 \bullet zLi[Li_{1/3}Mn_{2/3}]O_2$ pseudoternary system (Figure 6.1), to find materials with high capacity, good cycling performance, and high thermal stability. Due to the complexity of this ternary system, the $Li[Ni_{0.5}Mn_{0.5}]O_2 \bullet LiCoO_2$ binary system was chosen as the starting point. This binary system lies on the bottom axis in the pseudoternary system shown in Figure 6.1.

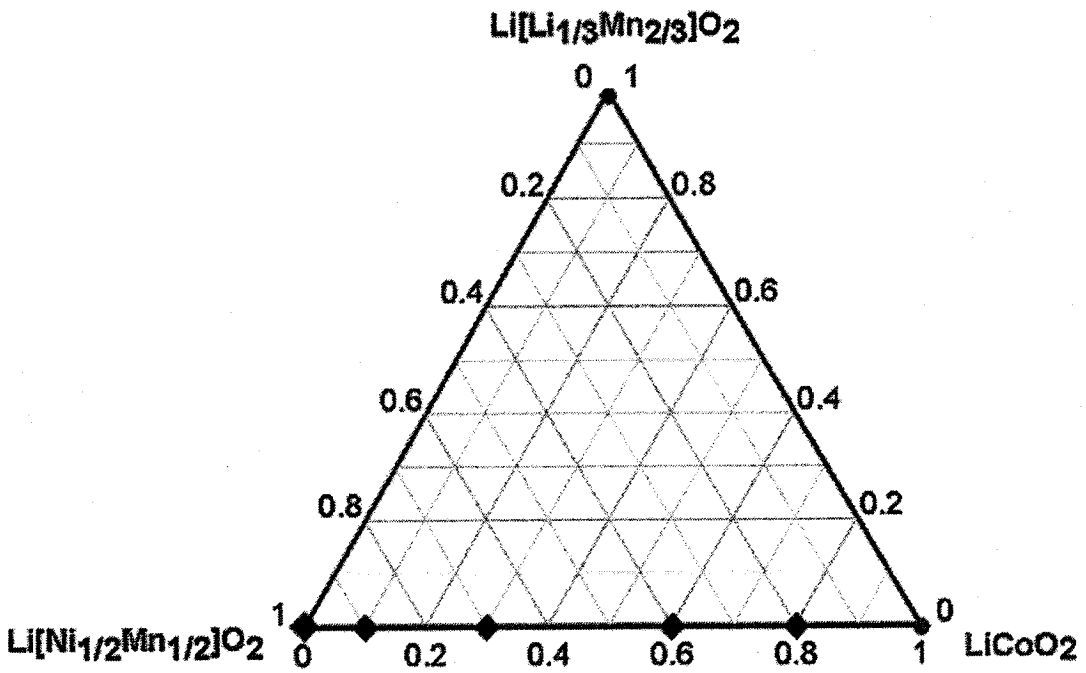

Figure 6.1 The compositions of studied $Li[(Ni_{0.5}Mn_{0.5})_xCo_{1-x}]O_2$ samples (x = 0.2, 0.4, 0.7, 0.9, and 1) indicated with "diamonds".

6.1 $Li[(Ni_{0.5}Mn_{0.5})_xCo_{1-x}]O_2$ (binary system between $Li[Ni_{0.5}Mn_{0.5}]O_2$ and $LiCoO_2$)

The layered materials, $Li[(Ni_{0.5}Mn_{0.5})_xCo_{1-x}]O_2$ $(0 < x \leq 1)$, pioneered by Ohzuku [25] and Lu *et al.* [24] in 2001, are attractive positive electrode materials for lithium-ion batteries because of their high capacity, good capacity retention, high rate capability, and also excellent high temperature stability.

In Section 6.1.1, a series of $Li[(Ni_{0.5}Mn_{0.5})_xCo_{1-x}]O_2$ (x = 0.2, 0.4, 0.7, 0.9, and 1) samples synthesized at 900°C are studied. The synthesis method is described in Section 2.1.3. The compositions of the samples are indicated by "diamonds" in Figure 6.1. The electrochemical properties of the five synthesized samples were tested in coin cells against a Li foil counter electrode. Furthermore, the thermal stability of $Li[(Ni_{0.5}Mn_{0.5})_xCo_{1-x}]O_2$ (x = 0.2, 0.4, 0.7, 0.9, and 1) samples after charging to 4.2 V or 4.4 V vs. Li was compared with 5 μm-size $LiCoO_2$ [sample (3) in Section 3.1.2].

In section 6.1.2, studies of $Li[(Ni_{0.5}Mn_{0.5})_{0.2}Co_{0.8}]O_2$ (x = 0.2) samples synthesized at different temperatures (900°C, 1000°C, and 1100°C) are reported. The results suggest that samples synthesized at 900°C are the best in terms of electrochemical properties and thermal stability.

Section 6.1.3 focuses on the structure, electrochemical properties, and thermal-stability of $Li[(Ni_{0.5}Mn_{0.5})_{0.4}Co_{0.6}]O_2$ (x = 0.4) samples synthesized at 900°C but by different synthesis methods. In Section 6.1.4, the thermal reaction sequence between charged $Li[(Ni_{0.5}Mn_{0.5})_xCo_{1-x}]O_2$ samples and EC/DEC solvent is studied. The reason for the thermal-stability improvement of $Li[(Ni_{0.5}Mn_{0.5})_xCo_{1-x}]O_2$ ($0.2 < x \leq 1$) samples over $LiCoO_2$ is discussed.

6.1.1 $Li[(Ni_{0.5}Mn_{0.5})_xCo_{1-x}]O_2$ (x = 0.2, 0.4, 0.7, 0.9, and 1) samples

6.1.1.1 Sample characterization by SEM, BET, and XRD

Figures 6.2b, c, d, e, and f show SEM micrographs of the $Li[(Ni_{0.5}Mn_{0.5})_xCo_{1-x}]O_2$ (x = 0.2, 0.4, 0.7, 0.9, and 1) samples synthesized at 900°C, respectively. The samples have similar primary particle sizes of approximately 0.3 μm. The SEM micrograph of the $LiCoO_2$ sample [5-μm size, the same sample as $LiCoO_2$ (3) in Section 3.1.2] is included in Figure 6.2a for comparison. The specific surface areas determined by single point BET of the $LiCoO_2$ and $Li[(Ni_{0.5}Mn_{0.5})_xCo_{1-x}]O_2$ (x = 0.2, 0.4, 0.7, 0.9, and 1) samples are approximately 0.1 $m^2 g^{-1}$, 5.7 $m^2 g^{-1}$, 4.4 $m^2 g^{-1}$, 3.5 $m^2 g^{-1}$, 3.6 $m^2 g^{-1}$, and 3.3 $m^2 g^{-1}$, respectively.

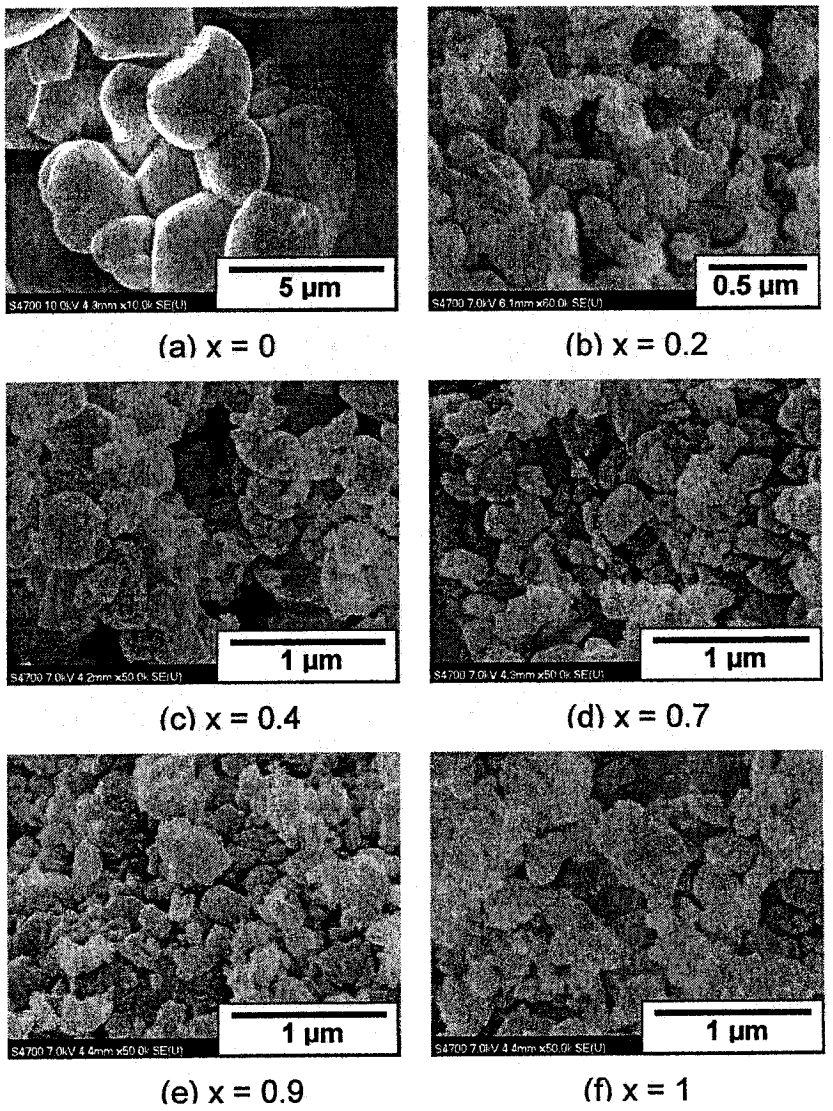

Figure 6.2 SEM micrographs of synthesized $Li[(Ni_{0.5}Mn_{0.5})_xCo_{1-x}]O_2$ samples (x = 0.2, 0.4, 0.7, 0.9, and 1). From the images the average particle size of the $LiCoO_2$ (sample 3 in Section 3.1.2) is approximately 5 µm in panel (a) and the primary particle size of $Li[(Ni_{0.5}Mn_{0.5})_xCo_{1-x}]O_2$ samples is about 0.3 µm.

Figure 6.3 shows the XRD patterns of $Li[(Ni_{0.5}Mn_{0.5})_xCo_{1-x}]O_2$ samples (x = 0.2, 0.4, 0.7, 0.9, and 1) synthesized at 900°C. There are no impurity peaks in the patterns that can be observed. The sharp XRD peaks indicate the high crystallinity of the synthesized samples. The best-fit lattice constants, *a* (Å), *c* (Å), and the *c/a* ratio, versus Co content, (1-x), in $Li[(Ni_{0.5}Mn_{0.5})_xCo_{1-x}]O_2$ are shown in Figure 6.4. As the concentration of Co in

the transition metal layer increases from 0 (x = 1), to 0.8 (x = 0.2), there is a decrease in both the *a* and *c* axes but an increase in the *c/a* ratio in Figure 6.4. These results are in good agreement with reference [23].

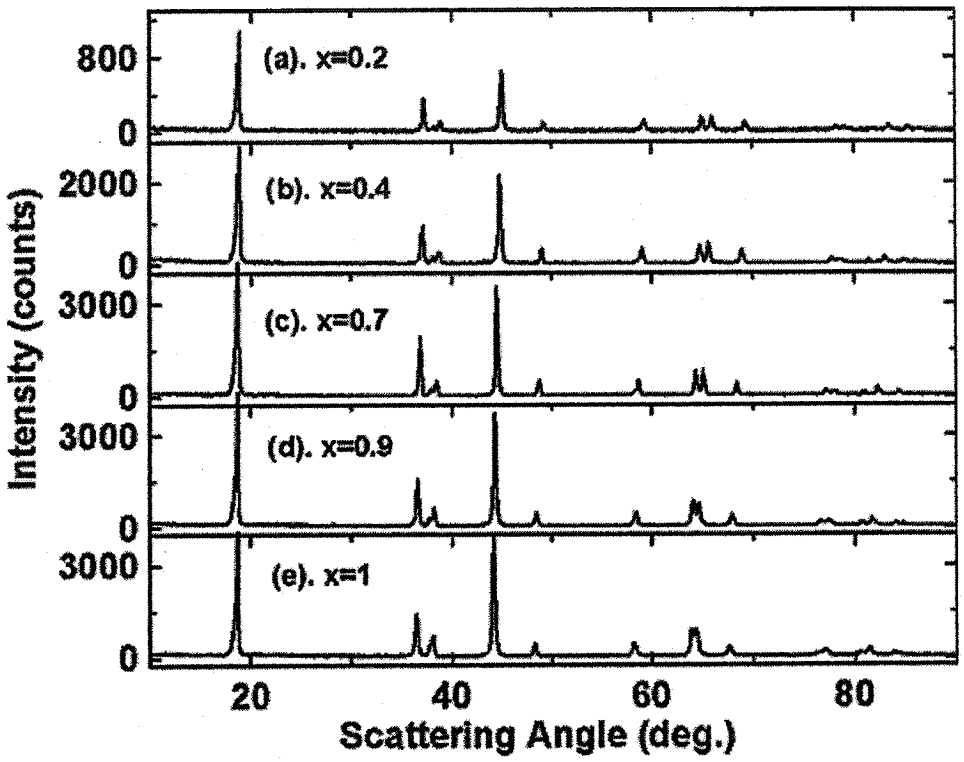

Figure 6.3 X-ray diffraction (XRD) patterns of $Li[(Ni_{0.5}Mn_{0.5})_xCo_{1-x}]O_2$ samples (x = 0.2, 0.4, 0.7, 0.9, and 1).

Figure 6.5 shows the amount of Ni in the lithium layer versus Co content, (1-x), in $Li[(Ni_{0.5}Mn_{0.5})_xCo_{1-x}]O_2$ (x = 0.2, 0.4, 0.7, 0.9, and 1) as determined by Rietveld refinement. Since the radius of the Ni^{2+} cation (0.69 Å) is close to that of Li^+ (0.76 Å), a small amount of Ni may occupy the 3a Li site. If this happens, it is assumed that the same amount of displaced Li occupies the 3b Ni site. Figure 6.5 shows that as the Co content increases from 0 (x = 1) to 0.8 (x = 0.2), the percentage of Ni in the Li layer decreases from approximately 9% to about 0.75%, in agreement with other published work [23]. The reduction in the number of Ni atoms in the Li layer with Co content has a substantial effect on the electrochemical properties of the electrode material that will be described in Section 6.1.1.2.

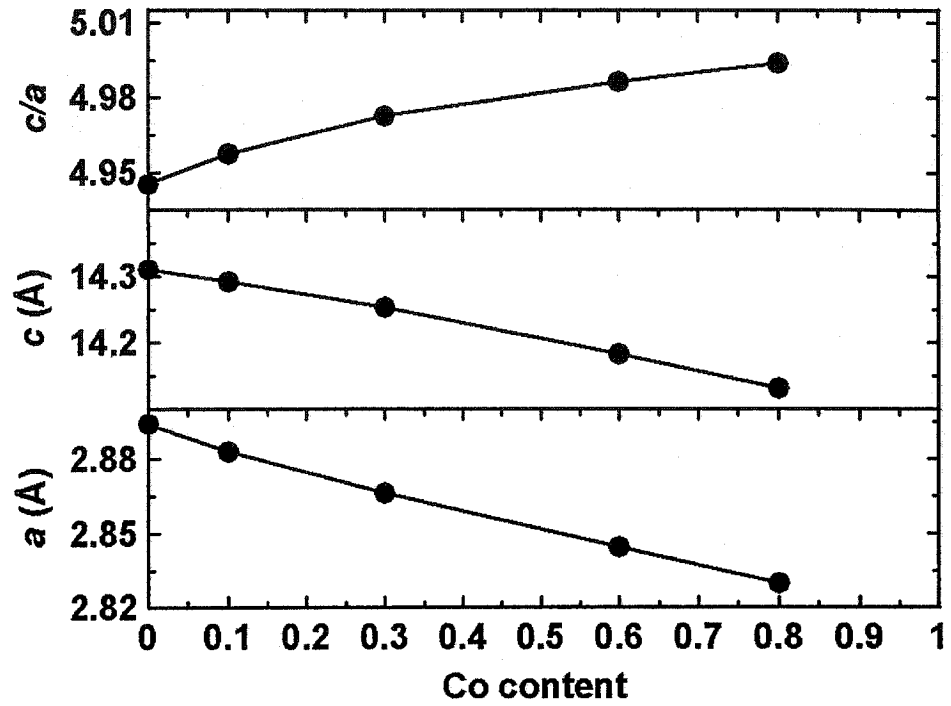

Figure 6.4 The lattice constants, *a* (Å), *c* (Å), and the *c/a* ratio, in $Li[(Ni_{0.5}Mn_{0.5})_xCo_{1-x}]O_2$ samples as the Co content, 1-x, increases.

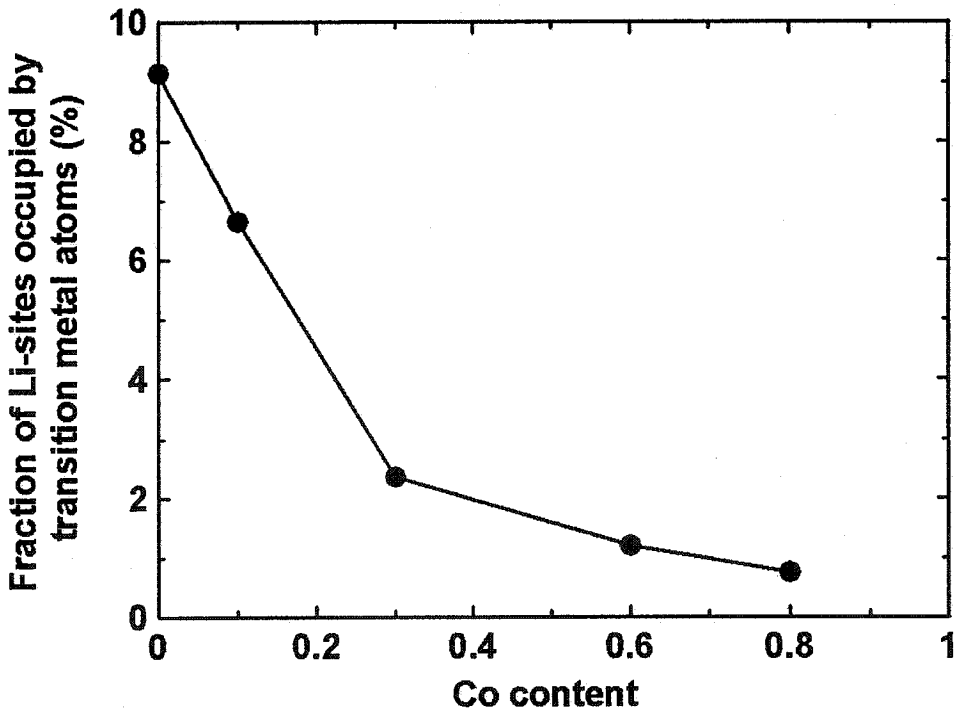

Figure 6.5 Fraction of lithium sites in the lithium layer of $Li[(Ni_{0.5}Mn_{0.5})_xCo_{1-x}]O_2$ occupied by transition metal atoms as a function of Co content, 1-x.

6.1.1.2 Electrochemical properties

Eberman *et al.* [80] studied the change of Li diffusion coefficient in $Li[(Ni_{0.5}Mn_{0.5})_xCo_{1-x}]O_2$ with x by the galvanostatic intermittent titration test (GITT). They found that, from x = 0.2 to x = 0.5, the diffusion coefficient is of the same order as in $LiCoO_2$, 10^{-9} cm^2 s^{-1}. When x increases from 0.5 to 1, the lithium diffusion coefficient falls rapidly to approximately 10^{-11} cm^2 s^{-1} (x = 0.76) and 10^{-12} cm^2 s^{-1} (x = 1). The decrease of lithium diffusion coefficient with x is believed to be related to the increase in the fraction of transition metal atoms (mainly Ni) in the lithium layer described in Section 6.1.1.1. Transition metal atoms in the Li layer apparently block the Li diffusion pathway.

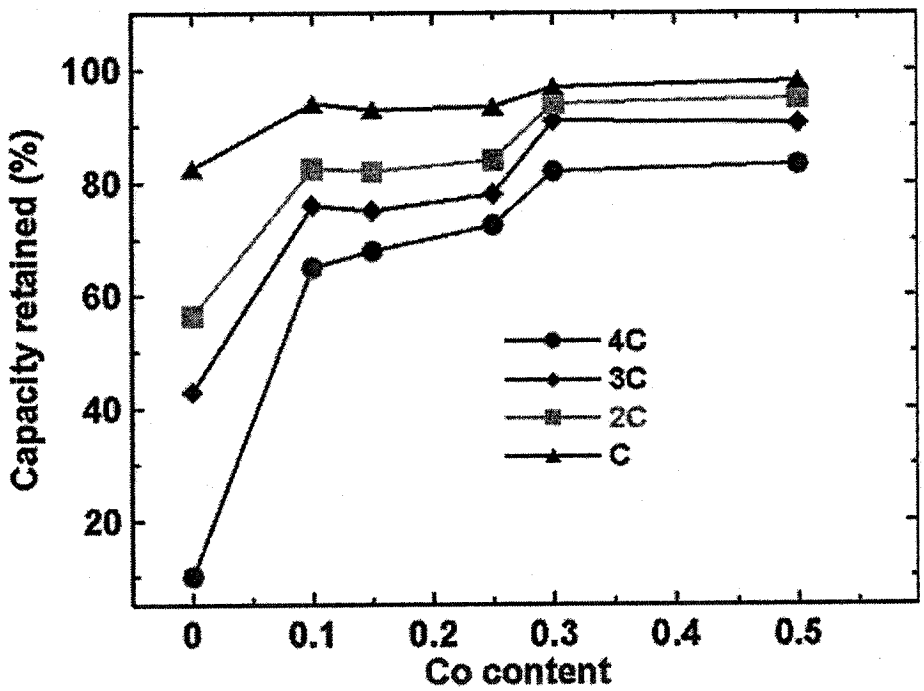

Figure 6.6 Capacity retained (%) as a function of Co content, 1-x, of $Li[(Ni_{0.5}Mn_{0.5})_xCo_{1-x}]O_2$ samples at different rates (4C, 3C, 2C, or C) [79]. Reprinted with permission from the authors.

The decrease of Li diffusion coefficient in positive electrode materials is usually believed to lead to a decrease in rate capability. Chen *et al.* [79] studied the relation between charge-discharge rate capability of $Li[(Ni_{0.5}Mn_{0.5})_xCo_{1-x}]O_2$ and Co content, 1-x, shown in Figure 6.6. Figure 6.6 shows the capacity retained (%) versus Co content in

$Li[Ni_xCo_{1-2x}Mn_x]O_2$ samples cycled between 2.5 and 4.4 V at four different rates, C, 2C, 3C, and 4C. It was found that when a small amount of Co was substituted for Ni and Mn, the rate capability improved greatly. For example, before the addition of Co, the discharge capacity of $Li[Ni_{0.5}Mn_{0.5}]O_2$ (x = 1) at 4C was below 10% of that at C/7. With the addition of only 10% Co in the transition metal layer, the discharge capacity of $Li[(Ni_{0.5}Mn_{0.5})_{0.9}Co_{0.1}]O_2$ (x = 0.9) at 4C improved to 65% of the discharge capacity at C/7. They also observed that the impact of Co content on the rate performance became less obvious when more Co (> 0.25) was substituted for Ni and Mn. This observation of rate capability change with Co content in the transition metal layer of $Li[(Ni_{0.5}Mn_{0.5})_xCo_{1-x}]O_2$ correlates well with the change of Li diffusion coefficient with Co content [80].

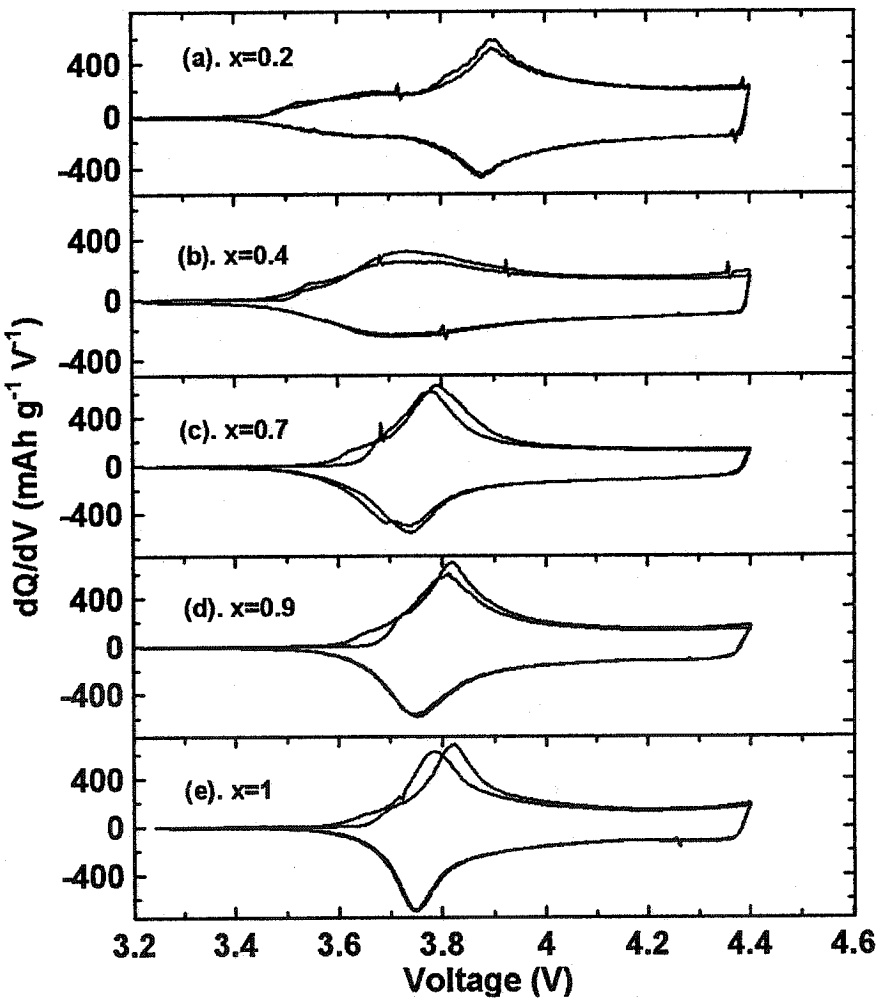

Figure 6.7 The differential capacity (dQ/dV) vs. potential (V) of $Li/Li[(Ni_{0.5}Mn_{0.5})_xCo_{1-x}]O_2$ cells cycling between 2.5 and 4.4 V at a rate of C/20.

Figure 6.7 shows the differential capacity (dQ/dV) vs. potential (V) for $Li/Li[(Ni_{0.5}Mn_{0.5})_xCo_{1-x}]O_2$ (x = 0.2, 0.4, 0.7, 0.9, and 1) cells cycling between 2.5 V and 4.4 V at a C/20 rate. The voltage change which occurred when the current switched from charge to discharge at the upper cutoff potential was observed to slightly increase from 13 mV, 15 mV, 23 mV, 33 mV, to 35 mV for the cells with samples of x increasing from 0.2, 0.4, 0.7, 0.9, to 1, respectively. These observations suggest that higher Co content samples (lower value of x) show higher rate capability, which agrees well with Chen's measurements in Figure 6.6.

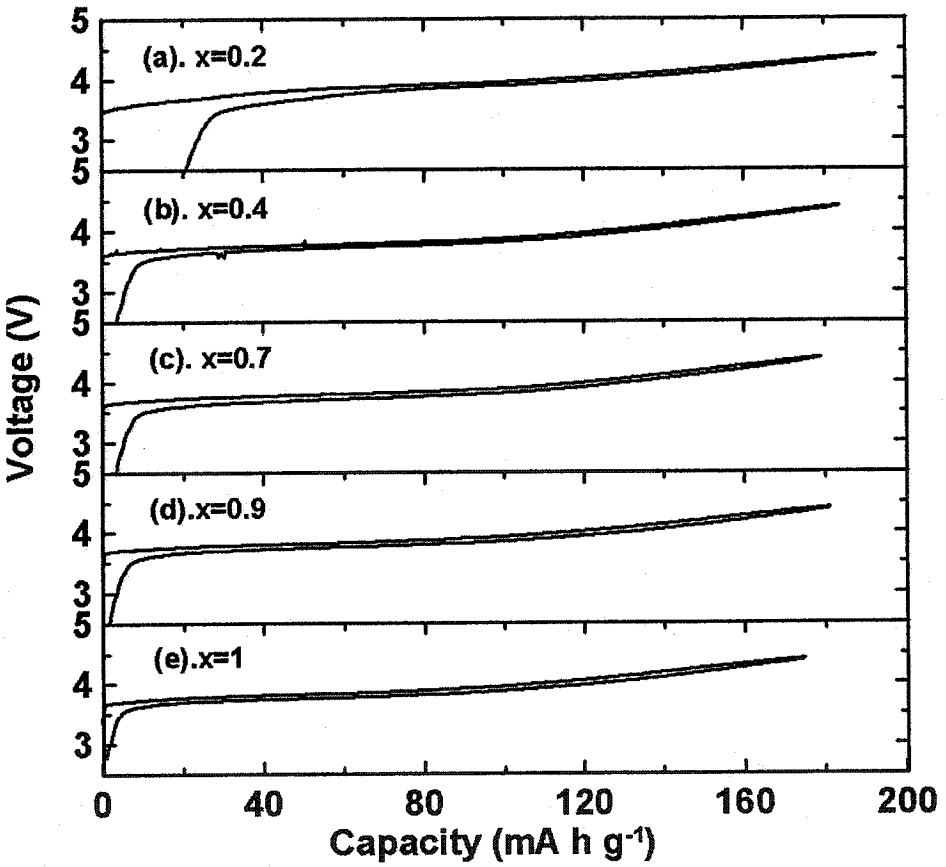

Figure 6.8 Potential (V) versus capacity (mA h g^{-1}) curves for the 1st cycle of the cells with $Li[(Ni_{0.5}Mn_{0.5})_xCo_{1-x}]O_2$ (x = 0.2, 0.4, 0.7, 0.9, and 1) samples synthesized at 900°C.

Figure 6.8 shows the potential (V) versus capacity (mA h g^{-1}) curves for the 1st cycle of the cells with $Li[(Ni_{0.5}Mn_{0.5})_xCo_{1-x}]O_2$ (x = 0.2, 0.4, 0.7, 0.9, and 1) samples synthesized at 900°C. The data was generated from the cells in Figure 6.7. The charge and discharge curves when x is 0.2 (Figure 6.8a) and 0.4 (Figure 6.8b) almost overlap.

This suggests high rate capability for these two samples with a high Co content of 80% and 60%, respectively. When the Co content decreases to 0.3 (x = 0.7 in Figure 6.8c), 0.1 (Figure 6.8d), and 0 (Figure 6.8e), the voltage gap between the charge and discharge curves becomes larger indicating poorer rate capability.

Figure 6.9 shows the discharge capacity (mA h g^{-1}) versus cycle number (2.5 V – 4.4 V, C/4) for the $Li[(Ni_{0.5}Mn_{0.5})_xCo_{1-x}]O_2$ (x = 0.2, 0.4, 0.7, 0.9, and 1) samples. All five samples show good capacity retention (over 80%) for 200 cycles. The samples of $Li[(Ni_{0.5}Mn_{0.5})_xCo_{1-x}]O_2$ with x = 0.2 and 0.4 show a capacity retention of over 85% for 200 cycles at C/4.

The results from Figures 6.6 to 6.9 clearly show the importance of maintaining the high Co content (1-x) in $Li[(Ni_{0.5}Mn_{0.5})_xCo_{1-x}]O_2$ to achieve high rate capability and good cycling performance of $Li[(Ni_{0.5}Mn_{0.5})_xCo_{1-x}]O_2$ samples.

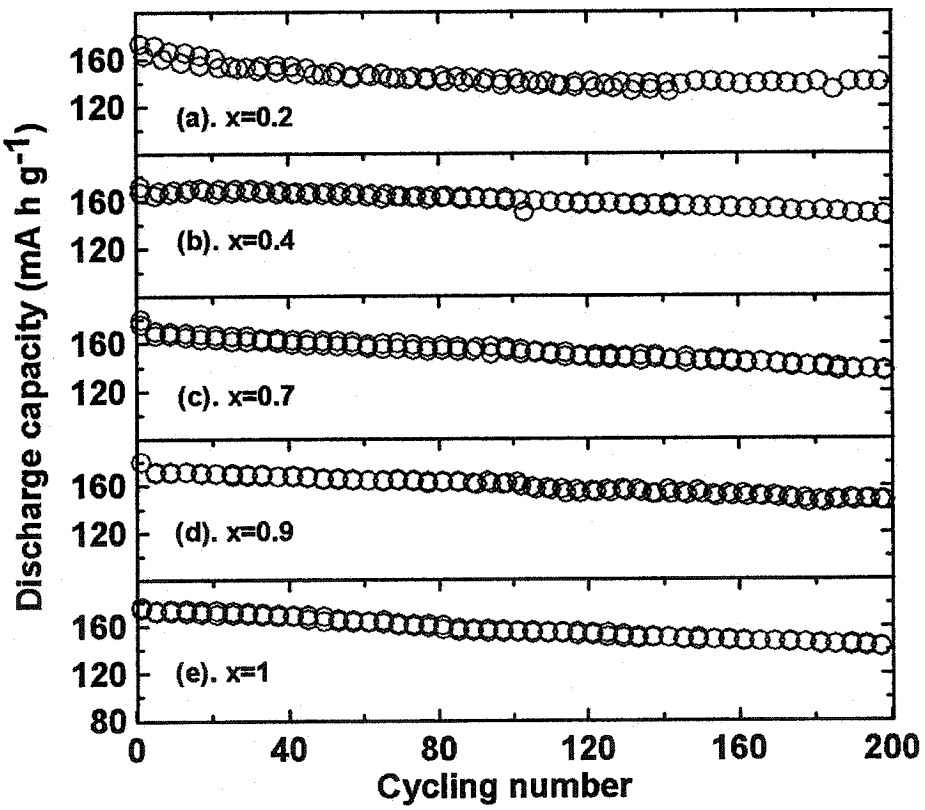

Figure 6.9 Discharge capacity (mA h g^{-1}) versus cycle number (2.5 V – 4.4 V, C/4) for the $Li[(Ni_{0.5}Mn_{0.5})_xCo_{1-x}]O_2$ (x = 0.2, 0.4, 0.7, 0.9, and 1) samples. Data from two cells are shown in each panel.

6.1.1.3 Thermal stability

Figure 6.10 shows the self-heating rate (SHR) versus temperature for the series of positive electrode materials, $Li[(Ni_{0.5}Mn_{0.5})_xCo_{1-x}]O_2$ (x = 0.2, 0.4, 0.7, 0.9, and 1) reacting with EC/DEC solvent. Results are shown for samples charged to 4.2 V (solid lines) or 4.4 V (dashed lines). Results for $LiCoO_2$ charged to 4.2 and 4.4 V are also included for comparison. The $LiCoO_2$, obtained from E-One/Moli Energy Ltd., has an average particle size of 5 μm and is the most stable $LiCoO_2$ sample that has been measured in Jeff Dahn's lab (Section 3.1.2). In the ARC experiments, 100 mg of charged electrode material and 100 mg of EC/DEC were added to the sample tubes.

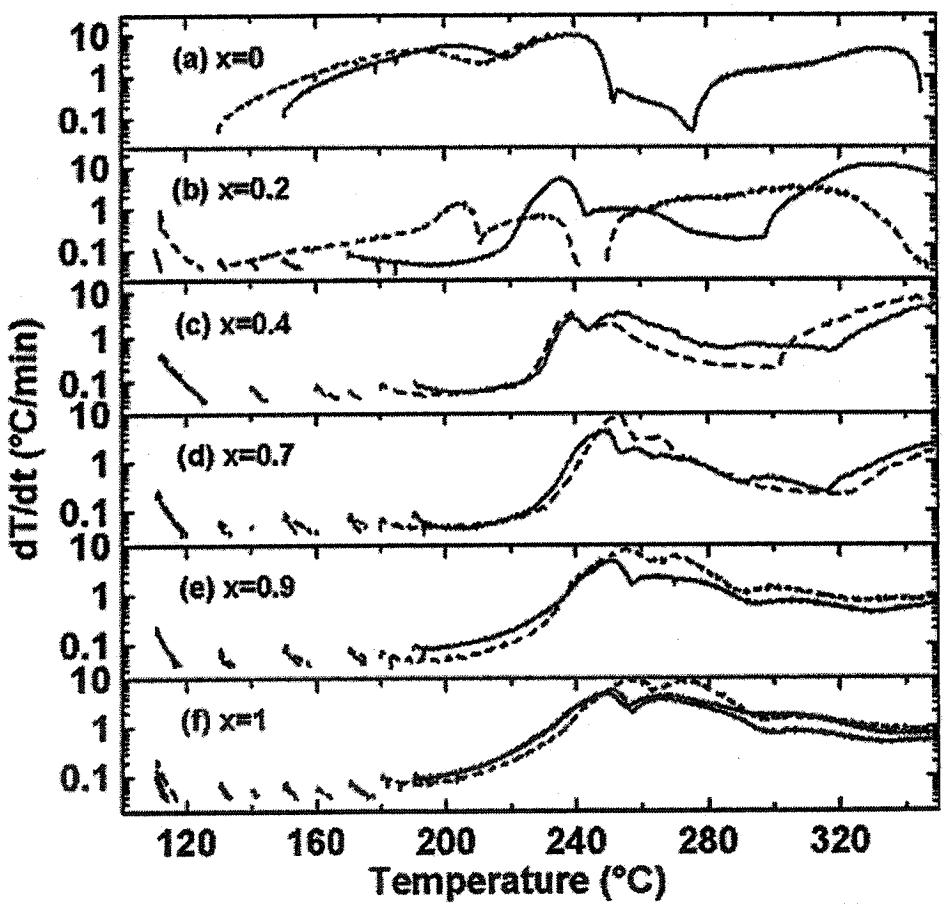

Figure 6.10 Self-heating rate versus temperature for 100 mg of $Li[(Ni_{0.5}Mn_{0.5})_xCo_{1-x}]O_2$ (x = 0.2, 0.4, 0.7, 0.9, and 1) charged to 4.2 V (solid lines) or 4.4 V vs. Li (dashed lines) heated with 100 mg of EC/DEC solvent. Samples were initially heated to 110°C before exotherm searching began.

Figures 6.10a and b clearly show that a sustained exothermic reaction between charged $Li[(Ni_{0.5}Mn_{0.5})_xCo_{1-x}]O_2$ with x = 0.2 (4.2 V) and EC/DEC solvent starts at 170°C, which is 20°C higher than the onset temperature of the reaction between $Li_{0.5}CoO_2$ (4.2 V) and EC/DEC. Furthermore, the self-heating rate of all the $Li[(Ni_{0.5}Mn_{0.5})_xCo_{1-x}]O_2$ samples is much lower than the self-heating rate of $Li_{0.5}CoO_2$ at all temperatures less than 220°C. As the Co concentration (1-x) decreases from 80% in Figure 6.10b to 60% in Figure 6.10c, the onset temperature increases to 190°C and the main exothermic peak shifts to higher temperatures. Figures 6.10c, d, e, and f show that the main exothermic peak for samples charged to both 4.2 and 4.4 V having x = 0.4, 0.7, 0.9 and 1 are about the same. This means that the thermal stability of $Li[(Ni_{0.5}Mn_{0.5})_xCo_{1-x}]O_2$ ($x \geq 0.4$, Co content ≤ 0.6) does not significantly improve with the further increase of the Ni and Mn concentration, x, in the transition metal layer.

Figure 6.11 shows the self-heating rate (SHR) versus temperature of 100 mg of $Li[(Ni_{0.5}Mn_{0.5})_xCo_{1-x}]O_2$ (x = 0.2, 0.4, 0.7, 0.9, and 1) samples charged to 4.2 V reacting with 30 mg of 1.0 M $LiPF_6$ EC/DEC electrolyte. In commercial lithium ion cells, such as 18650-size cells, the mass ratio of electrode material vs. electrolyte used is about 10:3. In this ARC measurement, therefore, the ratio of charged positive electrode material to electrolyte was chosen to be 100 mg:30 mg. Figure 6.11a shows that the $Li_{0.5}CoO_2$ sample starts to react exothermically with 1.0 M $LiPF_6$ EC/DEC electrolyte at about 140°C and displays thermal runaway at approximately 240°C. However, for $Li_{0.5}[(Ni_{0.5}Mn_{0.5})_{0.2}Co_{0.8}]O_2$ (x = 0.2) the onset temperature is about 170°C as shown in Figure 6.11b. Furthermore, the self-heating rate (SHR) in Figure 6.11b is lower than 0.15°C/min until 230°C, while the SHR of $Li_{0.5}CoO_2$ reacting with $LiPF_6$ EC/DEC approaches 0.2°C/min at only 150°C. It is clear that $Li[(Ni_{0.5}Mn_{0.5})_{0.2}Co_{0.8}]O_2$ (x = 0.2, 4.2 V) shows thermal advantages over $LiCoO_2$ (4.2 V) in $LiPF_6$ EC/DEC electrolyte. When x increases to 0.4 and above, the main exothermic peak in the ARC response (Figures 6.11c, d, e, and f) shifts to a higher temperature compared to the main exothermic peak in Figure 6.11b and therefore higher thermal stability is achieved.

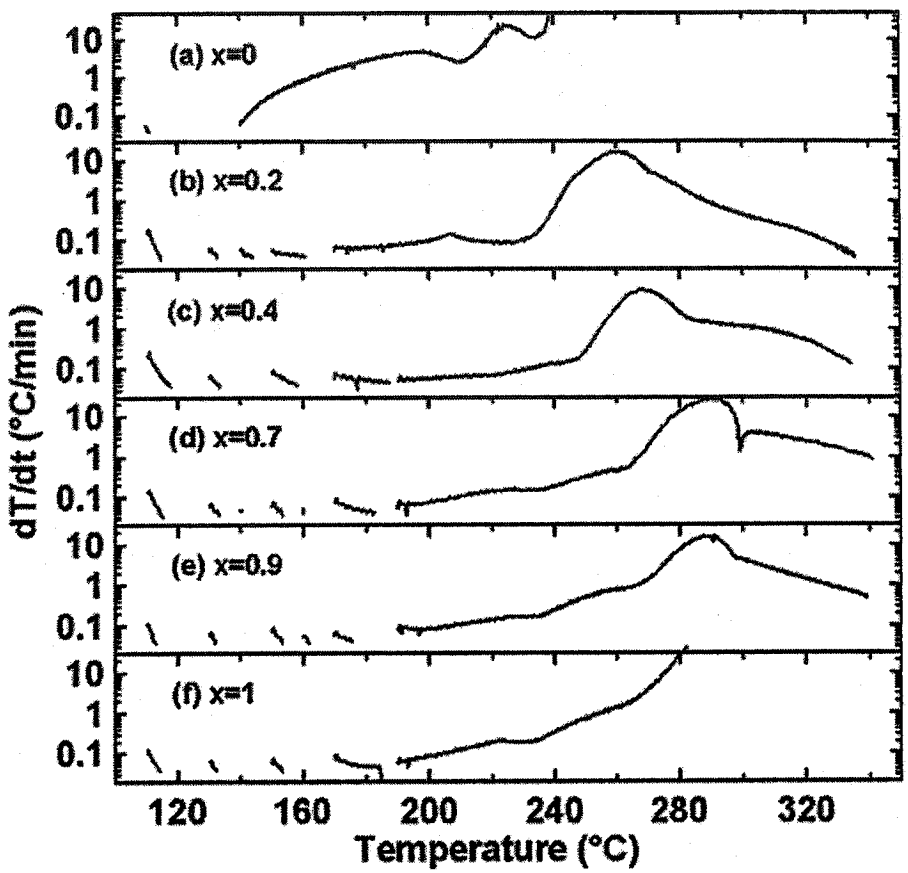

Figure 6.11 Self-heating rate versus temperature for 100 mg of $Li[(Ni_{0.5}Mn_{0.5})_xCo_{1-x}]O_2$ (x = 0.2, 0.4, 0.7, 0.9, and 1) charged to 4.2 V vs. Li heated with 30 mg of 1.0 M $LiPF_6$ EC/DEC electrolyte. Samples were initially heated to 110°C before exotherm searching began.

In summary, $Li[(Ni_{0.5}Mn_{0.5})_xCo_{1-x}]O_2$ samples in the range of $0.2 \leq x \leq 0.7$ give good rate capability and safety. This is because the rate capability and diffusion coefficient decreases with x (but is about constant for $x \leq 0.7$) and the safety increases with x (but is constant for $x \geq 0.4$). The $Li[(Ni_{0.5}Mn_{0.5})_{0.2}Co_{0.8}]O_2$ (x = 0.2) sample charged to 4.2 V still shows much higher thermal stability than $Li_{0.5}CoO_2$.

The effects of synthesis temperature on the electrochemical properties and thermal stability of $Li[(Ni_{0.5}Mn_{0.5})_{0.2}Co_{0.8}]O_2$ (x = 0.2) samples are discussed in next section.

6.1.2 $Li[(Ni_{0.5}Mn_{0.5})_{0.2}Co_{0.8}]O_2$ samples at 900°C, 1000°C, and 1100°C

$Li[(Ni_{0.5}Mn_{0.5})_{0.2}Co_{0.8}]O_2$ (x = 0.2) samples were synthesized at different temperatures, 900°C, 1000°C, and 1100°C. The synthesis method was described in Section 2.1.3.

6.1.2.1 Sample characterization by SEM, BET, and XRD

Figure 6.12 shows SEM micrographs of the $Li[(Ni_{0.5}Mn_{0.5})_{0.2}Co_{0.8}]O_2$ samples synthesized at different temperatures. Figure 6.12 shows that $Li[(Ni_{0.5}Mn_{0.5})_{0.2}Co_{0.8}]O_2$ samples synthesized at 900°C, 1000°C, and 1100°C have primary particle sizes of about 0.2 μm, 0.8 μm, and 8 μm, respectively. The specific surface areas determined by single point BET of the $Li[(Ni_{0.5}Mn_{0.5})_{0.2}Co_{0.8}]O_2$ samples made at 900°C, 1000°, and 1100°C were 5.7 $m^2 g^{-1}$, 1.6 $m^2 g^{-1}$, and 0.9 $m^2 g^{-1}$ respectively.

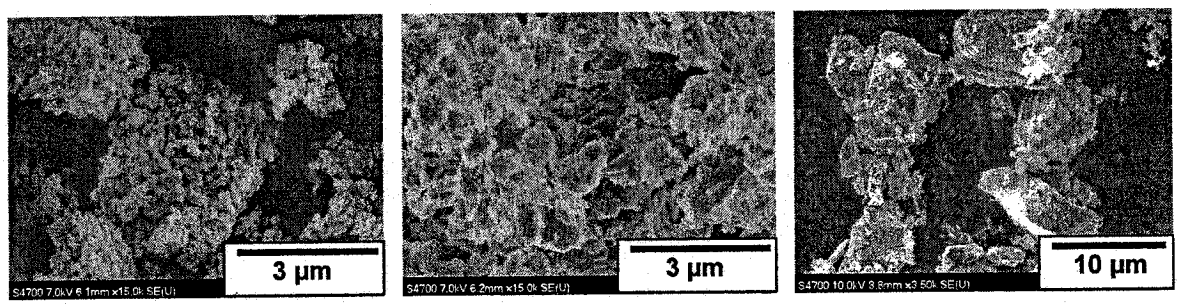

(a) 900°C (0.2 μm) **(b) 1000°C (0.8 μm)** **(c) 1100°C (8 μm)**

Figure 6.12 SEM micrographs of $Li[(Ni_{0.5}Mn_{0.5})_{0.2}Co_{0.8}]O_2$ samples synthesized at 900°C (a), 1000°C (b), and 1100°C (c). The primary particle sizes are approximately 0.2 μm, 0.8 μm, and 8 μm, respectively.

XRD diffraction patterns of $Li[(Ni_{0.5}Mn_{0.5})_{0.2}Co_{0.8}]O_2$ synthesized at 900°C, 1000°C, and 1100°C were measured and are shown in Figure 6.13. There are no obvious impurity peaks. As the synthesis temperature increases from 900°C to 1100°C, the XRD peaks of $Li[(Ni_{0.5}Mn_{0.5})_{0.2}Co_{0.8}]O_2$ become sharper. This suggests that more crystalline samples were obtained at higher synthesis temperatures, as expected.

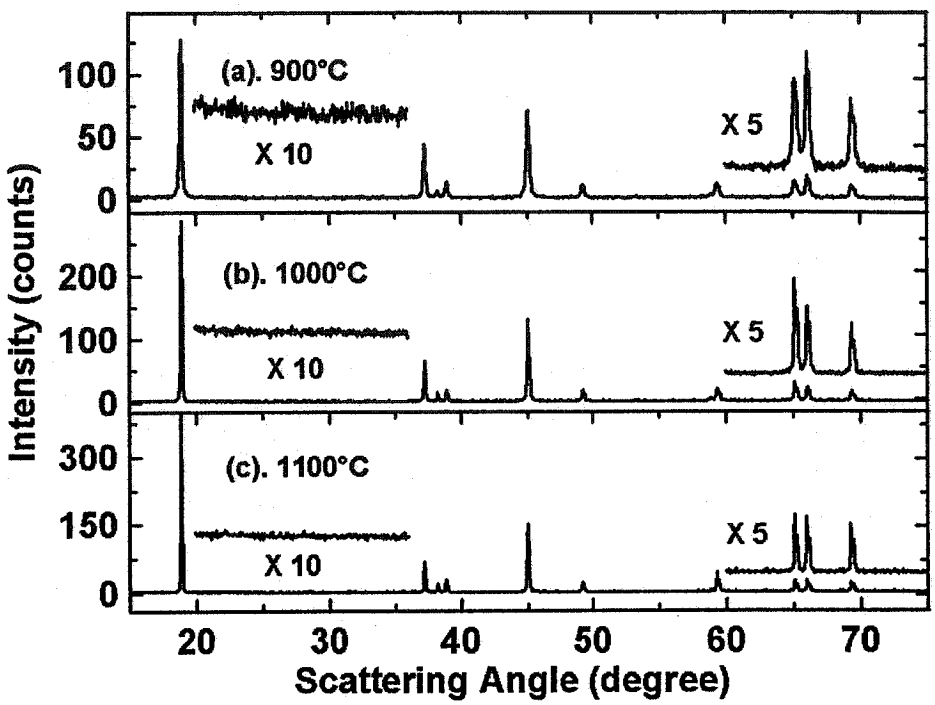

Figure 6.13 X-ray diffraction (XRD) patterns of $Li[(Ni_{0.5}Mn_{0.5})_{0.2}Co_{0.8}]O_2$ synthesized at 900°C (a), 1000°C (b), and 1100°C (c).

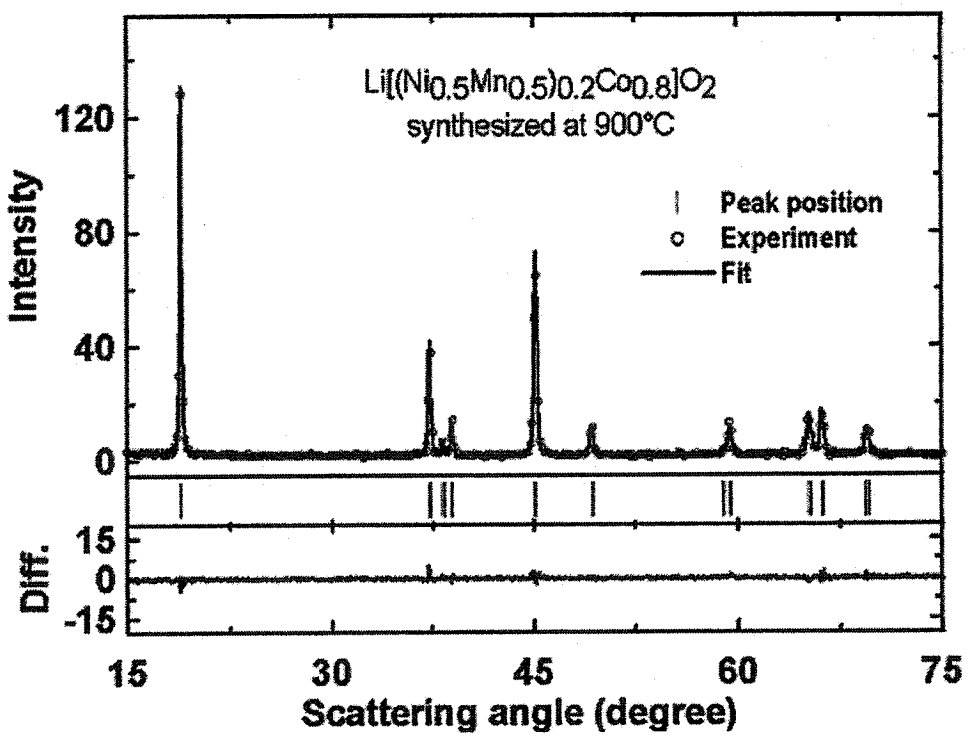

Figure 6.14 XRD pattern of $Li[(Ni_{0.5}Mn_{0.5})_{0.2}Co_{0.8}]O_2$ synthesized at 900°C and fitted pattern using Rietveld refinement.

Figure 6.14 shows the Rietveld refinement for $Li[(Ni_{0.5}Mn_{0.5})_{0.2}Co_{0.8}]O_2$ synthesized at 900°C. The Rietveld refinement results for $Li[(Ni_{0.5}Mn_{0.5})_{0.2}Co_{0.8}]O_2$ synthesized at 900°C, 1000°C, and 1100°C are shown in Table 6.1. The lattice constants (*a* and *c*) of $Li[(Ni_{0.5}Mn_{0.5})_{0.2}Co_{0.8}]O_2$ both increase slightly with synthesis temperature but the atomic percentage of transition metal atoms in the Li layer (u in Table 6.1) is around 0.7% ~ 0.8% for all three samples.

Table 6.1. Lattice constants of $Li[(Ni_{0.5}Mn_{0.5})_{0.2}Co_{0.8}]O_2$ synthesized at different temperatures (900°C, 1000°C, or 1100°C). The space group used for this refinement was R–3m ($^{\#}166$). "u" represents the atomic percentage of transition metal atoms in the Li atom layers. The Bragg R-factors are listed.

	$Li[Ni_{0.1}Co_{0.8}Mn_{0.1}]O_2$ synthesized at different temperature		
	900°C	1000°C	1100°C
a (Å)	2.8276(8)	2.8296(7)	2.8312(4)
c (Å)	14.1187(11)	14.1226(5)	14.1301(7)
O position	0,0,0.2412(4)	0,0,0.2401(9)	0,0,0.2337(10)
u	0.78%	0.70%	0.87%
R_{Bragg}	2.5%	2.7%	3.5%

6.1.2.2 Electrochemical properties

Figure 6.15 shows the differential capacity vs. potential for Li/ $Li[(Ni_{0.5}Mn_{0.5})_{0.2}Co_{0.8}]O_2$ cells cycling between 2.5 V and 4.4 V at a C/20 rate. Three cells were made for each positive electrode sample to test the reproducibility of the electrochemical measurements. The data from the three cells were almost identical and only results for one cell of each sample are shown in Figure 6.15. As the synthesis temperature increases from 900°C in panel (a), to 1000°C in panel (b), and to 1100°C in panel (c), the difference between the potential of the peak in differential capacity measured during charge and discharge increases from 20 mV, to 30 mV, and to 40 mV, respectively. In addition, the voltage change which occurred when the current switched from charge to discharge at the upper cutoff potential increases from 13 mV to 25 mV to 32 mV for the cells with samples synthesized at 900°C, 1000°C, and 1100°C,

respectively. These observations suggest that high temperature heating reduces the rate capability of the samples, probably due to increased primary particle size.

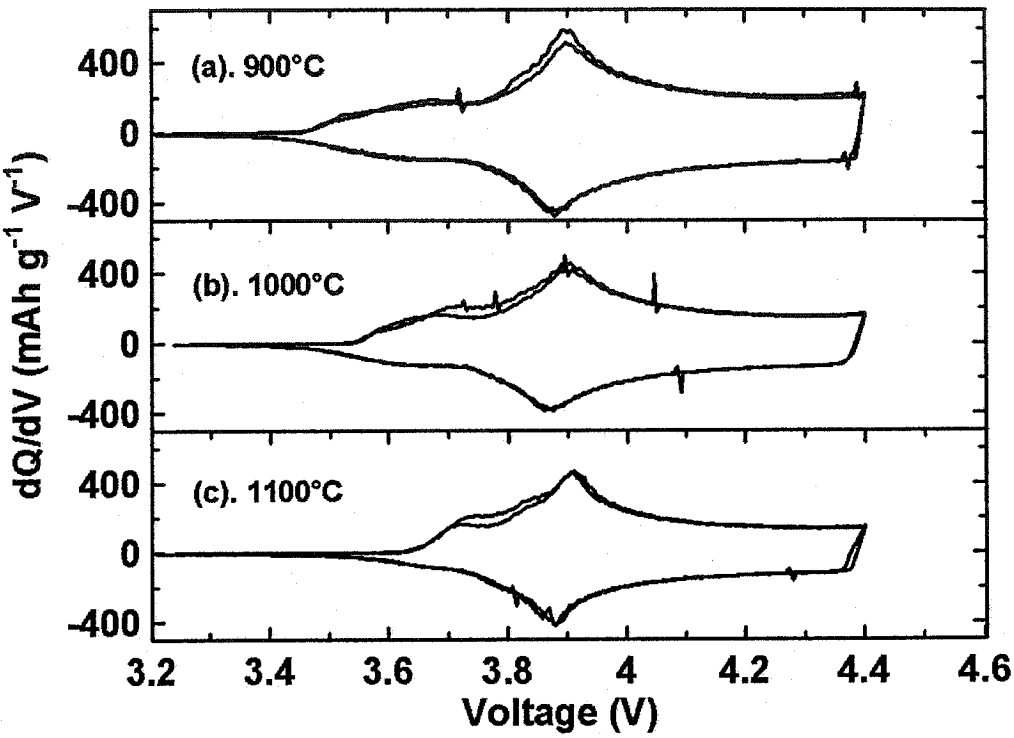

Figure 6.15 Differential capacity (dQ/dV) vs. potential (V) for Li/ $Li[(Ni_{0.5}Mn_{0.5})_{0.2}Co_{0.8}]O_2$ synthesized at 900°C, 1000°C, and 1100°C.

A close examination of Figure 6.15 shows that the capacity below 3.8 V is reduced as the synthesis temperature is increased. It was shown in reference [23] that the capacity below 3.8 V is caused by the oxidation of Ni^{2+} in this compound. Figure 6.16 shows a comparison of dQ/dV vs. V for $Li[(Ni_{0.5}Mn_{0.5})_xCo_{1-x}]O_2$ samples (x = 0.025, 0.05, and 0.1) and $LiCoO_2$ in the low potential region on a expanded scale. The shaded regions represent the difference in the second charge process between the Li/$Li[(Ni_{0.5}Mn_{0.5})_xCo_{1-x}]O_2$ cell and Li/$LiCoO_2$ cell. With the increase of Ni content (x/2) from 0.0125, 0.025, to 0.05 in $Li[(Ni_{0.5}Mn_{0.5})_xCo_{1-x}]O_2$, the shaded area in Figure 6.16 increases approximately from 11, 19, to 28 mA h g^{-1}. Therefore, the shaded region is believed to be caused by the oxidation of Ni^{2+} in the $Li[(Ni_{0.5}Mn_{0.5})_xCo_{1-x}]O_2$ (x = 0.025, 0.05, 0.1) samples. The lower capacity (below 3.8 V) of the $Li[(Ni_{0.5}Mn_{0.5})_{0.2}Co_{0.8}]O_2$ (x = 0.2) samples with a higher synthesis temperature, such as 1100°C in Figure 6.15, is

probably due to a lower Ni^{2+} concentration at the surface of the sample. By charge neutrality, the concentration of Mn^{4+} at the surface is also probably lower and hence the surface is probably Co-rich. An uneven distribution of cations (Ni^{2+}, Co^{3+}, and Mn^{4+}) in the $Li[(Ni_{0.5}Mn_{0.5})_{0.2}Co_{0.8}]O_2$ sample made at high synthesis temperatures (1000°C and 1100°C) should therefore impact their thermal stability, which will be addressed later.

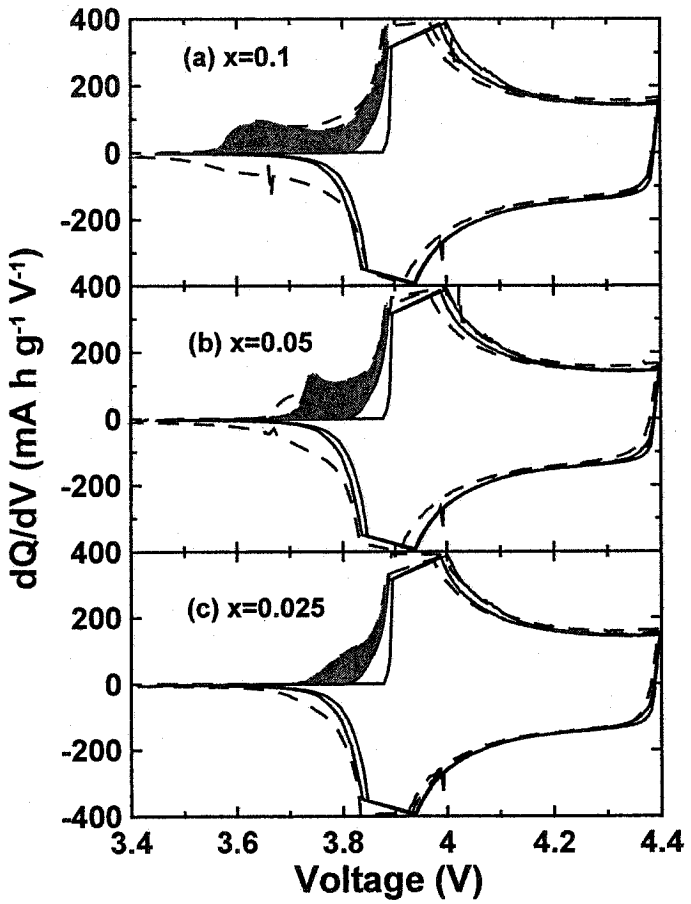

Figure 6.16 Differential capacity (dQ/dV) vs. potential (V) for $Li/Li[(Ni_{0.5}Mn_{0.5})_xCo_{1-x}]O_2$ cells with x = 0.025, 0.05, and 0.1 (dashed line) and $Li/LiCoO_2$ cell (solid line). The shaded region is the capacity due to the addition of Ni atoms [23]. Reprinted with permission from the authors.

Figure 6.17 shows the discharge capacity versus cycle number (2.5 V – 4.4 V, C/4) for the $Li[(Ni_{0.5}Mn_{0.5})_{0.2}Co_{0.8}]O_2$ samples prepared at different temperatures. The results are for the same cells used to produce the dQ/dV vs. V measurements in Figure 6.15. $Li[(Ni_{0.5}Mn_{0.5})_{0.2}Co_{0.8}]O_2$ synthesized at 900°C shows the highest discharge

capacity of about 170 mA h g^{-1} and the best capacity retention. About 85% of the initial capacity remained after 200 cycles.

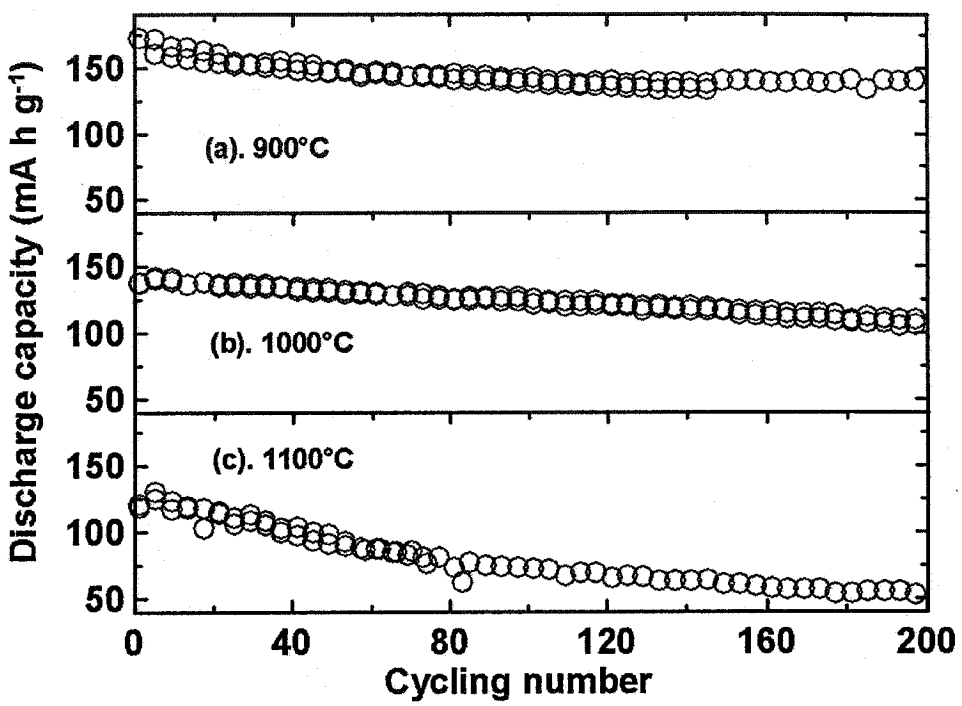

Figure 6.17 Capacity (mA h g^{-1}) vs. cycle number for Li/Li[$(Ni_{0.5}Mn_{0.5})_{0.2}Co_{0.8}$]$O_2$ cells (electrode material synthesized at 900°C, 1000°C, and 1100°C). Data for two cells are shown in each panel.

Figure 6.18 shows the potential (V) versus capacity (mA h g^{-1}) curves for the cells with Li[$(Ni_{0.5}Mn_{0.5})_{0.2}Co_{0.8}$]$O_2$ prepared at different temperatures. The dashed and solid lines show the potential versus capacity for the 1st and 175th cycle, respectively. The cell with Li[$(Ni_{0.5}Mn_{0.5})_{0.2}Co_{0.8}$]$O_2$ synthesized at 900°C has the largest capacity and the smallest charge-discharge polarization during both the 1st and 175th cycles. The results in Figures 6.17 and 6.18 indicate that the Li[$(Ni_{0.5}Mn_{0.5})_{0.2}Co_{0.8}$]$O_2$ sample synthesized at 900°C has a larger specific capacity, better rate capability, and better capacity retention than the samples synthesized at 1000°C or 1100°C.

The Li[$(Ni_{0.5}Mn_{0.5})_{0.2}Co_{0.8}$]$O_2$ sample synthesized at 1100°C shows the lowest capacity around 160 mA h g^{-1} during the first charging process. This may have been caused by partial lithium loss when the sample was fired at 1100°C.

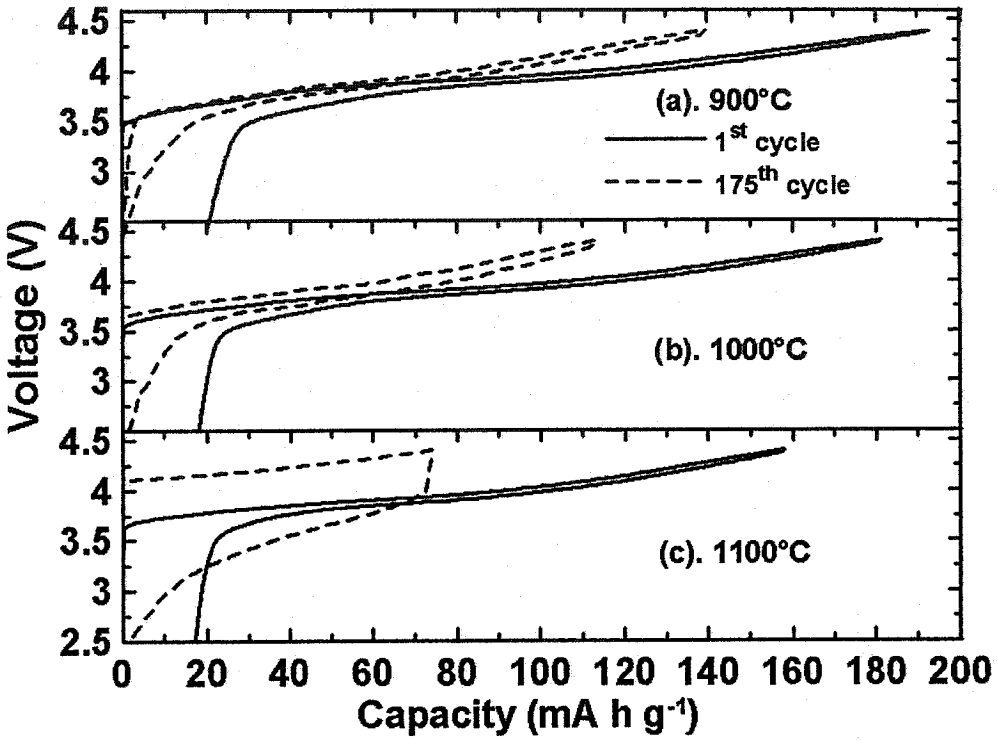

Figure 6.18 Voltage (V) vs. capacity (mA h g^{-1}) for $Li[(Ni_{0.5}Mn_{0.5})_{0.2}Co_{0.8}]O_2$ (900°C, 1000°C, and 1100°C) charged to 4.4 V for the 1st (solid) and 175th cycles (dashed line). The cells were charged and discharged using a nominal C/4 rate.

6.1.2.3 Thermal stability

Figure 6.19 shows the SHR vs. T for 100 mg of $Li[(Ni_{0.5}Mn_{0.5})_{0.2}Co_{0.8}]O_2$ (900°C, 1000°C, and 1100°C) charged to 4.2 V (solid line) or 4.4 V (dashed line) reacting with 100 mg of 1.0 M $LiPF_6$ EC/DEC electrolyte initially heated to 110°C. $Li[(Ni_{0.5}Mn_{0.5})_{0.2}Co_{0.8}]O_2$ (4.2 V) prepared at 900°C in panel (a) shows the highest thermal stability and no substantial exothermic signal until 210°C, compared with the onset temperature of 150°C for $Li_{0.5}CoO_2$ (5 μm) charged to 4.2 V vs. Li metal in EC/DEC solvent. All three samples of $Li[(Ni_{0.5}Mn_{0.5})_{0.2}Co_{0.8}]O_2$ charged to 4.4 V vs. Li show an ARC onset temperature around 130°C in EC/DEC solvent.

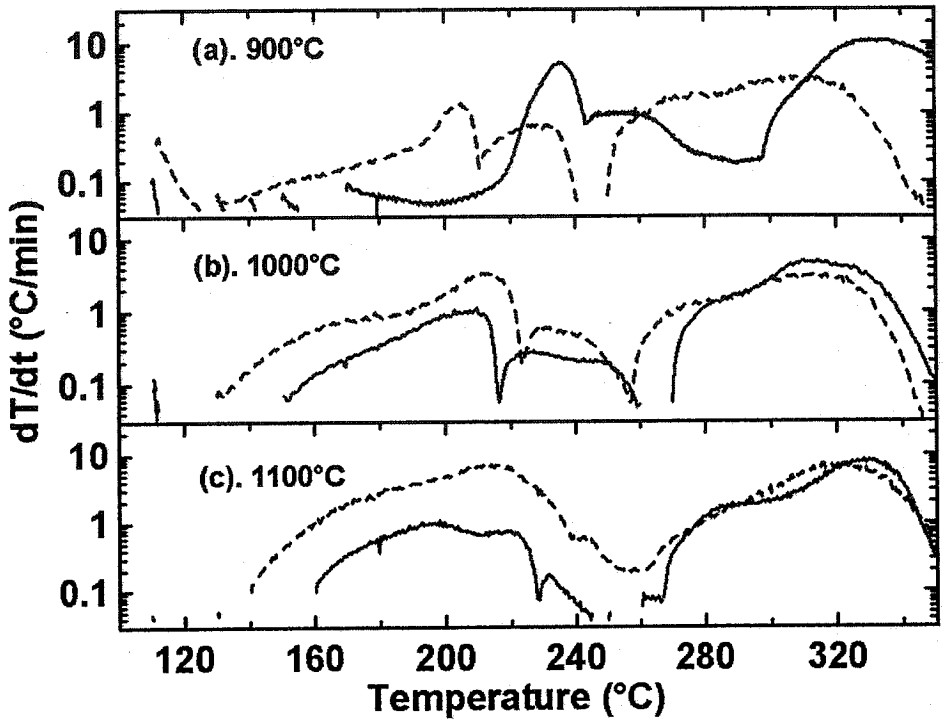

Figure 6.19 Self-heating rate versus temperature of 100 mg of $Li[(Ni_{0.5}Mn_{0.5})_{0.2}Co_{0.8}]O_2$ (900°C, 1000°C, and 1100°C) charged to 4.2 V (solid line) or 4.4 V (dashed line) heated with 100 mg of 1.0 M $LiPF_6$ EC/DEC electrolyte initially to 110°C.

The results in Figure 6.19 are very surprising, because the surface area of the samples decreases from about 5.7 $m^2\ g^{-1}$ to 0.9 $m^2\ g^{-1}$ as the samples are heated from 900°C to 1100°C. Because the reaction between the solid and the electrolyte proceeds at the solid surface it is natural to expect smaller self-heating rates for smaller surfaces of equal reactivity, such as a thermal-stability increase for $LiCoO_2$ samples as the particle size increases in Section 3.1.2. The fact that the 1100°C sample reacts most strongly suggests that its surface is much more reactive than that of the 900°C sample. This could happen if the surface was Co-rich, because the reactivity of $LiCoO_2$ charged to 4.2 V with EC/DEC is much stronger than that of $Li[(Ni_{0.5}Mn_{0.5})_{0.2}Co_{0.8}]O_2$.

The change of lattice constants with heat-treatment temperature shown in Table 6.1 is consistent with a Co-rich surface. Reference [23] shows that both *a* and *c* increase as the Ni and Mn contents in $Li[(Ni_{0.5}Mn_{0.5})_xCo_{1-x}]O_2$ increase. The rate of change of *a* with x is about 0.02 Å per 0.2 change in x and the change in *c* with x is about 0.05 Å per 0.2 change in x. The results in Table 6.1 for both *a* and *c* are consistent with an increase

in x in the bulk of the crystallites of 0.05 between 900 and 1100°C. Presumably the excess Co could be present at the surfaces of the particles and be responsible for the poor safety of the higher temperature samples. This agrees with the discussion surrounding Figures 6.15 and 6.16 presented several pages ago.

In summary, the $Li[(Ni_{0.5}Mn_{0.5})_{0.2}Co_{0.8}]O_2$ sample synthesized at 900°C shows better electrochemical properties (higher rate capability and better cycling performance) and higher thermal stability than the samples synthesized at higher temperatures of 1000°C and 1100°C. In next section, four different synthesis methods were used to synthesize $Li[(Ni_{0.5}Mn_{0.5})_{0.4}Co_{0.6}]O_2$ (x = 0.4) samples at 900°C. The electrochemical properties and thermal stability of the synthesized $Li[(Ni_{0.5}Mn_{0.5})_{0.4}Co_{0.6}]O_2$ samples are studied.

6.1.3 $Li[(Ni_{0.5}Mn_{0.5})_{0.4}Co_{0.6}]O_2$ (x = 0.4) by four different synthesis routes

The results in Section 6.1.1 suggest that $Li[(Ni_{0.5}Mn_{0.5})_{0.4}Co_{0.6}]O_2$ (x = 0.4) synthesized at 900°C by the co-precipitation method has good rate capability and high thermal stability (even when charged to 4.4 V). 3M Corp. (USA), the industrial partner of the author's group, is believed to be commercializing this cathode candidate for use in LIBs.

The most common way to synthesize $Li[(Ni_{0.5}Mn_{0.5})_{0.4}Co_{0.6}]O_2$ is to begin with a $(Ni_{0.5}Mn_{0.5})_{0.4}Co_{0.6}(OH)_2$ co-precipitate precursor having atomically mixed Ni, Co and Mn atoms and then fire with a Li salt, as described in Section 2.1.3. It may be the case that a particular desired precursor composition is not commercially available and an alternative synthesis strategy could be explored. For example, $Li[(Ni_{0.5}Mn_{0.5})_{0.4}Co_{0.6}]O_2$ samples could be attempted from a mixture of 0.4 moles of $Ni_{0.5}Mn_{0.5}(OH)_2$ and 0.6 moles of $Co(OH)_2$ if these precursors were readily available. There is no guarantee that this procedure would yield comparable materials, however.

This section focuses on the effects of different, yet related, synthesis routes for $Li[(Ni_{0.5}Mn_{0.5})_{0.4}Co_{0.6}]O_2$ on its structure, electrochemical properties and thermal stability. Four different synthesis routes were used to prepare $Li[(Ni_{0.5}Mn_{0.5})_{0.4}Co_{0.6}]O_2$. The structure, electrochemical performance and thermal stability of the synthesized samples were characterized by XRD, cycling behavior, and ARC, respectively.

6.1.3.1 Four different synthesis methods

Four different methods were used to synthesize $Li[(Ni_{0.5}Mn_{0.5})_{0.4}Co_{0.6}]O_2$ samples:

Method (I): The ground $(Ni_{0.5}Mn_{0.5})_{0.4}Co_{0.6}(OH)_2$ co-precipitate was mixed with $LiOH{\cdot}H_2O$ in a 1:1.03 molar ratio (3% excess lithium). The mixture was then fired in air using the same heating profile described in Section 2.1 to achieve $Li[(Ni_{0.5}Mn_{0.5})_{0.4}Co_{0.6}]O_2$ (I).

Method (II): the same synthesis method as method (I) was used except that Li_2CO_3 instead of $LiOH{\cdot}H_2O$ was used to make $Li[(Ni_{0.5}Mn_{0.5})_{0.4}Co_{0.6}]O_2$ (II).

Method (III): The precursor used was not $(Ni_{0.5}Mn_{0.5})_{0.4}Co_{0.6}(OH)_2$ but instead $(Ni_{0.5}Mn_{0.5})_{0.832}Co_{0.168}(OH)_2$ co-precipitate, which was obtained from Ilion Co. (New Zealand). The $(Ni_{0.5}Mn_{0.5})_{0.832}Co_{0.168}(OH)_2$ co-precipitate was mixed with a stoichoimetric amount of $LiOH{\cdot}H_2O$ (3% excess amount) and $Co(OH)_2$ calculated to make $Li[(Ni_{0.5}Mn_{0.5})_{0.4}Co_{0.6}]O_2$. The $Co(OH)_2$ precursor was precipitated by adding a $CoSO_4$ solution to a LiOH solution as described in the experimental section. The heating process used was the same as used in Method (I). This sample is called $Li[(Ni_{0.5}Mn_{0.5})_{0.4}Co_{0.6}]O_2$ (III).

Method (IV): The same procedure was used as in Method (III) except that Li_2CO_3 was used as the lithium source instead of $LiOH{\cdot}H_2O$. The synthesized sample is called $Li[(Ni_{0.5}Mn_{0.5})_{0.4}Co_{0.6}]O_2$ (IV).

6.1.3.2 Sample characterization by SEM, BET, and XRD

Figures 6.20a, b, c, and d show SEM micrographs of the $Li[(Ni_{0.5}Mn_{0.5})_{0.4}Co_{0.6}]O_2$ samples synthesized by methods (I), (II), (III), and (IV), respectively. $Li[(Ni_{0.5}Mn_{0.5})_{0.4}Co_{0.6}]O_2$ samples (I) and (II) have a similar average particle size of approximately 0.2 μm. The average particle size of samples (III) and (IV) is around 0.4 ~ 0.5 μm. The BET surface areas are approximately 4.4 $m^2\ g^{-1}$, 4.3 $m^2\ g^{-1}$, 2.5 $m^2\ g^{-1}$, and 2.7 $m^2\ g^{-1}$, respectively, for $Li[(Ni_{0.5}Mn_{0.5})_{0.4}Co_{0.6}]O_2$ samples (I), (II), (III), and (IV).

The XRD patterns of the $Li[(Ni_{0.5}Mn_{0.5})_{0.4}Co_{0.6}]O_2$ samples synthesized by the four different methods were measured and are shown in Figures 6.21 and 6.22. Figure 6.22 gives an expanded view of the high scattering angle region so that differences in

sample crystallinity can be examined. The XRD patterns appear similar and there are no obvious impurity peaks. However, the Bragg peaks for samples I and II are narrower than those for samples III and IV in Figure 6.22 (this is especially evident for the peak at 83°). This indicates that the former samples are more crystalline, even though they have a smaller particle size (See Figure 6.20). It was believed that the particles in samples III and IV probably have a distribution in their Co contents, due to their synthesis method. Since the lattice constant of $Li[(Ni_{0.5}Mn_{0.5})_xCo_{1-x}]O_2$ depends on x, any spread in Co content would lead to a broadening of high-angle Bragg peaks, as observed. The Rietveld refinement results of the XRD patterns are listed in Table 6.2. The lattice constants, *a* and *c*, are similar for the four $Li[(Ni_{0.5}Mn_{0.5})_{0.4}Co_{0.6}]O_2$ samples. The percentage of the Li site occupied by Ni atoms is approximately 1.4%, 1.3%, 1.2%, and 1.8%, respectively, for samples (I), (II), (III), and (IV).

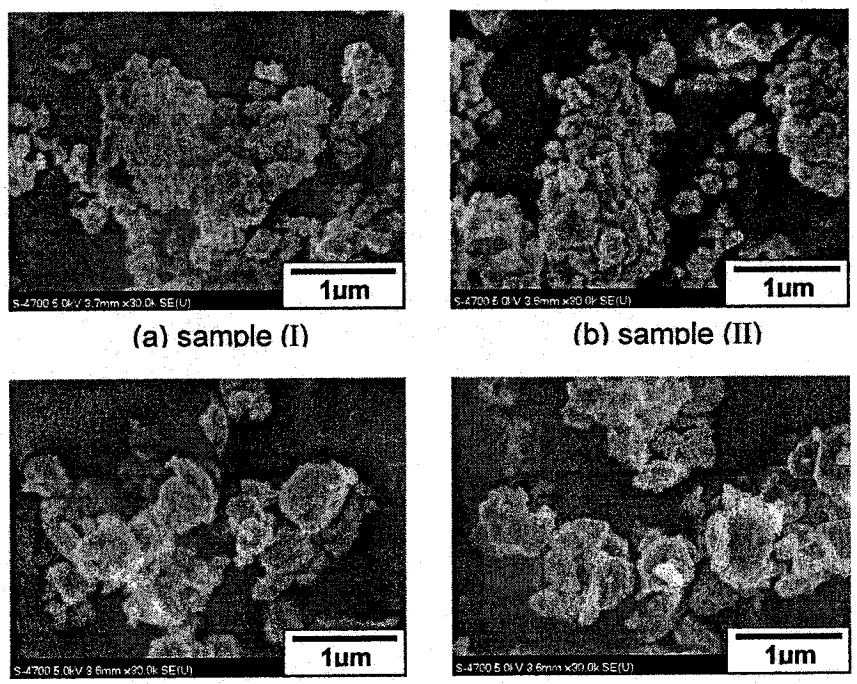

(a) sample (I) (b) sample (II)

(c) sample (III) (d) sample (IV)

Figure 6.20 SEM micrographs of $Li[(Ni_{0.5}Mn_{0.5})_{0.4}Co_{0.6}]O_2$ samples (I), (II), (III), and (IV). From the images the average particle size is approximately 0.2-0.3 μm for samples (I) and (II) and around 0.4-0.5 μm for samples (III) and (IV).

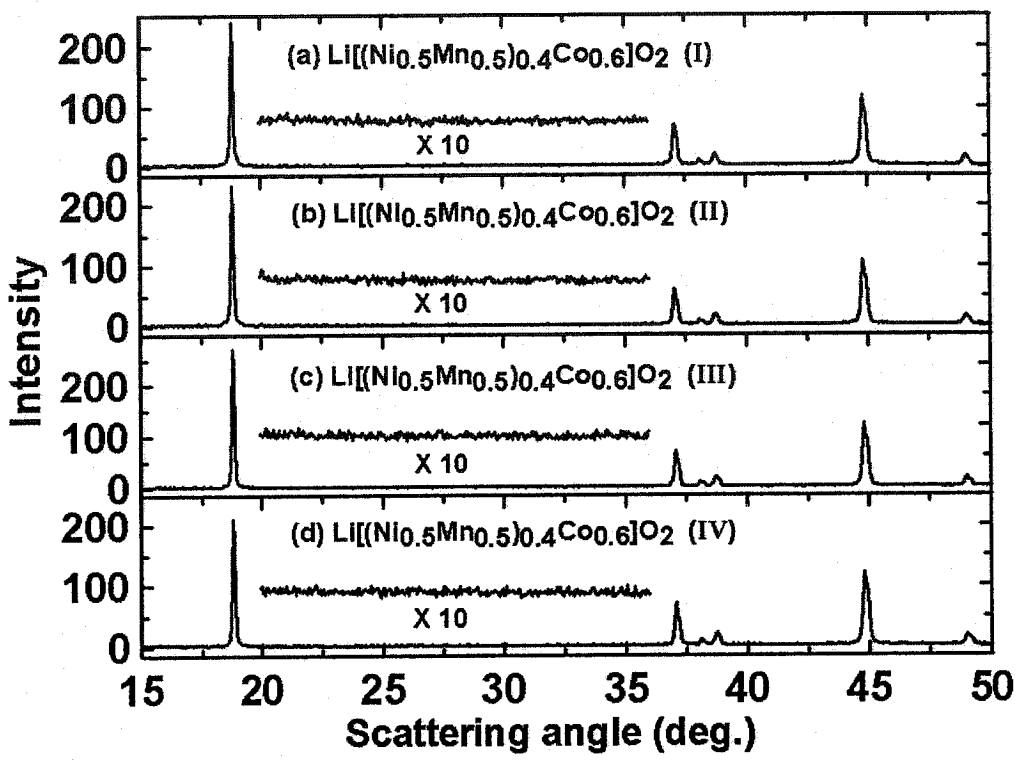

Figure 6.21 X-ray diffraction (XRD) patterns of $Li[(Ni_{0.5}Mn_{0.5})_{0.4}Co_{0.6}]O_2$ samples in the low scattering angle region from 15° to 50° to show the absence of impurities.

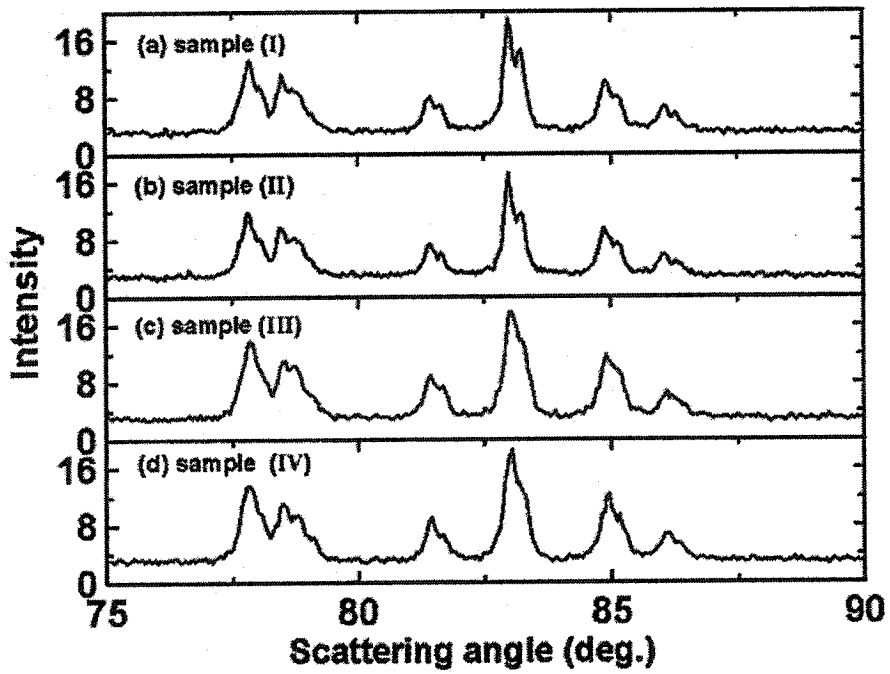

Figure 6.22 X-ray diffraction (XRD) patterns of $Li[(Ni_{0.5}Mn_{0.5})_{0.4}Co_{0.6}]O_2$ samples in the high scattering angle region from 75° to 90° to compare the widths of the Bragg peaks.

Table 6.2. Lattice constants and atom positions for the four $Li[(Ni_{0.5}Mn_{0.5})_{0.4}Co_{0.6}]O_2$ samples from the single-phase Rietveld refinement of the XRD patterns. The space group used for the refinement was R-3m (#166). "u" represents the percentage of the Li sites occupied by transition metal atoms. The Bragg R-factors are listed.

samples	*a* (Å)	*c* (Å)	O position	u	R_{Bragg}
(I)	2.8409(3)	14.1673(9)	0, 0, 0.2410(9)	1.4%	3.6%
(II)	2.8414(5)	14.1682(4)	0, 0, 0.2393(8)	1.3%	3.3%
(III)	2.8410(3)	14.1685(7)	0, 0, 0.2392(3)	1.2%	2.9%
(IV)	2.8411(7)	14,1660(6)	0, 0, 0.2416(9)	1.8%	3.0%

6.1.3.3 Electrochemical properties

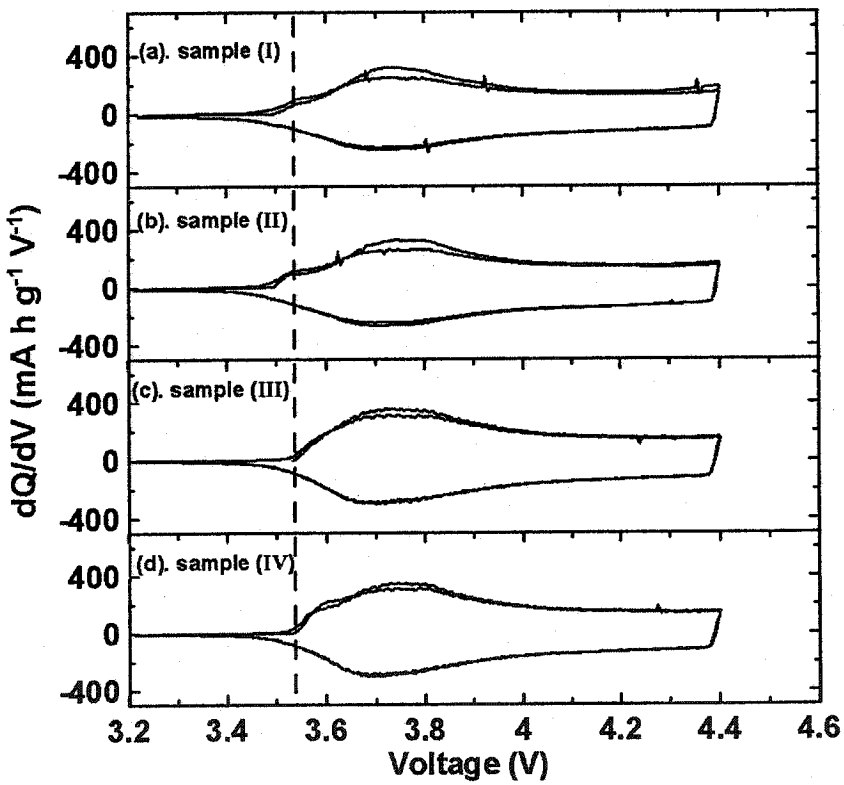

Figure 6.23 The differential capacity (dQ/dV) vs. potential (V) of Li/ $Li[(Ni_{0.5}Mn_{0.5})_{0.4}Co_{0.6}]O_2$ cells cycled between 2.5 V and 4.4 V at a rate of C/20.

Figure 6.23 shows the differential capacity vs. potential for Li/ $Li[(Ni_{0.5}Mn_{0.5})_{0.4}Co_{0.6}]O_2$ cells cycling between 2.5 V and 4.4 V at a C/20 rate. The voltage changes that occurred when the current switched from charge to discharge at the upper cutoff potential are about 15 mV, 15 mV, 18 mV, and 20 mV, respectively, for

samples (I), (II), (III), and (IV). This suggests that samples (I) and (II) have less impedance than samples (III) and (IV). This may be due to their smaller particle size. Furthermore, Figure 6.23 shows subtle differences in the differential capacities of the samples. Samples I and II have more capacity at lower potential than do samples III and IV. It has been shown previously that this capacity develops at small x in $Li[(Ni_{0.5}Mn_{0.5})_xCo_{1-x}]O_2$ due to the added Ni^{2+} [23]. The fact that this capacity is less pronounced in samples III and IV again points to potential problems in cation homogeneity.

Figure 6.24 shows the potential (V) versus capacity (mA h g^{-1}) curves for the cells having $Li[(Ni_{0.5}Mn_{0.5})_{0.4}Co_{0.6}]O_2$ electrodes. The cells are the same ones used to produce dQ/dV vs. V graphs in Figure 6.23. Apart from some small differences in irreversible capacity, the voltage profiles in Figure 6.24 for the 4 samples are almost indistinguishable. This shows the importance of careful differential capacity measurements like those in Figure 6.23. Each of the samples has almost the same reversible capacity.

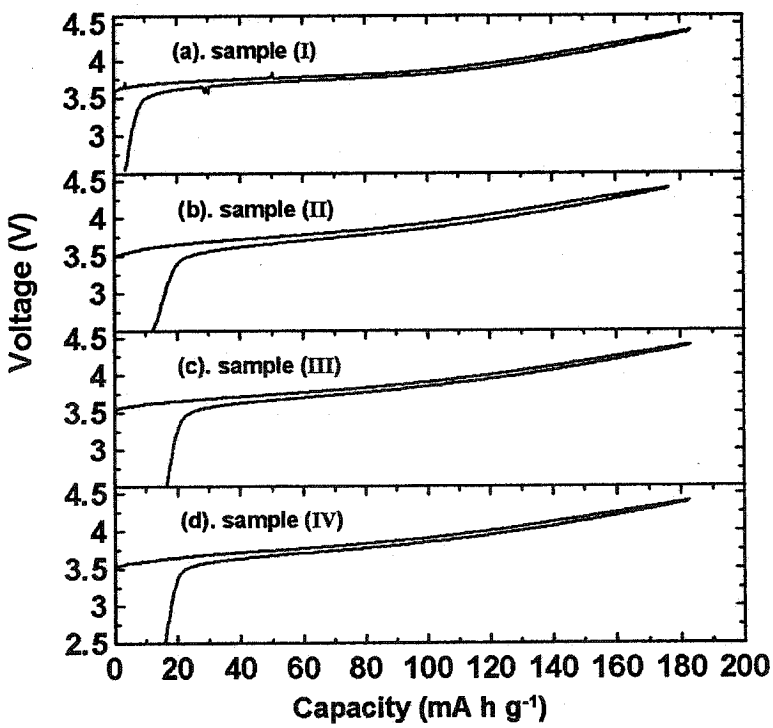

Figure 6.24 The potential (V) vs. capacity (mA h g^{-1}) of $Li/Li[(Ni_{0.5}Mn_{0.5})_{0.4}Co_{0.6}]O_2$ cells cycled between 2.5 V and 4.4 V at a rate of C/20.

Figure 6.25 shows the discharge capacity versus cycle number (2.5 V – 4.4 V, C/4) for the $Li[(Ni_{0.5}Mn_{0.5})_{0.4}Co_{0.6}]O_2$ samples. Data for two cells of each sample are shown here. Figure 6.25a shows that the cell with $Li[(Ni_{0.5}Mn_{0.5})_{0.4}Co_{0.6}]O_2$ sample (I) has the best capacity retention. Almost 90% of the initial capacity remained after 200 cycles. The results in Figures 6.23, 6.24, and 6.25 indicate that $Li[(Ni_{0.5}Mn_{0.5})_{0.4}Co_{0.6}]O_2$ sample (I) has lower impedance and higher capacity retention than the other samples.

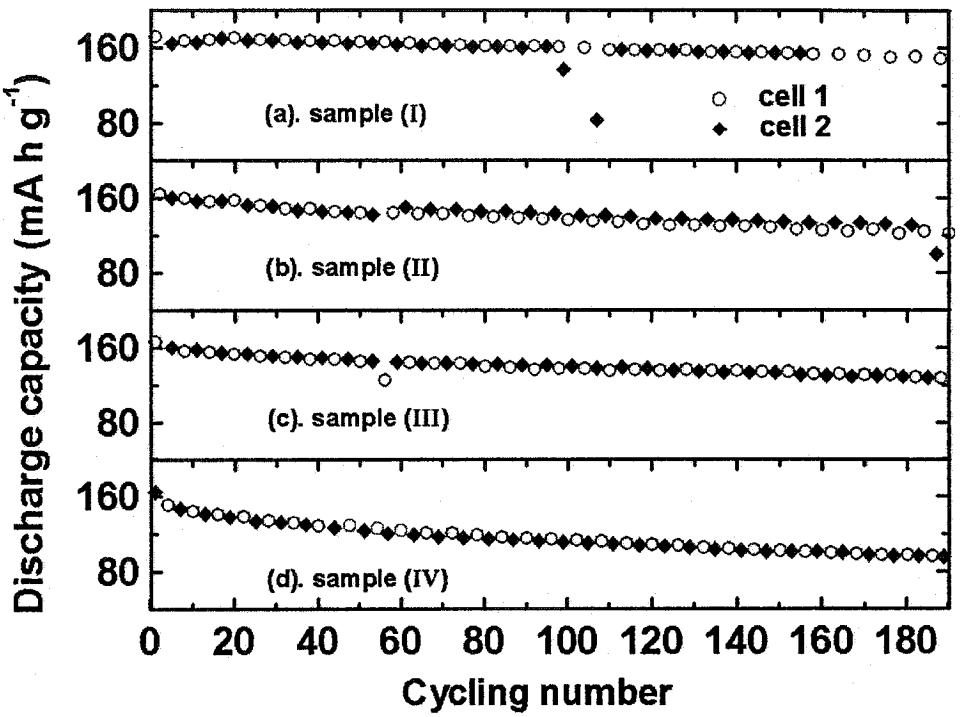

Figure 6.25 Capacity (mA h g^{-1}) vs. cycle number for the $Li/Li[(Ni_{0.5}Mn_{0.5})_{0.4}Co_{0.6}]O_2$ cells made from the four samples.

6.1.3.4 Thermal stability

Figure 6.26 shows the self-heating rate (SHR) versus temperature (T) for 100 mg of $Li[(Ni_{0.5}Mn_{0.5})_{0.4}Co_{0.6}]O_2$ charged to 4.2 V reacting with 100 mg of EC/DEC solvent. The sample was initially heated to 110°C before exotherm searching began. Comparative results for charged $LiCoO_2$ [sample (3) with 5 μm particle size, 4.2 V vs. Li] reacting with EC/DEC solvent are shown in Figure 6.26a. Figure 6.26 clearly shows that all four $Li[(Ni_{0.5}Mn_{0.5})_{0.4}Co_{0.6}]O_2$ samples start reacting exothermally with EC/DEC at a higher temperature than $LiCoO_2$, which reacts significantly with EC/DEC at 150°C.

$Li[(Ni_{0.5}Mn_{0.5})_{0.4}Co_{0.6}]O_2$ samples (I) and (II) synthesized from $(Ni_{0.5}Mn_{0.5})_{0.4}Co_{0.6}(OH)_2$ do not react significantly with EC/DEC until 220°C. These results are in good agreement with the data shown in Section 6.1.1. The SHR vs. T profiles for $Li[(Ni_{0.5}Mn_{0.5})_{0.4}Co_{0.6}]O_2$ samples (III) and (IV), made from $(Ni_{0.5}Mn_{0.5})_{0.832}Co_{0.168}(OH)_2$ and $Co(OH)_2$, reacting with EC/DEC shown in Figures 6.26d and 6.26e are very similar and their ARC onset temperatures in EC/DEC are around 170°C ~ 180°C.

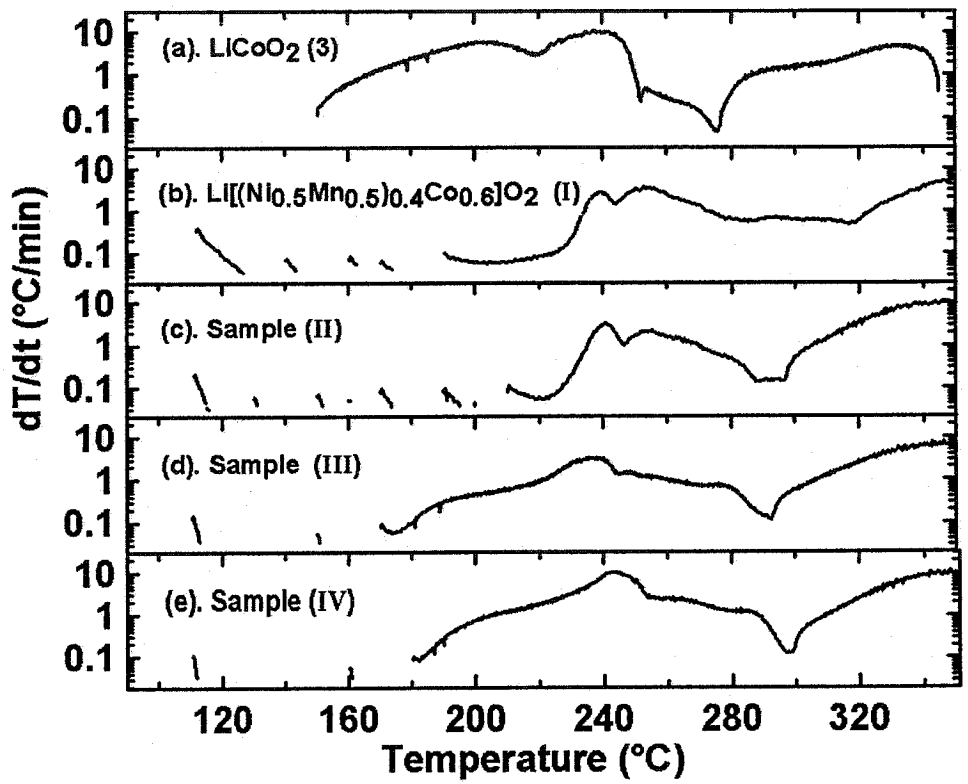

Figure 6.26 Self-heating rate (SHR) versus temperature (T) for 100 mg $Li[(Ni_{0.5}Mn_{0.5})_{0.4}Co_{0.6}]O_2$ samples charged to 4.2 V heated with 100 mg of EC/DEC solvent. The SHR vs. T of $LiCoO_2$ charged to 4.2 V reacting with EC/DEC has been added in panel (a) for comparison. Samples were initially heated to 110°C before exotherm searching began.

Figure 6.27 shows the SHR vs. T of 100 mg of the $Li[(Ni_{0.5}Mn_{0.5})_{0.4}Co_{0.6}]O_2$ and $LiCoO_2$ samples charged to 4.2 V reacting with 30 mg of 1.0 M $LiPF_6$ EC/DEC electrolyte. The ARC samples were initially heated to 110°C. The four $Li[(Ni_{0.5}Mn_{0.5})_{0.4}Co_{0.6}]O_2$ samples show much higher thermal stability than $LiCoO_2$ in

$LiPF_6$ EC/DEC electrolyte. $Li[(Ni_{0.5}Mn_{0.5})_{0.4}Co_{0.6}]O_2$ samples (I) and (II) show similar thermal stability in $LiPF_6$-based electrolyte as shown in Figures 6.27b and c, respectively, and they start reacting significantly with electrolyte above 200°C. $Li[(Ni_{0.5}Mn_{0.5})_{0.4}Co_{0.6}]O_2$ samples (III) and (IV) start thermally reacting with electrolyte at a relatively lower temperature of around 170°C ~ 180°C and both samples proceed to thermal runaway later at around 280°C.

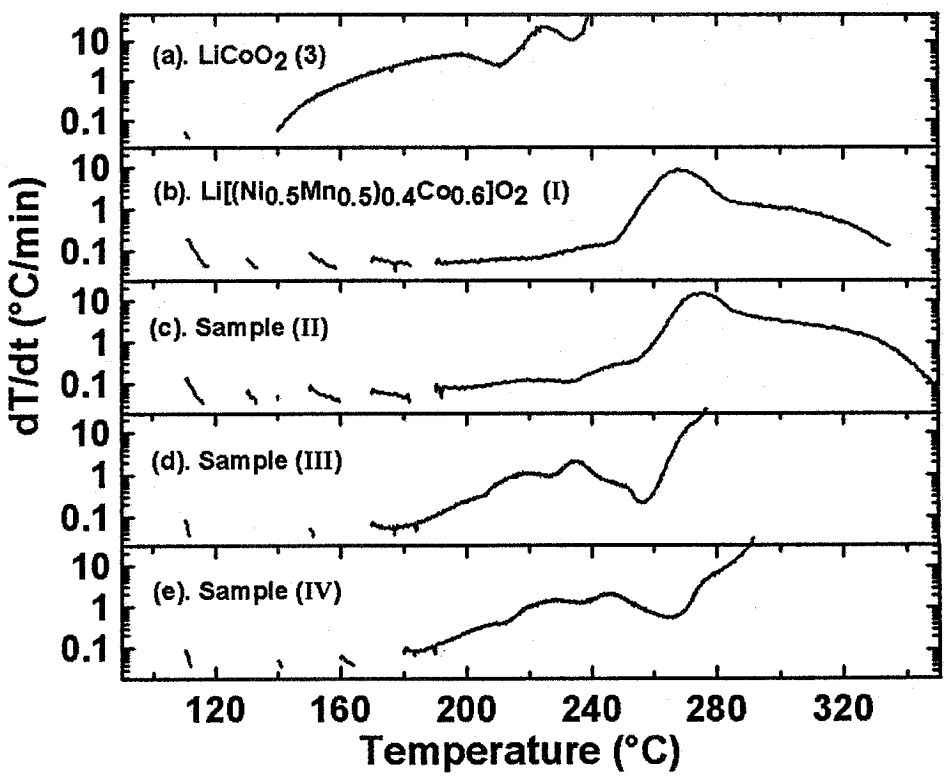

Figure 6.27 Self-heating rate (SHR) versus temperature for 100 mg of $LiCoO_2$ and $Li[(Ni_{0.5}Mn_{0.5})_{0.4}Co_{0.6}]O_2$ samples charged to 4.2 V vs. Li heated with 30 mg of 1.0 M $LiPF_6$ EC/DEC electrolyte. Samples were initially heated to 110°C before exotherm searching began.

The ARC results in Figures 6.26 and 6.27 clearly show that $Li[(Ni_{0.5}Mn_{0.5})_{0.4}Co_{0.6}]O_2$ samples synthesized from $(Ni_{0.5}Mn_{0.5})_{0.4}Co_{0.6}(OH)_2$ co-precipitate have superior thermal stability in EC/DEC solvent or $LiPF_6$ EC/DEC electrolyte than the samples synthesized from $(Ni_{0.5}Mn_{0.5})_{0.832}Co_{0.168}(OH)_2$ co-precipitate and $Co(OH)_2$. This is believed to be related to the Co distribution on the surface and bulk

of the $Li[(Ni_{0.5}Mn_{0.5})_{0.4}Co_{0.6}]O_2$ samples. The $(Ni_{0.5}Mn_{0.5})_{0.4}Co_{0.6}(OH)_2$ precursor was synthesized by the co-precipitation method and presumably has an even Co distribution. Therefore, $Li[(Ni_{0.5}Mn_{0.5})_{0.4}Co_{0.6}]O_2$ samples (I) and (II) synthesized by firing $(Ni_{0.5}Mn_{0.5})_{0.4}Co_{0.6}(OH)_2$ with $LiOH/Li_2CO_3$ presumably also have an even Co distribution. However, in order to achieve the targeted $Li[(Ni_{0.5}Mn_{0.5})_{0.4}Co_{0.6}]O_2$ samples from $(Ni_{0.5}Mn_{0.5})_{0.832}Co_{0.168}(OH)_2$ heated with $Co(OH)_2$, Co atoms have to diffuse into the $(Ni_{0.5}Mn_{0.5})_{0.832}Co_{0.168}(OH)_2$ bulk material and a Co concentration difference between the surface and bulk may exist. Evidence for this can be found in the width of the Bragg peaks for this sample. A higher Co concentration on the surface of the $Li[(Ni_{0.5}Mn_{0.5})_{0.4}Co_{0.6}]O_2$ sample (which touches the electrolyte) will certainly decrease its thermal stability, given that the thermal stability of $Li[(Ni_{0.5}Mn_{0.5})_xCo_{1-x}]O_2$ decreases as x decreases. This can explain why $Li[(Ni_{0.5}Mn_{0.5})_{0.4}Co_{0.6}]O_2$ samples (I) and (II) show higher thermal stability than samples (III) and (IV) in both EC/DEC solvent or in $LiPF_6$ based electrolyte.

In summary, $Li[(Ni_{0.5}Mn_{0.5})_{0.4}Co_{0.6}]O_2$ samples synthesized by firing $(Ni_{0.5}Mn_{0.5})_{0.4}Co_{0.6}(OH)_2$ co-precipitate with LiOH or Li_2CO_3 at 900°C exhibit good crystallinity, good cycling performance, and high thermal stability in both EC/DEC solvent and $LiPF_6$-based electrolyte.

Based on the results in Sections 6.1.1, 6.1.2, and 6.1.3, two conclusions can be made:

(1). The $Li[(Ni_{0.5}Mn_{0.5})_xCo_{1-x}]O_2$ samples ($0.4 \le x \le 0.7$) synthesized by firing $(Ni_{0.5}Mn_{0.5})_xCo_{1-x}(OH)_2$ co-precipitate with LiOH at 900°C have high lithium diffusion coefficient (comparable to $LiCoO_2$), good rate capability, and high thermal stability (much higher than $LiCoO_2$). The materials within this range are very promising positive electrode materials to be used in the next generation of lithium-ion batteries.

(2). An even distribution of Ni, Co, and Mn cations in the transition metal layer of $Li[(Ni_{0.5}Mn_{0.5})_xCo_{1-x}]O_2$ samples is the **key point** to produce high-quality samples with excellent electrochemical properties **and** high thermal stability. The $Li[(Ni_{0.5}Mn_{0.5})_xCo_{1-x}]O_2$ samples ($x<0.4$) synthesized at a high temperature of 1000°C or 1100°C or fired from $(Ni_{0.5}Mn_{0.5})_{0.832}Co_{0.168}(OH)_2$ and $Co(OH)_2$ co-precipitates at 900°C ($x = 0.4$) show

relatively poor thermal stability. This is probably due to a Co-rich surface for the synthesized samples.

In Section 6.1.4, the thermal reaction sequence between charged $Li[(Ni_{0.5}Mn_{0.5})_xCo_{1-x}]O_2$ samples (4.2 V vs. Li) with EC/DEC solvent is explored. The reason for the safety improvement of $Li[(Ni_{0.5}Mn_{0.5})_xCo_{1-x}]O_2$ ($0<x\leq1$) over $LiCoO_2$ is discussed as well.

6.1.4 Thermal reaction sequence of charged $Li[(Ni_{0.5}Mn_{0.5})_xCo_{1-x}]O_2$ samples (4.2 V)

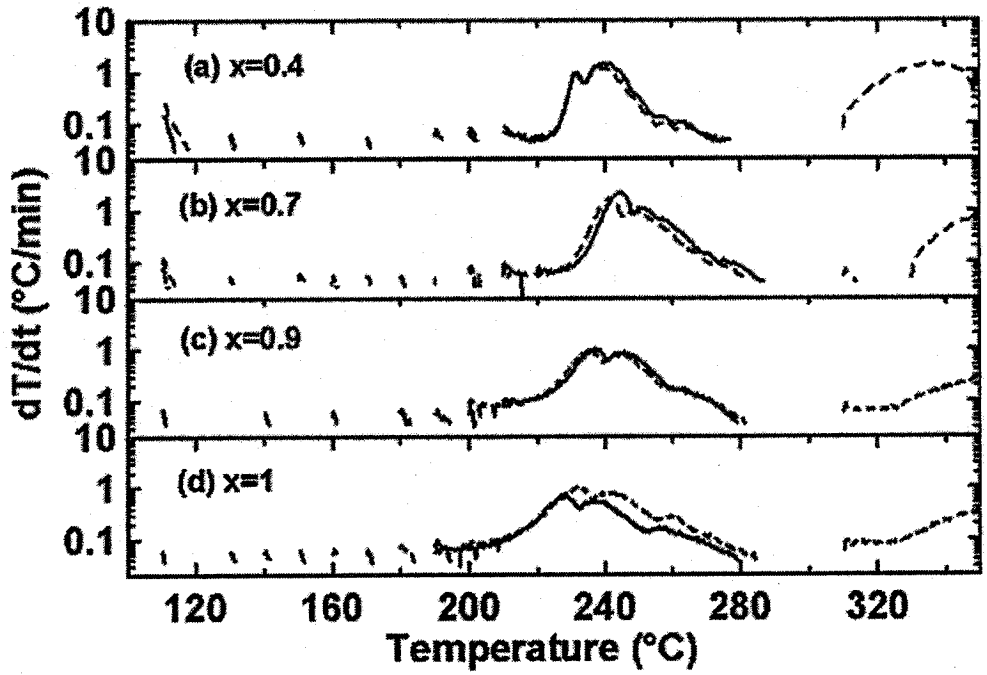

Figure 6.28 SHR vs. T for 50 mg of $Li[(Ni_{0.5}Mn_{0.5})_xCo_{1-x}]O_2$ (x = 0.4, 0.7, 0.9, and 1) charged to 4.2 V heated with 50 mg of EC/DEC solvent. There are two ARC measurements for each sample, one stopped at 290°C (solid line) and the other one at 350°C (dashed line).

The ARC curves of $Li[(Ni_{0.5}Mn_{0.5})_xCo_{1-x}]O_2$ samples with EC/DEC shown in Figure 6.10 contain several reaction steps which combine together to give an overall ARC response. In order to separate the individual reaction processes, the amount of both $Li[(Ni_{0.5}Mn_{0.5})_xCo_{1-x}]O_2$ and EC/DEC was decreased from 100 mg to 50 mg in ARC measurements and the data is shown in Figure 6.28. Two ARC measurements were

conducted for each sample with x = 0.4, 0.7, 0.9, or 1 in $Li[(Ni_{0.5}Mn_{0.5})_xCo_{1-x}]O_2$. One ARC measurement for each sample was stopped at 290°C (solid line) and the other one at 350°C (dashed line). 350°C is the highest safe temperature for the ARC. Even at 350°C thermal reactions were still continuing in the ARC tubes.

XRD patterns of the products of the reaction between the $Li[(Ni_{0.5}Mn_{0.5})_xCo_{1-x}]O_2$ (x = 0.4, 0.7, 0.9, and 1, 4.2 V) samples and EC/DEC to 290°C are shown in Figures 6.29 and 6.30. The main products are $[Li_qM_{1-q}]O$ with a rock-salt structure (M indicates metal ions, most likely Li^+, Mn^{4+}, Co^{3+}, and Ni^{2+}) together with $MnCO_3$ and M^*CO_3 (M^* represents a Co and Ni mixture) in Figure 6.29. Figure 6.30 gives an expanded view of the scattering angle region from 40° to 65° to more clearly show the Bragg peak shift of $[Li_qM_{1-q}]O$ with different metal compositions.

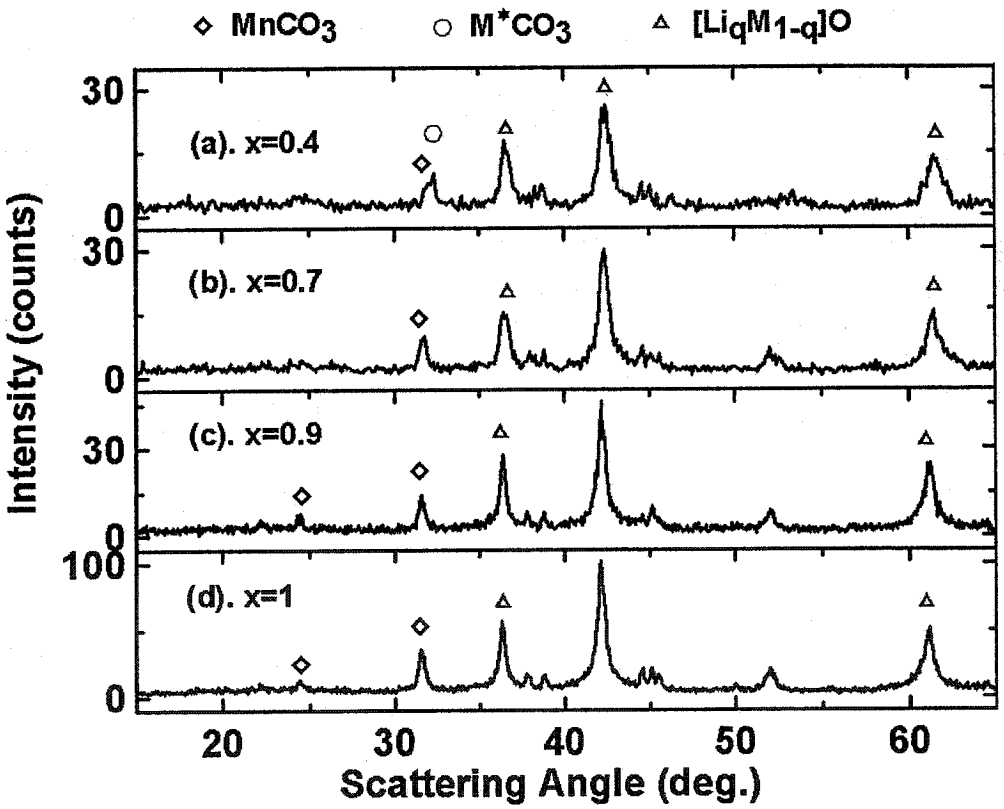

Figure 6.29 XRD patterns of $Li[(Ni_{0.5}Mn_{0.5})_xCo_{1-x}]O_2$ (x = 0.4, 0.7, 0.9, and 1) charged to 4.2 V after reacting with EC/DEC to 290°C in the ARC as shown by the solid line in Figure 6.28.

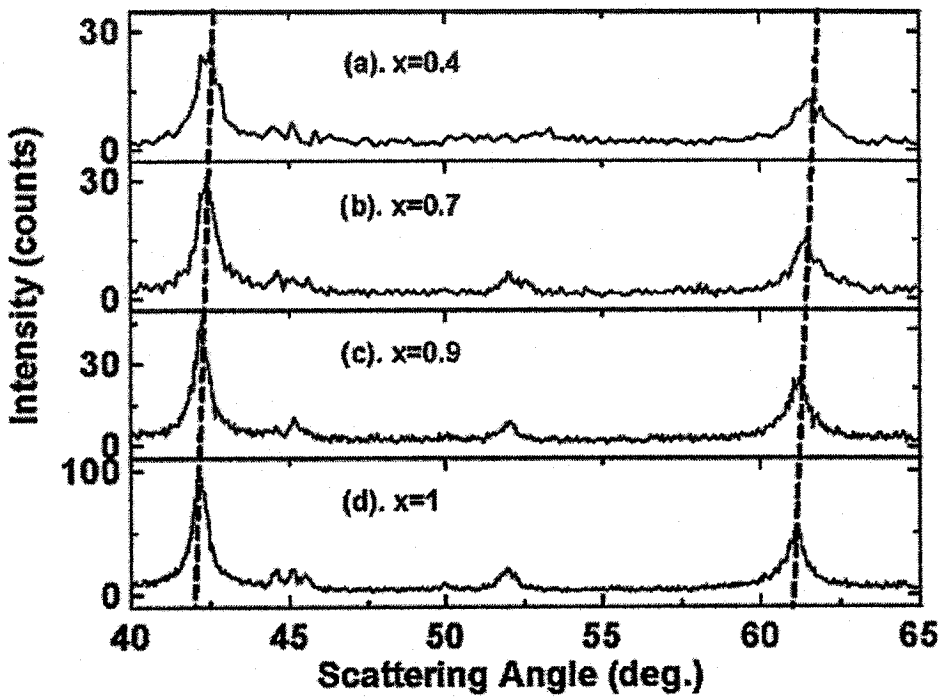

Figure 6.30 Expanded view of the XRD patterns in Figure 6.29.

$MnCO_3$, $CoCO_3$, and $NiCO_3$ adopt the same structure (R–3c, #167). Their lattice constants (*a* and *c*, Å) are shown in Table 6.3. The lattice constants, *a* and *c*, of $CoCO_3$ and $NiCO_3$ [147] are very similar and their XRD patterns are hard to distinguish. Therefore, a formula of M^*CO_3 was used to represent the XRD peaks for $(Ni\text{-}Co)CO_3$ in Figure 6.29. In the Rietveld profile refinements, Co will be used to replace M* since Co and Ni are adjacent elements in the periodic table and they have similar X-ray scattering factors. The possibility of the existence of $NiCO_3$ or $CoCO_3$ or co-existence of both compounds will be discussed later.

Table 6.3. Lattice constant (*a* and *c*, Å) for $MnCO_3$, $CoCO_3$, and $NiCO_3$. The space group is R-3c (#167).

Compounds	*a* (Å)	*c* (Å)
$MnCO_3$	4.790	15.694
$CoCO_3$	4.659	14.957
$NiCO_3$	4.609	14.737

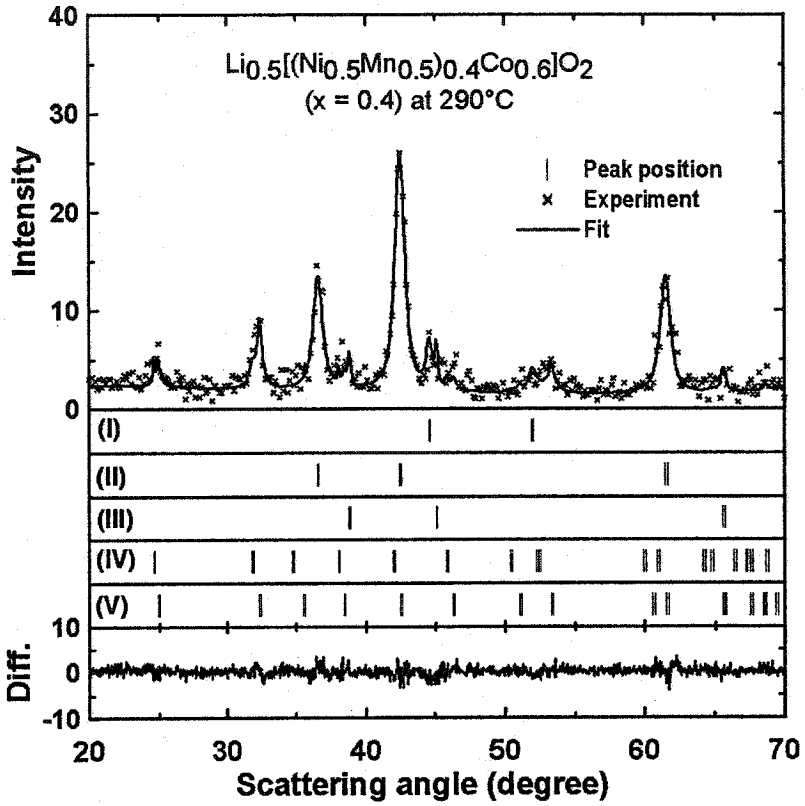

Figure 6.31 Rietveld profile fitting to the XRD pattern (Figure 6.29a) of the products from the reaction between $Li[(Ni_{0.5}Mn_{0.5})_{0.4}Co_{0.6}]O_2$ and EC/DEC at 290°C. Five phases are needed to describe this pattern. They are M metal (I), $[Li_qM_{1-q}]O$ (II), LiF (III), $MnCO_3$ (IV), and M^*CO_3 (V).

The Bragg peaks for M^*CO_3 and $MnCO_3$ in Figure 6.29a are relatively weak. In order to obtain strong evidence for the existence of M^*CO_3 and other phases, multi-phase Rietveld refinements of the XRD data were made and are shown in Figure 6.31. Only two Rietveld refinement results (Figures 6.29a and 6.29d) are shown here to save space. Figure 6.31 shows the refinement results for the data of Figure 6.29a. Five phases are needed to describe the experimental pattern. They are M metal (I), $[Li_qM_{1-q}]O$ (II), LiF (III), $MnCO_3$ (IV), and M^*CO_3 (V). The lattice constants, atom positions, and site occupation fractions, etc. for M metal (I) and $[Li_qM_{1-q}]O$ (II) phases are listed in Table 6.4a. The other phases such as LiF, $MnCO_3$, and M^*CO_3 are not included in Table 6.4 simply because their lattice constants and atom positions are fixed and well defined in literature [147]. The refinement results in Figure 6.31 and Table 6.4a strongly support the

existence of a $[Li_qM_{1-q}]O$ rock-salt phase together with a small amount of $MnCO_3$, M^*CO_3, M, and LiF in the products of the reaction between $Li[(Ni_{0.5}Mn_{0.5})_{0.4}Co_{0.6}]O_2$ (4.2 V) and EC/DEC in the ARC at 290°C.

Figure 6.32 shows the Rietveld refinement results for the XRD data in Figure 6.29d. Four phases are included in this refinement: M metal (I), $[Li_qM_{1-q}]O$ (II), LiF (III), and $MnCO_3$ (IV). The M^*CO_3 phase was not included because there are apparently no XRD peaks from M^*CO_3 in Figure 6.29d. The best refinement result is listed in Table 6.4d. Table 6.4 shows that the lattice constant, *a*, of the $[Li_qM_{1-q}]O$ rock-salt phase increases from 4.2689(2) Å, 4.2776(6) Å, 4.2881(2) Å, to 4.2964(3) Å as x in $Li[(Ni_{0.5}Mn_{0.5})_xCo_{1-x}]O_2$ increases from 0.4, 0.7, 0.9, to 1. This agrees well with the XRD peak shifts of the $[Li_qM_{1-q}]O$ phase shown in Figure 6.30.

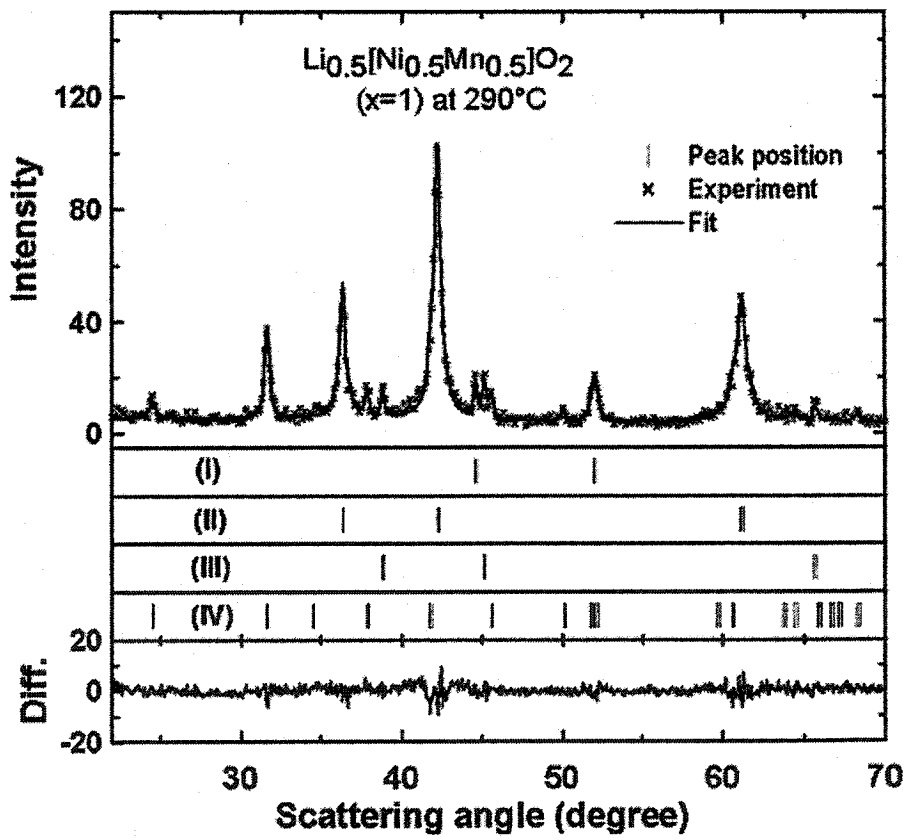

Figure 6.32 Rietveld profile fitting to the XRD pattern (Figure 6.29d) of the products from the reaction between $Li[Ni_{0.5}Mn_{0.5}]O_2$ and EC/DEC at 290°C. Four phases are needed to describe this pattern. They are M metal (I), $[Li_qM_{1-q}]O$ (II), LiF (III), and $MnCO_3$ (IV).

Table 6.4 Lattice constants and atom positions for the products of the reactions between $Li[(Ni_{0.5}Mn_{0.5})_xCo_{1-x}]O_2$ (x = 0.4, 0.7, 0.9, and 1) samples and EC/DEC in ARC experiments stopped at 290°C [shown in Figure 6.29]. Multi-phase Rietveld refinement was used. The space group used for the refinements is Fm3m ($^{\#}225$) for $[Li_qM_{1-q}]O$ rock-salt and M phases. "M" represents mixed transition metals (Ni, Co, and Mn). The Bragg R-factors are listed.

XRD curves in Figure 6.29	Phases	Lattice constant (a, Å)	Atom position	Fractional occupation	R_{Bragg} factor
(a)	M	a = 3.5300(5)	M: (0, 0, 0)	1	4.3%
	$[Li_qM_{1-q}]O$	a = 4.2689(2)	M: (0.5, 0.5, 0.5) O: (0, 0, 0)	0.8155(1) 1	3.5%
(b)	M	a = 3.5326(2)	M: (0, 0, 0)	1	3.0%
	$[Li_qM_{1-q}]O$	a = 4.2776(6)	M: (0.5, 0.5, 0.5) O: (0, 0, 0)	0.8021(4) 1	4.1%
(c)	M	a = 3.5462(3)	M: (0, 0, 0)	1	4.5%
	$[Li_qM_{1-q}]O$	a = 4.2881(2)	M: (0.5, 0.5, 0.5) O: (0, 0, 0)	0.8242(3) 1	3.3%
(d)	M	a = 3.5286(3)	M: (0, 0, 0)	1	2.0%
	$[Li_qM_{1-q}]O$	a = 4.2964(3)	M: (0.5, 0.5, 0.5) O: (0, 0, 0)	0.7848(5) 1	1.4%

Figure 6.33 shows XRD patterns of the products from the reaction between $Li[(Ni_{0.5}Mn_{0.5})_xCo_{1-x}]O_2$ (x = 0.4, 0.7, 0.9, and 1, 4.2 V) and EC/DEC after ARC tests stopped at 350°C (dashed lines in Figure 6.28). It is clear that $[Li_qM_{1-q}]O$ has been reduced to M metal and Li_2CO_3 as the temperature increases from 290°C to 350°C. A fraction of $[Li_qM_{1-q}]O$ remains at 350°C because the thermal reaction between $[Li_qM_{1-q}]O$ and EC/DEC was still incomplete at 350°C as shown in Figure 6.28 (dashed lines).

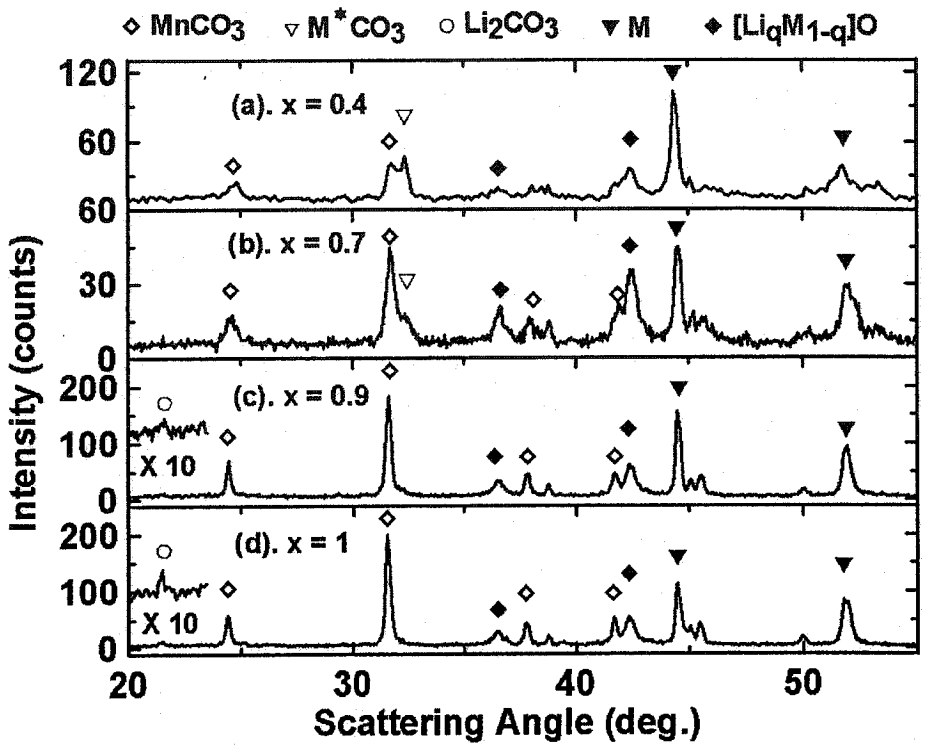

Figure 6.33 XRD patterns of $Li[(Ni_{0.5}Mn_{0.5})_xCo_{1-x}]O_2$ (x = 0.4, 0.7, 0.9, and 1) charged to 4.2 V after reacting with EC/DEC to 350°C as shown by the dashed lines in Figure 6.28.

Multi-phase Rietveld refinements of the four XRD curves in Figure 6.33 were performed and the results are listed in Table 6.5. The refinement results for the data in Figures 6.33a and 6.33d were selected to be shown in Figures 6.34 and 6.35, respectively. There are clear five phases coexisting in Figure 6.34, M metal (I), $[Li_qM_{1-q}]O$ (II), LiF (III), $MnCO_3$ (IV), and M^*CO_3 (V) (The Li_2CO_3 phase was not included in the XRD refinements in order to decrease the complexity of the multi-phase refinements). The peak splitting between $MnCO_3$ and M^*CO_3 at a scattering angle around 32° becomes more pronounced than in Figure 6.31 for the same $Li[(Ni_{0.5}Mn_{0.5})_{0.4}Co_{0.6}]O_2$ (4.2 V) sample stopped at only 290°C. This simply suggests that, as the temperature increases from 290°C to 350°C in ARC experiments, more crystalline M^*CO_3 and $MnCO_3$ are produced.

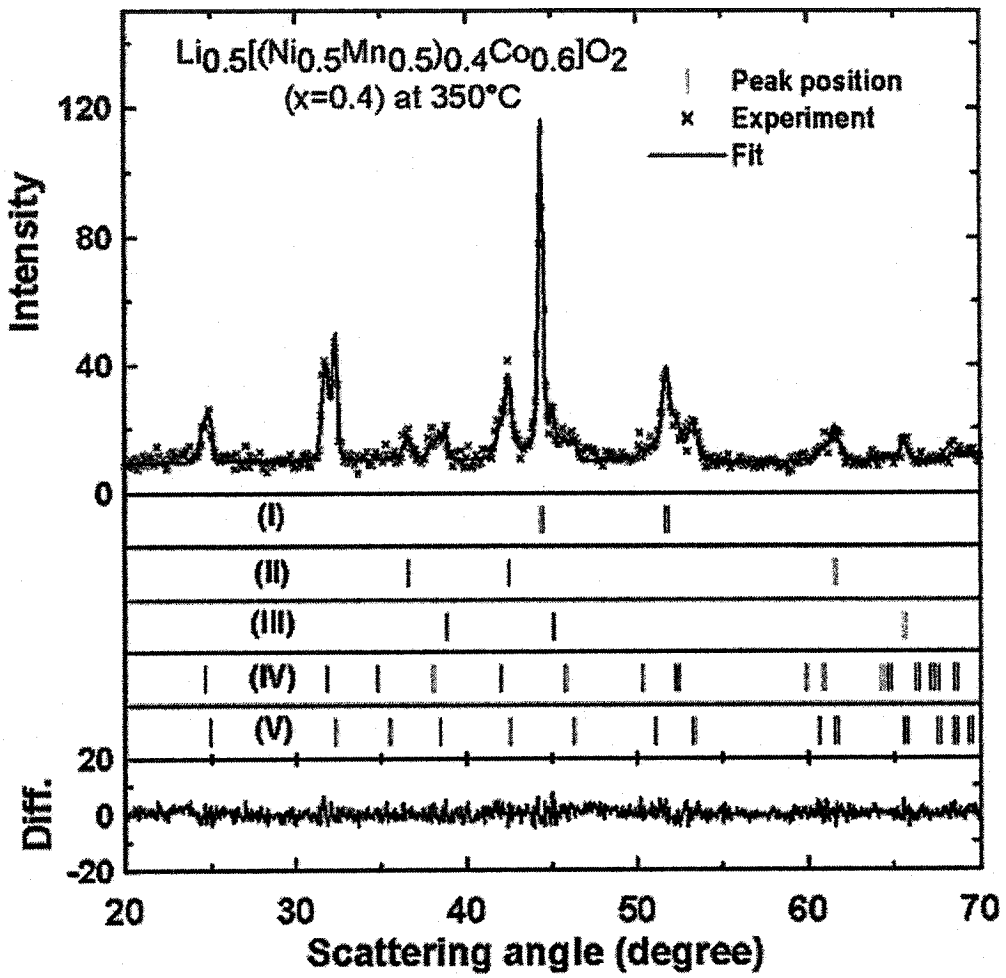

Figure 6.34 Rietveld profile fitting to the XRD pattern (Figure 6.33a) of the products from the reaction between $Li[(Ni_{0.5}Mn_{0.5})_{0.4}Co_{0.6}]O_2$ and EC/DEC at 350°C. Five phases are needed to describe this pattern. They are M metal (I), $[Li_qM_{1-q}]O$ (II), LiF (III), $MnCO_3$ (IV), and M^*CO_3 (V).

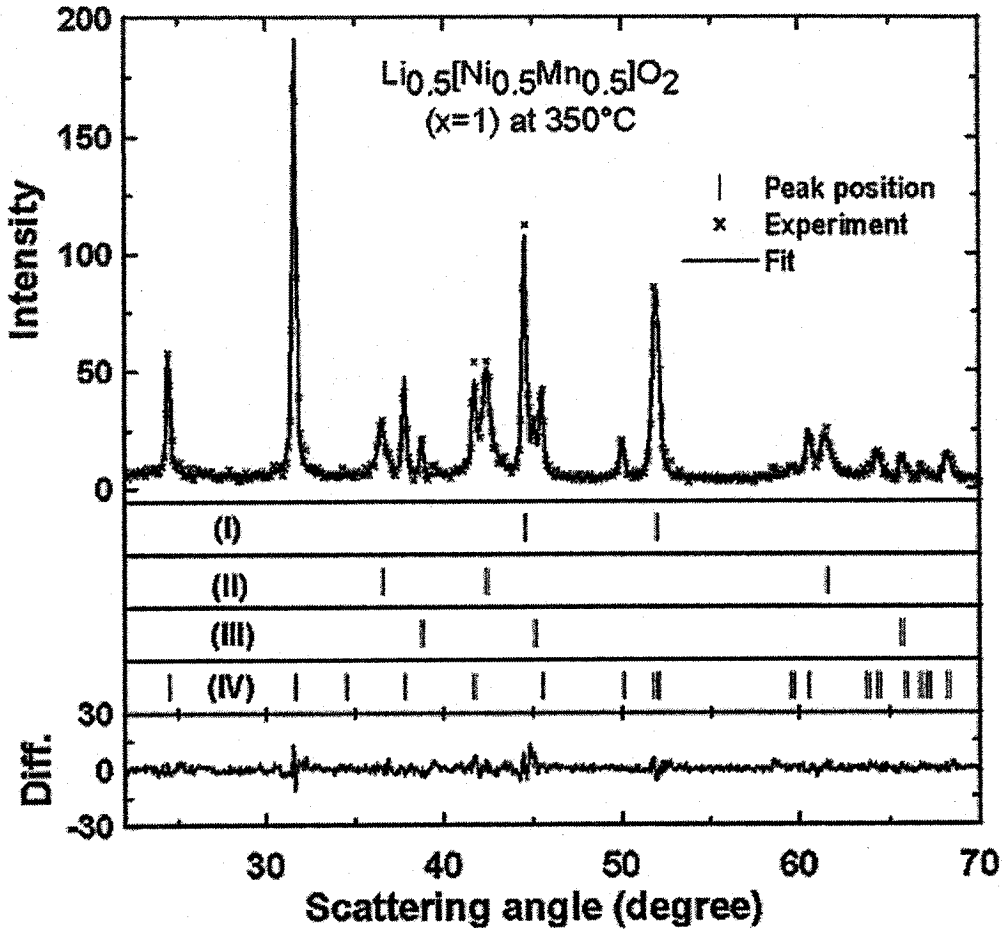

Figure 6.35 Rietveld profile fitting to the XRD pattern (Figure 6.33d) of the products from the reaction between $Li[Ni_{0.5}Mn_{0.5}]O_2$ and EC/DEC at 350°C. Four phases are needed to describe this pattern. They are M metal (I), $[Li_qM_{1-q}]O$ (II), LiF (III), and $MnCO_3$ (IV).

Table 6.5 Lattice constants and atom positions for the products of the reactions between $Li[(Ni_{0.5}Mn_{0.5})_xCo_{1-x}]O_2$ (x = 0.4, 0.7, 0.9, and 1) samples and EC/DEC in ARC experiments stopped at 350°C (shown in Figure 6.33). Multi-phase Rietveld refinement was used. The space group used for the refinements is Fm3m ($^{\#}225$) for $[Li_qM_{1-q}]O$ rock-salt and M phases. "M" represents mixed transition metals (Ni, Co, and Mn). The Bragg R-factors are listed.

XRD curves in Figure 6.33	Phases	Lattice constant (a, Å)	Atom position	Fractional occupation	R_{Bragg} factor
(a) x = 0.4	M	a = 3.5413(2)	M: (0, 0, 0)	1	0.6%
	$[Li_qM_{1-q}]O$	a = 4.2666(4)	M: (0.5, 0.5, 0.5) O: (0, 0, 0)	0.7375(2) 1	1.9%
(b) x = 0.7	M	a = 3.5331(7)	M: (0, 0, 0)	1	2.5%
	$[Li_qM_{1-q}]O$	a = 4.2661(1)	M: (0.5, 0.5, 0.5) O: (0, 0, 0)	0.7702(9) 1	1.8%
(c) x = 0.9	M	a = 3.5293(5)	M: (0, 0, 0)	1	2.8%
	$[Li_qM_{1-q}]O$	a = 4.2670(2)	M: (0.5, 0.5, 0.5) O: (0, 0, 0)	0.7750(4) 1	2.5%
(d) x = 1	M	a = 3.5308(3)	M: (0, 0, 0)	1	3.0%
	$[Li_qM_{1-q}]O$	a = 4.2728(6)	M: (0.5, 0.5, 0.5) O: (0, 0, 0)	0.7728(2) 1	1.8%

In order to explore the reaction sequence between $Li[(Ni_{0.5}Mn_{0.5})_{0.4}Co_{0.6}]O_2$ and EC/DEC between 200°C and 290°C, we conducted another two ARC tests on 50 mg of $Li[(Ni_{0.5}Mn_{0.5})_{0.4}Co_{0.6}]O_2$ (x = 0.4, 4.2 V) reacting with 50 mg of EC/DEC, stopping the tests at 242°C and 252°C, respectively. The results obtained are shown in Figures 6.36a and b. The ARC measurements of the samples (x = 0.4, 4.2 V) stopped at 290°C and 350°C have been included as panels c and d respectively, for comparison. These four ARC measurements for the same sample clearly show the good reproducibility of the ARC data. No other research group in the world can produce ARC data of this quality.

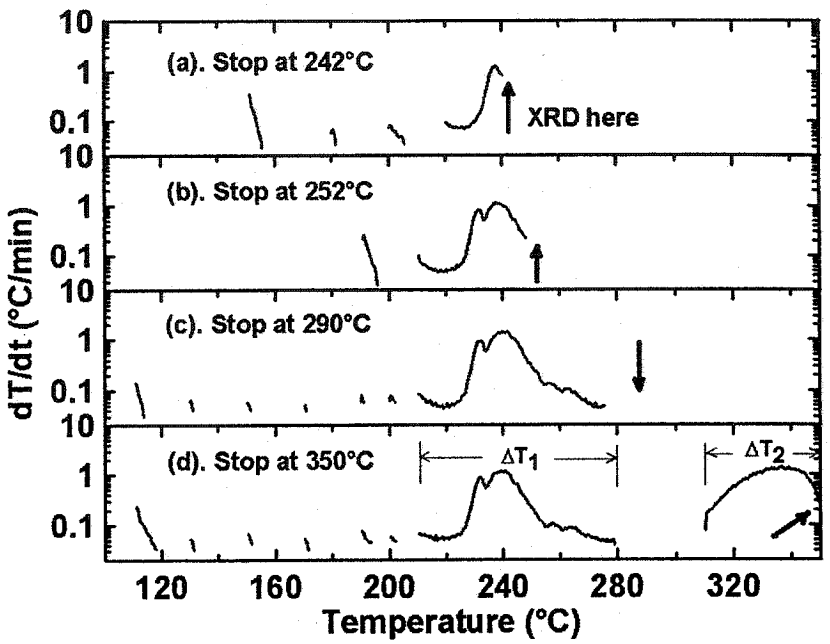

Figure 6.36 SHR vs. T for 50 mg of $Li[(Ni_{0.5}Mn_{0.5})_{0.4}Co_{0.6}]O_2$ (x = 0.4) charged to 4.2V heated with 50 mg of EC/DEC solvent.

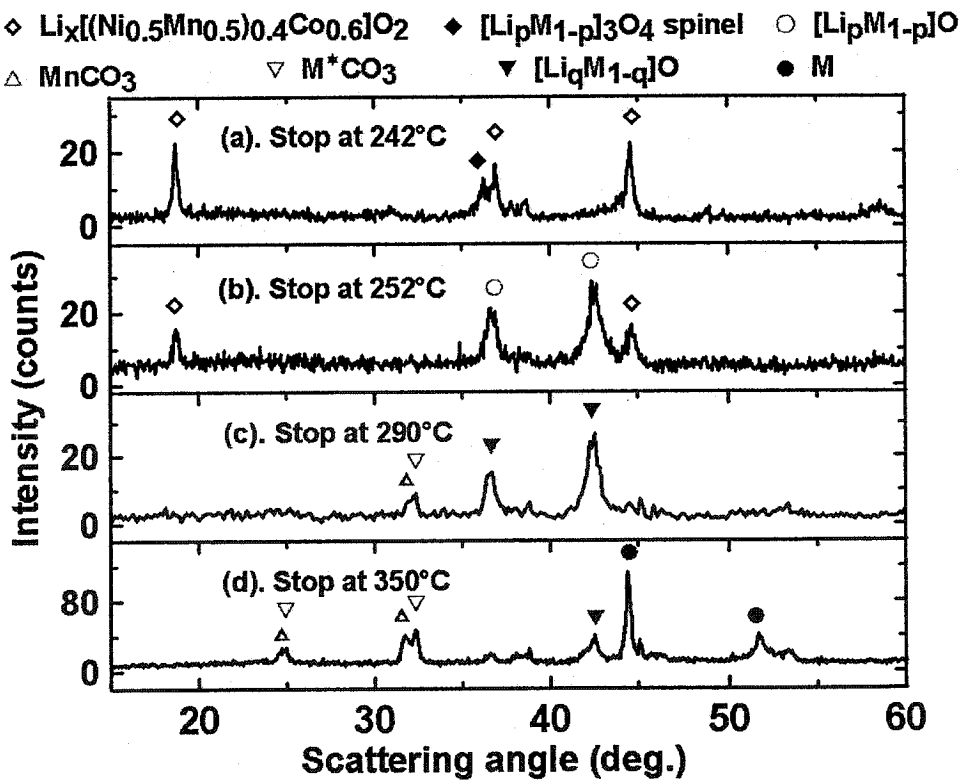

Figure 6.37 XRD patterns of $Li[(Ni_{0.5}Mn_{0.5})_{0.4}Co_{0.6}]O_2$ charged to 4.2 V after reacting with EC/DEC. ARC measurements are shown in Figure 6.36.

The XRD patterns for the reaction products of $Li[(Ni_{0.5}Mn_{0.5})_{0.4}Co_{0.6}]O_2$ (x = 0.4, 4.2 V) with EC/DEC heated to different temperatures are shown in Figure 6.37. The four XRD curves in Figure 6.37 were refined using the multi-phase Rietveld refinement program and the results are listed in Table 6.6. The fit to the XRD curve in Figure 6.37a is shown in Figure 6.38 (The fitted XRD curves in Figures 6.37c and d were already shown in Figures 6.31 and 6.34, respectively). There are two main phases, $[Li_pM_{1-p}]_3O_4$ spinel phase (I) and the original Li_xMO_2 layered-structure phase (III) together with a small amount of LiF [II] (Figure 6.38).

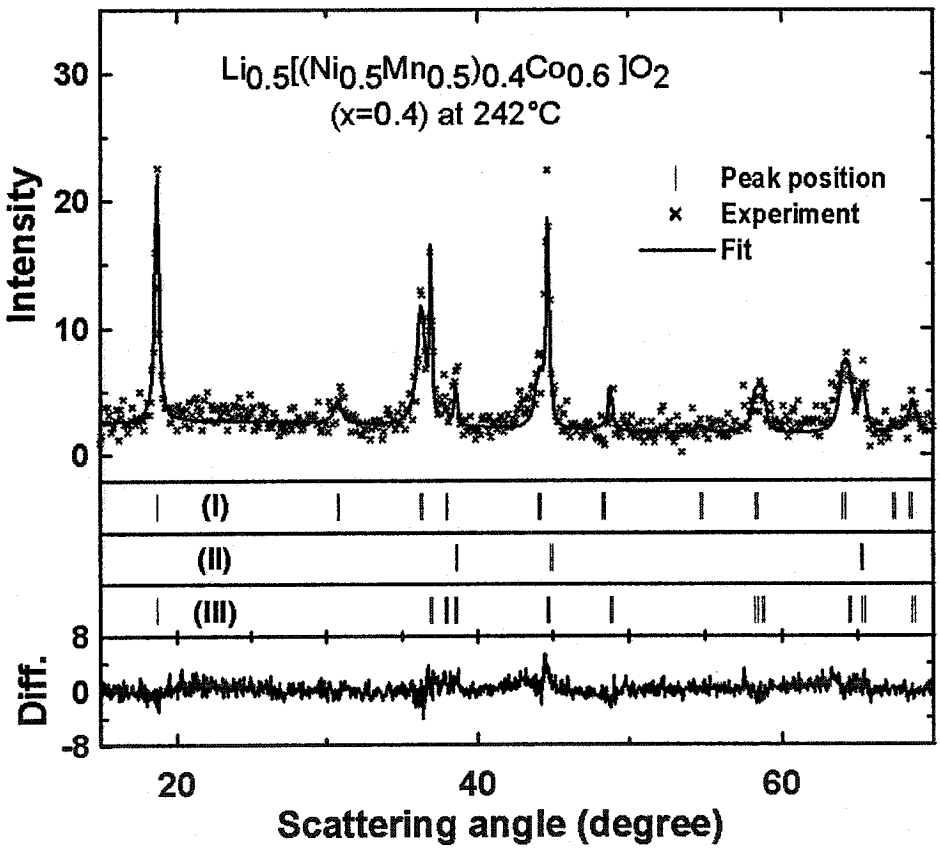

Figure 6.38 Rietveld profile fitting to the XRD pattern (Figure 6.37a) of the products from the reaction between $Li[(Ni_{0.5}Mn_{0.5})_{0.4}Co_{0.6}]O_2$ and EC/DEC at 242°C. Three phases are needed to describe this pattern. They are $[Li_pM_{1-p}]_3O_4$ (I), LiF (II), and Li_xMO_2 (III).

Table 6.6 Lattice constants and atom positions for the products of reactions between $Li[(Ni_{0.5}Mn_{0.5})_{0.4}Co_{0.6}]O_2$ and EC/DEC in ARC experiments stopped at different temperatures (shown in Figure 6.37). Multi-phase Rietveld refinement was used. The space groups used for the refinements were R-3m (#166) for the Li_xMO_2 phase and Fd3m (#227) for the $[Li_pM_{1-p}]_3O_4$ spinel, Fm3m (#225) for $[Li_pM_{1-p}]O$ rock-salt and M phases. "M" represents mixed transition metals (Ni, Co, and Mn). The Bragg R-factors are listed.

XRD curves in Figure 6.37	Phases	Lattice constant (Å)	Atom position	Fractional occupation	R_{Bragg} factor
(a) stopped at 242°C	$[Li_pM_{1-p}]_3O_4$	a = 8.2215(4)	M_1: (0.125, 0.125, 0.125) M_2: (0.5, 0.5, 0.5) O: (0.25469, 0.25469, 0.25469)	0.5445(5) 1.4554(5) 4	6.5%
	Li_xMO_2	a = 2.8551(2) c = 14.2525(7)	M: (0.5, 0.5, 0.5) O: (0, 0, 0)	1 2	6.8%
(b) stopped at 252°C	Li_xMO_2	a = 2.8588(2) c = 14.2939(5)	M: (0.5, 0.5, 0.5) O: (0, 0, 0)	1 2	2.7%
	$[Li_pM_{1-p}]O$	a = 4.2573(6)	M: (0.5, 0.5, 0.5) O: (0, 0, 0)	0.7655(6) 1	4.5%
(c) stopped at 290°C	M	a = 3.5300(5)	M: (0, 0, 0)	1	4.3%
	$[Li_qM_{1-q}]O$	a = 4.2689(2)	M: (0.5, 0.5, 0.5) O: (0, 0, 0)	0.8155(1) 1	3.5%
(d) stopped at 350°C	M	a = 3.5413(2)	M: (0, 0, 0)	1	0.6%
	$[Li_qM_{1-q}]O$	a = 4.2666(4)	M: (0.5, 0.5, 0.5) O: (0, 0, 0)	0.7375(2) 1	1.9%

Therefore, the thermal reaction sequence for $Li[(Ni_{0.5}Mn_{0.5})_{0.4}Co_{0.6}]O_2$ (x = 0.4, 4.2 V) and EC/DEC can be described as follows. $Li[(Ni_{0.5}Mn_{0.5})_{0.4}Co_{0.6}]O_2$ (4.2 V) starts to lose O_2 at approximately 220°C in the presence of EC/DEC, generating $[Li_pM_{1-p}]_3O_4$ spinel phase. This reaction step is similar to the reaction sequence that $LiCoO_2$ (4.2 V) follows. $Li_{0.5}CoO_2$ thermally first decomposes into Co_3O_4 spinel in the presence of EC/DEC [84, 52]. However, the reaction of $Li_{0.5}CoO_2$ with EC/DEC starts at a much

lower temperature of approximately 150°C (Section 3.1.2). From 242°C to 252°C, a second thermal process occurs where $[Li_pM_{1-p}]_3O_4$ spinel continuously reacts with EC/DEC producing $[Li_pM_{1-p}]O$ (rock-salt structure), which is similar with the thermal reaction of Co_3O_4 with EC/DEC generating CoO rock-salt [84, 86].

A third process happens between 252°C and 290°C. Mn, Ni, and Co cations move out of the spinel framework forming $MnCO_3$, M^*CO_3 and $[Li_qM_{1-q}]O$ rock-salt (Figure 6.29a). In the last process above, $[Li_qM_{1-q}]O$ is reduced to M metal by EC/DEC. This is not surprising because EC/DEC is able to reduce $Li_{0.5}CoO_2$ to Co metal [84, 86].

The most significant difference between the reactions of $Li_{0.5}[(Ni_{0.5}Mn_{0.5})_{0.4}Co_{0.6}]O_2$ and $Li_{0.5}CoO_2$ with EC/DEC is that the original Li_xMO_2 with the layered structure was completely consumed at 290°C (Figure 6.37c) but there is some $LiCoO_2$ left after the reaction between $Li_{0.5}CoO_2$ and EC/DEC at 350°C (Figure 3.25).

The four-process reaction sequence between $Li[(Ni_{0.5}Mn_{0.5})_{0.4}Co_{0.6}]O_2$ (4.2V) and EC/DEC can be summarized as follows (Note: The reactions below are not balanced since p and q are not known):

Process (1): $Li_x[(Ni_{0.5}Mn_{0.5})_{0.4}Co_{0.6}]O_2 + EC/DEC \rightarrow [Li_pM_{1-p}]_3O_4 + CO_2 + H_2O.$ [6-1]

(2): $[Li_pM_{1-p}]_3O_4 + EC/DEC \rightarrow [Li_pM_{1-p}]O + CO_2 + H_2O.$ [6-2]

(3): $[Li_pM_{1-p}]O + EC/DEC \rightarrow [Li_qM_{1-q}]O + MnCO_3/M^*CO_3 + CO_2 + H_2O.$ [6-3]

(4): $[Li_qM_{1-q}]O + EC/DEC \rightarrow M + CO_2 + H_2O.$ [6-4]

The heat (h) released from the thermal reaction between $Li[(Ni_{0.5}Mn_{0.5})_{0.4}Co_{0.6}]O_2$ (4.2V) and EC/DEC is calculated using the same method described in Section 2.1:

$$h = C_{Tot} \times \Delta T, \quad [6\text{-}5]$$

where ΔT is the temperature rise in the ARC measurement and C_{Tot} is the total heat capacity of the entire sample (electrode material, solvent, plus stainless steel ARC tube). A specific heat of 1.0 $J\ K^{-1}\ g^{-1}$ was used for $Li[(Ni_{0.5}Mn_{0.5})_{0.4}Co_{0.6}]O_2$ (4.2 V).

ΔT_1 shown in Figure 6.36d is approximately 70 K, which corresponds to the transformation of $Li[(Ni_{0.5}Mn_{0.5})_{0.4}Co_{0.6}]O_2$ (4.2 V) to the $[Li_qM_{1-q}]O$ phase. The reaction in the ARC measurement in Figure 6.36d is almost complete at 350°C. ΔT_2 is found to be approximately 50 K, corresponding to the reaction of $[Li_qM_{1-q}]O$ with EC/DEC to form M

metal. C_{Tot} is calculated to be 0.55 J K^{-1}. The heat released during each of the two processes, h_1 and h_2, were approximately 38 J and 27 J, respectively. The amount of active $Li[(Ni_{0.5}Mn_{0.5})_{0.4}Co_{0.6}]O_2$ (4.2 V) in 50 mg of electrode material is 50×(1.00-0.14) mg, accounting for the presence of the binder (7% by weight) and carbon black (7% by weight). Therefore, the exothermic heats based on the positive electrode weight for the two processes are approximately 895 J g^{-1} and 640 J g^{-1}. These data are slightly larger than the heat released during the analogous two processes of $Li_{0.5}CoO_2$ reacting with EC/DEC, 820 J g^{-1} from the reaction from $Li_{0.5}CoO_2$ to CoO rock-salt and 540 J g^{-1} from the further reaction to Co metal [84, 86]. The small difference may result from surface area effects as the synthesized $Li[(Ni_{0.5}Mn_{0.5})_{0.4}Co_{0.6}]O_2$ has a particle size of only 0.2 μm compared to the 5 μm particle size of $LiCoO_2$.

The ARC results show that a similar amount of heat is released when either $Li[(Ni_{0.5}Mn_{0.5})_{0.4}Co_{0.6}]O_2$ or $LiCoO_2$ (both charged to 4.2 V vs. Li) **completely** react with EC/DEC solvent. The improved thermal stability of charged $Li[(Ni_{0.5}Mn_{0.5})_{0.4}Co_{0.6}]O_2$ over $LiCoO_2$ is evidenced by the higher transformation temperature of the $Li[(Ni_{0.5}Mn_{0.5})_{0.4}Co_{0.6}]O_2$ (4.2V) layered compound to the $[Li_pM_{1-p}]_3O_4$ spinel starting from around 220°C compared with 150°C for the transformation of $Li_{0.5}CoO_2$ to Co_3O_4 in the presence of EC/DEC solvent. References [11, 52, 148, 149] showed that partial substitution of Ni with Co to form $LiNi_xCo_{(1-x)}O_2$ improves the thermal stability of $LiNiO_2$, although it is still much worse than $LiCoO_2$. This strongly suggests that it is the presence of Mn^{4+} in $Li[(Ni_{0.5}Mn_{0.5})_{0.4}Co_{0.6}]O_2$ (4.2V) that is responsible for the improved thermal stability of $Li[(Ni_{0.5}Mn_{0.5})_{0.4}Co_{0.6}]O_2$ relative to $LiCoO_2$.

Guilmard and Delmas [150, 151] studied the decomposition mechanisms of $Li_{0.5}Ni_{1.02}O_2$, $Li_{0.5}Ni_{0.89}Mn_{0.16}O_2$, and $Li_{0.5}Ni_{0.9}Mn_{0.1}O_2$ layered cathodes using TGA-MS under an argon atmosphere. The three cathodes underwent similar phase transitions from a layered phase at the beginning, through a pseudo-spinel phase, finally to a MO (M indicating metal ions) rock-salt phase, which is similar to the reaction sequence between $Li[(Ni_{0.5}Mn_{0.5})_{0.4}Co_{0.6}]O_2$ and EC/DEC. However, the final phase transition from rock-salt compounds to pure metal (Co or Ni) was not observed in Guilmard' studies. This is because they conducted their experiments in an inert atmosphere, where EC/DEC (a reducing agent) is absent. Guilmard found that both $Li_{0.5}Ni_{0.89}Mn_{0.16}O_2$, and

$Li_{0.5}Ni_{0.9}Mn_{0.1}O_2$ layered compounds start changing to a pseduo-spinel phase at around 240°C in TGA, compared to a 200°C phase transition temperature for $Li_{0.5}Ni_{1.02}O_2$ transforming to $[LiNi_{2.04}]O_4$ spinel [150, 151]. This suggests that Mn substitution for Ni in $LiNiO_2$ causes a decrease in the kinetics of the transformation to the pseudo-spinel phase, which inhibits the rate of O_2-release and hence increases the thermal stability.

The XRD patterns (Figure 6.33) of the products from the reactions between $Li[(Ni_{0.5}Mn_{0.5})_xCo_{1-x}]O_2$ samples and EC/DEC at 350°C show that the XRD peaks for M^*CO_3 (M = Co and Ni mixture) at around 32.5° are pronounced for the samples with x = 0.4 and 0.7 (Figures 6.33a and b). The Co content, 1-x, is 0.6 and 0.3 in these two cases. However, when x equals 0.9 (Figure 6.33c, 10% Co) or 1 (Figure 6.33d, no Co), there is no XRD evidence for the existence of M^*CO_3. This suggests that M^*CO_3 is simply $CoCO_3$. The refinement results in Figure 6.34 show that the lattice constants, *a* and *c*, of M^*CO_3 are 4.697 Å and 15.196 Å, respectively, which are closer to the lattice constants of $CoCO_3$ as listed in Table 6.3. This also suggests that M^*CO_3 is more likely $CoCO_3$.

The free energies of formation (ΔG_f°) of the transition metal carbonates, $MnCO_3$, $CoCO_3$, and $NiCO_3$, are compared in Table 6.7 [114, 117]. The carbonates are believed to come from the reaction between MO and CO_2 at high temperatures and pressures in the ARC experiments. Therefore, ΔG_f° for MO is also included in Table 6.7. The free-energy differences (ΔG_f) between $MnCO_3$ and MnO or between $CoCO_3$ and CoO are both around –460 kJ mol^{-1}, which is significantly lower than ΔG_f between $NiCO_3$ and NiO (approximately –400 kJ mol^{-1}). This suggests that $MnCO_3$ and $CoCO_3$ are more likely to be produced from MO and CO_2 than $NiCO_3$ at standard conditions (1 atmosphere and 25°C). Although the ARC experiments were conducted at high pressure and high temperature, the free energy of formation comparisons still show the relative sequence to form MCO_3. This also suggests that M^*CO_3 is probably $CoCO_3$.

Further work is needed to fully understand the reasons for the increased thermal stability of $Li[(Ni_{0.5}Mn_{0.5})_xCo_{1-x}]O_2$ ($x \geq 0.4$) samples over $LiCoO_2$.

Table 6.7 The standard free energies of formation (ΔG_f°) of MCO_3 and MO compounds and their differences (ΔG_f) from references [114, 117]. M represents the transition metals (Mn, Co, and Ni).

M	Free energy, ΔG_f°, kJ mol^{-1}		$\Delta G_f = (\Delta G_f^\circ)_{MCO3} - (\Delta G_f^\circ)_{MO}$ kJ mol^{-1}
	MO	MCO_3	
Mn	-363	-817	-454
Co	-254	-713	-459
Ni	-212	-612	-400

6.2 $Li[(Ni_{1/2}Mn_{1/2})_x(Li_{1/3}Mn_{2/3})_{1-x}]O_2$ samples, the $Li[Ni_{1/2}Mn_{1/2}]O_2 \bullet Li[Li_{1/3}Mn_{2/3}]O_2$ binary system

In the last section, a series of samples in the $Li[Ni_{1/2}Mn_{1/2}]O_2 \bullet LiCoO_2$ binary system were synthesized and their electrochemical properties and thermal stability were studied. The results suggested that $Li[(Ni_{1/2}Mn_{1/2})_xCo_{1-x}]O_2$ ($0.4 \leq x \leq 0.7$) samples have high specific discharge capacity around 170 mA h g^{-1} (4.4 V) and excellent thermal stability (much higher than $LiCoO_2$).

This section focuses on another binary system, $Li[Ni_{1/2}Mn_{1/2}]O_2 \bullet Li[Li_{1/3}Mn_{2/3}]O_2$, which is the left edge of the $Li[Ni_{1/2}Mn_{1/2}]O_2 \bullet LiCoO_2 \bullet Li[Li_{1/3}Mn_{2/3}]O_2$ pseudoternary system (shown in Figure 6.39).

The samples in the $Li[Ni_{1/2}Mn_{1/2}]O_2 \bullet Li[Li_{1/3}Mn_{2/3}]O_2$ binary can be written as $Li[(Ni_{1/2}Mn_{1/2})_x(Li_{1/3}Mn_{2/3})_{1-x}]O_2$ ($0 < x \leq 1$). The $Li[(Ni_{1/2}Mn_{1/2})_x(Li_{1/3}Mn_{2/3})_{1-x}]O_2$ samples adopt the same layered-structure as $LiCoO_2$ (Section 1.3.2) and were pioneered by Lu and Dahn in 2001 [67]. Later on, the $Li[(Ni_{1/2}Mn_{1/2})_x(Li_{1/3}Mn_{2/3})_{1-x}]O_2$ materials attracted much attention mainly because they can deliver a high discharge capacity over 220 mA h g^{-1} [67, 70]. The $Li[(Ni_{1/2}Mn_{1/2})_x(Li_{1/3}Mn_{2/3})_{1-x}]O_2$ samples all displayed a plateau at about 4.5 V vs. lithium metal during the first charge, which was believed to correspond to oxygen loss concomitant with Li extraction [67, 70, 77]. Subsequent to this plateau, the materials can reversibly cycle over 220 mA h g^{-1} (almost one Li atom per formula unit) between 2.0 V and 4.6 V.

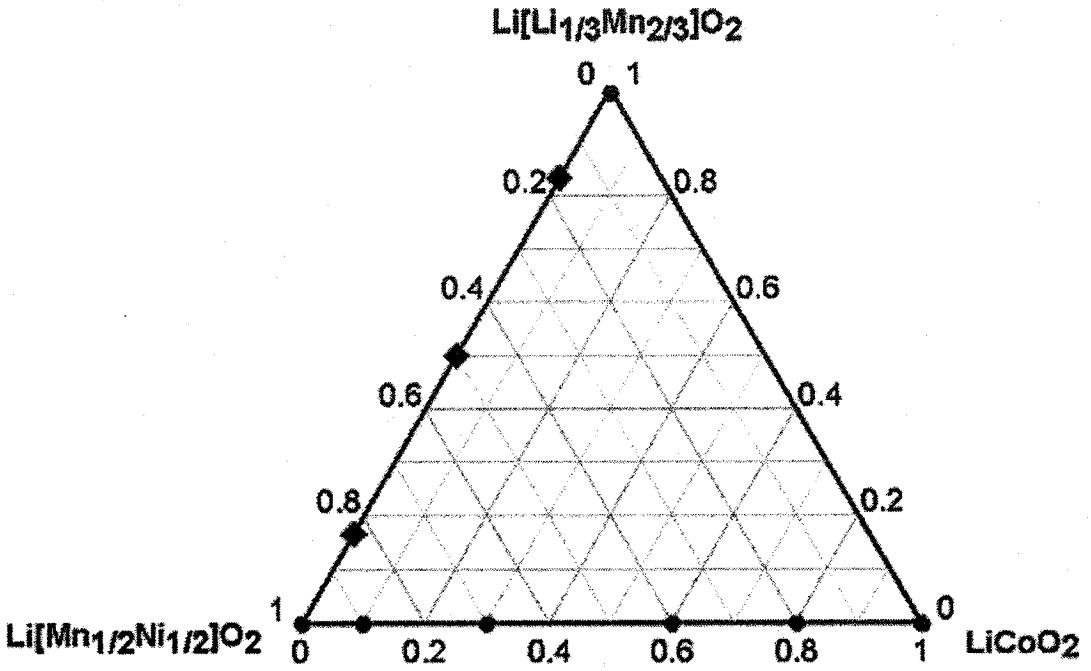

Figure 6.39 The compositions of $Li[(Ni_{1/2}Mn_{1/2})_x(Li_{1/3}Mn_{2/3})_{1-x}]O_2$ (x = 1/6, 1/2, and 5/6) studied compounds indicated with "diamonds".

However, so far, there is only one report of the thermal stability of $Li[(Ni_{1/2}Mn_{1/2})_x(Li_{1/3}Mn_{2/3})_{1-x}]O_2$ (x = 5/6) samples. Lu *et al.* [24] reported DSC experiments on charged electrode materials and found that the reaction between charged $Li[(Ni_{1/2}Mn_{1/2})_x(Li_{1/3}Mn_{2/3})_{1-x}]O_2$ (x = 5/6) and electrolyte moved to lower temperature as the charging potential increased. Thermal stability measurements at high potentials are very important in order to assess whether the high capacity (over 220 mA h g^{-1}) available in these materials can be harnessed in practical cells that must also pass numerous abuse tests.

In this section, the thermal stability of charged $Li[(Ni_{1/2}Mn_{1/2})_x(Li_{1/3}Mn_{2/3})_{1-x}]O_2$ (x = 1/6, 1/2, and 5/6) samples synthesized at 900°C is characterized using ARC in EC/DEC and $LiPF_6$ based electrolyte. (The compositions of these three samples are indicated with "diamonds" in Figure 6.39.)

6.2.1 Sample characterizations by SEM, BET, and XRD

Figure 6.40 shows the SEM micrographs of the $Li[(Ni_{1/2}Mn_{1/2})_x(Li_{1/3}Mn_{2/3})_{1-x}]O_2$ (x = 1/6, 1/2, 5/6 and 1) samples. These four samples have a small primary particle size of approximately 0.2 μm. The specific surface areas determined by single point BET of the $Li[(Ni_{1/2}Mn_{1/2})_x(Li_{1/3}Mn_{2/3})_{1-x}]O_2$ (x = 1/6, 1/2, 5/6 and 1) samples are approximately 3.6, 3.9, 3.5, and 3.3 $m^2 g^{-1}$ respectively.

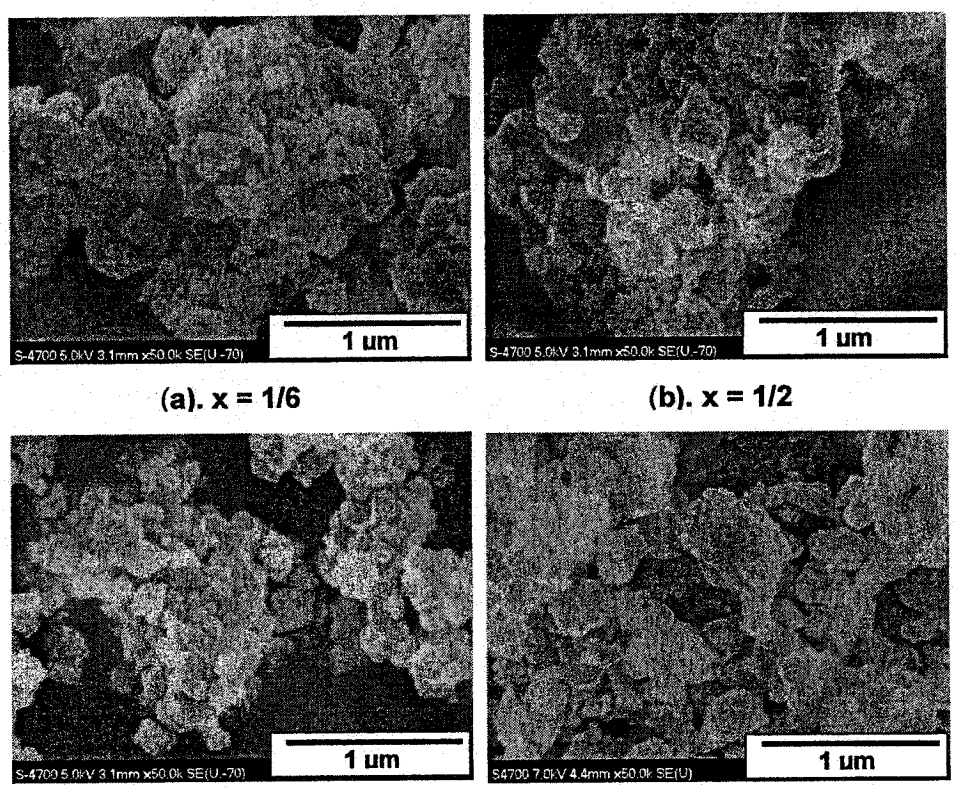

(a). x = 1/6 (b). x = 1/2

(c). x = 5/6 (d). x = 1

Figure 6.40 SEM micrographs of $Li[(Ni_{1/2}Mn_{1/2})_x(Li_{1/3}Mn_{2/3})_{1-x}]O_2$ (x = 1/6, 1/2, 5/6 and 1) samples. From the images the average primary particle size of these four samples is approximately 0.2 μm.

The XRD patterns of the $Li[(Ni_{1/2}Mn_{1/2})_x(Li_{1/3}Mn_{2/3})_{1-x}]O_2$ (x = 1/6, 1/2, and 5/6) samples synthesized at 900°C were measured and are shown in Figures 6.41a, b, and c respectively. The small XRD peaks at around 21, 22, 24, and 28° in Figure 6.41a clearly show the superlattice ordering of Li and Mn in the predominantly transition-metal layer, which is in good agreement with reference [67]. As x increases from 1/6 in panel a to 5/6

in panel c, the width of the XRD peaks of the samples becomes larger and the samples become less crystalline.

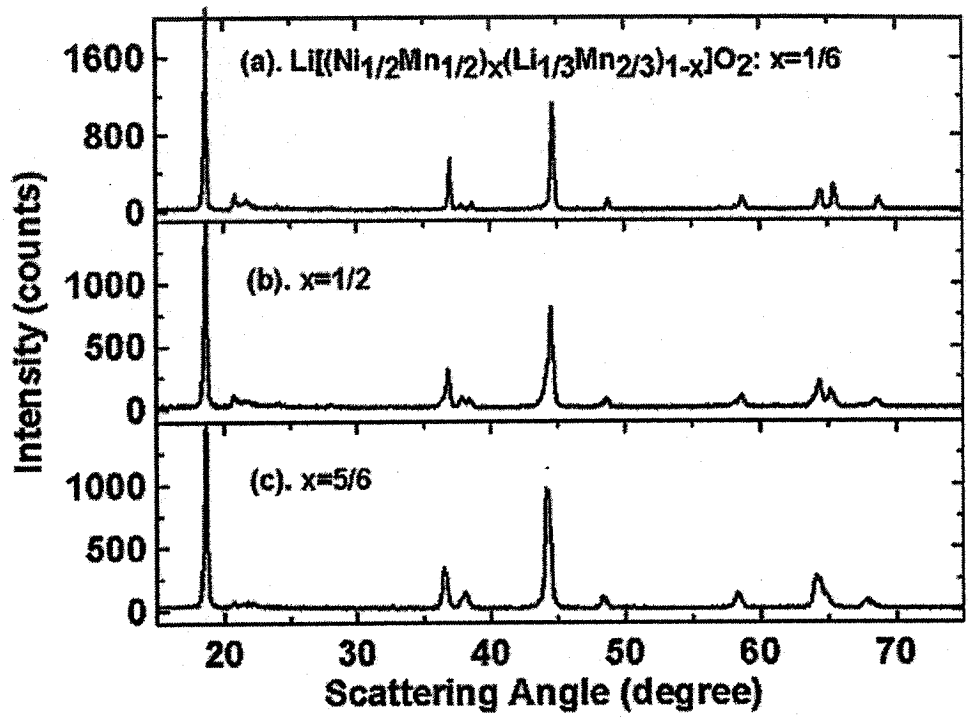

Figure 6.41 The X-ray diffraction (XRD) patterns of the $Li[(Ni_{1/2}Mn_{1/2})_x(Li_{1/3}Mn_{2/3})_{1-x}]O_2$ (x = 1/6, 1/2, and 5/6) samples shown in panels (a), (b), and (c), respectively.

An interesting thing happened when the $Li[(Ni_{1/2}Mn_{1/2})_x(Li_{1/3}Mn_{2/3})_{1-x}]O_2$ pellet electrode was charged to 4.8 V vs. Li in a coin cell constructed as shown in Figure 2.4. The specific charging capacity of $Li[(Ni_{1/2}Mn_{1/2})_x(Li_{1/3}Mn_{2/3})_{1-x}]O_2$ to 4.8 V vs. Li is approximately 350 mA h g^{-1} (x = 1/6), 310 mA h g^{-1} (x = 1/2), and 250 mA h g^{-1} (x = 5/6) [24, 70]. For the coin type cells used to prepare samples (4.8 V) for ARC measurements, the electrode masses were 500 mg of $Li[(Ni_{1/2}Mn_{1/2})_x(Li_{1/3}Mn_{2/3})_{1-x}]O_2$ and 500 mg, 440 mg, and 360 mg of MCMB to coulometrically balance cells with $Li[(Ni_{1/2}Mn_{1/2})_x(Li_{1/3}Mn_{2/3})_{1-x}]O_2$ positive electrodes having x = 1/6, 1/2, and 5/6, respectively. Coin cells with 500 mg positive electrodes of $Li[(Ni_{1/2}Mn_{1/2})_x(Li_{1/3}Mn_{2/3})_{1-x}]O_2$ with x = 1/6 and x = 1/2 **vented** after about 85 and 110 hours, respectively, of charging at 1 mA because of pressure buildup due to O_2 release during the plateau around

4.5 V vs. Li [24]. These cells were redesigned and the electrode mass of $Li[(Ni_{1/2}Mn_{1/2})_x(Li_{1/3}Mn_{2/3})_{1-x}]O_2$ with x = 1/6 and x = 1/2 was decreased to 300 mg. The amount of MCMB was adjusted to coulometrically balance the cells. The redesigned cells did not open during the charging process to 4.8 V. When cells successfully charged to 4.8 V were slowly pried open in the argon-filled glove box, the cell lid suddenly popped off with a pinging sound due to the pressure buildup. This did not occur for the cells charged to 4.45 V, before the oxygen-release plateau. These observations strongly support oxygen-release during the 4.5 V plateau during the first charge of $Li[(Ni_{1/2}Mn_{1/2})_x(Li_{1/3}Mn_{2/3})_{1-x}]O_2$ [24, 70].

6.2.2 Electrochemical properties

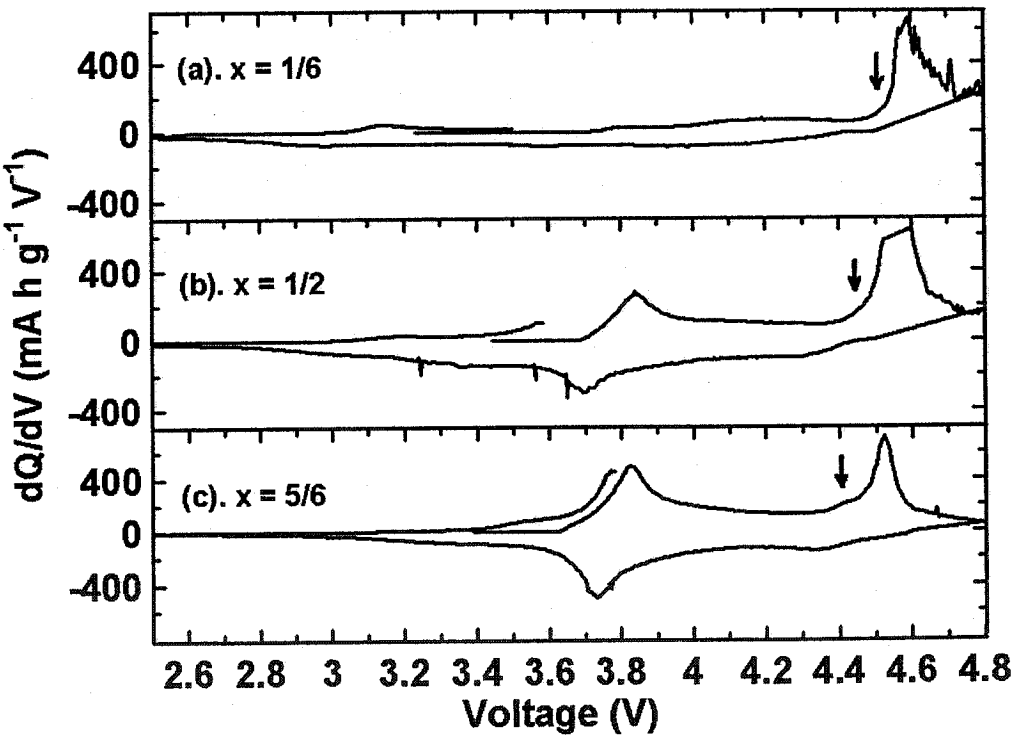

Figure 6.42 The differential capacity [dQ/dV (mA h g^{-1} V^{-1})] versus potential (V) of $Li[(Ni_{1/2}Mn_{1/2})_x(Li_{1/3}Mn_{2/3})_{1-x}]O_2$ with x = 1/6 in panel (a), 1/2 in (b), and 5/6 in (c) from 2.5 V ~ 4.8 V measured at a rate of C/30 (about 10 mA g^{-1}).

Figure 6.42 shows the differential capacity vs. potential for the first cycle of Li/ $Li[(Ni_{1/2}Mn_{1/2})_x(Li_{1/3}Mn_{2/3})_{1-x}]O_2$ cells cycling between 2.5 V and 4.8 V at a C/30 rate.

The "black arrow" in Figure 6.42 shows the potential at the beginning of the oxygen-release plateau during the first charge process. The oxygen-release plateau begins at approximately 4.5, 4.45 and 4.4 V for samples with x = 1/6, 1/2 and 5/6, respectively.

Figure 6.43 shows the potential (V) versus capacity (mA h g^{-1}) curves for the 1st cycle of the cells with $Li[(Ni_{1/2}Mn_{1/2})_x(Li_{1/3}Mn_{2/3})_{1-x}]O_2$ samples (x = 1/6, 1/2, and 5/6) synthesized at 900°C. The data was generated from the cells described by Figure 6.42. The voltage plateau for O_2 release started when the capacity of the $Li[(Ni_{1/2}Mn_{1/2})_x(Li_{1/3}Mn_{2/3})_{1-x}]O_2$ sample reached 50 mA h g^{-1} [x = 1/6 in panel (a)], 100 mA h g^{-1} [x = 1/2 in panel (b)], and 150 mA h g^{-1} [x = 5/6 in panel (c)].

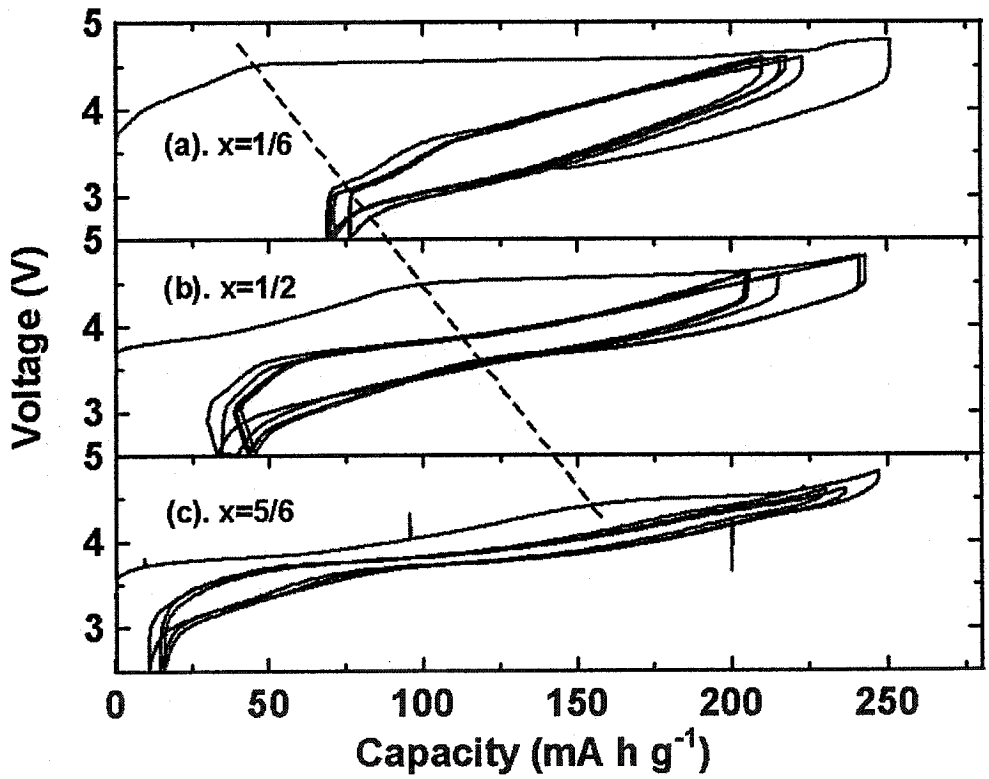

Figure 6.43 Potential (V) versus capacity (mA h g^{-1}) for the 1st cycle of the cells with $Li[(Ni_{1/2}Mn_{1/2})_x(Li_{1/3}Mn_{2/3})_{1-x}]O_2$ samples (x = 1/6, 1/2, and 5/6).

Figures 6.44a, b, and c show the discharge capacity versus cycle number (2.5 V ~ 4.6 V, C/6) for the $Li[(Ni_{1/2}Mn_{1/2})_x(Li_{1/3}Mn_{2/3})_{1-x}]O_2$ samples with x = 1/6, 1/2 and 5/6, respectively. The results are for the same cells used to produce the dQ/dV vs. V measurements in Figure 6.42. Data for two cells are shown in each panel to illustrate the

reproducibility of the electrochemical measurements. The three samples all show good capacity retention during cycling. The sample with x = 5/6 shown in Figure 6.44c shows high discharge capacity of approximately 195 mA h g^{-1} after 100 cycles and about 95% capacity retention at C/6. This capacity is about 30 ~ 40 mA h g^{-1} higher than the layered compounds, $Li[(Ni_{1/2}Mn_{1/2})_xCo_{1-x}]O_2$ (x = 0.2, 0.4, 0.7, 0.9, and 1) charged to 4.4 V vs. Li [23, 76, 152, 153].

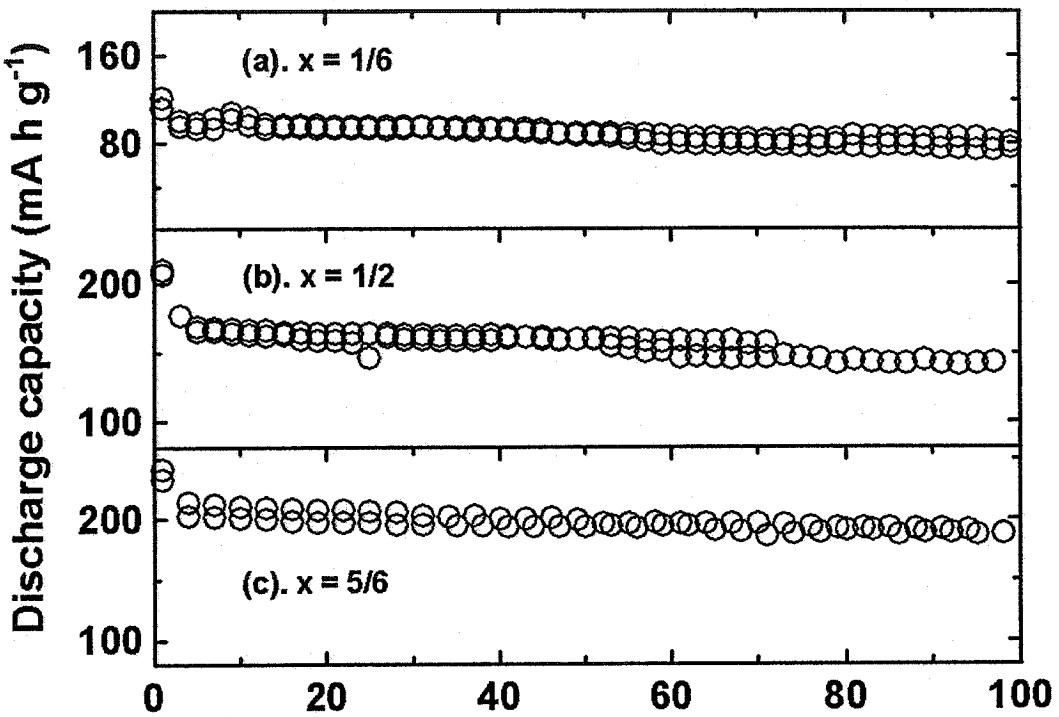

Figure 6.44 The discharge capacity (mA h g^{-1}) versus cycle number of $Li[(Ni_{1/2}Mn_{1/2})_x(Li_{1/3}Mn_{2/3})_{1-x}]O_2$ with x = 1/6 in panel (a), 1/2 in (b), and 5/6 in (c). Cells were charged and discharged between 2.5 V and 4.6 V at a rate of C/6.

6.2.3 Thermal stability

Figure 6.45 shows SHR vs. T for samples of $Li[(Ni_{1/2}Mn_{1/2})_x(Li_{1/3}Mn_{2/3})_{1-x}]O_2$ charged before the oxygen-release plateau [4.5 V (x = 1/6), 4.45 V (x = 1/2), and 4.4 V (x = 5/6)] reacting with EC/DEC solvent in Figure 6.45a, b, and c, respectively. Figure 6.45d shows the SHR vs. T for the sample with x = 1, $Li[Mn_{1/2}Ni_{1/2}]O_2$, charged to 4.4 V vs. Li reacting with EC/DEC solvent for comparison. The sample with x = 1/6 shows the lowest thermal stability among the four samples in EC/DEC and significant self-heating

starts around 150°C. As x increases from 1/6 to 5/6, the main exothermic peak shifts to higher temperature and higher thermal stability is obtained.

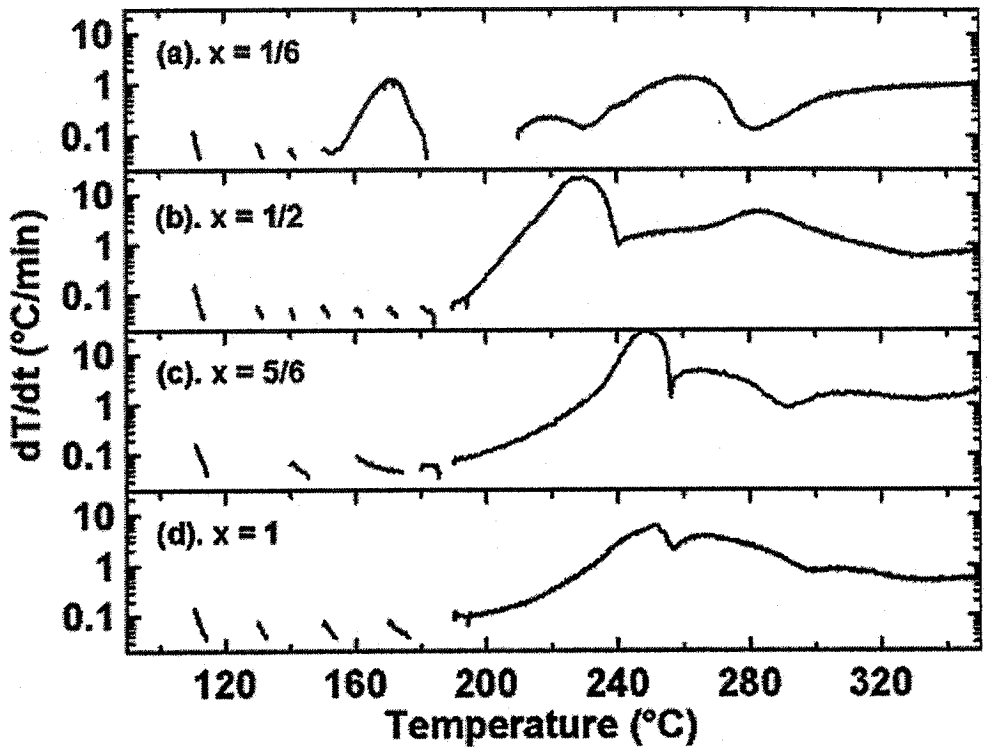

Figure 6.45 Self-heating rate (SHR) versus temperature (T) for 100 mg of $Li[(Ni_{1/2}Mn_{1/2})_x(Li_{1/3}Mn_{2/3})_{1-x}]O_2$ samples charged to 4.5 V (x = 1/6), 4.45 V (x = 1/2), and 4.4 V (x = 5/6) reacting with 100 mg of EC/DEC solvent. Figure 6.45d shows the SHR vs. T of $Li[Ni_{1/2}Mn_{1/2}]O_2$ charged to 4.4 V vs. Li reacting with EC/DEC for comparison. All samples were initially heated to 110 °C

Figure 6.46 shows the SHR vs. T for 100 mg of $Li[(Ni_{1/2}Mn_{1/2})_x(Li_{1/3}Mn_{2/3})_{1-x}]O_2$ (x = 1/6, 1/2, and 5/6) samples charged to 4.8 V vs. Li reacting with 100 mg of EC/DEC (solid lines) or 30 mg of 1.0 M $LiPF_6$ EC/DEC electrolyte (dashed lines), shown in panels (b), (c), and (d), respectively. The ARC samples were initially heated to 110°C. All three samples charged to 4.8 V show relatively poor thermal stability and they all react significantly with EC/DEC above 130°C. The thermal stability of $Li[(Ni_{1/2}Mn_{1/2})_x(Li_{1/3}Mn_{2/3})_{1-x}]O_2$ samples charged to 4.8 V is worse than

$Li[(Ni_{1/2}Mn_{1/2})_xCo_{1-x}]O_2$ (x = 0.2, 0.4, 0.7, 0.9, and 1) charged to either 4.2 V or 4.4 V vs. Li (Section 6.1.1).

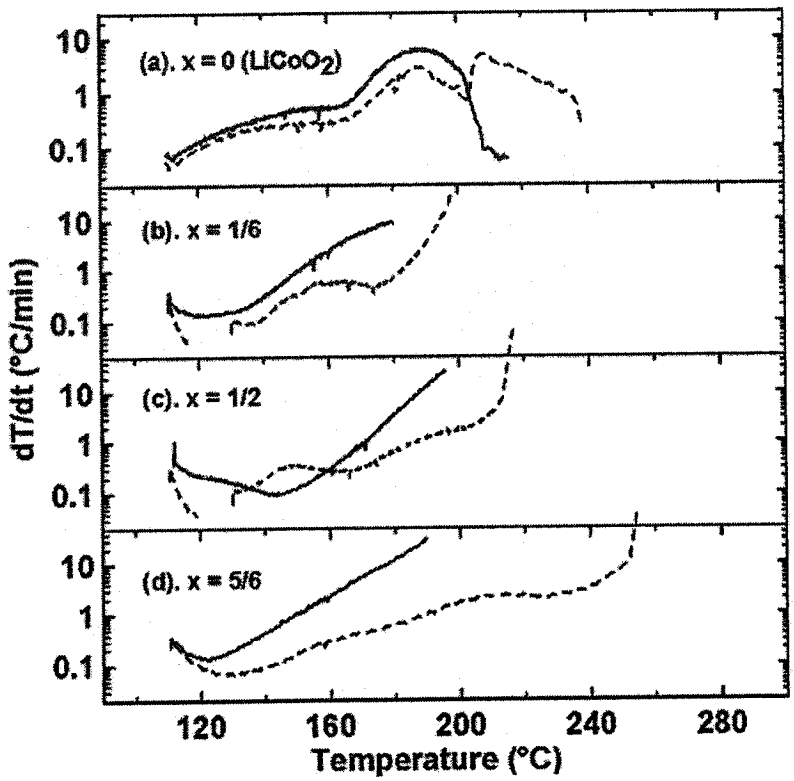

Figure 6.46 Self-heating rate (SHR) versus temperature (T) of 100 mg of $Li[(Ni_{1/2}Mn_{1/2})_x(Li_{1/3}Mn_{2/3})_{1-x}]O_2$ charged to 4.8 V vs. Li reacting with 100 mg of EC/DEC solvent (solid line) or 30 mg of 1.0 M $LiPF_6$ EC/DEC electrolyte (dashed line) shown in panels (b), (c), (d), and (e). Figure 6.46a shows the SHR vs. T of $LiCoO_2$ (sample 1 in Section 3.1.2 with a particle size of about 0.8 μm) charged to 4.2 V vs. Li reacting with EC/DEC (solid line) or 1.0 M $LiPF_6$ EC/DEC (dashed line) for comparison. The ARC samples were all initially heated to 110°C.

The relatively poor thermal stability of $Li[(Ni_{1/2}Mn_{1/2})_x(Li_{1/3}Mn_{2/3})_{1-x}]O_2$ samples charged across the oxygen-release plateau may limit their application as positive electrode materials in lithium-ion batteries, although this series of compounds delivers a high specific capacity up to 225 mA h g^{-1} (2.5 V ~ 4.8 V at C/6). However, the reactivity of 0.8 μm $LiCoO_2$ (4.2 V) in Section 3.1.2 was found to be quite poor. Figure 6.46a shows that the onset temperature for the reaction of 0.8 μm $LiCoO_2$ charged to 4.2 V with

EC/DEC or electrolyte is not so different from the onset temperature of 0.2 μm $Li[(Ni_{1/2}Mn_{1/2})_x(Li_{1/3}Mn_{2/3})_{1-x}]O_2$ charged to 4.8 V. This suggests that larger particle size $Li[(Ni_{1/2}Mn_{1/2})_x(Li_{1/3}Mn_{2/3})_{1-x}]O_2$ will have higher onset temperature and better thermal stability, just like large particle size $LiCoO_2$. Therefore, efforts should focus on increasing the particle size of $Li[(Ni_{1/2}Mn_{1/2})_x(Li_{1/3}Mn_{2/3})_{1-x}]O_2$ to improve safety, while maintaining specific capacity and rate capability.

6.3 x $Li[Ni_{1/2}Mn_{1/2}]O_2$ • y $LiCoO_2$ • z $Li[Li_{1/3}Mn_{2/3}]O_2$ pseudoternary system (x + y + z = 1)

In Sections 6.1 and 6.2, positive electrode materials in two binary systems, x $Li[Ni_{1/2}Mn_{1/2}]O_2$ • y $LiCoO_2$ and x $Li[Ni_{1/2}Mn_{1/2}]O_2$ • z $Li[Li_{1/3}Mn_{2/3}]O_2$, were synthesized and studied. In this section, the positive electrode materials in the x $Li[Mn_{1/2}Ni_{1/2}]O_2$ • y $LiCoO_2$ • z $Li[Li_{1/3}Mn_{2/3}]O_2$ pseudoternary system were studied. The results show that $Li[(Ni_{0.5}Mn_{0.5})_xCo_y(Li_{1/3}Mn_{2/3})_z]O_2$ samples having a composition between $1/6 \leq z \leq 1/3$ and $1/12 \leq y \leq 1/4$ show high discharge capacity (approximately 200 mA h g^{-1} between 2.5 – 4.6 V at C/6) and excellent cycling performance (above 97% capacity retention for 80 cycles). In addition, these samples charged to 4.8 V show less reactivity with $LiPF_6$ EC/DEC electrolyte than $LiCoO_2$ [sample (3) in Section 3.1.2, 5.0 μm particle size)] charged to only 4.2 V.

6.3.1 Introduction

Recently, a number of researchers have been studying positive electrode materials in the pseudoternary system x $Li[Ni_{1/2}Mn_{1/2}]O_2$ • y $LiCoO_2$ • z $Li[Li_{1/3}Mn_{2/3}]O_2$ (x + y + z = 1) in the hope of finding the optimum materials with excellent electrochemical properties and high thermal stability. Figure 6.47 shows the compositions of materials studied by a number of researchers in the recent literature. Zhang *et al.* [154] studied materials in the x $Li[Ni_{1/2}Mn_{1/2}]O_2$ • y $LiCoO_2$ • z $Li[Li_{1/3}Mn_{2/3}]O_2$ system with x = 0.6 and y + z = 0.4. They reported electrochemical and structural results, but no safety-related results. The compositions studied by Zhang *et al.* are indicated in Figure 6.47. Johnson *et al.* [155] and Park *et al.* [156] studied materials in the x $Li[Ni_{1/2}Mn_{1/2}]O_2$ • y

$LiCoO_2$ • z $Li[Li_{1/3}Mn_{2/3}]O_2$ system with y = 0 (compositions indicated in Figure 6.47). They did not report safety-related results. Park *et al.* [73] studied materials in the x $Li[Ni_{1/2}Mn_{1/2}]O_2$ • y $LiCoO_2$ • z $Li[Li_{1/3}Mn_{2/3}]O_2$ system with x = 0 but did not report safety-related results. Yu *et al.* [157] reported results on a material in the x $Li[Ni_{1/2}Mn_{1/2}]O_2$ • y $LiCoO_2$ • z $Li[Li_{1/3}Mn_{2/3}]O_2$ system with x = 0.64, y = 0 and z = 0.36, but no safety-related results were provided. Sun *et al.* [158] and Shin *et al.* [159] studied materials in the x $Li[Ni_{1/2}Mn_{1/2}]O_2$ • y $LiCoO_2$ • z $Li[Li_{1/3}Mn_{2/3}]O_2$ system with z = 0 but did not report safety-related results. Kim *et al.* [160, 161] studied materials with z = 0.3 and x + y = 0.7, but did not report safety related results. Kang and Amine [71] studied the material with x = 1/2, y = 0 and z = 1/2, but did not report any safety related results. It is astonishing to us that numerous researchers can propose electrode materials as possibly viable without doing safety-related studies. Only previous work in Dahn's lab [77] on materials with x + z = 1 and y = 0, that were carefully characterized structurally and electrochemically in [70], reports safety-related characteristics of materials in the x $Li[Mn_{1/2}Ni_{1/2}]O_2$ • y $LiCoO_2$ • z $Li[Li_{1/3}Mn_{2/3}]O_2$ system. Safety related studies of materials in the pseudoternary system are badly lacking.

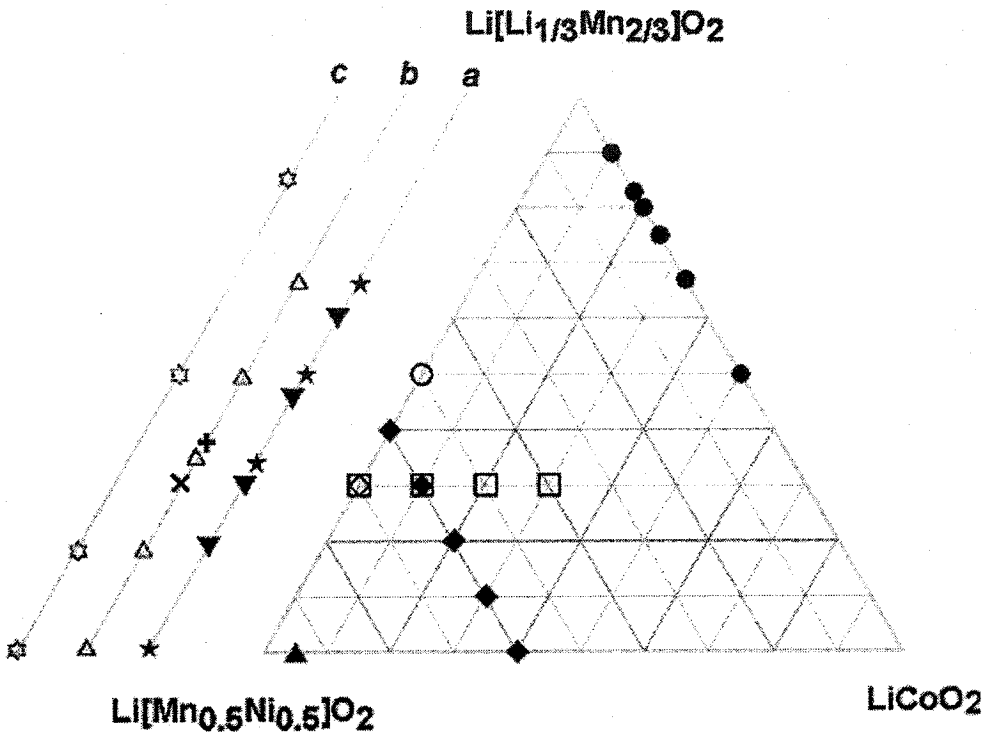

Figure 6.47 Solid solution samples with compositions in the $LiCoO_2$ • $Li[Mn_{1/2}Ni_{1/2}]O_2$ • $Li[Li_{1/3}Mn_{2/3}]O_2$ ternary system described in references [70, 77, 154-161]. Lines a, b, and c represent the binary system between $Li[Mn_{1/2}Ni_{1/2}]O_2$ and $Li[Li_{1/3}Mn_{2/3}]O_2$ phases. This axis has been included three times to help distinguish the large number of data. The compositions indicated with a "◆" are from reference [154] by Zhang *et al.* Compositions indicated by a "□" are from reference [160] by Kim *et al.* Compositions indicated by a "◇" are from reference [161] by Kim *et al.* "○" from reference [71] by Kang *et al.* "▲" from [158] by Sun *et al.* "★" from [156] by Park *et al.* "▼" from [159] by Shin *et al.* "✚" from Yu *et al.* [157], "✕" from Johnson *et al.* [155], "●" from Park *et al.* [73]. The compositions indicated by "☼" and "△" are from previous work [70 and 77] of Jeff Dahn's lab.

The goal in this section is to characterize a series of samples in the x $Li[Ni_{1/2}Mn_{1/2}]O_2$ • y $LiCoO_2$ • z $Li[Li_{1/3}Mn_{2/3}]O_2$ system (x + y + z = 1) for their electrochemical properties (specific capacity, rate capability, capacity retention) and their thermal reactivity with electrolyte in the charged state. In order to decide which

compositions might be most attractive for study, a review of the electrochemical properties reported in references [70, 77, 154-161] was made.

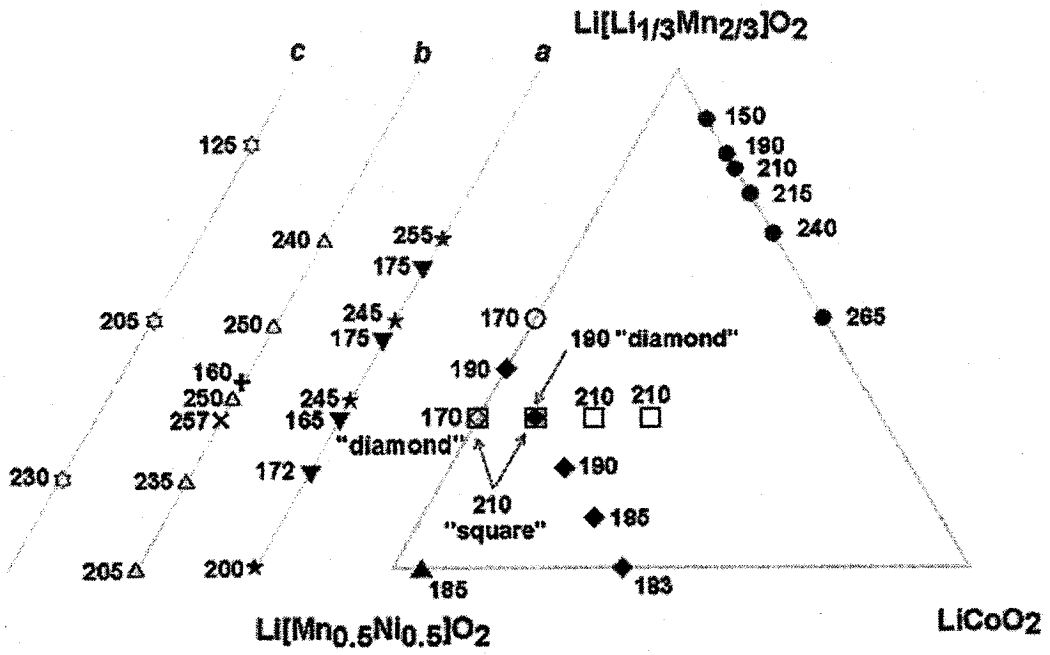

Figure 6.48 Discharge capacity (mA h g^{-1}, first discharge cycle) of layered compounds with different compositions described in references [70, 77, 154-161]. Different potential limits for cycling were used by the various authors as indicated below. "◆" 2.5 - 4.6 V from [154] by Zhang *et al.* "□" 2.5 - 4.6 V from [160] by Kim *et al.* "◇" 2.5 - 4.6 V from [161] by Kim *et al.* "○" 2.0 – 4.6 V from [71] by Kang *et al.* "▲" 2.5 - 4.6 V from [158] by Sun *et al.* "★" 2.0 - 4.8 V from [156] by Park *et al.* "▼" 2.0 - 4.6 V from [169] by Shin *et al.* "✚"2.5 – 4.8 V from Yu *et al.* [157], "✕" 2.0 - 5.0 V from Johnson *et al.* [155], "●"2.0 – 4.8 V from Park *et al.* [73]. The compositions indicated by "☼" and "△" (2.5 - 4.8 V) are from previous work [70 and 77] of Jeff Dahn's lab.

Figure 6.48 shows the reversible specific capacity measured for materials charged through the 4.5 V plateau associated with oxygen loss and then cycled between about 2.5 and 4.6 V (details are in the caption to Figure 6.48). Figure 6.49 shows the capacity retention in % for materials cycled repeatedly between about 2.5 and 4.6 V for about 50 cycles (details are in the caption of Figure 6.49). The results in Figures 6.48 and 6.49 show that materials with the highest specific capacity, best capacity retention and best

safety (2.5 - 4.6 V) could be found in the area with $y < 0.6$ and $z < 0.4$. Work by Eberman *et al.* [80] and Chen *et al.* [79] on materials with $z = 0$ suggests that materials with y near 0 will have poor rate capability. Work by MacNeil and Dahn [23] and by Jiang and Dahn [75, 76] in Section 6.1 on materials with $z = 0$ suggests that safety will be compromised if the Co content, y, is made too large. Therefore, samples with the compositions indicated by the triangles in Figure 6.50 were chosen for synthesis and their electrochemical and safety-related properties were studied. The data points indicated by the circles are the subject of previous work described in Sections 6.1 and 6.2 where electrochemical and safety-related properties were reported [75-77].

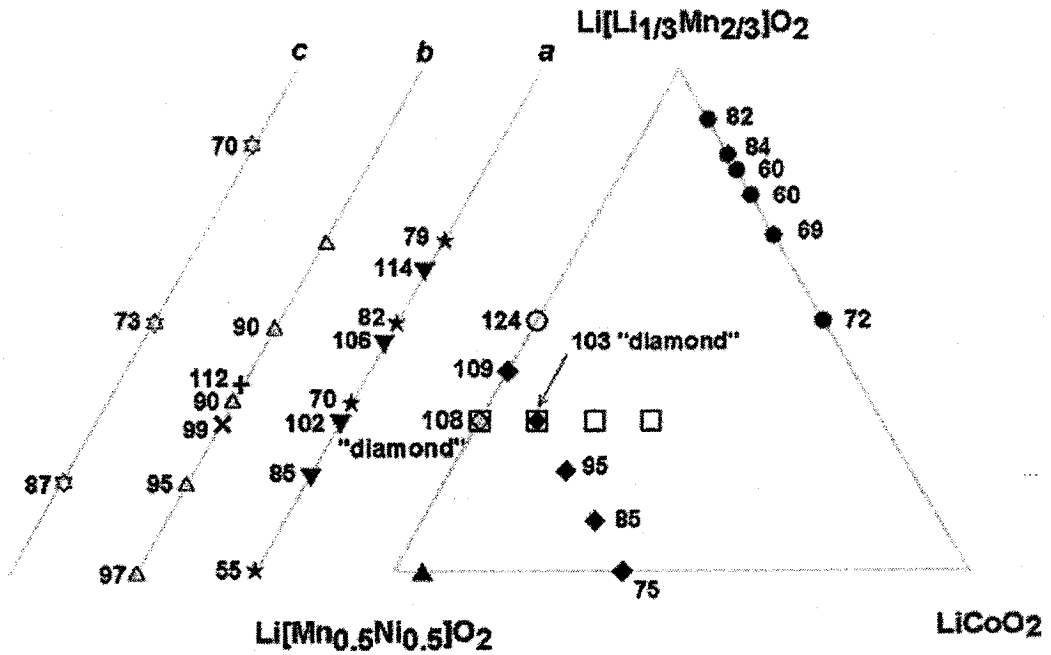

Figure 6.49 Percent capacity retention over a specified number of cycles of solid solution electrode materials with the compositions indicated. "◆" 2.5 - 4.6 V, 70 cycles from [154] by Zhang *et al.* "□" 2.5 - 4.6 V, 15 cycles from [160] by Kim *et al.* "◇" 2.5 - 4.6 V, 35 cycles from [161] by Kim *et al.* "○" 2.0 – 4.6 V, 65 cycles from [71] by Kang *et al.* "▲" 2.5 - 4.6 V, 10 cycles from [158] by Sun *et al.* "★" 2.0 - 4.8 V, 50 cycles from [156] by Park *et al.* "▼" 2.0 - 4.6 V, 50 cycles from [159] by Shin *et al.*, "✚" 2.5 – 4.8 V, 10 cycles from Yu *et al.* [157], "✕" 2.0 - 5.0 V, 10 cycles from Johnson *et al.* [155], "●" 2.0 – 4.8 V, 20 cycles from Park *et al.* [73]. The compositions indicated by "☼" and "△" (2.5 - 4.8 V) are from the previous work [70, 77] of Jeff Dahn's lab.

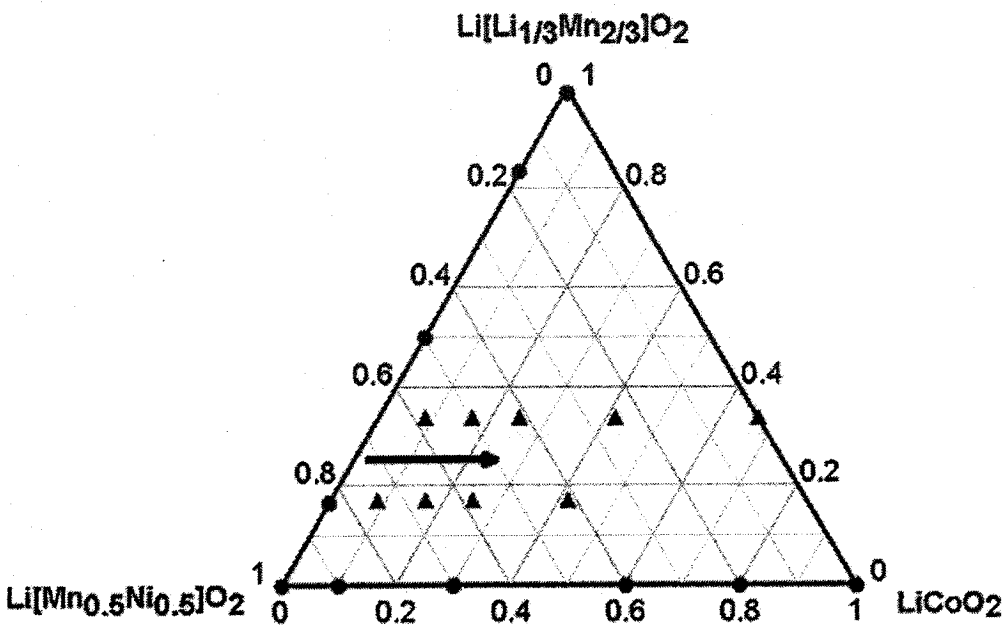

Figure 6.50 The composition of the x $Li[Mn_{1/2}Ni_{1/2}]O_2$ • y $LiCoO_2$ • z $Li[Li_{1/3}Mn_{2/3}]O_2$ (x + y + z = 1) samples studied in this section of this thesis are indicated by triangles. Two rows of samples, one with z = 1/6 and one with z = 1/3 were evaluated. The circles on the left and bottom edges of this ternary system show the composition of samples described in references [75-77] for comparison.

In this section, x $Li[Ni_{1/2}Mn_{1/2}]O_2$ • y $LiCoO_2$ • z $Li[Li_{1/3}Mn_{2/3}]O_2$ (x + y + z = 1) materials with z = 1/6 and 1/3 and y = 0, 1/12, 1/6, 1/4 and 5/12 (also z = 1/3, y = 2/3), fired at two different temperatures, 900°C or 1000°C, are studied. The synthesis method is described in Section 2.1.3. The effects of the composition on the particle size, lattice constants, cation mixing, electrochemical properties, and thermal stability of the x $Li[Ni_{1/2}Mn_{1/2}]O_2$ • y $LiCoO_2$ • z $Li[Li_{1/3}Mn_{2/3}]O_2$ (x + y + z = 1) positive electrode materials were studied. The structure, electrochemical performance and thermal stability of the synthesized samples were characterized by XRD, electrochemical studies in two-electrode coin cells, and ARC, respectively.

6.3.2 $Li[(Ni_{1/2}Mn_{1/2})_xCo_y(Li_{1/3}Mn_{2/3})_z]O_2$ samples (z = 1/6 and 1/3)

6.3.2.1 Sample characterization by SEM and XRD

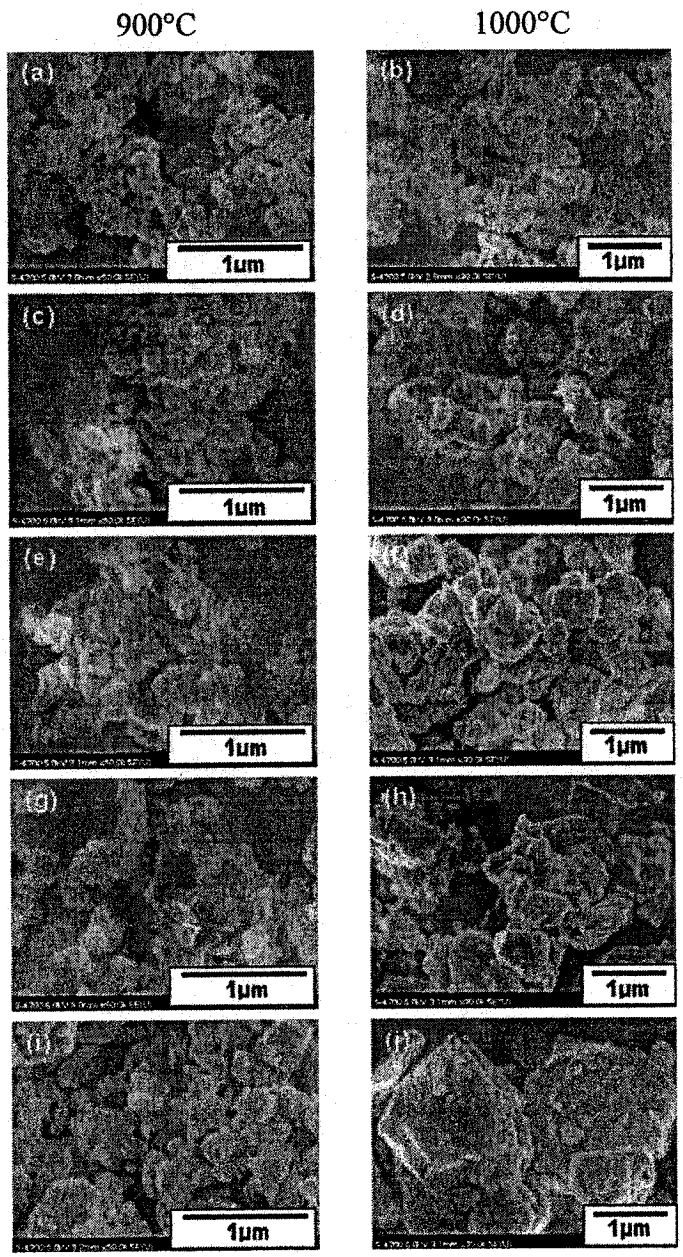

Figure 6.51 SEM micrographs of x $Li[Mn_{1/2}Ni_{1/2}]O_2$ • y $LiCoO_2$ • 1/3 $Li[Li_{1/3}Mn_{2/3}]O_2$ (x + y = 2/3) solid solution samples synthesized at 900°C with Co content, y, increasing from 1/12 in panel (a), 1/6 (c), 1/4 (e), 5/12 (g), to 2/3 (i). SEM micrographs of the samples with the same composition fired at 1000°C are shown in the right hand column for comparison.

Figure 6.51 shows SEM micrographs of the x $Li[Ni_{1/2}Mn_{1/2}]O_2$ • y $LiCoO_2$ • z $Li[Li_{1/3}Mn_{2/3}]O_2$ (x + y + z = 1) samples with z = 1/3. The five micrographs in the left column of Figure 6.51 (panels a, c, e, g, and i) are for samples heated to 900°C and clearly show an average particle size of around 0.3 μm for samples with y (Co content) = 1/12, 1/6, 1/4, 5/12, and 2/3, respectively. The particle size of the samples synthesized at 1000°C increased significantly to about 0.5 μm, 0.7 μm, 0.8 μm, 1 μm, to 2 μm for Co contents, y, of 1/12, 1/6, ¼, 5/12, and 2/3, respectively, as shown in the right column of micrographs in Figure 6.51. This suggests that the particle size of x $Li[Ni_{1/2}Mn_{1/2}]O_2$ • y $LiCoO_2$ • z $Li[Li_{1/3}Mn_{2/3}]O_2$ (x + y + z = 1) samples can be changed by the Co content, y, and the synthesis temperature.

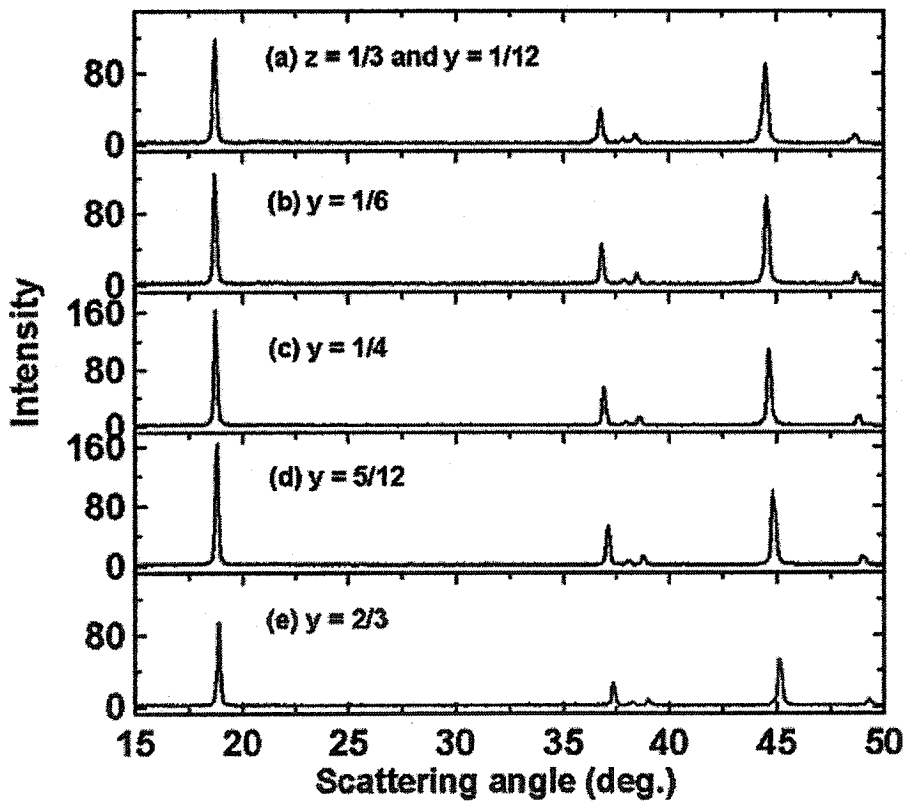

Figure 6.52 X-ray diffraction (XRD) patterns of x $Li[Mn_{1/2}Ni_{1/2}]O_2$ • y $LiCoO_2$ • 1/3 $Li[Li_{1/3}Mn_{2/3}]O_2$ (x + y = 2/3) samples (1000°C) with different Co content, y = 1/12, 1/6, ¼, 5/12, and 2/3 in the low scattering angle region from 15° to 50° show the absence of any impurities.

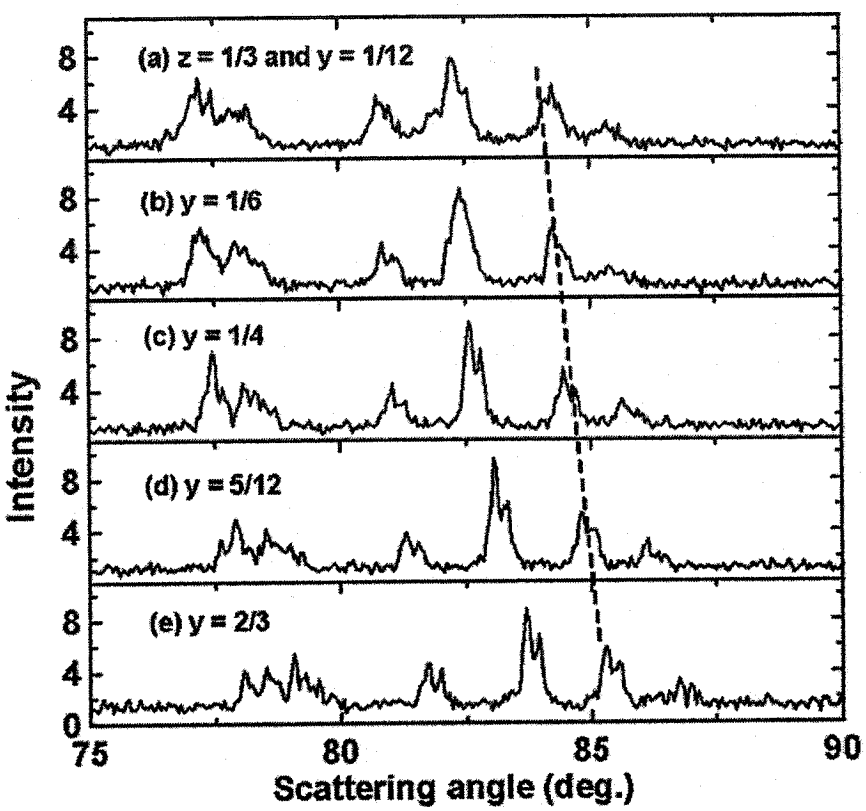

Figure 6.53 X-ray Diffraction (XRD) patterns of x $Li[Mn_{1/2}Ni_{1/2}]O_2$ • y $LiCoO_2$ • 1/3 $Li[Li_{1/3}Mn_{2/3}]O_2$ (x + y = 2/3) samples (1000°C) with different Co content, y = 1/12, 1/6, ¼, 5/12, and 2/3 in the high scattering angle region from 75° to 90° show the increase in crystallinity with Co content, y.

The XRD patterns of the x $Li[Ni_{1/2}Mn_{1/2}]O_2$ • y $LiCoO_2$ • z $Li[Li_{1/3}Mn_{2/3}]O_2$ (x + y + z = 1) samples with z = 1/3 and y = 1/12, 1/6, ¼, 5/12, and 2/3 synthesized at 1000°C were measured and are shown in Figures 6.52 and 6.53. Figure 6.53 gives an expanded view of the high scattering angle region so that differences in sample crystallinity can be examined. There are no discernable Bragg peaks from impurities in any of these samples. It is very clear that the Bragg peak indicated with dashed line in Figure 6.53 shifts to higher scattering angle as the Co content, y, increases. Furthermore, that Bragg peak and the one to its left in Figure 6.53 become sharper and the $K_{\alpha1}/K_{\alpha2}$ splitting becomes clearer as the Co content increases. This indicates that the $Li[(Ni_{1/2}Mn_{1/2})_xCo_y(Li_{1/3}Mn_{2/3})_{1/3}]O_2$ (x + y = 2/3) samples are more crystalline at higher

Co content. This result is consistent with the larger particle size of the samples with higher Co content shown in Figure 6.51.

The Rietveld refinement results of the XRD patterns in Figures 6.52 and 6.53 are listed in Table 6.8. The lattice constants, *a* (Å), *c* (Å), and *c/a*, versus Co content (y) in the x $Li[(Ni_{1/2}Mn_{1/2})_xCo_y(Li_{1/3}Mn_{2/3})_{1/3}]O_2$ (x + y = 2/3) samples synthesized at 900°C or 1000°C are shown in Figure 6.54. As the Co content increases, the lattice constants *a* and *c* decrease but *c/a* increases, similar to the effects of Co content on the lattice constant of $Li[(Ni_{1/2}Mn_{1/2})_xCo_{1-x}]O_2$ samples synthesized at 900°C [75, 76]. The effect of different synthesis temperatures of 900°C or 1000°C on the lattice constants is slight. Figure 6.55 shows that the addition of Co significantly decreases the fraction of Li-sites occupied by transition metal atoms, most likely Ni, for samples synthesized both at 900°C and 1000°C. The percent of the Li sites occupied by transition metal atoms is about 5.3% for $Li[(Ni_{1/2}Mn_{1/2})_{7/12}Co_{1/12}(Li_{1/3}Mn_{2/3})_{1/3}]O_2$ (900°C) and only 1.2% for $Li[(Ni_{1/2}Mn_{1/2})_{1/4}Co_{5/12}(Li_{1/3}Mn_{2/3})_{1/3}]O_2$ (900°C). A larger fraction of transition metal atoms in the Li layer at low Co content will presumably block lithium diffusion paths and hence impact the rate capability [79, 80].

Table 6.8 Lattice constants and atom positions of x $Li[Mn_{1/2}Ni_{1/2}]O_2$ • y $LiCoO_2$ • 1/3 $Li[Li_{1/3}Mn_{2/3}]O_2$ (x + y = 2/3) samples with different Co content (y = 1/12, 1/6, 1/4, and 5/12) synthesized at 900°C or 1000°C from the Rietveld refinement of the XRD patterns. The space group used for the refinement was R-3m (#166). "u" represents the percentage of the Li site occupied by transition metal atoms (presumably Ni). The Bragg R-factors are listed.

sample	T	*a* (Å)	*c* (Å)	O position	u	R_{Bragg}
y = 1/12	900°C	2.8669(0)	14.2654(0)	0, 0, 0.2442(4)	5.3%	3.5%
	1000°C	2.8681(0)	14.2740(0)	0, 0, 0.2432(0)	4.1%	3.2%
y = 1/6	900°C	2.8621(0)	14.2527(0)	0, 0, 0.2432(9)	3.1%	3.3%
	1000°C	2.8621(3)	14.2597(2)	0, 0, 0.2433(1)	3.5%	3.0%
y = 1/4	900°C	2.8558(1)	14.2382(4)	0, 0, 0.2425(6)	1.8%	2.8%
	1000°C	2.8562(0)	14.2410(0)	0, 0, 0.2427(6)	1.9%	2.3%
y = 5/12	900°C	2.8415(3)	14.1942(8)	0, 0, 0.2414(6)	1.2%	2.5%
	1000°C	2.8416(3)	14.1973(2)	0, 0, 0.2405(2)	1.3%	2.6%

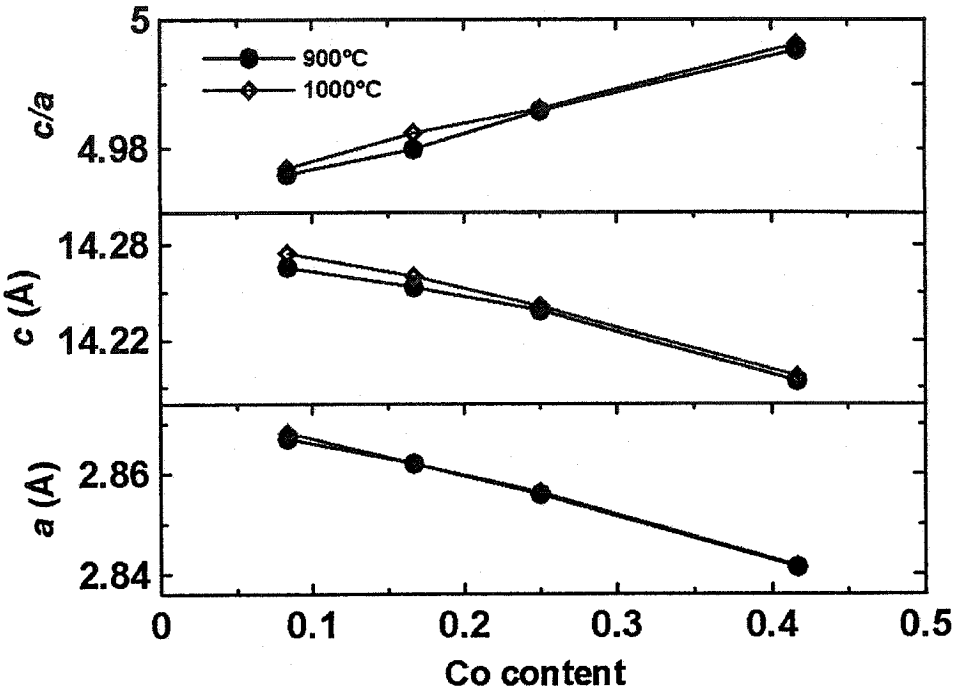

Figure 6.54 The lattice constants, *a* (Å), *c* (Å), and the *c/a* ratio in x $Li[Mn_{1/2}Ni_{1/2}]O_2$ • y $LiCoO_2$ • 1/3 $Li[Li_{1/3}Mn_{2/3}]O_2$ (x + y = 2/3) solid solution samples (900°C or 1000°C) as the Co content, y, increases.

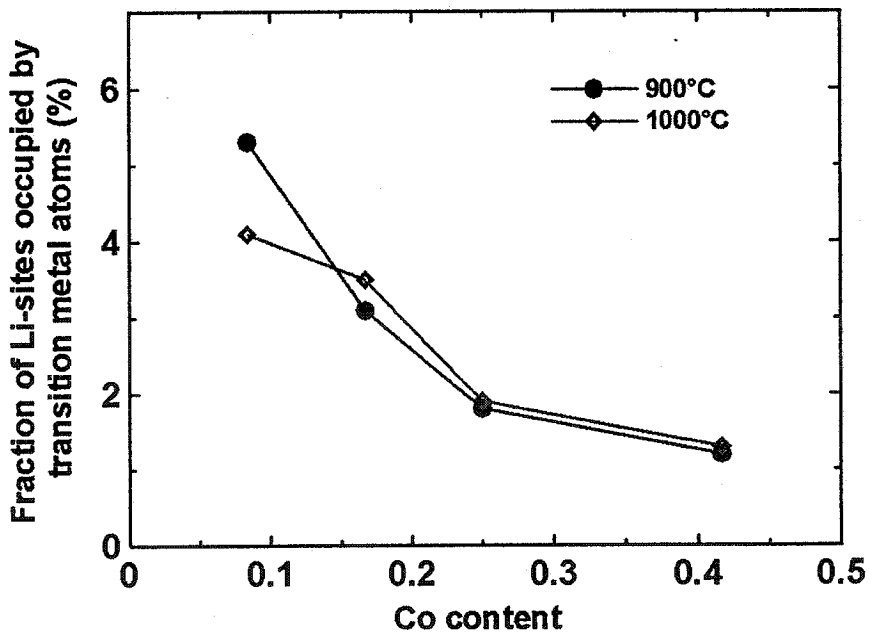

Figure 6.55 Fraction of lithium sites in the lithium layer of x $Li[Mn_{1/2}Ni_{1/2}]O_2$ • y $LiCoO_2$ • 1/3 $Li[Li_{1/3}Mn_{2/3}]O_2$ (x + y = 2/3) samples (900°C or 1000°C) occupied by transition metal atoms as a function of Co content, y.

6.3.2.2 Electrochemical properties and thermal stability

The rate capability of the $Li[(Ni_{1/2}Mn_{1/2})_xCo_y(Li_{1/3}Mn_{2/3})_{1/3}]O_2$ (x + y = 2/3) samples was tested using the signature discharge method [162] as illustrated in Figure 6.56. A coin cell using the synthesized sample as the positive electrode and Li metal as the negative electrode was cycled at a specific rate, for example C/4. When the cell potential reached the upper cutoff potential, for example 4.6 V in Figure 6.56, the cell was then discharged at a 2C rate to the low cutoff potential around 2.5 V. The cell was then left open circuit for 30 minutes as indicated by the dashed lines in Figure 6.56 until the next discharge process at half of the original discharge current, C rate. The cell was sequentially discharged in this way until the last discharge rate was C/16. After that, the cell was charged and discharged again at a normal rate of C/4. A signature discharge test was performed every 20 cycles during extended cycle life testing at C/4.

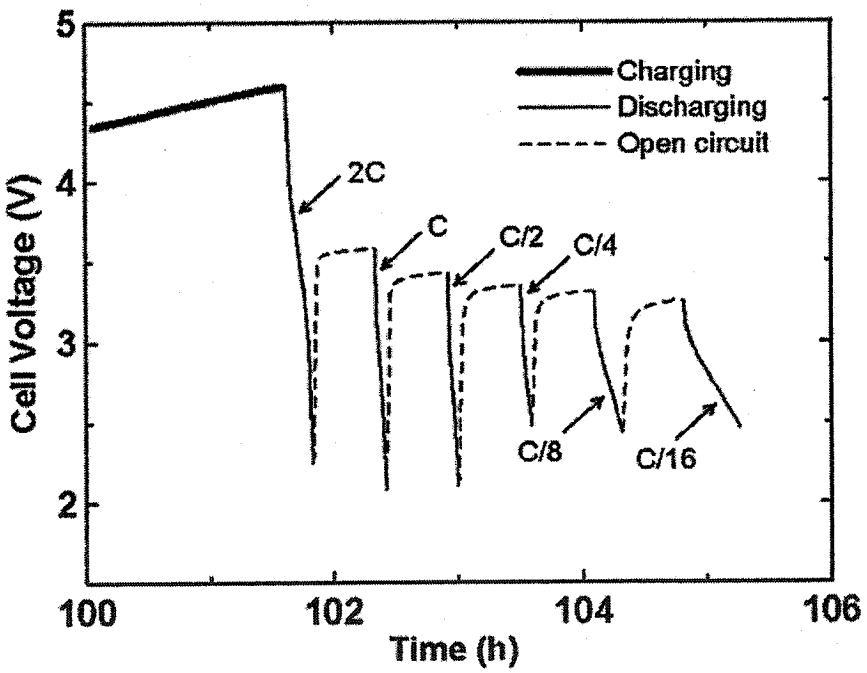

Figure 6.56 Signature discharge method to test the rate capability of positive electrode materials. After charging to the high cut-off voltage, the electrode was discharged at a high rate of 2C (solid line) followed by a half an hour open circuit (dashed line). The electrode was then discharged at one half of the original current, C rate. This discharge sequence was repeated a total of 5 times until the discharge rate decreased to C/16.

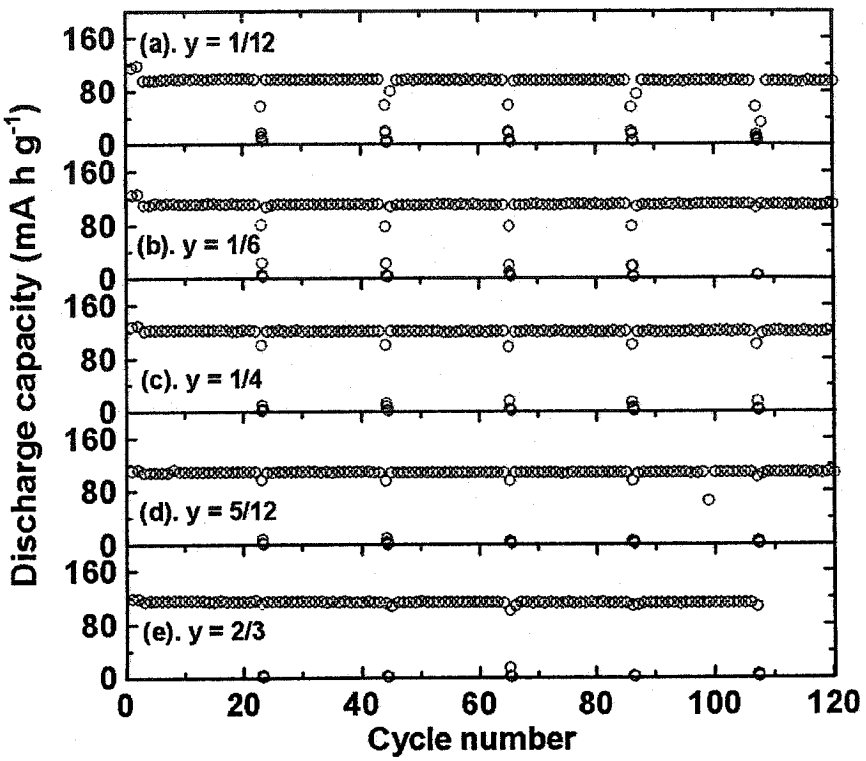

Figure 6.57 Capacity (mA h g^{-1}) vs. cycle number for the x $Li[Mn_{1/2}Ni_{1/2}]O_2$ • y $LiCoO_2$ • 1/3 $Li[Li_{1/3}Mn_{2/3}]O_2$ (x + y = 2/3) samples (1000°C) with y = 1/12, 1/6, 1/4, 5/12, and 2/3. The cells were cycled between 2.5 V and 4.3 V at C/4. Every 20 cycles, the cell was programmed to proceed to the signature discharge test to measure the rate capability.

Figure 6.57 shows the discharge capacity versus cycle number (2.5 V – 4.3 V, C/4) for the $Li[(Ni_{1/2}Mn_{1/2})_xCo_y(Li_{1/3}Mn_{2/3})_{1/3}]O_2$ (x + y = 2/3) samples synthesized at 1000°C. Two nominally identical cells of each electrode material were tested and gave almost indistinguishable results. All five samples described by Figure 6.57 exhibit excellent cycling performance, above 97% capacity retained after 110 cycles. The first signature discharge test occurs at cycle 24, and the capacity attained during each of the sequential current steps is plotted, all at cycle 24. Most important is the capacity attained at a 2C discharge rate, which is the point with the largest capacity. The capacity attained at 2C is less than the capacity attained at C/4, during the stable cycling of the cell, but it approaches the C/4 capacity as the Co content, y, increases (from panel a to panel e in Figure 6.57). In fact, the 2C rate capacity and the C/4 rate capacity of the cell having an electrode with y = 2/3 and z = 1/3, are almost the same. Furthermore, all of the five

samples do not show any dependence of the rate capability on cycle number because the 2C rate capacity is roughly constant during each signature discharge measurement which strongly suggests that the cell resistance does not significantly increase during the cycles indicated.

Figure 6.58 shows the capacity delivered (in % of C/4 capacity) as a function of discharge rate for the $Li[(Ni_{1/2}Mn_{1/2})_xCo_y(Li_{1/3}Mn_{2/3})_{1/3}]O_2$ (x + y = 2/3) samples as measured during the cycle 24 signature discharge measurement in Figure 6.57. This clearly shows the increase in rate capability when the Co content, y, is increased.

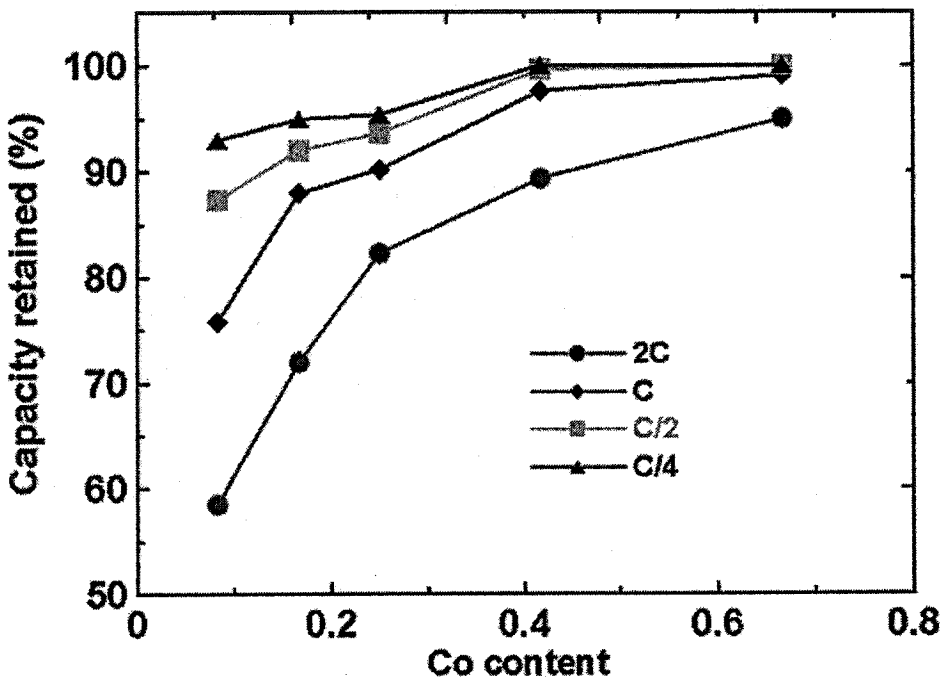

Figure 6.58 Capacity (%) retained as a function of discharge rate for x $Li[Mn_{1/2}Ni_{1/2}]O_2$ • y $LiCoO_2$ • 1/3 $Li[Li_{1/3}Mn_{2/3}]O_2$ (x + y = 2/3) samples (1000°C) from the first signature discharge test in Figure 6.57. These samples have **not** been charged through the oxygen release plateau.

Samples of $Li[(Ni_{1/2}Mn_{1/2})_xCo_y(Li_{1/3}Mn_{2/3})_{1/6}]O_2$ (x + y = 5/6, z = 1/6) were also synthesized at two different temperatures (900°C and 1000°C). As for the samples having z = 1/3, described in Figures 6.58, the particle size, sample crystallinity and rate capability (charged to 4.3V) increases with Co content, y, for the samples with z = 1/6. All the four samples with z = 1/6 show excellent cycling performance and above 95%

capacity retention during 110 cycles between 2.5 and 4.3 V at C/4. The results are not shown here to save space.

In order to obtain high discharge capacity, the nine $Li[(Ni_{1/2}Mn_{1/2})_xCo_y(Li_{1/3}Mn_{2/3})_z]O_2$ (x + y + z = 1) samples were charged to 4.8 V across the O_2 loss plateau [70, 77]. Figure 6.59 shows the potential (V) versus capacity (mA h g^{-1}) curves for the cells having electrodes of $Li[(Ni_{1/2}Mn_{1/2})_xCo_y(Li_{1/3}Mn_{2/3})_{1/3}]O_2$ (x + y = 2/3) (heated to 900°C) measured at a rate of C/30. There is a plateau due to the simultaneous removal of lithium and oxygen starting at approximately 4.4 V. After the O_2 loss during the first charge, the $Li[(Ni_{1/2}Mn_{1/2})_xCo_y(Li_{1/3}Mn_{2/3})_{1/3}]O_2$ (x + y = 2/3) electrodes show a large reversible discharge capacity as large as 230 mA h g^{-1}. With the increase of Co content from y = 1/12 in Figure 6.59a to 2/3 in Figure 6.59e, the irreversible capacity increases slightly from about 40 mA h g^{-1} to around 80 mA h g^{-1}. The reason for this behavior is unknown.

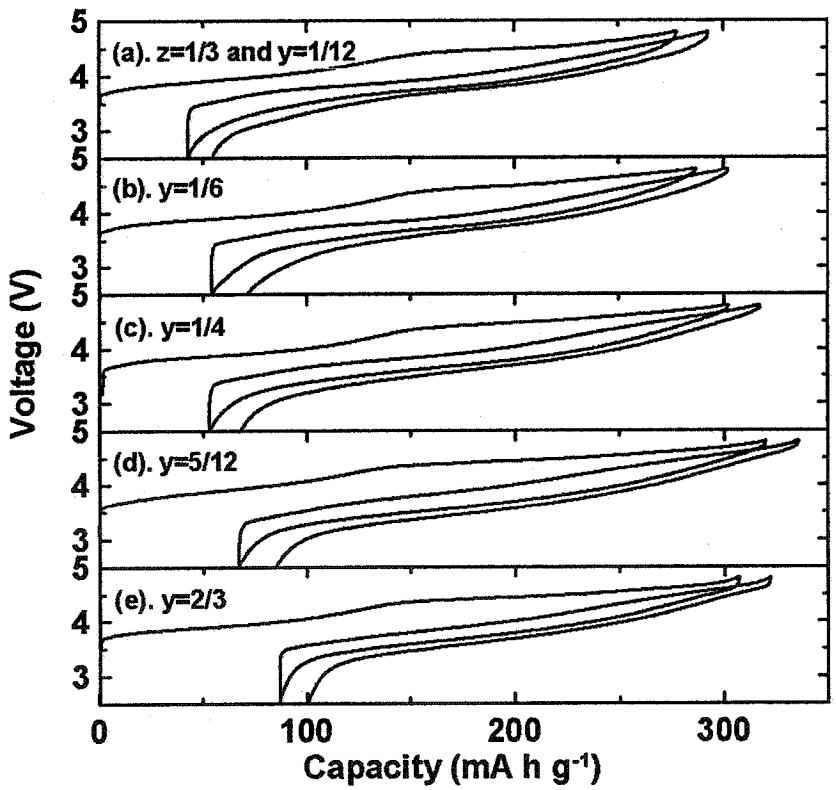

Figure 6.59 The potential (V) vs. specific capacity (mA h g^{-1}) of Li/{x $Li[Mn_{1/2}Ni_{1/2}]O_2$ • y $LiCoO_2$ • 1/3 $Li[Li_{1/3}Mn_{2/3}]O_2$ (x + y = 2/3) (900°C)} cells charged and discharged between 2.5 and 4.8 V at a rate of C/30.

Figure 6.60 shows the differential capacity vs. potential for Li/{ $Li[(Ni_{1/2}Mn_{1/2})_xCo_y(Li_{1/3}Mn_{2/3})_{1/3}]O_2$ (x + y = 2/3) (heated to 900°C)} cells generated from the data in Figure 6.59. There are two major peaks in differential capacity above 4.3 V that occur during the first charge process, one between 4.3 V and 4.5 V and the other around 4.7 V. When $Li[(Ni_{1/2}Mn_{1/2})_xCo_y(Li_{1/3}Mn_{2/3})_{1/3}]O_2$ (x + y = 2/3) electrodes were charged to 4.8 V, the O_2 loss process was apparently completed. The reasons for the changes in differential capacity with Co content, y, are still unclear. It is possible that samples with small Ni content (small x) might form the O1 phase [163], like $LiCoO_2$, when all available lithium is removed. This could lead to an extra peak in differential capacity as observed for $LiCoO_2$ at the highest potentials [163].

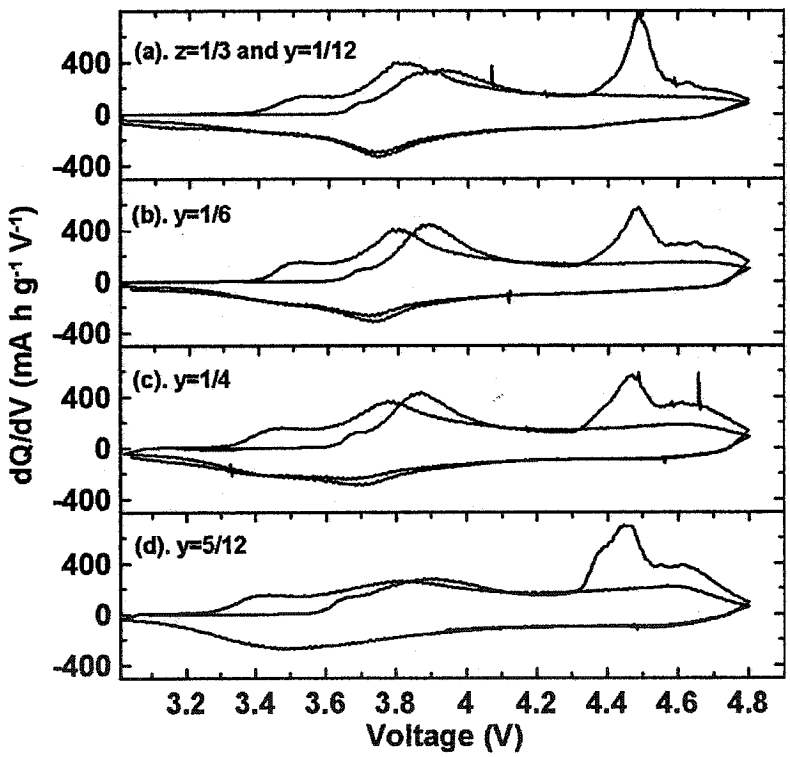

Figure 6.60 The differential capacity (dQ/dV) vs. potential (V) of Li/{x $Li[Mn_{1/2}Ni_{1/2}]O_2$ • y $LiCoO_2$ • 1/3 $Li[Li_{1/3}Mn_{2/3}]O_2$ (x + y = 2/3) (900°C)} cells charged and discharged between 2.5 and 4.8 V at a rate of C/30.

Figure 6.61 shows the discharge capacity versus cycle number (2.5 V – 4.6 V, C/6) for the $Li[(Ni_{1/2}Mn_{1/2})_xCo_y(Li_{1/3}Mn_{2/3})_{1/3}]O_2$ (x + y = 2/3) (heated to 900°C) samples

after 2 initial cycles between 2.5 V and 4.8 V at C/30. The cells described by Figure 6.61 are the same cells used to produce the data in Figures 6.59 and 6.60. All cells were given a signature discharge test at the 25th, 46th and 67th cycles starting with a 2C rate as described in Figure 6.56 to test the rate capability of the samples. The samples of $Li[(Ni_{1/2}Mn_{1/2})_xCo_y(Li_{1/3}Mn_{2/3})_{1/3}]O_2$ (x + y = 2/3) (heated to 900°C) with y = 1/12 in Figure 6.61a, y = 1/6 in Figure 6.61b, y = ¼ in Figure 6.61c, and y = 5/12 in Figure 6.61d show a discharge capacity of about 200 mA h g^{-1} at C/6 and excellent capacity retention of up to 97% over 70 cycles.

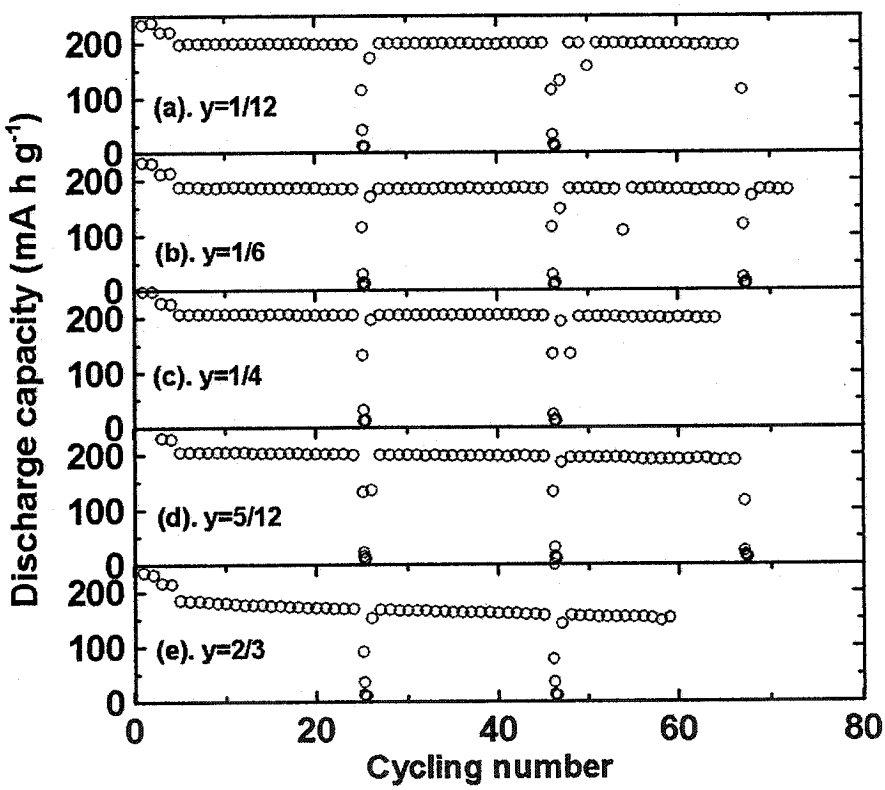

Figure 6.61 Capacity (mA h g^{-1}) vs. cycle number for the Li/{ $Li[(Ni_{1/2}Mn_{1/2})_xCo_y(Li_{1/3}Mn_{2/3})_{1/3}]O_2$ (x + y = 2/3) (900°C)} cells cycled between 2.5 V and 4.6 V at C/6 after traversal of the O_2-loss plateau. The cells used to produce this data are the same as the cells described in Figures 6.59 and 6.60.

Figure 6.62 shows the capacity retained (% of C/4) by $Li[(Ni_{1/2}Mn_{1/2})_xCo_y(Li_{1/3}Mn_{2/3})_{1/3}]O_2$ (x + y = 2/3) (900°C) electrodes at different rates,

2C, C, C/2, and C/4. The data was generated from the first signature discharge test at cycle 25 in Figure 6.61. The rate capability does not increase significantly with Co content, y, after the samples have been charged through the O_2 loss plateau, in contrast to the significant increase of rate capability with Co content for the same electrodes charged only to 4.3 V as shown in Figure 6.58. All the electrode compositions described by Figure 6.62 show about 60% capacity at a 2C rate. A comparison of Figures 6.58 and 6.62 indicates that the rate capability was seriously impacted after the O_2 loss process which occurs during the 4.5 V plateau in the first charge. It is possible that a fraction of transition metal atoms move into the Li layer after the O_2 loss process, which will reduce the Li diffusion constant hence the rate capability as well. Careful X-ray diffraction work is needed to confirm this and could be the focus of future work.

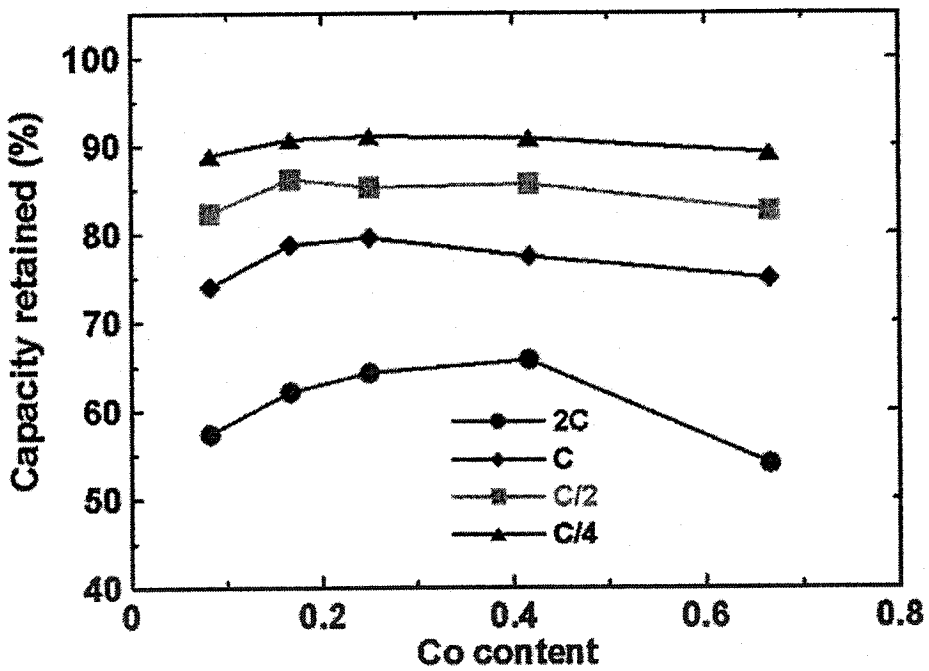

Figure 6.62 Capacity (%) retained as a function of discharge rate for $Li[(Ni_{1/2}Mn_{1/2})_xCo_y(Li_{1/3}Mn_{2/3})_{1/3}]O_2$ (x + y = 2/3) samples (900°C) from the first signature discharge test in Figure 6.61. These samples **have been** charged through the oxygen release plateau.

Apart from the relatively low rate capability after O_2 loss, $Li[(Ni_{1/2}Mn_{1/2})_xCo_y(Li_{1/3}Mn_{2/3})_{1/3}]O_2$ (x + y = 2/3) (900°C) electrodes show very high discharge capacity up to 200 mA h g^{-1} at a C/6 rate between 2.5 and 4.6 V and have excellent capacity retention of about 96% after 80 cycles. The capacity retention of the sample with y = 2/3 in Figure 6.61e is substantially worse. It will be very important and interesting to characterize the thermal reactivity of the samples charged to 4.8 V with EC/DEC solvent or $LiPF_6$-based electrolyte.

Figure 6.63 shows the self-heating rate (SHR) versus temperature (T) of 100 mg of $Li[(Ni_{1/2}Mn_{1/2})_xCo_y(Li_{1/3}Mn_{2/3})_{1/3}]O_2$ (x + y = 2/3) (900°C) electrodes charged to 4.8 V vs. Li metal reacting with 100 mg of EC/DEC solvent (solid line) or 30 mg of 1.0 M $LiPF_6$ EC/DEC (dashed line). The samples were initially heated to 110°C before exotherm searching began. In commercial lithium ion cells, such as 18650-size cells, the mass ratio of electrode material vs. electrolyte used is about 10:3. In this ARC measurement, therefore, the ratio of charged positive electrode material to electrolyte was chosen to be 100 mg:30 mg. The charged samples of $Li[(Ni_{1/2}Mn_{1/2})_xCo_y(Li_{1/3}Mn_{2/3})_{1/3}]O_2$ (x + y = 2/3) (900°C) show high reactivity with EC/DEC solvent. The sample with y = 1/12 described by Figure 6.63a reacts with EC/DEC (solid line) and exhibits a SHR around 0.5°C/min at 110°C which slowly decreases to 0.15°C/min at around 135°C then increases to thermal runaway at 185°C. As the Co content, y, increases from 1/12 in Figure 6.63a to 2/3 in Figure 6.63e, the charged samples clearly show a higher SHR at 110°C, and proceed to thermal runaway at a lower temperature when reacting with EC/DEC (solid lines). This obviously suggests that adding Co decreases the thermal stability of $Li[(Ni_{1/2}Mn_{1/2})_xCo_y(Li_{1/3}Mn_{2/3})_{1/3}]O_2$ (x + y = 2/3) (900°C) samples. Figure 6.63 shows that adding $LiPF_6$ salt into EC/DEC solvent significantly increases the thermal stability of $Li[(Ni_{1/2}Mn_{1/2})_xCo_y(Li_{1/3}Mn_{2/3})_{1/3}]O_2$ (x + y = 2/3) (900°C) samples charged to 4.8 V, which is in good agreement with reference [77] where the same effect is noted for $LiCoO_2$. Still, the effect of increased Co content, y, is to reduce the thermal stability, even in the presence of $LiPF_6$.

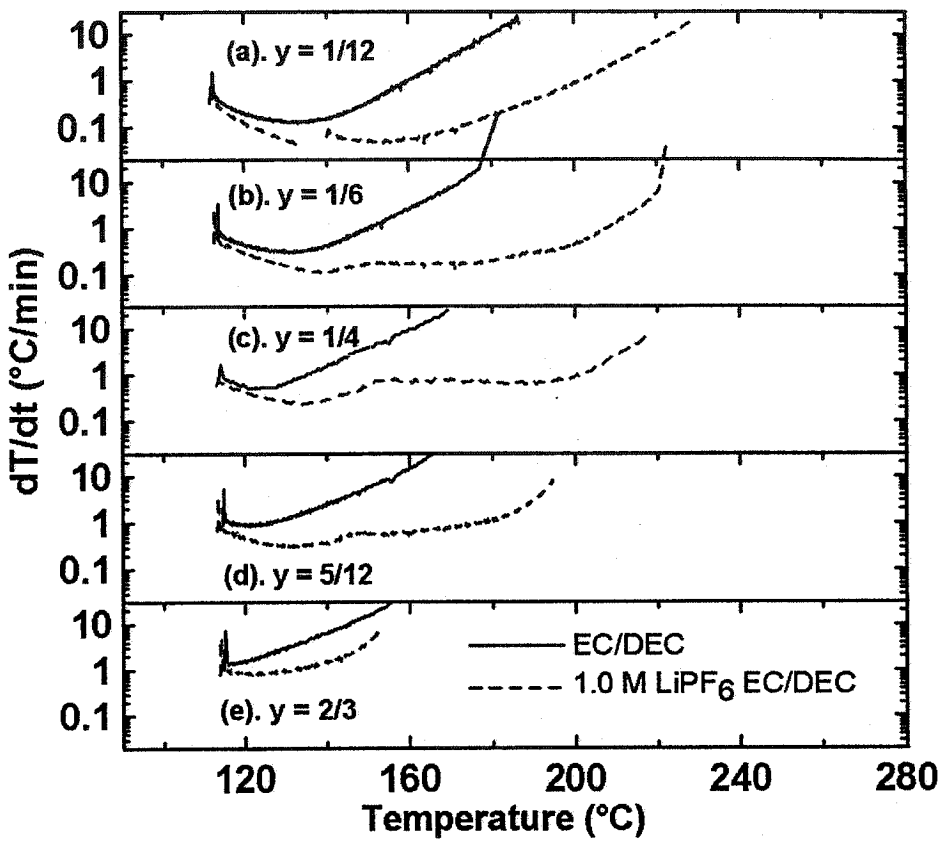

Figure 6.63 Self-heating rate (SHR) versus temperature (T) for 100 mg of $Li[(Ni_{1/2}Mn_{1/2})_xCo_y(Li_{1/3}Mn_{2/3})_{1/3}]O_2$ (x + y = 2/3) samples (900°C) charged to 4.8 V vs. Li heated with 100 mg of EC/DEC solvent (solid line) or 30 mg of 1.0 M $LiPF_6$ EC/DEC (dashed line). Samples were initially heated to 110°C before exotherm searching began.

Figure 6.64 shows the comparison of the self-heating rate versus temperature of $Li[(Ni_{1/2}Mn_{1/2})_xCo_y(Li_{1/3}Mn_{2/3})_{1/3}]O_2$ (x + y = 2/3) samples synthesized at 900°C vs. 1000°C in the solid and dashed line, respectively, reacting with 30 mg of 1.0 M $LiPF_6$ EC/DEC electrolyte. The self-heating rate versus temperature of charged $LiCoO_2$ [sample (3), 5 μm particle size, 4.2 V)] with $LiPF_6$ EC/DEC was added in Figure 6.64a for comparison and is shown by the heavy line [75, 76]. The samples with y = 1/12 and y = 1/6 synthesized at 1000°C show excellent thermal stability in $LiPF_6$-based electrolyte as indicated by dashed lines in Figures 6.64a and b, respectively. The onset temperatures for significant reaction in both samples is approximately 160°C, which is about 20°C higher than the onset temperature of $LiCoO_2$ charged to only 4.2 V. The samples

synthesized at 1000°C clearly show higher thermal stability in $LiPF_6$-based electrolyte than the samples made at 900°C. This is because the samples synthesized at 1000°C have larger particle size than the samples made at 900°C (shown clearly in Figure 6.51) and hence have a smaller surface area in contact with the electrolyte [86].

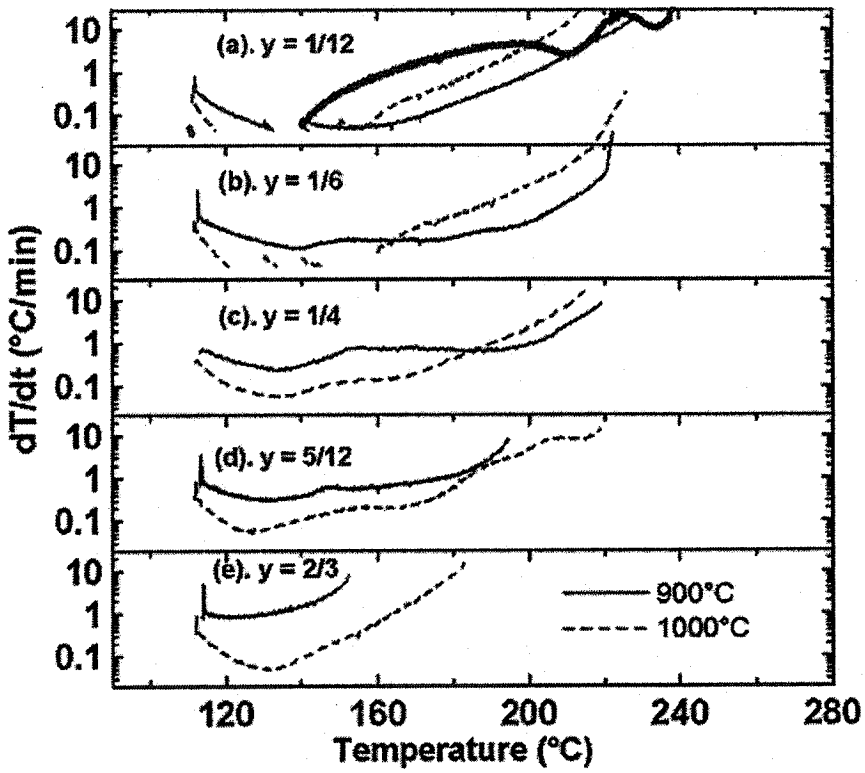

Figure 6.64 Self-heating rate (SHR) versus temperature (T) for 100 mg of $Li[(Ni_{1/2}Mn_{1/2})_xCo_y(Li_{1/3}Mn_{2/3})_{1/3}]O_2$ (x + y = 2/3) samples charged to 4.8 V heated with 30 mg of 1.0 M $LiPF_6$ EC/DEC (solid line - 900°C and dashed line - 1000°C). The SHR vs. T of $LiCoO_2$ charged to 4.2 V reacting with 1.0 M $LiPF_6$ EC/DEC has been added to panel a for comparison (bold line).

In order to compare the thermal-stability of the samples more conveniently, a parameter proportional to the average self-heating rate between 110°C and 180°C of 100 mg of charged electrode material in the presence of 30 mg of 1.0 M $LiPF_6$ EC:DEC electrolyte was developed. The average positive electrode self-heating rate between 110°C and 180°C is important in determining the response of charged Li-ion cells to oven exposure and short circuit tests. The area, S, between the self-heating rate versus

temperature curve and the x-axis was measured for all the samples. The area, S, is shown shaded in Figure 6.65 for a representative data set plotted on logarithmic and linear scales. S was calculated from the graph plotted on the linear scale as in Figure 6.65b. S has units of K^2 min^{-1}. The average SHR could be calculated as S/70 (K min^{-1}), but S is simply reported here. Samples with small values of S will show less reactivity and hence yield safer Li-ion cells than samples with large values of S. By including the value of S for $LiCoO_2$ (5 μm particles) charged to 4.2 V for comparison, the samples that should yield safer Li-ion cells than those using large particle $LiCoO_2$ can be identified.

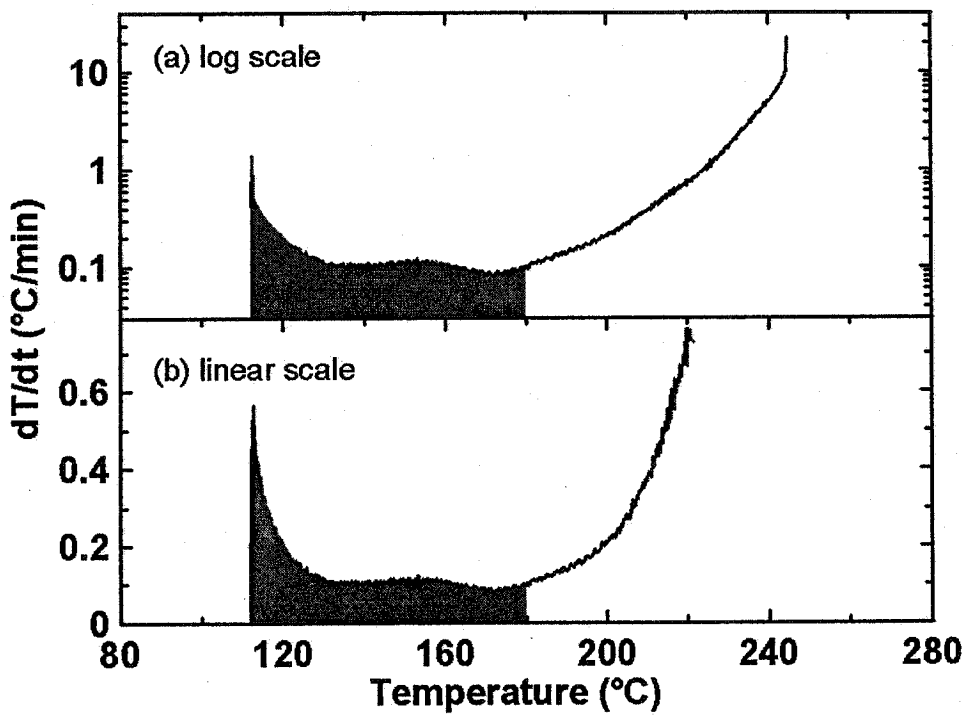

Figure 6.65 The area under the self-heating rate versus temperature curve between 110°C and 180°C is indicated by the shaded region. Panel a is plotted on a logarithmic vertical scale, like Figure 6.64. Panel b is plotted on a linear vertical scale. The parameter, "S", is the area of the shaded region in panel b.

The electrochemical and thermal properties of the $Li[(Ni_{1/2}Mn_{1/2})_xCo_y(Li_{1/3}Mn_{2/3})_{1/6}]O_2$ (x + y = 5/6) samples with y = 1/12, 1/6, ¼, and 5/12 synthesized at 900°C and 1000°C, were also tested as described above. The raw data

is not shown here to save space. However, the data for these samples is included in the summary figures to be described now. Figure 6.66 shows the specific discharge capacity of $Li[(Ni_{1/2}Mn_{1/2})_xCo_y(Li_{1/3}Mn_{2/3})_z]O_2$ (x + y + z = 1) samples synthesized at 900°C or 1000°C between 2.5 and 4.6 V at C/30 after charging through the O_2 loss plateau. There are results for 9 different compositions and 18 different samples (each composition heated to 2 temperatures) displayed in this ternary system. Each different composition is indicated by a black dot. For example, the top row of black dots closer to the $Li[Li_{1/3}Mn_{2/3}]O_2$ corner of the Gibbs' triangle represents the of $Li[(Ni_{1/2}Mn_{1/2})_xCo_y(Li_{1/3}Mn_{2/3})_{1/3}]O_2$ (x + y = 2/3) samples with y = 1/12, 1/6, ¼, 5/12, or 2/3. The data listed above and below the black dots represents the specific discharge capacity from 2.5 V to 4.6 V at C/30 for the samples synthesized at 900°C and 1000°C, respectively. All 9 samples synthesized at 900°C exhibit discharge capacities up to 230 mA h g^{-1}. The samples fired at 1000°C show slightly lower discharge capacity than the samples with the same composition fired at 900°C. The cause of this is not understood yet.

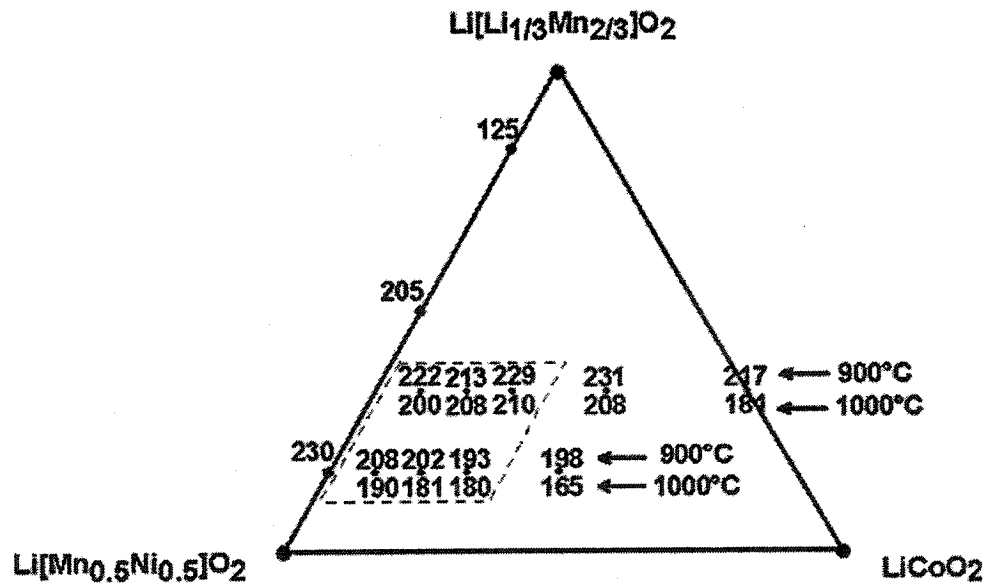

Figure 6.66 Specific discharge capacity (mA h g^{-1}) of $Li[(Ni_{1/2}Mn_{1/2})_xCo_y(Li_{1/3}Mn_{2/3})_z]O_2$ (x + y + z = 1) samples (z = 1/6 or 1/3) synthesized at 900°C or 1000°C cycled from 2.5 to 4.6 V vs. Li at C/30.

Figure 6.67 shows the specific discharge capacity between 2.5 and 4.6 V of all the synthesized $Li[(Ni_{1/2}Mn_{1/2})_xCo_y(Li_{1/3}Mn_{2/3})_z]O_2$ (x + y + z = 1) samples at a higher rate of C/6 instead of C/30 as shown in Figure 6.66. The samples with z = 1/3 synthesized at 900°C show a high discharge capacity near 210 mA h g^{-1} in good agreement with the results from [161] by Kim *et al.* indicated by the "□" points in Figure 6.48. When the synthesis temperature increases to 1000°C, the discharge capacity of these samples decreases to approximately 190 mA h g^{-1}. Samples with attractive capacity have been highlighted by a dashed box.

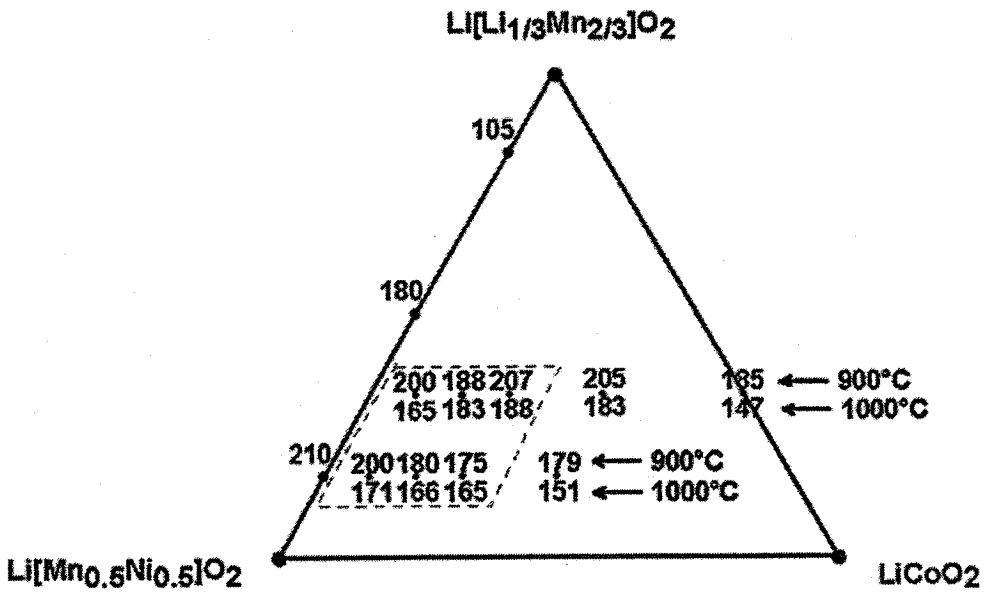

Figure 6.67. Specific discharge capacity (mA h g^{-1}) of $Li[(Ni_{1/2}Mn_{1/2})_xCo_y(Li_{1/3}Mn_{2/3})_z]O_2$ (x + y + z = 1) samples (z = 1/6 or 1/3) synthesized at 900°C or 1000°C cycled from 2.5 to 4.6 V vs. Li at C/6.

Figure 6.68 shows the percent capacity retention of the $Li[(Ni_{1/2}Mn_{1/2})_xCo_y(Li_{1/3}Mn_{2/3})_z]O_2$ (x + y + z = 1) samples cycled between 2.5 and 4.6 V at C/6 after 70 cycles. The samples within the same dashed box as indicated in Figure 6.68 show excellent cycling performance, above 97% capacity retention over 70 cycles at C/6. The samples with high Co content have relatively poor cycling performance especially for the samples heated to 1000°C.

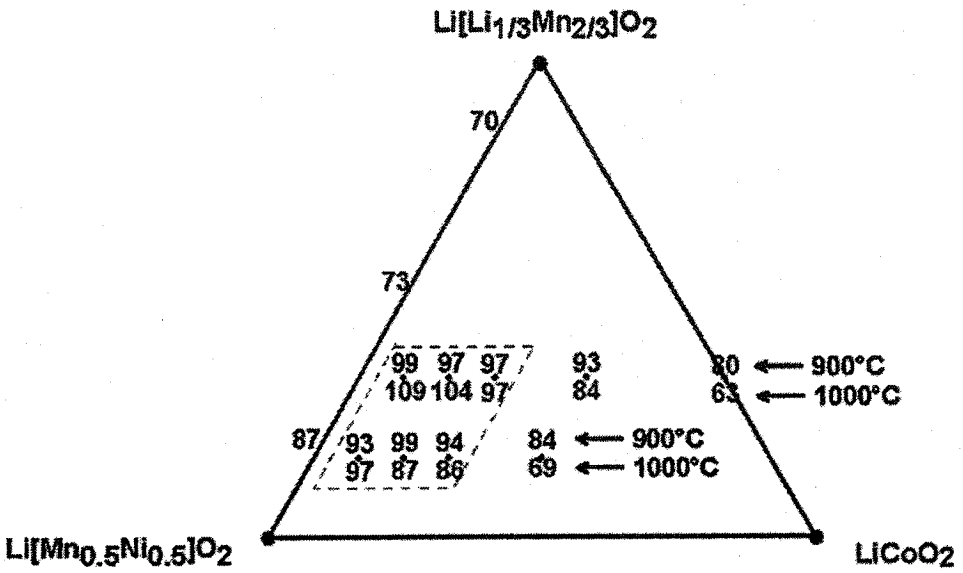

Figure 6.68 The percent capacity retention (%) of the $Li[(Ni_{1/2}Mn_{1/2})_xCo_y(Li_{1/3}Mn_{2/3})_z]O_2$ (x + y + z = 1) solid solution samples cycled between 2.5 and 4.6 V at C/6 for 70 cycles.

Figure 6.69 shows the thermal stability comparisons by plotting S (described in Figure 6.65b) versus composition of the samples. To reiterate, S, is the area under the self-heating rate versus temperature curve between 110 and 180°C for 100 mg of electrode material heated in the presence of 30 mg of 1.0 M $LiPF_6$ EC/DEC. The $Li[(Ni_{1/2}Mn_{1/2})_xCo_y(Li_{1/3}Mn_{2/3})_z]O_2$ (x + y + z = 1) samples were charged to 4.8 V before testing, while samples indicated along the left and bottom axis of Figure 6.69 were charged to 4.8 V and 4.2 V, respectively (The latter results were calculated from the data presented in Sections 6.1 and 6.2 and in references [77] and [76]). The variation of S with x, y and z in x $Li[(Ni_{1/2}Mn_{1/2})_xCo_y(Li_{1/3}Mn_{2/3})_z]O_2$ (x + y + z = 1) samples charged to 4.8 V shows several trends. First, S increases as the $LiCoO_2$ content, y, increases at fixed $Li[Li_{1/3}Mn_{2/3}]O_2$ content, z. Second, for the samples charged to 4.8 V, S increases as the $Li[Li_{1/3}Mn_{2/3}]O_2$ content, z, increases at fixed values of the $LiCoO_2$ content, y. The samples within the dashed box in Figure 6.69 show an average value of S of about 9 K^2 min^{-1}, which is still much better than $LiCoO_2$ charged to 4.2 V only.

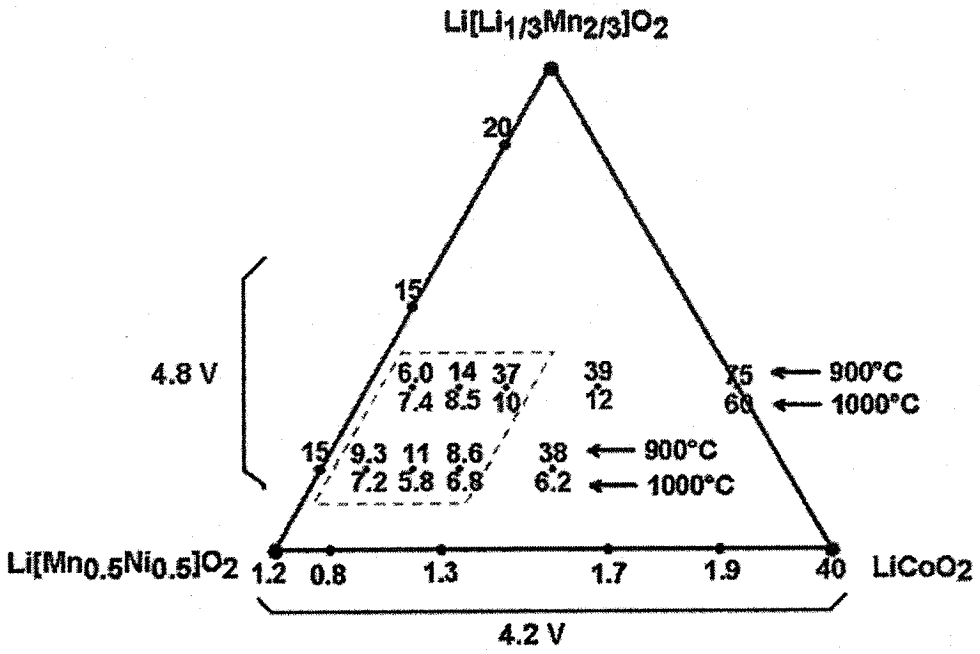

Figure 6.69 Thermal reactivity, S, (described in Figure 6.65) of $Li[(Ni_{1/2}Mn_{1/2})_xCo_y(Li_{1/3}Mn_{2/3})_z]O_2$ (x + y + z = 1) samples made at 900°C or 1000°C charged to 4.8 V reacting with 1.0 M $LiPF_6$ EC/DEC. The values of S obtained in earlier ARC studies of $Li[(Ni_{1/2}Mn_{1/2})_x(Li_{1/3}Mn_{2/3})_{1-x}]O_2$ (x = 1/6, 1/2, and 5/6) charged to 4.8 V [77] and $Li[(Ni_{0.5}Mn_{0.5})_xCo_{1-x}]O_2$ (x = 0.2, 0.4, 0.7, 0.9, and 1) and $LiCoO_2$ charged 4.2 V [76] reacting with 1.0 M $LiPF_6$ EC/DEC were added for comparison.

The rate capability (2.5 - 4.6 V) of the $Li[(Ni_{1/2}Mn_{1/2})_xCo_y(Li_{1/3}Mn_{2/3})_z]O_2$ (x + y + z = 1) samples is compared in Figure 6.70. The numbers indicated in Figure 6.70 are the percentage of the C/4 capacity retained at a 2C discharge rate. The rate capability of the samples is relatively low, approximately 65% discharge capacity retained at 2C. There is no obvious trend to better rate capability with composition after the samples are charged through the oxygen release plateau.

In summary, the $Li[(Ni_{1/2}Mn_{1/2})_xCo_y(Li_{1/3}Mn_{2/3})_z]O_2$ (x + y + z = 1) samples within the dashed box in Figures 6.66-6.70 ($1/6 \leq z \leq 1/3$ and $1/12 \leq y \leq 1/4$) show a high discharge capacity near 200 mA h g^{-1}, excellent cycling performance (above 97% capacity retention at C/6 over 70 cycles between 2.5 and 4.6 V), and good thermal stability, much safer than $LiCoO_2$ (5 μm size) charged to 4.2 V in $LiPF_6$ EC/DEC

electrolyte. One reason to use compositions with values of y near 1/4 may be the increased particle size that these compositions show (Figure 6.51) that can lead to materials with higher tap density. Positive electrode materials selected from within the dashed box in Figures 6.66-6.70 are probably acceptable for energy cells used in cell phones, laptops, and so on, provided methods to deal with the released oxygen [77] during the first charge above 4.5 V can be developed for practical cells.

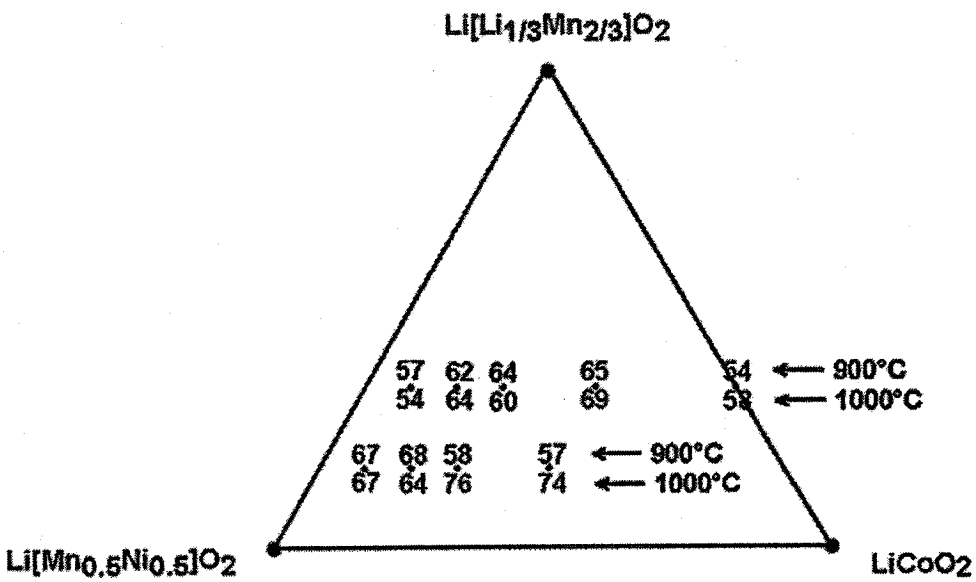

Figure 6.70 The percentage of C/4 discharge capacity obtained at a 2C discharge for Li/{ $Li[(Ni_{1/2}Mn_{1/2})_xCo_y(Li_{1/3}Mn_{2/3})_z]O_2$ $(x + y + z = 1)$} cells cycled between 2.5 and 4.6 V after O_2 loss.

Chapter 7 Conclusions and future work

The thermal stability of lithium-ion cells has been attracted attention recently for two major reasons. (1). Attempts to make large-size cells used in power tools, E-bikes and EVs. Large cells have lower surface area to volume ratios and hence heat dissipation is more problematic than 18650 cells. Safety problems, therefore, for large cells are more serious. (2). Next generation high-capacity electrodes (both negative and positive electrodes) will increase the energy density of lithium-ion cells meaning even an 18650-size cell may face safety concerns.

This thesis presented studies of the thermal stability of electrode materials (both negative and positive electrodes) in electrolytes to understand their reactivity. A search for new positive electrode materials with high thermal stability was made. Cell chemistries expected to have high tolerance to thermal abuse were suggested.

7.1 Conclusions

Lithiated MCMB ($Li_{0.81}C_6$) starts to react with EC/DEC solvent at 100°C to produce Li alkylcarbonate first at low temperature and Li_2CO_3 at around 250°C. The heat released from the complete reaction between $Li_{0.81}C_6$ and EC/DEC was calculated to be approximately 215 kJ mol^{-1} of lithium. Adding $LiPF_6$ salt into EC/DEC improves the thermal stability of $Li_{0.81}C_6$ as shown by ARC measurements. This is because $Li_{0.81}C_6$ reacts with PF_5 (from the thermal decomposition of $LiPF_6$) producing LiF that is incorporated into the SEI on $Li_{0.81}C_6$ to slow the reaction of $Li_{0.81}C_6$ with electrolyte. The thermal stability of $Li_{0.81}C_6$ is improved if the electrolyte salt is changed from $LiPF_6$ to LiBOB. $Li_{0.81}C_6$ does not significantly react with LiBOB EC/DEC until 170°C, compared to a 90°C onset temperature in $LiPF_6$-based electrolyte.

$Li_{0.5}CoO_2$ ($LiCoO_2$ charged to 4.2 V vs. Li) proceeds in a step-wise thermal reaction in EC/DEC solvent. $Li_{0.5}CoO_2$ transforms into Co_3O_4 (spinel phase), then to CoO (rock-salt phase), finally to Co metal at elevated temperatures. O_2 is liberated in the three stepwise reactions and combusts EC/DEC solvent releasing heat. $LiCoO_2$ samples with larger particle size show higher thermal stability. $LiCoO_2$ with a particle size around 5 μm starts reacting significantly with EC/DEC solvent at 150°C, compared to a 110°C onset temperature for $LiCoO_2$ (0.8 μm) in EC/DEC. The addition of $LiPF_6$ salt into

EC/DEC solvent reduces the reactivity of $Li_{0.5}CoO_2$. Unlike the $Li_{0.81}C_6$ anode, $Li_{0.5}CoO_2$ is more reactive in LiBOB electrolyte than in $LiPF_6$ electrolyte. The thermal reaction between $Li_{0.5}CoO_2$ and LiBOB EC/DEC begins at approximately 120°C.

Since LiBOB EC/DEC shows higher thermal stability for $Li_{0.81}C_6$ but lower stability for $Li_{0.5}CoO_2$ than $LiPF_6$ based electrolyte, it is interesting to compare the oven-test results of C/$LiCoO_2$ cells (18650-size) in $LiPF_6$ or LiBOB based electrolytes. It was found that: (1) 18650 cells containing LiBOB electrolyte generate almost no heat between 80 and 120°C. This is because of the lack of negative electrode ($Li_{0.81}C_6$)/electrolyte reactivity and positive electrode ($Li_{0.5}CoO_2$) /electrolyte reactivity in this temperature range from ARC results; (2) 18650 cells containing $LiPF_6$ electrolyte generate heat between about 80 and 120°C because of the negative electrode/electrolyte reaction as shown by ARC; and (3) 18650 cells containing LiBOB electrolyte generate substantial heat above 130°C and this is exactly where the positive electrode/electrolyte reaction begins powerfully in ARC tests. The good agreement between the ARC results and the oven test shows that ARC is an excellent technique to study the thermal stability of single electrode materials in electrolyte.

ARC was used to compare the thermal stability of negative electrodes with different lithium binding energies, $Li_7Ti_5O_{12}$ (1.55 eV) and $Li_{0.5}VO_2$ (B) (2.45 eV) as well as $Li_{0.81}C_6$ (0.1 eV). All three electrode materials similarly react with EC/DEC to form Li_2CO_3 and the heat released decreases with the lithium binding energy of the material. The released heat was measured to be 215 kJ mol^{-1} of Li for $Li_{0.81}C_6$, 110 kJ mol^{-1} of Li for $Li_7Ti_5O_{12}$, and 54 kJ mol^{-1} for $Li_{0.5}VO_2$ (B). Negative electrode materials with higher lithium binding energy have higher thermal stability in EC/DEC solvent.

The thermal stability of two well-known, alternative positive electrode materials, $LiMn_2O_4$ and $LiFePO_4$ were studied, since they have higher thermal stability than $LiCoO_2$. Charged $LiMn_2O_4$ (λ-MnO_2) starts to react with EC/DEC at around 190°C. The main product from the reaction between λ-MnO_2 and EC/DEC is Mn_3O_4. The heat from this reaction was calculated to be around 96 kJ mol^{-1} of λ-MnO_2, which is much lower than 142 kJ mol^{-1} (of $Li_{0.5}CoO_2$) from the reaction of $Li_{0.5}CoO_2$ with EC/DEC. However, both λ-MnO_2 and $Li_{0.5}CoO_2$ show a similar amount of heat, approximately 280 ~ 290 kJ mol^{-1} of oxygen combusted. Furthermore, the SHR vs. T data of λ-MnO_2 reacting with

EC/DEC was fitted with an Avrami-Erofeev model and the kinetic triplet (E_a, γ, and reaction model) was extracted.

Charged $LiFePO_4$ ($FePO_4$) shows much higher thermal stability in EC/DEC solvent than $Li_{0.5}CoO_2$ and λ-MnO_2. $FePO_4$ begins generating heat in EC/DEC at about 300°C and, unlike $Li_{0.5}CoO_2$ the thermal stability of $FePO_4$ is almost constant as the particle size decreases from 15 μm to 3 μm. Charged $FePO_4$ appears to have a solid-state phase-transition at around 300°C and the heat released from this reaction does not depend on the area of contact between $FePO_4$ and EC/DEC at all. Therefore, it is believed that $FePO_4$ does not react with EC/DEC so that the particle size of $FePO_4$ does not affect its thermal stability. LiBOB EC/DEC shows much higher thermal stability for $FePO_4$ than $LiPF_6$ EC/DEC electrolyte. So far, $LiFePO_4$ is the only positive electrode material that shows higher thermal stability in LiBOB based electrolyte than $LiPF_6$ EC/DEC. Therefore, two battery systems expected to have high tolerance to thermal abuse were suggested, graphite/LiBOB EC:DEC/$LiFePO_4$ and $Li_4Ti_5O_{12}$/LiBOB EC:DEC/$LiFePO_4$.

The pseudoternary system, $xLi[Ni_{1/2}Mn_{1/2}]O_2 \bullet yLiCoO_2 \bullet zLi[Li_{1/3}Mn_{2/3}]O_2$ ($x + y + z = 1$), was explored for positive electrode materials with large capacity and high thermal stability. The positive electrode materials in this pseudoternary system have attracted much attention recently because of their excellent electrochemical properties. However, the high thermal stability, the most striking advantage of these materials over $LiCoO_2$, has been almost "neglected" by most other researchers. The careful and complete characterization of the positive electrode materials in the $xLi[Ni_{1/2}Mn_{1/2}]O_2 \bullet yLiCoO_2 \bullet zLi[Li_{1/3}Mn_{2/3}]O_2$ ($x + y + z = 1$) pseudoternary system in morphology, structure, electrochemical properties, and thermal stability is one of the biggest contributions of this thesis.

The $xLi[Ni_{1/2}Mn_{1/2}]O_2 \bullet (1-x)LiCoO_2$ binary system (can be written as $Li[(Ni_{1/2}Mn_{1/2})_xCo_{1-x}]O_2$ with $0 < x \leq 1$), was first studied. The rate capability and Li diffusion coefficient of $Li[(Ni_{1/2}Mn_{1/2})_xCo_{1-x}]O_2$ samples increases with Co content, 1-x (but are about constant for $x \leq 0.7$) and the safety increases with x (but is about constant for $x \geq 0.4$). Therefore, samples with $0.4 \leq x \leq 0.7$ have high discharge capacity (around 170 mA h g^{-1} between 2.5 V and 4.4 V), good cycling performance (up to nearly 90% capacity retention after 200 cycles at C/4), high rate capability (comparable to $LiCoO_2$),

and high thermal stability (much higher than $LiCoO_2$). Two positive electrode candidates, $Li[(Ni_{1/2}Mn_{1/2})_{0.4}Co_{0.6}]O_2$ (x = 0.4) and $Li[(Ni_{1/2}Mn_{1/2})_{2/3}Co_{1/3}]O_2$ (x = 2/3), are being commercialized by 3M Corp. (USA), the industrial partner of Jeff Dahn's lab. Sanyo (Japan), one of the biggest lithium ion battery producers, has already used $Li[(Ni_{1/2}Mn_{1/2})_xCo_{1-x}]O_2$ (x = 2/3) materials to improve the specific capacity and thermal stability of commercial cells [164]. It is probably worth noting that 3M's entire business in positive electrode materials is based on inventions made at Dalhousie University.

Samples in the $xLi[Ni_{1/2}Mn_{1/2}]O_2 \bullet (1-x)Li[Li_{1/3}Mn_{2/3}]O_2$ binary system show a high capacity, over 200 mA h g^{-1}, after an O_2 loss process occurring during the first charge at approximately 4.5 V vs. Li and acceptable thermal stability. The impact of adding cobalt to this binary system was studied. Results show $xLi[Ni_{1/2}Mn_{1/2}]O_2 \bullet yLiCoO_2 \bullet zLi[Li_{1/3}Mn_{2/3}]O_2$ ($x + y + z = 1$) samples with $1/12 \leq y \leq 1/4$ and $1/6 \leq z \leq 1/3$ have a high discharge capacity near 200 mA h g^{-1} (2.5 ~ 4.6 V at C/6), excellent cycling performance (above 97% capacity retention for 70 cycles) and are much safer than $LiCoO_2$ (5μm size) charged to 4.2 V in $LiPF_6$ EC/DEC electrolyte. The particle size of the $Li[(Ni_{1/2}Mn_{1/2})_xCo_y(Li_{1/3}Mn_{2/3})_{1-x-y}]O_2$ samples increase with Co content, x. One reason to use compositions with values of y near ¼ may be the increased particle size that can lead to materials with higher tap density. Positive electrode materials selected from the composition range above are probably acceptable for energy cell used in cells phones, laptops, and so on.

7.2 Future work

The long-term goal of this research is to understand reactions between cell components, such as solvents, salts, electrolytes, negative electrodes and positive electrodes at elevated temperatures. This knowledge will guide us in the search for battery systems with high thermal stability. There still remains a large amount of work to do.

(1). Solvents. The solvents now used in the commercial lithium ion cells are mainly alkyl carbonates, such as EC, DEC, PC, DMC, EMC, and so on. Thermal problems during abuse conditions are caused by the exothermic reactions between charged electrode

materials and electrolytes as described in this thesis. Charged positive electrodes, such as Li_xCoO_2, Li_xMnO_4, etc. are reduced by EC/DEC and combustion of the solvents occurs. Alkyl carbonate solvents have high flammability. For instance, DMC, DEC, and EMC have a low flash points of approximately 18°C, 33°C, and 23°C, respectively [96, 97]. One idea for safer cells is to use solvents with no flash point (NFP) or nonflammable electrolytes [165].

Some methyl fluorinated ethers (MFE) and trimethyl phosphate (TMP) have been added into commonly-used solvents (EC, DEC, etc) as flame retardants to decrease flammability and even make nonflammable electrolytes [165]. The thermal stability of different positive electrode materials in such nonflammable electrolytes can be quickly and accurately characterized by ARC experiments. The thermal stability of negative electrode materials in such nonflammable electrolytes needs to be studied as well.

(2) Lithium salts. The lithium salt in a lithium-ion cell plays a large role in the electrochemical properties and thermal stability. $LiPF_6$ is still the only successfully commercialized salt in lithium ion cells. By itself, $LiPF_6$ is not a stable salt and it starts to decompose to LiF and PF_5 at approximately 70°C. However, the addition of $LiPF_6$ into EC/DEC increases the thermal stability of both $Li_{0.81}C_6$ and $Li_{0.5}CoO_2$ electrodes. LiBETI [$LiN(SO_2CF_2CF_3)_2$] is a very stable salt and does not decompose until 320°C in TGA. However, the addition of LiBETI into EC/DEC seriously lowers the safety of Li_xC_6 [166]. An ARC experiment on 100 mg of $Li_{0.81}C_6$ in 100 mg of 1.0 M LiBETI electrolyte went to thermal runaway at round 180°C [166]. LiBOB is a stable salt and does not decompose until 300°C in TGA experiments in inert gas. There is a clear irreversible voltage plateau at around 1.8 V vs. Li when graphite reacts with Li in LiBOB EC/DEC electrolyte due to SEI formation, which apparently inhibits the reactivity of $Li_{0.81}C_6$ with EC/DEC. These results suggest the formation of a stable SEI on $Li_{0.81}C_6$ is a key to improve the thermal stability of the $Li_{0.81}C_6$ electrode. Although the addition LiBOB into EC/DEC improves the thermal stability of $Li_{0.81}C_6$, it increases the reactivity of positive electrodes, such as $Li_{0.5}CoO_2$, λ-MnO_2, and $Li_{0.5}[(Ni_{0.5}Mn_{0.5})_{0.2}Co_{0.8}]O_2$ [60] (except $LiFePO_4$). The reaction mechanism between positive electrode materials and LiBOB based electrolytes needs further investigation. New salts are desired to improve the thermal stability of both negative and positive electrode materials.

The addition of $LiPF_6$ into EC/DEC decreases the thermal stability of λ-MnO_2, $FePO_4$, and $Li_{0.5}[(Ni_{0.5}Mn_{0.5}]_xCo_{1-x}]O_2$ ($0.4 \leq x \leq 1$). These charged electrodes do not significantly react with EC/DEC until 190°C or even higher temperature. The addition of $LiPF_6$ reduces their thermal stability simply because $LiPF_6$ EC/DEC begins exothermic decomposition reactions in a similar temperature range. A new salt is needed to increase the thermal stability of these "safe" cathodes to an even higher level.

A breakthrough in lithium-ion batteries possibly will be a new electrolyte (new salt + solvent with flame retardant additive) that enables safer and larger batteries for EV and HEV applications.

3. Negative electrode materials. Metal alloys (such as SiSn) give high specific capacity up to 3500 mA h g^{-1}, compared to a theoretical capacity of 372 mA h g^{-1} for graphite. The thermal stability of such metal alloy electrodes needed to be characterized. Based on thermal-stability studies of negative electrode materials with different lithium binding energies, it was concluded that materials with higher lithium binding energy have higher thermal stability. Metal alloys have an average lithium binding energy around 0.3~1.0 V vs. Li, which is higher than $Li_{0.81}C_6$ (around 0.1 V). Therefore, provided surface areas can be made small, lithiated metal alloys should have a slightly higher thermal stability than $Li_{0.81}C_6$ in solvents or electrolytes.

4. Positive electrode materials. In this thesis, it was shown that the thermal-stability of the three charged positive electrode materials varies as, $Li[Ni_{0.5}Mn_{0.5}]O_2 \geq LiCoO_2 \geq Li[Ni_xCo_{1-x}]O_2$ ($0 < x < 1$). This strongly suggests that it is the presence of Mn that is responsible for the much higher thermal stability of $Li[(Ni_{0.5}Mn_{0.5})_xCo_{1-x}]O_2$ ($0.4 \leq x \leq 1$) over $LiCoO_2$. This may be caused by the higher bond enthalpies for Mn-O than for Co-O and Ni-O (listed in Table 5.3). This could make the release of O_2 more difficult, which would increase the thermal stability of the positive electrode materials containing Mn, such as $LiMn_2O_4$ and $Li[(Ni_{0.5}Mn_{0.5})_xCo_{1-x}]O_2$ ($0.4 \leq x \leq 1$).

The capacity leap if metal alloys are used as negative electrode materials in lithium-ion cells gives further urgency in the search for high-capacity positive electrodes in order to balance the capacities of the electrodes in the cells. $Li[(Ni_{0.5}Mn_{0.5})_xCo_y(Li_{1/3}Mn_{2/3})_z]O_2$ ($x + y + z = 1$) samples having a composition between $1/6 \leq z \leq 1/3$ and $1/12 \leq y \leq ¼$ show a discharge capacity over 200 mA h g^{-1},

which is about 50% higher than $LiCoO_2$ (around 140 mA h g^{-1}, 4.2 V). However, this improvement is not enough compared to the high capacity of metal alloys, up to 3500 mA h g^{-1}.

The general route to attaining the highest capacity of a positive electrode material is to utilize all the possible oxidation states of a compound during the reaction with Li. Tarascon proposed nanoparticles of transition metal oxides (MO, where M is Co, Ni, Cu, or Fe) as negative electrode materials [167, 168]. During the charge/discharge process, the following reaction occurs:

$$2Li^+ + 2e^- + MO \leftrightarrow Li_2O + M. \qquad [7\text{-}1]$$

Such materials show a high specific capacity of up to 700 mA h g^{-1}g and good cyclability (nearly 100% capacity retention after 100 cycles). The output voltage of reaction [7-1] can be improved by using metal fluorides (MF) instead of MO [169, 170]. Badway and Amatucci [169, 171, 172] cycled carbon-metal-fluoride-nanocomposites containing FeF_3 and achieved a high capacity of up to 237 mA h g^{-1} between 2.5 V and 4.5 V. Such materials after charging are believed to be very safe, since there will be no oxygen released at high temperatures. It will be interesting to check this out.

5. Full lithium-ion cells. This thesis shows that $Li_{0.81}C_6$, $Li_7Ti_5O_{12}$, and $FePO_4$ electrodes present high thermal stability in LiBOB based electrolyte. Therefore, full lithium-ion cells, graphite or $Li_4Ti_5O_{12}$/LiBOB EC:DEC/$LiFePO_4$, should have high tolerance to thermal abuse. It will be very exciting to do abuse tests of such cells.

References

1. H. Takeshita, presentation at *The 20th International Seminar & Exhibit on Primary & Secondary Batteries*, March 2003.

2. W. Schalkwijk and B. Scrosati, *Advances in Lithium-ion Batteries*, Kluwer Academic/Plenum Publishers, New York, 2002.

3. K. Xu, M.S. Ding, S. Zhang, J.L. Allen, and T.R. Jow, *J. Electrochem. Soc.*, **149**, A622-A626 (2002).

4. K. Xu, S. Zhang, J.L. Allen, and T.R. Jow, *J. Electrochem. Soc.*, **149**, A1079 (2002).

5. Y. Baba, S. Okada, J-I Yamaki, *Solid State Ionics*, **148**, 311 (2002).

6. J. S. Gnanaraj, E. Zinigrad, L. Asraf, H.E. Gottlieb, M. Sprecher, M. Schmidt, W. Geissler, and D. Aurbach, *J. Electrochem. Soc.*, **150**, A1533 (2003).

7. Y. Hyung, D. Vissers, G. Henriksen, K. Amine, P. Roth, and D. Doughty, Abstract #243, *The 204th Meeting of the Electrochemical Society*, Orlando, Florida, Oct 12-16, 2003.

8. R. Spotnitz and J. Franklin, *Journal of Power Sources,* **113**, 81 (2003).

9. Y. Nishi, *Journal of Power Sources,* **100**, 101 (2001).

10. N. Sato, *Journal of Power Sources,* **99**, 70 (2001).

11. Ph. Biensan, B. Simon, J.P. Peres, A. Guibert, M. Broussely, J.M. Bodet, and F. Perton, *Journal of Power Sources,* **81-82**, 906 (1999).

12. D. Doughty, P. Butler, R. Jungst, and E. Roth, *Journal of Power Sources*, **110**, 357 (2002).

13. www.agmbat.co.uk/liiontechnology.html/

14. K. Sayamasa, H. Yagi, Y. Kato, S. Matsuta, H. Tarui, and S. Fujitani, Abstract #52, *The 11th International Meeting of Lithium Batteries*, Monterey, CA (2002).

15. L.Y. Beaulieu, K.C. Hewitt, R.L. Turner, A. Bonakdarpour, A.A. Abdo, L. Christensen, K.W. Eberman, L.J. Krause, and J.R. Dahn, *J. Electrochem. Soc.*, **150**, A149 (2003).

16. L.Y. Beaulieu, T.D. Hatchard, A. Bonakdarpour, M.D. Fleischauer, and J.R. Dahn, *J. Electrochem. Soc.*, **150**, A1457 (2003).

17. K.D. Kepler, J.T. Vaughey, and M.M. Thackeray, *Electrochem. Solid-State Lett.*, **2** 307 (1999).

18. H.Y. Lee, and S.M. Lee, *Journal of Power Sources,* **112**, 649 (2002).

19. H. Kim, J. Choi, H, J, Sohn, and T. Kang, *J. Electrochem. Soc.*, **146**, 4401 (1999).

20. A. Hayashi, M. Nakai, M. Tatsumisago, T. Minami, and M. Katada, *J. Electrochem. Soc.*, **150**, A582 (2003).

21. S. Jouanneau, K.W. Eberman, L.J. Krause, and J.R. Dahn, *J. Electrochem. Soc.*, **150**, A1637 (2003).

22. Z. Lu and J.R. Dahn, *J. Electrochem. Soc.*, **148**, A710 (2001).

23. D.D. MacNeil, Z. Lu, and J.R. Dahn, *J. Electrochem. Soc.*, **149**, A1332 (2002).

24. Z. Lu, D.D. MacNeil, and J.R. Dahn, *Electrochem. Solid-State Lett.*, **4**, A191 (2001).

25. T. Ohzuku and Y. Makimura, *Chemistry Letters*, **8**, 744 (2001).

26. R.M. Dell, *Solid State Ionics*, **134**, 139 (2000).

27. M. Armand, *Materials for Advanced Batteries*, Plenum, New York (1980).

28. G. Ceder, Y-M. Chiang, D.R. Sadoway, M.K. Aydinol, Y-I. Jang, and B. Huang, *Nature*, **392**, 694 (1998).

29. M. Richard and J.R. Dahn, *Journal of Power Sources*, **83**, 71 (1999).

30. D. Aurbach, *Journal of Power Sources,* **89**, 206 (2000).

31. F. Kong, R. Kostechi, G. Nadeau, X. Song, K. Zaghib, K. Kinoshita, and F. McLarnon, *Journal of Power Sources,* **97-98**, 58 (2001)

32. R. L. Turner, US Patent 20020162606 (2002).

33. M. Richard and J.R. Dahn, *J Electrochem Soc.*, **146**, 2068 (1999).

34. M. Richard and J.R. Dahn, *J Electrochem Soc.*, **146**, 2078 (1999).

35. M. Richard, Ph. D Thesis, Dalhousie University (1998).

36. S. Bourderau, T. Brousse, and D.M. Schleich, *Journal of Power Sources,* **81-82**, 233 (1999).

37. H. Jung, M. Park, Y-G. Yoon, G-B. Kim, S-K. Joo, *Journal of Power Sources,* **115**, 346 (2003).

38. M. Obrovac, Abstract #425, *The 204th Meeting of the Electrochemical Society*, Orlando, Florida, Oct 12-16, 2003.

39. T. Takamura, S. Ohara, J. Suzuki, and K. Sekine, Abstract #23, *LIBD 2003*, Bordeaux-Arcachon, France, 14-19 September, 2003.

40. L.Y. Beaulieu, S.D. Beattie, and J.R. Dahn, *J. Electrochem. Soc.*, **150**, A419 (2003).

41. J. Li, H. Li, Z. Wang, L. Chen, and X. Huang, *Journal of Power Sources,* **107**, 1 (2002).

42. B. Veeraraghavan, A. Durairajan, B. Haran, B. Popov, and R. Guidotti, *J. Electrochem. Soc.*, **149**, A675 (2002)

43. S. Yang, F. Quan, P.Y. Zavalij, and M.S. Whittingham, Abstract #22, *LIBD 2003*, Bordeaux-Arcachon, France, 14-19 September, 2003.

44. G.A. Nazri, Abstract #75, *LIBD 2003*, Bordeaux-Arcachon, France, 14-19 September, 2003.

45. L. Beaulieu, T.D. Hatchard, A. Bonakdarpour, M. Fleischauer, and J.R. Dahn, *J. Electrochem. Soc.*, **150**, A1457 (2003).

46. L. Beaulieu, K.W. Eberman, L.J. Krause, and J.R. Dahn, *Electrochem. Solid-State Lett.*, **4**, A137 (2001).

47. http://www.mineralsuk.com/britmin/cobalt_23Apr04.pdf (World Mineral Statistics Database).

48. J.R. Dahn, E.W. Fuller, M. Obrovac, U. von Sacken, *Solid State Ionics,* **69**, 265 (1994).

49. D.D. MacNeil and J.R. Dahn, *J. Electrochem Soc.*, **148**, A1211 (2001).

50. D.D. MacNeil, T.D. Hatchard, and J.R. Dahn, *J. Electrochem Soc.*, **148**, A663 (2001).

51. T.D. Hatchard, D.D. MacNeil, A. Basu, and J.R. Dahn, *J. Electrochem Soc.*, **148**, A755 (2001).

52. D.D. MacNeil, Ph.D Thesis, Dalhousie University, 2001.

53. K. Amine, I. Belharouak, J. Liu, A. Kahaian, D. Vissers, and G. Henriksen, Abstract #419, *The 204th Meeting of the Electrochemical Society*, Orlando, Florida, Oct 12-16, 2003.

54. L-F. Wang, C-C. Ou, K. A. Striebel, and J-S. Chen, *J. Electrochem. Soc.*, **150**, A905 (2003).

55. G.G. Amatucci, N. Pereira, T. Zheng, and J.M. Tarascon, *J. Electrochem. Soc.*, **148**, A171 (2001).

56. J-F. Lee, Y-W. Tsai, R. Santhanam, B.J. Hwang, M-H. Yang, and D-G. Liu, *Journal of Power Sources,* **119-121**, 721 (2003).

57. J. Liu, A. Kahaian, and K. Amine, Abstract #257, *The 204th Meeting of the Electrochemical Society*, Orlando, Florida, Oct 12-16, 2003.

58. B. Morton, Vancouver Sun, www.canada.com/vancouver/vancouversun/index.html, January 26th, 2005.

59. A.S. Andersson, J.O. Thomas, B. Kalska, and L. Haggstrom, *Electrochemical Solid-State Letters,* **3**, 66 (2000).

60. J. Jiang and J.R. Dahn, *Electrochem. Commun.*, **6**, 39 (2004).

61. M. Takahashi, H. Ohtsuka, K. Akuto, and Y. Sakurai, Abstract #345, *The 204th Meeting of the Electrochemical Society*, Orlando, Florida, Oct 12-16, 2003.

62. J. Molenda, A. Stoklosa, and T. Bak, *Solid State Ionics*, **36**, 53 (1989).

63. S-Y. Chung, J.T. Bloking, and Y-M. Chiang, *Nature Materials*, **1**, 123-128 (2002).

64. N. Ravet, S. Besner, M. Simoneau, A. Vallee, and A. Armand, Canadian Patent, 2,307,119.

65. Z. Chen and J.R. Dahn, *J. Electrochem. Soc.*, **149**, A1184 (2002).

66. J. Jiang and J.R. Dahn, *Electrochimica Acta*, (accepted).

67. Z. Lu, D. D. MacNeil, and J.R. Dahn, *Electrochem. Solid-State Lett.*, **4**, A200 (2001).

68. A. Hammami, N. Raymond, and M. Armand, *Nature*, **424**, 635 (2003).

69. K. Numata, C. Sakaki, and S. Yamanaka, *Chemistry Letters,* 725 (1997).

70. Z. Lu and J.R. Dahn, *J. Electrochem. Soc.*, **149**, A815 (2002).

71. S-H. Kang and K. Amine, *Journal of Power Sources,* **124**, 533 (2003).

72. K.S. Park, M.H. Cho, S.J. Jin, and K.S. Nahm, *Electrochem. Solid-State Lett.,* **7**, A239 (2004).

73. Y.J. Park, Y-S. Hong, X. Wu, M.G. Kim, K.S. Ryu, and S.H. Chang, *J. Electrochem. Soc.,* **151**, A720 (2004).

74. D.A.R. Barkhouse and J.R. Dahn, accepted for publication in *J. Electrochem. Soc.*

75. J. Jiang, T. Buhrmester, K.W. Eberman, L.J. Krause, and J.R. Dahn, *J. Electrochem. Soc.,* **152**, A19 (2005).

76. J. Jiang, K.W. Eberman, L.J. Krause, and J.R. Dahn, *J. Electrochem. Soc.,* 152, A566 (2005).

77. J. Jiang and J.R. Dahn, submitted to *Electrochimica Acta.*

78. K. Numata, C. Sakaki, and S. Yamanana, *Solid State Ionics,* **117**, 257 (1999).

79. Y. Sun, C. Ouyang, Z. Wang, X. Huang, and L. Chen, *J. Electrochem. Soc.,* **151**, A504 (2004).

80. K. Eberman and L. Krause, Abstract #402, *The 204th Meeting of The Electrochemical Society,* Orlando, Florida, October 12-16, 2003.

81. S.E. Sloop, J.K. Pugh, S. Wang, J.B. Kerr, and K. Kinoshita, *Electrochem. Solid-State Lett.,* **4**, A42 (2001).

82. A.D. Holding, D. Pletcher, and R.V. H. Jones, *Electrochim. Acta,* **34**, 1529 (1989).

83. J.T. Dudley, D.P. Wilkinson, G. Thomas, R. LeVae, S. Woo, et al., *Journal of Power Sources,* **35**, 59 (1991).

84. D.D. MacNeil and J.R. Dahn, *J. Electrochem. Soc,* **148**, A1205 (2001).

85. J. Jiang and J.R. Dahn, *Electrochem. Solid-State Lett.,* **6**, A180 (2003).

86. J. Jiang and J.R. Dahn, *Electrochimica Acta,* **49**, 2661 (2004).

87. J. Jiang and J.R. Dahn, *Electrochimica Acta,* **49**, 4599 (2004).

88. J. Jiang and J.R. Dahn, *J. Electrochem. Soc.*, **151**, A609 (2004).

89. W. Xu and C.A. Angell, *Electrochem. Solid-State Lett.,* **4**, E1 (2001).

90. K. Xu, S. Zhang, T.R. Jow, W. Xu, and C.A. Angell, *Electrochem. Solid-State Lett.*,**5**, A26 (2002).

91. N. Katayama, T. Kawamura, Y. Baba, and J-I. Yamaki, *Journal of Power Sources,* **109**, 321 (2002).

92. K. Xu, S. Zhang, B.A. Poese, and T.R. Jow, *Electrochem. Solid-State Lett.*, **5**, A259 (2002).

93. K. Sato, I. Yamazaki, S. Okada, J-I. Yamaki, *Solid State Ionics,* **148**, 463 (2002).

94. J-I. Yamaki, I. Yamazaki, M. Egashira, and S. Okada, *Journal of Power Sources,* **102**, 288 (2001).

95. M. Ihara, B.T. Hang, K. Sato, M. Egshira, S. Okada, and J-I. Yamaki, *J. Electrochem. Soc.*, **150**, A1476 (2003).

96. J. Arai, H. Katayama, and H. Akahoshi, *J. Electrochem. Soc.*, **149**, A217 (2002).

97. J. Arai, *J. Electrochem. Soc.*, **150**, A219 (2003).

98. H. Maleki, G. Deng, A. Anani, and J.N. Howard, *J. Electrochem. Soc.*, **146**, 3224 (1999).

99. H. Maleki, G. Deng, I. Kerzhner-Haller, A. Anani, and J.N. Howard, *J. Electrochem. Soc.*, **147**, 4470 (2000).

100. D. Aurbach, E. Zinigrad, Y. Cohen, and H. Teller, *Solid State Ionics*, **148**, 405 (2002).

101. J-I. Yamaki, H. Takatsuji, T. Kawamura, and M. Egashira, *Solid State Ionics*, **148**, 241 (2002).

102. J-I Yamaki, Y. Baba, N. Katayama, H. Takatsuji, M. Egashira, and S. Okada, *Journal of Power Sources,* **119-121**, 789 (2003).

103. Underwriter Laboratories Inc., *Standard for Safety 1642 – Lithium Batteries*, April (1995).

104. D.I. Townsend and J.C. Tou, *Thermochemica Acta,* **37**, 1 (1980).

105. D.D. MacNeil, S. Trussler, H. Fortier, and J.R. Dahn, *Thermochimica Acta*, **386**, 153 (2002).

106. J.C. Oxley, J.L. Smith, E.Rogers, W. Ye, A.A. Aradi, and T.J. Henly, *Energy and Fuels,* **14**, 1251 (2000).

107. J.C.M. Torfs, L. Deij, A.J. Dorrepaal, and J.C. Heijens, *Anal. Chem.*, **56**, 2863 (1984).

108. E. Gimzewski and G. Audley, *Thermochimica Acta,* **214**, 129 (1993).

109. J.R. Dahn, B. Van, and U. Vonsacken, U.S. Patent 4,965,150 (1990).

110. R.A. Dunlap, D.A. Small, D.D. MacNeil, M.N. Obrovac, J.R. Dahn, *Journal of Alloys and Compounds*, **289**, 135 (1999).

111. Rietica v1.71, windows version of LHPM; R. J. Hill and C. J. Howard, *J. Appl. Crystallogr.*, **18** (1985) 173.

112. A.F. Wells, *Structural Inorganic Chemistry*, Clarendon Press, Oxford, 1984.

113. Z. Tao, J.N. Reimers, and J.R. Dahn, *Physical Review B*, **51**, 734 (1995).

114. R.C. Weast, D.R. Lide, and M.J. Astle, *CRC Handbook of Chemistry and Physics,* CRC Press, Inc., Florida, 70th edition, 1989.

115. A. Du Pasquier, F. Disma, T. Bowmer, A.S. Gozdz, G.G. Amatucci, and J.M. Tarascon, *J. Electrochem. Soc.*, **145**, 472 (1998).

116. D. Aurbach, M.L. Daroux, P.W. Faguy, and E. Yeager, *J. Electrochem. Soc.*, **134**, 1611 (1987).

117. P.J. Linstrom and W.G. Mallard, Eds., NIST Chemistry WebBook, NIST Standard Reference Database Number 69, March 2003, National Institute of Standards and Technology, Gaithersburg MD, 20899 (http://webbook.nist.gov).

118. K. Xu, U. Lee, S. Zhang, M. Wood, and T.R. Jow, *Electrochem. Solid-State Lett.*, **6**, A144 (2003).

119. H. Kawaji, M. Takematsu, T. Tojo, T. Atake, A. Hirano, and R. Kanno, *Journal of Thermal Analysis and Calorimetry,* **68**, 833 (2002).

120 H. Kawaji, T. Oka, T. Tojo, T. Atake, A. Hirano, and R. Kanno, *Solid State Ionics,* **152-153**, 195 (2002).

121 M. Tachibana, T. Tojo, H. Kawaji, T. Atake, M. Yonemura, and R. Kanno, *Physical Review B,* **68**, 094421 (2003).

122. H.S. Carslaw and J.C. Jaeger, *Conduction of Heat in Solids*, Second Edition, Clarendon Press, Oxford (1959).

123. T.D. Hatchard, D.D. MacNeil, D.A. Stevens, L. Christensen and J.R. Dahn, *Electrochem. Solid State Lett.*, **3**, 305 (2000).

124. K.M. Colbow, J.R. Dahn, and R.R. Haering, *Journal of Power Sources,* **26**, 397 (1989).

125. T. Ohzuku, A. Ueda, and N. Yamamoto, *J. Electrochem. Soc.*, **142**, 1431 (1995).

126. W. Li and J.R. Dahn, *J. Electrochem. Soc.*, **142**, 1742 (1995).

127. M. Zhang and J.R. Dahn, *J. Electrochem. Soc.*, **143**, 2730 (1996).

128. K. Nakahara, R. Nakajima, T. Matsushima, and H. Majima, *Journal of Power Sources,* **117**, 131 (2003).

129. D.W. Murphy, P.A. Christian, F.J. DiSalvo, J.N. Carides, and J.Y. Waszczak, *J. Electrochem. Soc.*, **128**, 2053 (1981).

130. S. Andersson, *Acta Cryst.*, **15**, 201 (1962).

131. Ch. Leroux, G. Nihoul, and G. Van Tendeloo, *Physical Review B,* **57**, 5111 (1998).

132. A.S. Andersson, J.O. Thomas, B. Kalska, and L. Haggstrom, *Electrochem. Solid-State Lett.*, **3**, 66 (2002).

133. G.G. Amatucci and J.M. Tarascon, *J. Electrochem. Soc.*, **149**, K31 (2002).

134. A.K. Pahdi, K.S. Najundaswamy, and J.B. Goodenough, *J. Electrochem. Soc.,* **144,** 1188 (1997)

135. Y. Gao and J.R. Dahn, *J. Electrochem. Soc.,* **143,** 100 (1996)

136. X.Q. Yang, X. Sun, S.J. Lee, J. McBreen, S. Mukerjee, M.I. Daroux, and X.K. Xing, *Electrochem. Solid-State Lett.*, **2**, 157 (1999).

137. O. Schilling, Ph.D Thesis, Dalhousie University, Canada (1997).

138. D.D. MacNeil, L. Christensen, J. Landucci, J.M. Paulsen, and J.R. Dahn, *J. Electrochem. Soc.,* **147,** 970 (2000).

139. C.H. Bamford and C.F.H. Tipper, *Comprehensive Chemical Kinetics,* (Vol. 22), Elsevier Scientific Publishing Company, 1980.

140. C. Drouet and P. Alphonse, *J. Mater. Chem.*, **12**, 3058 (2002).

141. B.V. Lvov, *Thermochimica Acta,* **364**, 99 (2000).

142. A.K. Nikumbh, A.E. Athare, and S.K. Pardeshi, *Thermochimica Acta,* **326**, 187 (1999).

143. B. Malecka, E. Drozdz-Ciesla, and A. Malecki, *Journal of Thermal Analysis and Calorimetry,* **68**, 819 (2002).

144. B. Makecka, E. Drozdz-Ciesla, and P.K. Olszewski, *Journal of Thermal Analysis and Calorimetry,* **74**, 485 (2003).

145. D.D. MacNeil and J.R. Dahn, *J. Phys. Chem. A,* **105**, 4430 (2001).

146. A.S. Andersson, B. Kalska, L. Häggström, and J.O. Thomas, *Solid State Ionics,* **130** (2000) 41.

147. R.W.G. Wyckoff, *Crystal Structure,* 2nd edition, Volumes 1, 2, and 3, Robert E. Krieger Publishing Company, 1981.

148. H. Arai, S. Okada, Y. Sakurai, and J.I. Yamaki, *J. Electrochem. Soc.,* **144,** 3117 (1997).

149. J. Cho, H. Jung, Y.C. Park, G. Kim, and H.S. Lim, *J. Electrochem. Soc.,* **147,** 15 (2000).

150. M. Guilmard, L. Croguennec, D. Denux, and C. Delmas, *Chem. Mater.,* **15**, 4476 (2003).

151. M. Guilmard, L. Croguennec, D. Denux, and C. Delmas, *Chem. Mater.,* **15**, 4484 (2003).

152. J.K. Ngala, N.A. Chernova, M. Ma, M. Mamak, P.Y. Zavalij, and M.S. Whittingham, *J. Mater, Chem.,* **14**, 214 (2004)

153. M.S. Whittingham, *Chemical Reviews,* **104**, 4271 (2004).

154. L. Zhang, K. Takada, N. Ohta, L. Wang, T. Sadaki, and M. Watanabe, *Materials Letters,* **58**, 3197 (2004).

155. C.S. Johnson, J-S. Kim, C. Lefief, N. Li, J.T. Vaughey, M.M. Thackeray, *Electrochemistry Communications*, **6**, 1085 (2004).

156. Y.J. Park, M.G. Kim, Y-S. Hong, X. Wu, K.S. Ryu, and S.H. Chang, *Solid State Communications,* **127**, 509 (2003).

157. L.H. Yu, Y.L. Cao, H.X. Yang, X.P. Ai, and Y.Y. Ren, *Materials Chemistry and Physics*, **88**, 353 (2004).

158. Y-K. Sun, S-H. Kang, and K. Amine, *Materials Research Bulletin,* **39**, 819 (2004).

159. S-S. Shin, Y-K. Sun, and K. Amine, *Journal of Power Sources*, **112**, 634 (2002).

160. J-H. Kim, C.W. Park, and Y-K. Sun, *Solid State Ionics,* **164**, 43 (2003).

161. J-H. Kim, C.S. Yoon, and Y-K. Sun, *J. Electrochem. Soc.,* **150**, A538 (2003).

162. M. Doyle, J. Newman, and J.N. Reimers, *Journal of Power Sources,* **52**, 211 (1994).

163. Z. Chen, Z. Lu, and J.R. Dahn, *J. Electrochem. Soc.,* **149**, A1064 (2002).

164. SANYO Electric Co., Ltd., News Release, *"SANYO to Start Production of Prismatic Lithium ion Batteries that Utilize the Neo Hybrid Positive Electrode"*, November 1st, 2004. (http://www.global-sanyo.com/news/0411/1101-e.html).

165. K. Xu, M.S. Ding, S. Zhang, J.L. Allen, and T.R. Jow, *J. Electrochem. Soc.,* **149**, A622 (2002).

166. J. Jiang and J.R. Dahn, "*Effects of Electrolyte Salt on the Thermal Stability of $Li_{0.81}C_6$ in Electrolyte for Lithium-ion Batteries*", Abstract #42 in Lithium-ion Battery Discussion on Electrode Materials (2003 LIBD), Bordeaux-Arcachon, France, September 14-19 (2003).

167. P. Poizot, S. Laruelle, S. Grugeon, L. Dupond, and J.M. Tarascon, *Nature,* **407** (2000).

168. J.M. Tarascon and M. Armand, *Nature,* **414**, 359 (2001).

169. F. Badway, I. Plitz, F. Cosandey. N. Pereira, and G.G. Amatucci, *"Reversible conversion enabled by metal fluoride nanocomposites: a new avenue to ultra high energy density positive electrodes"*, Abstract #82 in Lithium-ion Battery Discussion on Electrode Materials (2003 LIBD), Bordeaux-Arcachon, France, September 14-19 (2003).

170. H. Li, G. Richter, and J. Maier, *Advanced Materials,* **15**, 736 (2003).

171. F. Badway, F. Cosandey, N. Pereira, and G.G. Amatucci, *J. Electrochem. Soc.,* **150**, A1318 (2003).

172. F. Badway, N. Pereira, F. Cosandey, and G.G. Amatucci, *J. Electrochem. Soc.,* **150**, A1209 (2003).